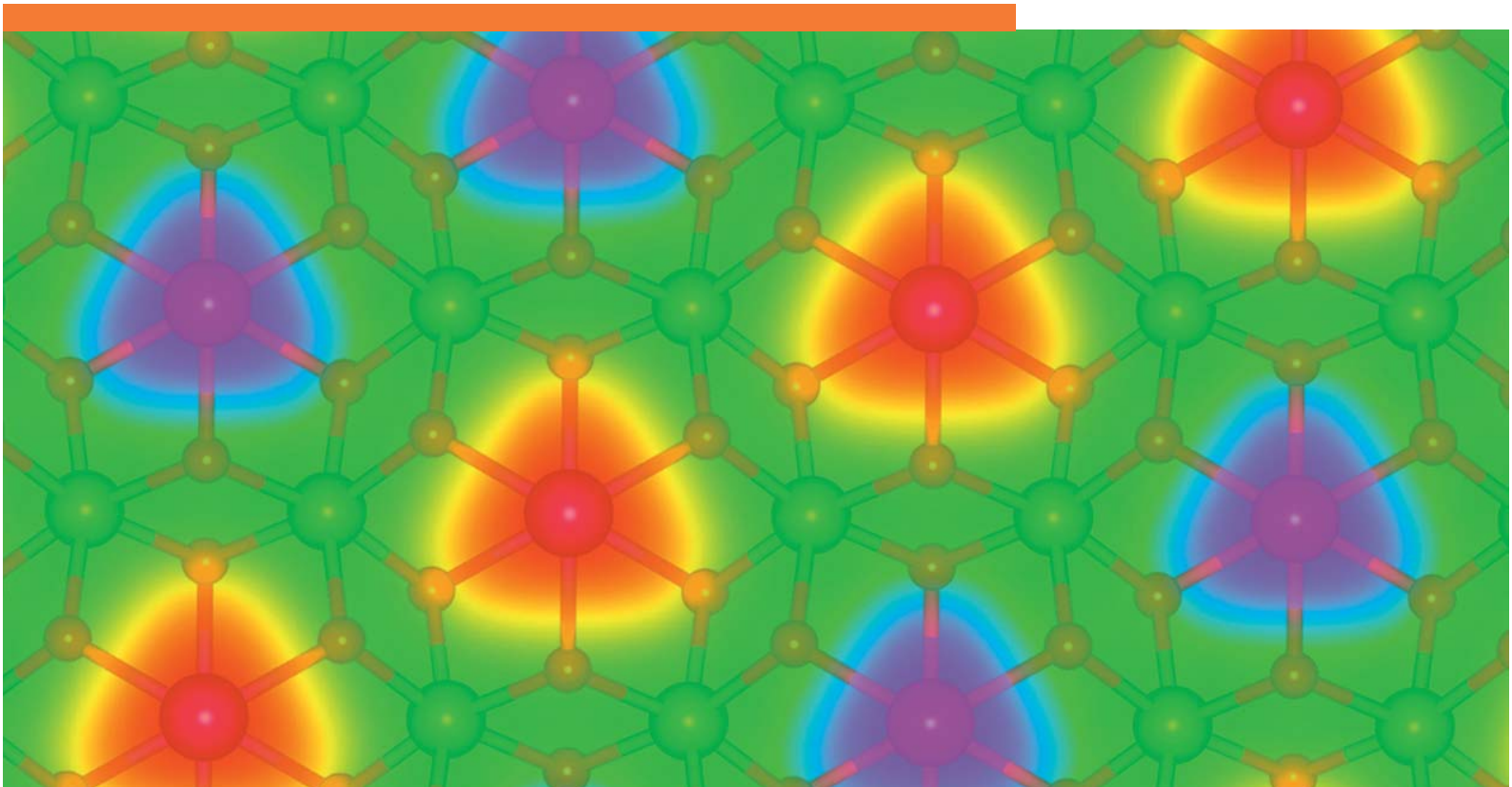# ANNUAL REPORT 2022

Institute of Ion Beam Physics
and Materials Research

HZDR-123

Wissenschaftlich-Technische Berichte
HZDR–123

Annual Report 2022

Institute of Ion Beam Physics and Materials Research

Editors

J. Fassbender, M. Helm,
M. Zahn, P. Zahn

HZDR

HELMHOLTZ ZENTRUM
DRESDEN ROSSENDORF

Cover Picture - On the hunt for ultra-thin materials using data mining

Two-dimensional (2D) materials are traditionally associated with the sheets forming bulk layered crystals bonded by weak van der Waals interactions. The recent surprising synthesis of atomically thin 2D sheets from *non*-van der Waals bonded oxides opens up a new perspective for this diverse class of nanostructures. By leveraging data-driven research principles and a structure-based search criterion several dozens of candidates of this new materials class could be predicted.

The figure shows the semitransparent structure of germanium manganese oxide ($GeMnO_3$), one of the newly discovered 2D materials, superimposed on its surface magnetic structure. The atomic species are represented by the following colors: manganese (Mn) magenta, germanium (Ge) green, and oxygen (O) red.

The color pattern depicts regions in the vicinity of magnetic ions where the magnetization points out of the plane (red) or into the plane (blue). This strong spatial variation of the magnetic information could, for instance, play a crucial role for data storage applications.

Image: © HZDR / Rico Friedrich

This report is also available at https://www.hzdr.de/FWI.

Helmholtz-Zentrum Dresden - Rossendorf e.V.
Institute of Ion Beam Physics and Materials Research (IIM)

Bautzner Landstraße 400
01328 Dresden
Germany

Directors	Prof. Dr. M. Helm	Prof. Dr. J. Fassbender
Phone	+49 351 260 2260	+49 351 260 3096
Fax	+49 351 260 3285	+49 351 260 3285
Email	m.helm@hzdr.de	j.fassbender@hzdr.de

www.hzdr.de/FWI

Preface by the directors

The year 2022 gave us first indications of the end of COVID-19 pandemic, also through the resurgence of on-site conferences and other business trips. Yet occasional online zoom conferences will for sure stay with us, since everybody has recognized their usefulness in certain situations. Yet without break, the world has entered another severe crisis through the Russian invasion of Ukraine. This also has had manifold implications for international collaborations and has shown us that science cannot be completely separated from politics. In addition, the subsequent price increases, in particular for energy, scientific equipment and civil construction place a strong financial burden on us. Increasing wages, well-deserved for our staff, will however put severe restrictions on future personnel planning at the institute.

The scientific productivity of the institute has remained on a very high level, counting 174 publications with an average impact factor as high as 7.4. Eight outstanding and representative publications are reprinted in this Annual Report. An amazing number of 24 new third-party projects were granted, among them 14 DFG projects. The total number of simultaneously active DFG projects amounted to 30 in December 2022!

In the annual competition for HZDR prizes, our institute was again very successful: Dr. Ruslan Salikhov, together with Dr. Sergey Kovalev from the Institute of Radiation Physics, received the HZDR Forschungspreis for their joint work on spin-wave excitation by Terahertz (THz) radiation. Dr. Klara Lünser was awarded an HZDR Doktorandenpreis for her thesis entitled "Martensitische Phasenumwandlungen und Zwillingsbildung in epitaktisch gewachsenen Nickel-Titan-Schichten".

The new 1-MV facility for accelerator mass spectrometry (AMS), is being set up at NEC (National Electrostatics Corporation). Construction of the dedicated building to house the accelerator, the SIMS and including additional chemistry laboratories is finished by mid-2023. Then one AMS injection system featuring also an ion cooler can be installed. Factory tests of the remaining parts of the AMS system are scheduled for 2023 at NEC as well.

In the course of developing a strategy for the HZDR - **HZDR 2030+** Moving Research to the NEXT Level for the NEXT Gens - *six research focus areas* for our institute were identified, those include

- Interaction of highly charged, low-energy or focused ion beams with solid surfaces, including atomistic simulations,

- Accelerator mass spectrometry,

- Ion-based synthesis and modification of semiconductor structures for nano- and optoelectronics,

- Ultrafast and terahertz spectroscopy of low-energy excitations in semiconductors and quantum materials, in particular using the free-electron laser at ELBE,

- Structural and electronic properties of 2D materials,

- Hybrid quantum systems as a link between photonics, electronics and magnonics,

- Magnonics and opto-spintronics: new hardware concepts for neuromorphic computing.

Last year also brought the establishment of a new department on "Quantum Technologies". This was a consequence of the successful work of PD Dr. Georgy Astakhov, who also received a high-rank international offer. His new position as department head enabled us to keep him at HZDR and thus strengthen our activities in this important, rising research field. Also a new Young Investigator Group on "Autonomous Materials Thermodynamics" was established jointly with DRESDEN concept - the alliance of TU Dresden with other research institutes in the Dresden area, with Dr. Rico Friedrich as its leader.

Finally, we would like to cordially thank all partners, friends, and organizations who supported our progress in 2022. First and foremost we thank the Executive Board of the Helmholtz-Zentrum Dresden-Rossendorf, the Ministry of Science, Culture and Tourism of the Free State of Saxony, and the Ministries of Education and Research, and of Economic Affairs and Climate Action of the Federal Government of Germany. Many partners from universities, industry and research institutes all around the world contributed essentially, and play a crucial role for the further development of the institute. Last but not least, the directors would like to thank all members of our institute for their efforts in these very special times and excellent contributions in 2022.

Prof. Manfred Helm   Prof. Jürgen Fassbender

Contents

Selected Publications

Statistics

Selected Publications

5 μm

Copyright remarks

The following journal articles are reprinted with kind permission from:

Mid- and far-infrared localized surface plasmon resonances in chalcogen-hyperdoped silicon
Wang, M.; Yu, Y.; Prucnal, S.; Berencén, Y.; Shaikh, M.S.; Rebohle, L.; Khan, M.B.; Zviagin, V.;
Hübner, R.; Pashkin, A.; Erbe, A.; Georgiev, Y.M.; Grundmann, M.; Helm, M.; Kirchner, R.; Zhou, S.
Nanoscale **14**, 2826 (2022)

RESEARCH ARTICLE

Fully Encapsulated and Stable Black Phosphorus Field-Effect Transistors

Himani Arora,* Zahra Fekri, Yagnika Nandlal Vekariya, Phanish Chava, Kenji Watanabe, Takashi Taniguchi, Manfred Helm, and Artur Erbe

Black phosphorus (BP) has quickly gained popularity in the scientific community owing to its interesting semiconducting properties, such as direct bandgap, high mobility, and intrinsic ambipolar behavior. However, its sensitivity to oxygen, moisture, and other air species has restricted its integration into active devices. Here, the lithography-free via-encapsulation scheme to fabricate fully-encapsulated BP-based field-effect transistors (FETs) is employed. The full encapsulation is achieved by sandwiching the BP layers between the top and bottom hexagonal boron nitride (hBN) layers; top hBN passivating the BP layer from the environment and bottom hBN acting as a spacer and suppressing charge transfer to the BP layer from the SiO_2 substrate. The embedded via-metal electrodes allow the authors to perform reliable electrical measurements of the BP FETs. Based on these results, it is found that the electronic properties of the via-encapsulated BP FETs are significantly improved compared to unencapsulated devices. This further establishes that the via-contacting scheme leads to superior results compared to graphene-hBN heterostructures and bare hBN layers combined with evaporated metal contacts (both use top and bottom hBN to encapsulate BP) by revealing higher mobility, lower hysteresis, and long-term ambient-stability in BP FETs.

1. Introduction

Research on semiconducting 2D materials (2DMs) has demonstrated the potential of these materials for future electronics.[1–5] On the one hand, the already established 2D semiconductors,

such as transition metal dichalcogenides (TMDCs) (MoS_2, WS_2, etc.) are being intensively studied, on the other hand, the search for novel 2D materials is at a rapid pace.[6–10] In the last years, black phosphorus (BP), also known as few-layer phosphorene, an allotrope of phosphorus, has come into the limelight.[4,11–13] Monolayer BP or phosphorene is a one-atom-thick sheet of covalently bonded phosphorus atoms arranged in a puckered honeycomb structure with in-plane anisotropy.[14–16] Individual layers, when stacked onto each other, are held together by weak van der Waals (vdW) forces to form multilayered or bulk structures, which can be easily cleaved into thin layers using an adhesive tape.[17] Unlike TMDCs, BP has a direct bandgap at all layer thicknesses, which varies from ≈0.3 eV in bulk to ≈2 eV in monolayers, hence covering a broad detection spectrum from ultraviolet to infrared wavelengths.[14,16,18,19] The presence of this direct and tunable bandgap together with high electrical mobilities of ≈1000 cm^2 V^{-1} s^{-1} reported at room temperature in BP help to overcome some of the drawbacks of graphene (Gr) and TMDCs in applications as field effect transistors (FETs).[15,20] Thus, these materials seem to be ideally suited for applications in electronics and optics that are based on FETs. In addition, FETs based on BP have shown intrinsic ambipolar conduction, indicating its possible use in reconfigurable electronics.

Despite the intriguing properties of BP, its integration into active devices is severely hampered because of its poor chemical stability under ambient conditions. The degradation of BP flakes can be observed easily under an optical microscope.[17,21,22] Several reports revealed the formation of pits and bubbles on the surface of freshly exfoliated BP within a few hours of air exposure, which kept growing over time in shape, height, and roughness until the BP flake is fully disintegrated and etched away from the substrate.[17,21,22] Castellanos-Gomez et al. attributed the degradation of BP to a strong out-of-plane dipole moment on its surface which makes it very hydrophilic.[17] The strong dipole–dipole interactions between water and BP distort the lattice structure and modify its surface morphology. Using X-ray photoelectron spectroscopy measurements Wood et al. revealed amorphization of pristine BP and eventual degradation to PO$_x$ in air, indicating permanent damage to the structural

H. Arora, Z. Fekri, Y. N. Vekariya, P. Chava, M. Helm, A. Erbe
Helmholtz Zentrum Dresden Rossendorf
Bautzner Landstrasse 400, 01328 Dresden, Germany
E-mail: h.arora@hzdr.de
K. Watanabe
Research Center for Functional Materials
National Institute for Materials Science
Tsukuba 305-0044, Japan
T. Taniguchi
International Center for Materials Nanoarchitectonics
National Institute for Materials Science
1-1 Namiki, Tsukuba 305-0044, Japan

12   Selected Publications

ADVANCED
SCIENCE NEWS ─────────
www.advancedsciencenews.com

ADVANCED
MATERIALS
TECHNOLOGIES
www.advmattechnol.de

and chemical integrity of the BP flakes.[21] Because the surface is the first one to come in contact with air, the degradation starts there and slowly penetrates deeper into the layers. However, the 2D layers are not only sensitive to air but also to other environmental influences such as charge traps in the dielectric, chemical contaminations and resists during lithographic processes, and physical damages during metal evaporations, which lead to fast and uncontrollable morphological changes and poor device performance.[8,23,24] Therefore, an effective encapsulation technique is necessary to passivate the 2D layers against various degrading factors in order to study their fundamental properties as well as to achieve high-performance and stable devices.

In the last years, several encapsulation schemes were demonstrated to passivate the BP layers. Doganov et al. deposited Gr or hBN flakes on freshly exfoliated BP flakes in an Ar-filled glovebox for encapsulation.[25] The devices were fabricated by spinning poly(methyl methacrylate) (PMMA) resist, followed by e-beam lithography and thermal evaporation of the metal contacts. The mobilities at room temperature for both holes and electrons calculated in these devices were $\approx$10 cm^2 V^{-1} s^{-1}, substantially below the expected values. In addition, large hysteresis in both positive and negative gate voltage sweep directions was observed. In another approach, encapsulation by atomic layer deposition (ALD) of alumina (Al$_2$O$_3$) was demonstrated.[21,26–30] The Al$_2$O$_3$ encapsulated BP FETs revealed a room temperature hole mobility of $\approx$100 cm^2 V^{-1} s^{-1}. Long-term stability of up to 17 months was reported by Grasser et al.[30] However, the effectiveness of the Al$_2$O$_3$ encapsulation is largely dependent on the ALD process conditions, which makes it a complex process.[26,29,34]

Moreover, both techniques passivate the top surface of BP and the bottom part rests on the SiO$_2$ substrate. Because of the presence of hydroxyl groups, SiO$_2$ has been shown to deteriorate the performance of FETs and result in large hysteresis by inducing charge disorder at the interface.[24,31–33] Furthermore, both techniques leave some parts of BP unexposed in order to evaporate the metal electrodes. This might cause degradation at the contacts and result in large contact resistances, tunnel barriers, and further unreliability in the I–V measurements.[16] Particularly for alumina encapsulation, a recent study reported that the fixed oxide charges in the Al$_2$O$_3$ layer can induce energy-band bending near the metal contact edge and randomly modulate the type of conduction in BP devices.[28]

In this work, we have addressed these challenges by employing via-contacts to fabricate FETs based on fully encapsulated BP layers. Via-contacts are metal electrodes embedded within hBN flakes. They allow us to simultaneously achieve encapsulation and an electrical connection to the underlying 2D layer without any direct lithographic patterning. The full encapsulation is achieved by sandwiching the BP layers in a layer-by-layer fashion between the bottom hBN (suppresses the charge transfer from SiO$_2$) and top hBN containing the via-contacts (passivates the BP layer from air and provides electrical connection to carry out the measurements). We also fabricated BP FETs by depositing Gr-contacts and evaporation of metal-contacts, both using top and bottom hBN to fully encapsulate the BP layer, which allowed a direct comparison of different passivation techniques. Based on our results, we find that the via-encapsulation technique passivates the BP layers from various degrading factors and preserves their electrical

properties. Via-BP FETs show the best performance with improved hole and electron mobilities and negligible hysteresis as compared to other device architectures tested in this work. We observe a crossover in current as a function of temperature and back-gate voltage. In addition, via-BP FETs are found to be ambient stable for over 5 weeks, which is considerably longer than top-hBN-encapsulated devices. The via-encapsulation scheme is a versatile and robust technique. The via-contacts can be fabricated in different shapes and sizes, which is particularly advantageous for randomly sized mechanically exfoliated flakes. We believe that this technique can open ways for fundamental studies as well as towards the integration of air-sensitive 2D materials in technological applications.

2. Experimental Section

2.1. Via-Contact Fabrication

The fabrication of the via-contacts employed in this work is shown in microscope images in **Figure 1**a. The hBN flakes were exfoliated from their bulk crystal using an adhesive tape and deposited onto a 285 nm SiO$_2$/Si substrate. Crack- and residue-free hBN flakes with uniform thicknesses of 30–50 nm were identified using optical contrast. The SiO$_2$/Si substrate was then spin-coated with EL11 and PMMA A4 at 3000 rpm, followed by post-baking at 150 °C for 10 min. The PMMA layers served as the resist layer for the subsequent patterning of hBN using e-beam lithography. To develop the patterns, the substrate was immersed first into the developer solution of deionized (DI) water and isopropanol (3:7) for 1 min and then 30 s into isopropanol as a stopper followed by N$_2$ blow dry. To etch holes into patterned hBN flakes, inductively coupled plasma reactive ion etching (Oxford ICP-RIE) was used. A gas mixture of SF$_6$:O$_2$ (40:4 sccm) was supplied at 60 W for 1 min to generate the plasma. The etched holes were then filled with 20 to 30 nm Ni followed by 30 nm Au using an e-beam evaporator at a deposition rate of 1 Å s^{-1}. To obtain the via-contacts, the final step was metal lift-off, where the sample was immersed in acetone for 2–3 h, followed by isopropanol rinsing and blown dry with N$_2$.

2.2. VdW Assembly of hBN/BP/via-hBN Stacks

The heterostructure assembly was carried out inside an N$_2$-filled glovebox to prevent ambient exposure of the BP layers and to minimize the contaminations at the hBN/BP interfaces. The first step involved picking up a via-hBN (hBN flake carrying via-contacts prepared as described in Section 2.1.) from a dummy Si/SiO$_2$ substrate using a PDMS (Polydimethylsiloxane)/PPC (Poly propylene carbonate) transfer slide at the micromanipulator as described in the previous work.[24] Next, BP was exfoliated from its bulk crystal (bought commercially from *2dSemiconductors*) inside the N$_2$-filled glovebox and transferred onto an hBN flake (bottom dielectric) resting on a 285 nm SiO$_2$/Si substrate. To form the hBN/BP/via-hBN heterostructure, the PDMS/PPC stamp containing the via-hBN was stacked onto the BP flake in such a way that the metal electrodes covered it entirely. Figure 1b illustrates the schematic of vdW assembly of
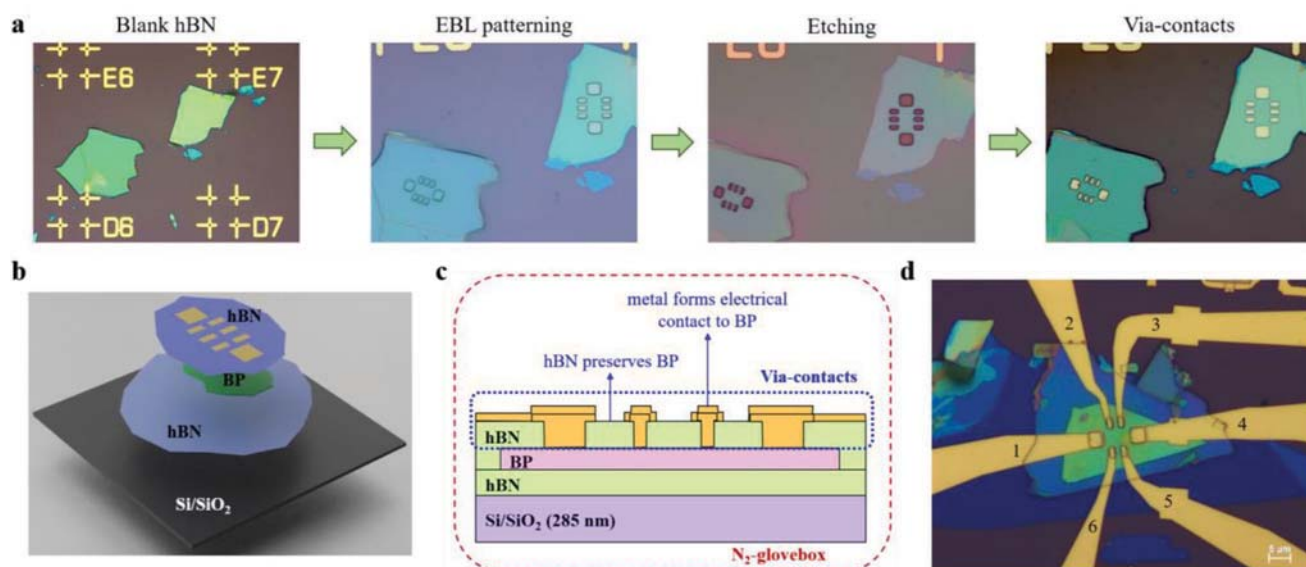
Figure 1. Fabrication of Ni/Au via-contacts and via-BP FETs. a) Illustration of via-contact fabrication steps. b) schematic of vdW assembly of hBN/BP/via-hBN stacks. c) via-BP device schematic, BP is fully encapsulated between bottom hBN and top via-hBN. d) Optical microscopic image of a via-BP FET with multiple contacts numbered from 1 to 6 (Scale: 5 µm).

hBN/BP/via-hBN stacks. The substrate was then removed from the glovebox and processed further to make extended metal bars and contact pads (5 nm Ti/30 nm Ni/80 nm Au) where measurement probes were placed. Figure 1c shows the cross-sectional schematic of the via-BP FET device. The bottom hBN layer suppressed the charge transfer from SiO_2 while the top hBN passivated the BP layer from air. The metal embedded into the top hBN formed an electrical connection to the underlying BP layer. The optical micrograph in Figure 1d shows the top view of one of the BP-via FETs fabricated in this work. The six contact pads were numbered from 1 to 6.

3. Results and Discussion

The two-probe electrical characterization of the via-BP FET is carried out in a back-gated configuration under atmospheric conditions and is shown in **Figure 2**. In this configuration, the highly p-doped Si-substrate serves as a back gate. The high

concentration of dopants ensures that the conductivity of the Si is large enough to define gate voltages even at temperatures down to 4.2 K. The BP flake is ≈22 nm thick and the bottom hBN is ≈30 nm as confirmed with atomic force microscopy. BP layers with thicknesses >15 nm are usually preferred for device fabrication because of improved field-effect mobility and their relative stability demonstrated previously.[15,26,35–37] The output curve of our via-BP FET shown in Figure 2a exhibits linear I–V characteristics and large current densities, indicating a low resistance contact between Ni and BP. Current saturation is not observed even at $V_{ds} = \pm1$ V, implying that even higher current values are achievable. Most likely the large equivalent oxide thickness (≈317 nm) causes poor coupling of the gate electrode to the BP which can hinder obtaining current saturation.[38,39]

The transfer curve in Figure 2b shows an ambipolar behavior with a dominant p-type conductance, which may be attributed to a good alignment between the valence band of BP and the high work function of Ni (5.1 eV), resulting in an improved hole injection from Ni contacts to BP channel.[15,35,40] The two-probe
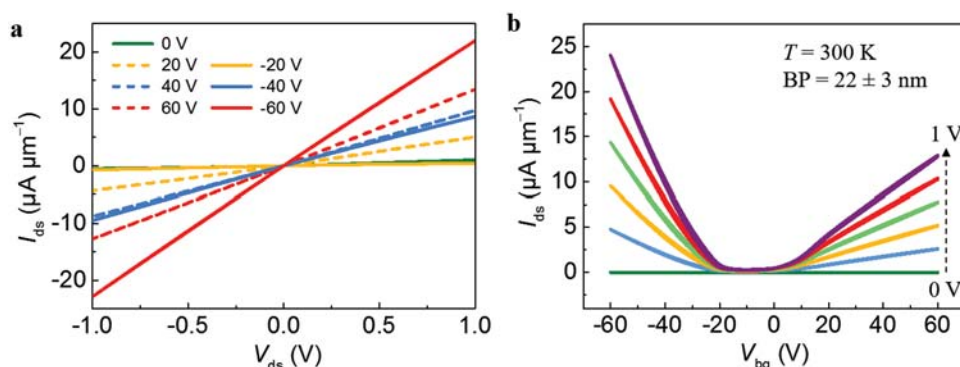
Figure 2. Two-probe electrical characterization of ~22 nm thick BP-via device at room T. a) Output curve at various back-gate voltages. b) Transfer curve at regular intervals of V_{ds} from 0 to 1 V, showing ambipolar behavior.
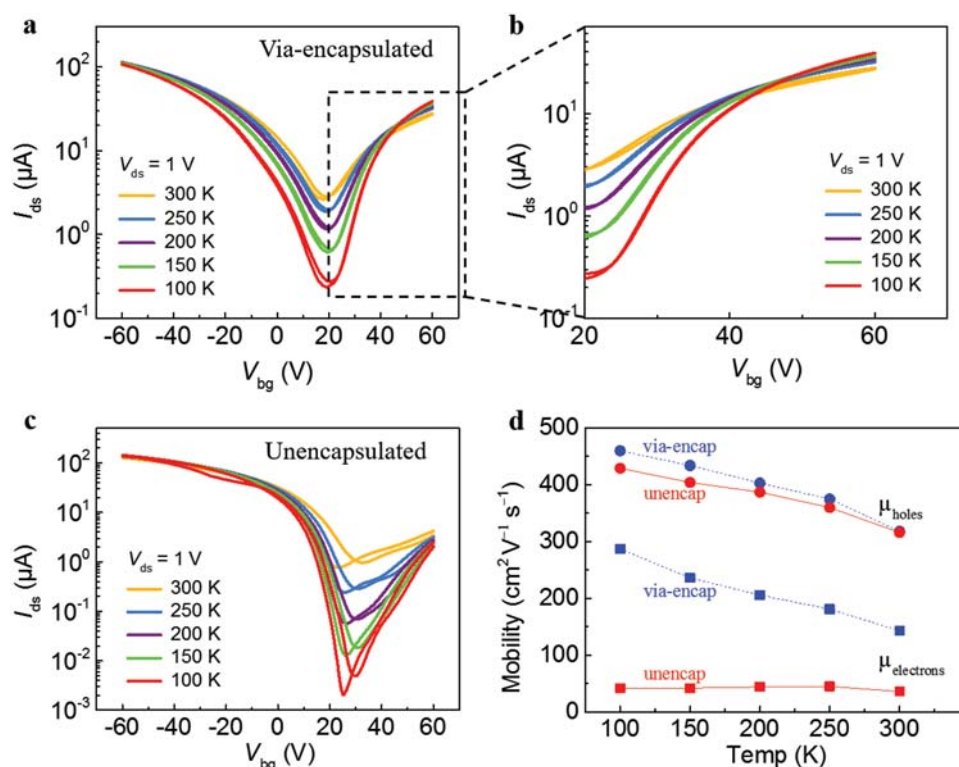
Figure 3. Temperature-dependent electrical characterization of via-encapsulated and unencapsulated devices based on a ≈50 nm thick BP flake. a) Semi-log transfer curves at $V_{ds} = 1$ V for the via-encapsulated device at regular temperature intervals from 300 to 100 K. b) Zoomed image of the metal–insulator transition as a function of back-gate voltage. c) Semi-log transfer curves at $V_{ds} = 1$ V for the unencapsulated device at regular temperature intervals from 300 to 100 K. d) hole and electron two-probe mobility for encapsulated and unencapsulated devices as a function of temperature.

field-effect mobility (μ_{FE}) at room temperature is calculated to be 596 cm² V⁻¹ s⁻¹ for holes and 172 cm² V⁻¹ s⁻¹ for electrons; the higher hole mobility is in agreement with the previous discussion. Taking advantage of the multi-electrode geometry of the via-contacts, we also calculated the four-probe mobility of a via-BP FET. High hole mobility of 720 cm² V⁻¹ s⁻¹ and electron mobility of 143 cm² V⁻¹ s⁻¹ are obtained at room temperature for an ≈18 nm thick via-BP device and bottom hBN of ≈40 nm. It is worth stating that the via-BP FETs fabricated in this work have shown much higher mobility values than the values obtained with other encapsulation schemes for similar BP thicknesses.[26,28,33,36]

To test the efficacy of via-contacts at low temperatures, we carried out two-probe electrical characterization as a function of temperature from 300 K down to 100 K (**Figure 3**). The via-BP device is fabricated with ≈50 nm thick BP, and via-contacts Ni (30 nm)/Au (hBN thickness can be found in Supporting Information) Figure S3 and Figure S4. For a consistent comparison, an unencapsulated device with the same BP thickness and a metal configuration of Ti (5 nm)/Ni (30 nm)/Au is also fabricated. Figure 3a shows the semi-log transfer curve of the via-encapsulated device at different temperatures. A strong dependence of electrical conductivity on temperature for both holes and electrons is observed. The relationship between temperature and electrical conductivity shows a transition as a function of gate voltage at a crossover point of ≈48 V (Figure 3b). Below a specific gate

voltage (<48 V) the conductance increases with increasing temperature. Above this value, the conductance decreases with increasing temperature. This transition has been reported before in 2D semiconductors including MoS₂, InSe, and BP in great detail and is usually associated with the tuning of the charge carrier density with applied gate voltages.[41–44] According to Kis et al., below a critical carrier concentration, the electrons are strongly localized and transport is dominated by the hopping-type mechanism. At higher gate voltage, the carrier density increases further and the channel exhibits a metallic behavior, weak electron localization, and an associated band-like charge transport which may be a reason for the observed transition.[41,43,45] The transfer curve of the unencapsulated device, exhibits an insulating behavior at all gate voltages (Figure 3c), which could be caused by the formation of tunnel barriers and pinning of the Fermi level at the metal–semiconductor interface. Park et al. emphasized that good contacts with low contact resistance are required to observe such a change in behavior in 2D layers, thus supporting our claim that the via-contacts form good contacts to the underlying BP layers.[46] Additionally, to be able to observe a metallic behavior in BP, extrinsic scattering mostly coming from the substrate and ambient influences must be eliminated which was provided by the via-encapsulation technique in our study.

The field-effect mobility (μ_{FE}) is calculated and is presented as a function of temperature in Figure 3d. Both hole and

Annual Report IIM 2022, HZDR-123

15

**ADVANCED
SCIENCE NEWS**
www.advancedsciencenews.com

**ADVANCED
MATERIALS
TECHNOLOGIES**
www.advmattechnol.de

electron mobilities of the via-encapsulated device increase monotonically with decreasing temperature, reaching a maximum of 460 and 287 cm^2 V^{-1} s^{-1} at 100 K, respectively. The increase in mobilities with decreasing temperature is attributed to the suppression of phonon scattering as discussed previously for other 2D semiconductors.[42,43,47–49] Additionally, it can be seen that the encapsulated device shows negligible hysteresis at all temperatures whereas the unencapsulated device shows increased hysteresis because of trapped charges in the SiO$_2$ substrate and absorbents from the atmosphere, leading to unreliability in the interpretation of threshold voltage and subthreshold swing.[24] The transfer characteristics were done with a sweep rate of ≈2.5 V s^{-1} (further details can be found in Supporting Information) Figure S9 and S10. We also observe a decrease in off-currents with lowering temperatures in both devices, most likely due to suppression of thermionic emission and the influence of the Schottky barriers at the contacts.[48,50] The Schottky barriers are higher for the unencapsulated devices, possibly leading to a larger suppression of off-current in this case. This decrease of off-currents results in an increase in the on-off ratio with decreasing temperature, because the on-currents are barely affected by temperature changes.

Apart from this work, a few other techniques have been developed to fabricate encapsulated BP FETs, some of which were discussed in the previous section. To compare the effectiveness of different encapsulation schemes, we fabricated devices with two different encapsulation schemes (**Figure 4**) and compared their results with the results obtained for the via-BP device in Figure 2. Note that the BP thicknesses for all three device configurations are kept within the range of 20 ± 2 nm. Figure 4a shows the schematic of an encapsulated BP FET with few-layer Gr contacts fabricated in this work. The whole assembly is encapsulated in top and bottom hBN with some parts of Gr protruding outside for subsequent fabrication of the extended metal bars. The choice of Gr as electrodes is based on its tunable work function that has enabled low resistance contacts to

Table 1. Comparison of hole and electron mobilities obtained with different encapsulation schemes for BP FETs. BP thickness = 20 ± 5 nm.

Encapsulation technique	BP thickness [nm]	Two-probe mobility at room temperature [cm^2 V^{-1} s^{-1}]		References
		Holes	Electrons	
Via-encapsulation	20	596	172	
Gr-contacts + top/bottom hBN	20	105	42	
Ni-contacts + top/bottom hBN	20	189	52	
Without encapsulation	18.7	170.5	–	[56]
Al$_2$O$_3$	5–25	200	–	[27]
Al$_2$O$_3$	20	0.96	–	[57]
Al$_2$O$_3$	15	310	89	[58]

other 2D semiconductors.[16,51–53] As compared to Figure 2a, the output curve of the Gr-BP FET (Figure 4b) shows non-linear characteristics, indicating the presence of a barrier at the Gr/BP interface. Consequently, a much lower μ_{FE} is measured for this device as compared to the μ_{FE} for the via-BP device in Figure 2b (summarized in **Table 1**). Furthermore, long-term stability could not be guaranteed in these stacks, because hBN does not seal the protruding Gr contact perfectly, allowing air to enter through small open pockets and initiating the degradation of the BP channel. Figure 4d shows the schematic of another encapsulation scheme where the BP layer is deposited on a bottom hBN, followed by direct lithographic patterning of Ni metal contacts, and lastly deposition of a top hBN layer. The output curve in Figure 4e shows non-linear characteristics between Ni and BP. From the transfer curve (Figure 4f), low μ_{FE}, large hysteresis, and unipolar p-type conductance are observed. The poor performance of this device can be explained by the degradation of pristine BP to PO$_x$ on air exposure and
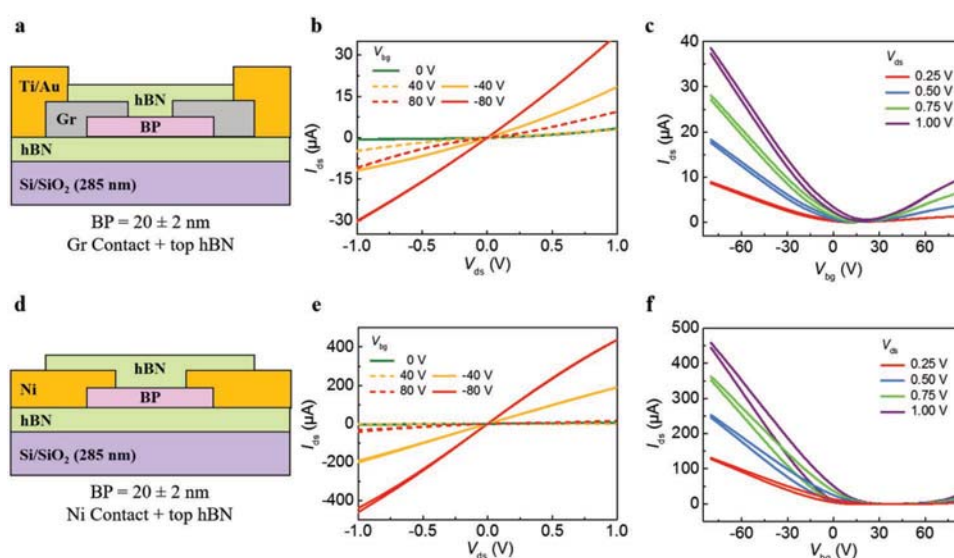
Figure 4. Encapsulation schemes for BP. a) Schematic of a Gr-contacted fully encapsulated BP FET. b,c) Output and transfer curves of the device in (a). d) Schematic of a Ni-contacted fully encapsulated BP FET. e,f) Output and transfer curves of the device in (d).
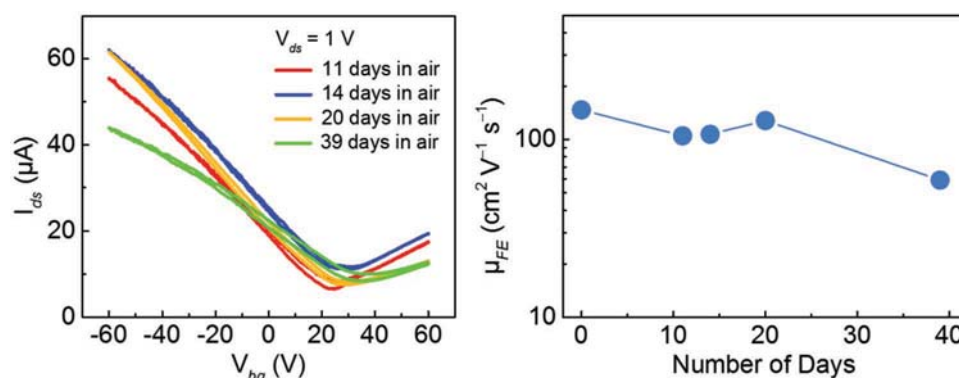
Figure 5. Electrical characterization of a via-BP FET over time. a) Transfer curves for a via-BP FET, measured as a function of ambient exposure time. b) Hole mobility for the same device as a function of ambient exposure time.

during lithographic processing. This oxide exhibits a higher work function and transfers holes to the BP channel, making it more p-type.[54,55]

Table 1 summarizes the comparison of hole and electron mobilities obtained with different encapsulation schemes for BP FETs in our devices and other studies with similar BP thickness. The results obtained with other encapsulation schemes prove that the via-encapsulation is more effective in preserving BP in its pristine form and yielding higher-performance devices. To further elucidate its effectiveness over time, we stored and measured via-BP FETs in the air for over a period of 5 weeks. Time-dependent transfer curves are shown in **Figure 5**a. Figure 5b shows the evolution of hole mobility over time. Both curves reveal good ambient stability of the device for up to three weeks, after which the conductance and mobility start to decline slowly. As compared to unencapsulated BP layers, which degrade completely within a few hours, this is a considerable improvement in the preservation of the BP layers in air.

4. Conclusion

The sensitivity of few-layered BP towards ambient conditions, bottom dielectrics, and other chemicals during fabrication processes complicates the evaluation of its intrinsic properties and hampers its integration into active devices. In this work, we demonstrated the lithography-free via-encapsulation technique to obtain high-quality and stable BP-based transistor devices. In this method, not only the BP layers are passivated to prevent the influence of the environment as well as of trapped charges at the SiO_2 surface by being sandwiched between top and bottom hBN, but also contacted by embedded via-metal electrodes allowing us to perform reliable electrical measurements. In this work, we fabricated several via-encapsulated BP FETs with BP thicknesses in the range of 18–50 nm. The devices showed enhanced mobility, lower hysteresis, and long-term ambient stability as compared to devices fabricated with a graphene-hBN heterostructure or bare hBN layers without any embedded metals. The use of the via technique for BP-based transistors, therefore, opens the way for studying the electrical properties of the BP layers in detail and preparing the material for electronic applications.

Supporting Information

Supporting Information is available from the Wiley Online Library or from the author.

Acknowledgements

Conflict of Interest

The authors declare no conflict of interest.

Data Availability Statement

The data that support the findings of this study are available from the corresponding author upon reasonable request.

Keywords

[1] W. Cao, J. Kang, D. Sarkar, W. Liu, K. Banerjee, *IEEE Trans. Electron Devices* **2015**, *62*, 3459.

[2] S. B. Desai, S. R. Madhyapathy, A. B. Sachid, J. P. Llinas, Q. Wang, G. H. Ahn, G. Pitner, M. J. Kim, J. Bokor, C. Hu, H. S. P. Wong, A. Javey, *Science* **2016**, *354*, 99.

[3] D. Akinwande, N. Petrone, J. Hone, *Nat. Commun.* **2014**, *5*, 5678.

[4] G. Fiori, F. Bonaccorso, G. Iannaccone, T. Palacios, D. Neumaier, A. Seabaugh, S. K. Banerjee, L. Colombo, *Nat. Nanotechnol.* **2014**, *9*, 768.

[5] H. Arora, S. Park, R. Dong, A. Erbe, *Opt. Photonics News* **2020**, *31*, 36.

[6] M. Pumera, Z. Sofer, *Adv. Mater.* **2017**, *29*, 1605299.

[7] R. Dong, P. Han, H. Arora, M. Ballabio, M. Karakus, Z. Zhang, C. Shekhar, P. Adler, P. S. Petkov, A. Erbe, S. C. B. Mannsfeld, C. Felser, T. Heine, M. Bonn, X. Feng, E. Cánovas, *Nat. Mater.* **2018**, *17*, 1027.

[8] H. Arora, A. Erbe, *InfoMat* **2021**, *3*, 662.

[9] H. Cai, Y. Gu, Y. C. Lin, Y. Yu, D. B. Geohegan, K. Xiao, *Appl. Phys. Rev.* **2019**, *6*, 041312.

[10] H. Arora, *Ph.D. Degree Thesis*, Technische Universität Dresden, **2020**.

[11] Y. Liu, X. Duan, Y. Huang, X. Duan, *Chem. Soc. Rev.* **2018**, *47*, 6388.

[12] K. S. Novoselov, A. Mishchenko, A. Carvalho, A. H. Castro Neto, *Science* **2016**, *353*, 461.

[13] M. Chhowalla, D. Jena, H. Zhang, *Nat. Rev. Mater.* **2016**, *1*, 16052.

[14] X. Mu, J. Wang, M. Sun, *Mater. Today Phys.* **2019**, *8*, 92.

[15] L. Li, Y. Yu, Y. C. Ye, Q. Ge, X. Ou, H. Wu, D. Feng, X. H. Chen, Y. Zhang, *Nat. Nanotechnol.* **2014**, *9*, 372.

[16] A. Avsar, I. J. Vera-Marun, J. Y. Tan, K. Watanabe, T. Taniguchi, A. H. Castro Neto, B. Özyilmaz, *ACS Nano* **2015**, *9*, 4138.

[17] A. Castellanos-Gomez, L. Vicarelli, E. Prada, J. O. Island, K. L. Narasimha-Acharya, S. I. Blanter, D. J. Groenendijk, M. Buscema, G. A. Steele, J. V. Alvarez, H. W. Zandbergen, J. J. Palacios, H. S. J. van der Zant, *2D Mater.* **2014**, *1*, 025001.

[18] V. Tran, R. Soklaski, Y. Liang, L. Yang, *Phys. Rev. B: Condens. Matter Mater. Phys.* **2014**, *89*, 235319.

[19] M. Buscema, D. J. Groenendijk, S. I. Blanter, G. A. Steele, H. S. J. van der Zant, A. Castellanos-Gomez, *Nano Lett.* **2014**, *14*, 3347.

[20] H. Liu, A. T. Neal, Z. Zhu, Z. Luo, X. Xu, D. Tománek, P. D. Ye, *ACS Nano* **2014**, *8*, 4033.

[21] J. D. Wood, S. A. Wells, D. Jariwala, K. S. Chen, E. Cho, V. K. Sangwan, X. Liu, L. J. Lauhon, T. J. Marks, M. C. Hersam, *Nano Lett.* **2014**, *14*, 6964.

[22] S. P. Koenig, R. A. Doganov, H. Schmidt, A. H. Castro Neto, B. Özyilmaz, *Appl. Phys. Lett.* **2014**, *104*, 103106.

[23] H. Arora, T. Schönherr, A. Erbe, *IOP Conf. Ser.: Mater. Sci. Eng.* **2017**, *198*, 012002.

[24] H. Arora, Y. Jung, T. Venanzi, K. Watanabe, T. Taniguchi, R. Hübner, H. Schneider, M. Helm, J. C. Hone, A. Erbe, *ACS Appl. Mater. Interfaces* **2019**, *11*, 43480.

[25] R. A. Doganov, E. C. T. O'Farrell, S. P. Koenig, Y. Yeo, A. Ziletti, A. Carvalho, D. K. Campbell, D. F. Coker, K. Watanabe, T. Taniguchi, A. H. C. Neto, B. Özyilmaz, *Nat. Commun.* **2015**, *6*, 6647.

[26] J. Na, Y. T. Lee, J. A. Lim, D. K. Hwang, G. T. Kim, W. K. Choi, Y. W. Song, *ACS Nano* **2014**, *8*, 11753.

[27] J. S. Kim, Y. Liu, W. Zhu, S. Kim, D. Wu, L. Tao, A. Dodabalapur, K. Lai, D. Akinwande, *Sci. Rep.* **2015**, *5*, 8989.

[28] H. Liu, A. T. Neal, M. Si, Y. Du, P. D. Ye, *IEEE Electron Device Lett.* **2014**, *35*, 795.

[29] Y. Y. Illarionov, M. Waltl, G. Rzepa, J.-S. Kim, S. Kim, A. Dodabalapur, D. Akinwande, T. Grasser, *ACS Nano* **2016**, *10*, 9543.

[30] Y. Y. Illarionov, M. Waltl, G. Rzepa, T. Knobloch, J.-S. Kim, D. Akinwande, T. Grasser, *npj 2D Mater. Appl.* **2017**, *1*, 23.

[31] C. R. Dean, A. F. Young, I. Meric, C. Lee, L. Wang, S. Sorgenfrei, K. Watanabe, T. Taniguchi, P. Kim, K. L. Shepard, J. Hone, *Nat. Nanotechnol.* **2010**, *5*, 722.

[32] G. H. Lee, X. Cui, Y. D. Kim, G. Arefe, X. Zhang, C. H. Lee, F. Ye, K. Watanabe, T. Taniguchi, P. Kim, J. Hone, *ACS Nano* **2015**, *9*, 7019.

[33] H. S. Ra, A. Y. Lee, D. H. Kwak, M. H. Jeong, J. S. Lee, *ACS Appl. Mater. Interfaces* **2018**, *10*, 925.

[34] S. A. Wells, A. Henning, J. T. Gish, V. K. Sangwan, L. J. Lauhon, M. C. Hersam, *Nano Lett.* **2018**, *18*, 7876.

[35] Z. P. Ling, S. Sakar, S. Mathew, J. T. Zhu, K. Gopinadhan, T. Venkatesan, K. W. Ang, *Sci. Rep.* **2015**, *5*, 18000.

[36] Y. Cao, A. Mishchenko, G. L. Yu, K. Khestanova, A. P. Rooney, E. Prestat, A. V. Kretinin, P. Blake, M. B. Shalom, C. Woods, J. Chapman, G. Balakrishnan, I. V. Grigorieva, K. S. Novoselov, B. A. Piot, M. Potemski, K. Watanabe, T. Taniguchi, S. J. Haigh, A. K. Geim, R. V. Gorbachev, *Nano Lett.* **2015**, *15*, 4914.

[37] F. Xia, H. Wang, Y. Jia, *Nat. Commun.* **2014**, *5*, 4458.

[38] H. Wang, X. Wang, F. Xia, L. Wang, H. Jiang, Q. Xia, M. L. Chin, M. Dubey, S.-J. Han, *Nano Lett.* **2014**, *14*, 6424.

[39] S. B. Mitta, M. S. Choi, A. Nipane, F. Ali, C. Kim, J. T. Teherani, J. Hone, W. J. Yoo, *2D Mater.* **2020**, *8*, 012002.

[40] F. Telesio, G. le Gal, M. Serrano-Ruiz, F. Prescimone, S. Toffanin, M. Peruzzini, S. Heun, *Nanotechnology* **2020**, *31*, 334002.

[41] C. L. Wu, H. Yuan, H. Li, Y. Gong, H. Y. Hwang, Y. Cui, *Nano Lett.* **2018**, *18*, 2387.

[42] P. H. Ho, Y. R. Chang, Y. C. Chu, M. K. Li, C. A. Tsai, W. H. Wang, C. H. Ho, C. W. Chen, P. W. Chiu, *ACS Nano* **2017**, *11*, 7362.

[43] B. Radisavljevic, A. Kis, *Nat. Mater.* **2013**, *12*, 815.

[44] Y. Saito, Y. Iwasa, *ACS Nano* **2015**, *9*, 3192.

[45] H. Liu, H. S. Choe, Y. Chen, J. Suh, C. Ko, S. Tongay, J. Wu, *Appl. Phys. Lett.* **2017**, *111*, 102101.

[46] M. J. Park, S. G. Yi, J. H. Kim, K. H. Yoo, *Nanoscale* **2015**, *7*, 15127.

[47] N. Ma, D. Jena, *Phys. Rev. X* **2014**, *4*, 011043.

[48] X. Yan, H. Wang, I. Sanchez Esqueda, *Nano Lett.* **2019**, *19*, 482.

[49] H. J. Chuang, B. Chamlagain, M. Koehler, M. M. Perera, J. Yan, D. Mandrus, D. Tománek, Z. Zhou, *Nano Lett.* **2016**, *16*, 1896.

[50] A. V. Penumatcha, R. B. Salazar, J. Appenzeller, *Nat. Commun.* **2015**, *6*, 8948.

[51] W. Luo, Y. Cao, P. Hu, K. Cai, Q. Feng, F. Yan, T. Yan, X. Zhang, K. Wang, *Adv. Opt. Mater.* **2015**, *3*, 1418.

[52] A. K. Singh, C. Hwang, J. Eom, *ACS Appl. Mater. Interfaces* **2016**, *8*, 34699.

[53] S. Das, R. Gulotty, A. V. Sumant, A. Roelofs, *Nano Lett.* **2014**, *14*, 2861.

[54] C. H. Wang, J. A. C. Incorvia, C. J. McClellan, A. C. Yu, M. J. Mleczko, E. Pop, H. S. P. Wong, *Nano Lett.* **2018**, *18*, 2822.

[55] M. T. Edmonds, A. Tadich, A. Carvalho, A. Ziletti, K. M. O'Donnell, S. P. Koenig, D. F. Coker, B. Özyilmaz, A. H. C. Neto, M. S. Fuhrer, *ACS Appl. Mater. Interfaces* **2015**, *7*, 14557.

[56] Y. Du, H. Liu, Y. Deng, P. D. Ye, *ACS Nano* **2014**, *8*, 10035.

[57] C. Chen, N. Youngblood, R. Peng, D. Yoo, D. A. Mohr, T. W. Johnson, S. H. Oh, M. Li, *Nano Lett.* **2017**, *17*, 985.

[58] W. Zhu, M. N. Yogeesh, S. Yang, S. H. Aldave, J.-S. Kim, S. Sonde, L. Tao, N. Lu, D. Akinwande, *Nano Lett.* **2015**, *15*, 1883.

NANO LETTERS

Letter

Data-Driven Quest for Two-Dimensional Non-van der Waals Materials

Rico Friedrich,* Mahdi Ghorbani-Asl, Stefano Curtarolo, and Arkady V. Krasheninnikov

Cite This: *Nano Lett.* 2022, 22, 989–997

ACCESS | 📊 Metrics & More | 📰 Article Recommendations | 🅢🅘 Supporting Information

ABSTRACT: Two-dimensional (2D) materials are frequently associated with the sheets forming bulk layered compounds bonded by van der Waals (vdW) forces. The anisotropy and weak interaction between the sheets have also been the main criteria in the computational search for new 2D systems, predicting ~2000 exfoliable compounds. However, some representatives of a new type of non-vdW 2D systems, without layered 3D analogues, were recently manufactured. For this novel materials class, data-driven design principles are still missing. Here, we outline a set of 8 binary and 20 ternary candidates by filtering the AFLOW-ICSD database according to structural prototypes. The oxidation state of the surface cations regulates the exfoliation energy with low oxidation numbers leading to weak bonding—a useful descriptor to obtain novel 2D materials also providing clear guidelines for experiments. A vast range of appealing electronic, optical, and magnetic properties make the candidates attractive for various applications and particularly spintronics.

KEYWORDS: *2D materials, exfoliation, data-driven research, computational materials science, high-throughput computing*
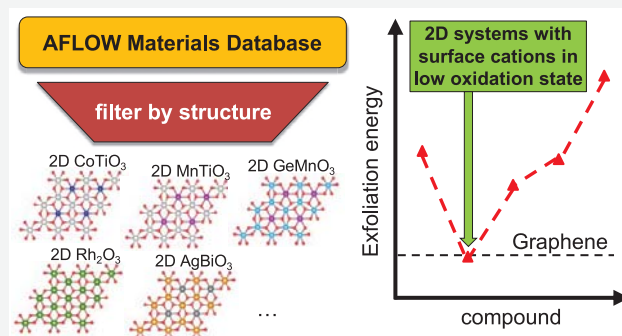
The isolation of single graphene sheets,[1] which proved that two-dimensional (2D) systems can exist, gave rise to the discovery of many 2D materials with unique superconducting,[2,3] electronic,[4–6] magnetic,[7–9] and topological[10] properties. In addition to being testbeds for studying the behavior of systems in reduced dimensions, 2D materials hold great promise for various applications in optoelectronics,[4,11,12] catalysis,[13,14] and the energy sector.[15–17] The research effort has been mainly concentrated on the systems which have bulk counterparts representing anisotropic crystals with layers held together by van der Waals (vdW) forces, with the most prominent example being graphene and graphite. The weak interlayer interaction leads to a natural structural separation of the 2D subunits in the crystals, therefore making mechanical[18] or liquid-phase[19] exfoliation possible.

At the same time, the layered structure allows developing rigorous screening criteria for exfoliability to be employed on large materials databases—outlining data-driven high-throughput investigations as an ideal tool for the discovery and design of 2D compounds.[20–28] Such studies predicted several thousands of vdW 2D systems and were used to set up computational databases.[21–23,25,26]

Unexpectedly, a new direction in the research on 2D systems was opened in 2018, after the experimental realization of atomically thin sheets from non-vdW bonded compounds by a special chemical exfoliation process.[29,30] The first representatives of these non-vdW 2D materials were hematene and ilmenene obtained from the earth-abundant ores hematite (α-

Fe$_2$O$_3$) and ilmenite (FeTiO$_3$), followed by other systems derived from chromite (FeCr$_2$O$_4$),[31] magnetite (Fe$_3$O$_4$),[32] pyrite (FeS$_2$),[33,34] chromium sulfide,[35] manganese selenide (α-MnSe$_2$),[36] metal diborides,[37] boro-carbides,[38] and diamond-like germanium (α-Ge).[39]

While traditional vdW compounds have chemically saturated bonds at the surface of 2D subunits, the aforementioned materials show qualitatively new features. As they are obtained from nonlayered systems, they exhibit dangling bonds and surface states, making them more tunable by adsorbates.[40] They have already shown great potential for electronic[41] and optoelectronic[42] applications and by exhibiting enhanced photocatalytic activity for water splitting[29,30] and photoconductivity.[36] Moreover, they may also offer a versatile playground for magnetism and spintronics in reduced dimensions.[43] The first studies mostly focusing on hematene indicate, for instance, tunable magnetic ordering,[29,30,40,44–47] as well as spin canting.[48]

Although there have been significant experimental efforts to generalize recipes for their synthesis,[37,38,41,47,50] computational
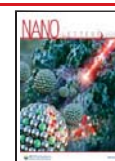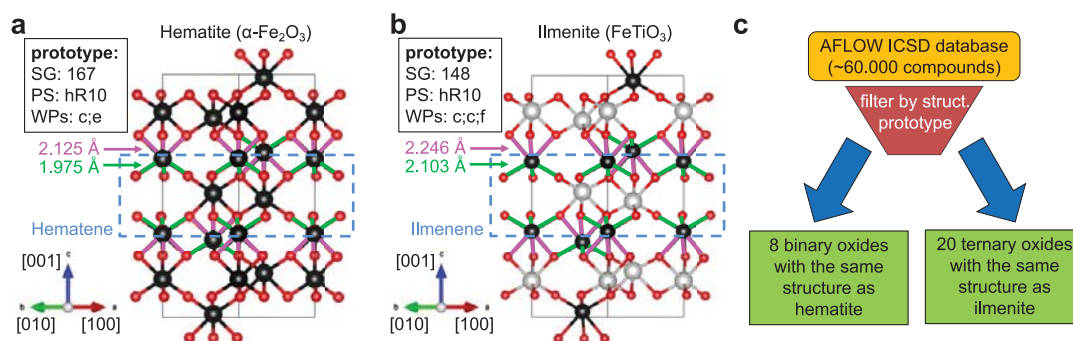
Figure 1. Structural prototypes of non-vdW 2D materials. Atomic structures of (a) hematite (α-Fe_2O_3) and (b) ilmenite ($FeTiO_3$), the first non-vdW bulk materials with 2D analogues.[29,30] Long (weak) bonds are highlighted in magenta, and short (strong) bonds are indicated in green as obtained from PBE+U. For both prototypes, space groups (SGs), Pearson symbols (PSs), and Wyckoff positions (WPs) are indicated in the respective boxes. In each case, the exfoliable [001] facet (monolayer) is indicated in the blue dashed frame leading to hematene and ilmenene 2D materials. Colors: Fe, black; O, red; and Ti, light gray.[49] The black line denotes the conventional unit cell. (c) Schematic workflow illustrating how the candidate systems were obtained from the AFLOW ICSD database using structural information as an input.

design principles based on data-driven concepts for outlining non-vdW 2D materials are still missing. It is obvious that the descriptors developed for vdW-bonded systems are not applicable, since they rely on identifying layered subunits in the structure.

Here, we resolve this issue by screening the AFLOW database[51] using the structure of the previously realized representatives as an input and identify 28 non-vdW potentially synthesizable 2D materials. We further show that they exhibit a vast range of promising electronic, optical, and magnetic properties, suggesting in particular spintronic applications. The oxidation state of the cations at the surface of the 2D slab is outlined as a key quantity determining the easy exfoliation of the systems, thus providing an enabling descriptor for the discovery of novel 2D materials.

■ OUTLINING MORE CANDIDATES

Hematite and ilmenite, Figure 1a,b—the first non-vdW materials with 2D analogous[29,30]—can be used as a template for screening the AFLOW-ICSD database containing ~60 000 compounds, Figure 1c. This library primarily incorporates materials realized experimentally. When closely investigating the structure of the hematite and ilmenite prototypes, one recognizes that the Fe−O bond lengths are strongly anisotropic. As indicated in Figure 1a, for hematite, there are three long (weak) bonds of 2.125 Å and three shorter (stronger) ones of 1.975 Å highlighted in magenta and green, respectively, for each Fe close to the exfoliation planes. When slicing the structure between the Fe cations as indicated by the blue dashed lines, one only cuts through the weak (long) bonds. For any other surface termination, one would need to break stronger bonds. For $FeTiO_3$, the situation is similar exhibiting Fe−O bonds of 2.246 and 2.103 Å (see Figure 1b). We believe that this natural separation of the bond strengths together with electrostatic considerations is key to the exfoliability of these materials. It is a characteristic of the outlined prototypes and thus reveals their particular suitability for the emergence of non-vdW 2D systems. (The Ti−O bond lengths in $FeTiO_3$ are also anisotropic amounting to 1.944 and 2.078 Å. Ti is, however, not the terminating ion at the surface of ilmenene as found consistently by experiment[30] and calculations. This is related to its higher oxidation state (Ti^{4+} vs Fe^{2+}), making this configuration energetically unfavorable as discussed in detail in the text below.) We thus look for other

systems with the same structural prototype.[52,53] Two structures are regarded to have the same prototype if their space group (SG), Pearson symbol (PS), and Wyckoff positions (WPs) match, which are indicated for α-Fe_2O_3 (corundum) and $FeTiO_3$ in Figure 1.

The search yields the 8 binary and 20 ternary oxides (excluding P, As, and Sb, as these are not typical cation species) listed in Table 1. (Structural data are retrieved via the

Table 1. Binary and Ternary Compositions with the Same Structures as Hematite and Ilmenite[a]

binaries		ternaries			
composition	mag.	composition	mag.	composition	mag.
Al_2O_3 (72)	no	$MgTiO_3$ (28)	no	$CaSnO_3$ (1)	no
Fe_2O_3 (63)	yes	$FeTiO_3$ (21)	yes	$CdGeO_3$ (1)	no
Cr_2O_3 (52)	yes	$GeMgO_3$ (7)	no	$CdTiO_3$ (1)	no
V_2O_3 (20)	yes	$MgSiO_3$ (7)	no	$CoMnO_3$ (1)	yes
Ti_2O_3 (15)	yes	$GeMnO_3$ (6)	yes	$CuVO_3$ (1)	no
Rh_2O_3 (4)	no	$MnTiO_3$ (5)	yes	$GeZnO_3$ (1)	no
Ga_2O_3 (3)	no	$NiTiO_3$ (5)	yes	$MnNiO_3$ (1)	yes
In_2O_3 (3)	no	$AgBiO_3$ (2)	no	$SiZnO_3$ (1)	no
		$BiNaO_3$ (2)	no	$SnZnO_3$ (1)	no
		$CoTiO_3$ (2)	yes	$TiZnO_3$ (1)	no

[a]Binary compositions with the same structural prototype as hematite (α-Fe_2O_3) and ternary compositions with the same structural prototype as ilmenite ($FeTiO_3$) from the AFLOW- ICSD database. The numbers in brackets after the compound formulas of each system indicate the frequency of occurence in the database. Whether the structure was found to exhibit magnetic moments is also indicated.

AFLOW APIs[54,55] and web interfaces[51] as well as the library of crystallographic prototypes.[56]) We decided to focus on oxides since these are abundant materials and typically of high interest for technological applications. For each composition, the listed frequency of occurrence in the database (in brackets after the formula) gives a first indication how common the system is. These candidates are now investigated for the formation of the corresponding 2D sheets perpendicular to the [001] direction (called [001] facets) in analogy to the template systems. This facet has been outlined as thermodynamically favorable for hematene.[29,40] Here, the monolayer structures according to refs 29 and 30 and Figure 1a,b are considered, which are referred to as 2D systems in the following. This limit provides
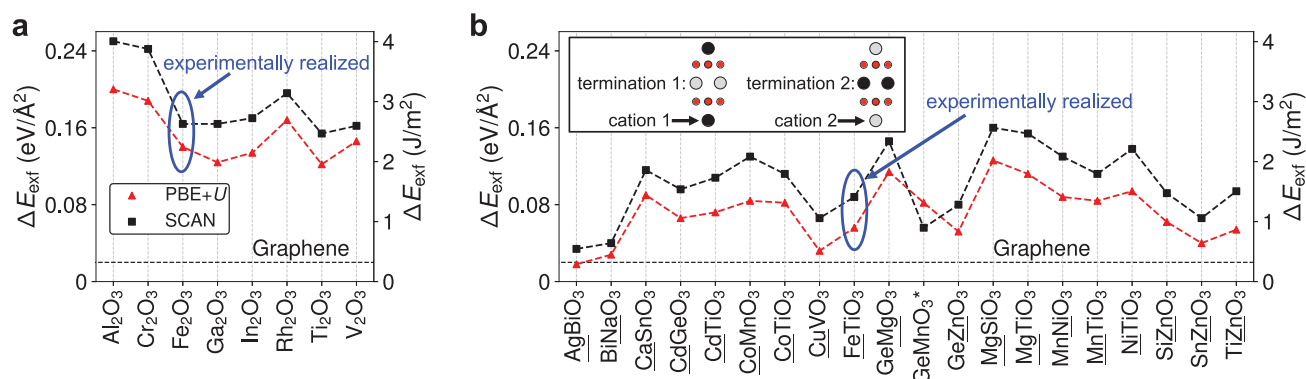
Figure 2. Exfoliation energies. Exfoliation energies of investigated (a) binary and (b) ternary systems for two different functionals. As a reference, the exfoliation energy of graphene[25,58] is indicated by the dashed horizontal black lines. For the ternaries, the data for the slabs with the energetically favorable termination are plotted, and the terminating element is underlined at the bottom axis. The inset indicates the two possible terminations. In the case of $GeMnO_3$ (marked by "*"), PBE+U favors Mn termination, while for SCAN Ge termination is preferred. Note that, for Al_2O_3, $BiNaO_3$, $GeMgO_3$, and $MgSiO_3$, PBE+U reduces to plain PBE. Data points for 2D systems realized experimentally[29,30] are highlighted. The dashed lines connecting the data points are visual guides.

an upper energetic bound to obtain 2D sheets from a given material.[40]

A recent study in ref 57 demonstrated that the relation between the in-plane tearing energy and the out-of-plane peeling energy controls the length to thickness aspect ratio of liquid-exfoliated nanosheets, implying that layered materials with large mechanical anisotropy prefer to yield nanosheets with large aspect ratios. Similarly, one can expect that nonlayered materials with anisotropic bonding schemes can also be exfoliated into nonlayered quasi-2D materials according to this assessment.[33,38] Such an exfoliation process might also lead to surface passivation due to the liquid environment.[32]

■ EXFOLIATION ENERGIES

The exfoliation energies ΔE_{exf} are computed as the energy difference between relaxed 2D and bulk systems in accordance with ref 59. This work demonstrated the strict equivalence of the binding energy between facets/layers in the bulk and the exfoliation energy from the surface of the material. The results are presented in Figure 2. They were obtained by relaxing both the ionic positions and the cell shape of the 2D sheets. In Figures S1 and S2, a comparison of the calculated exfoliation energies also including results from different functionals as well as from relaxing different degrees of freedom of the systems is presented showing that these 2D materials primarily gain energy due to the ionic relaxation (see also the paragraphs on structural properties below). For vdW bonded compounds, relaxations of 2D substructures could be omitted when calculating inter-*layer* binding energies,[25] which is, however, not a good approximation for the present non-vdW systems. Note that, for the ternaries (Figure 2b), either of the two cation species can be at the surface of the 2D slabs. The graph includes the results for the energetically more stable termination, and the respective terminating element is underlined at the bottom axis. A plot comparing the exfoliation energies obtained with the different terminations is given in Figure S3.

The values are presented for the two DFT methodologies, PBE+U and SCAN. The former is a standard approach for transition metal based systems, which has been used in several previous studies on hematene.[29,40,44] The latter is a more sophisticated method, which has been demonstrated to

provide accurate structures and energies for diversely bonded systems.[60] Both approximations show similar trends and magnitudes of the exfoliation energy with SCAN generally giving higher values. As a reference, the ΔE_{exf} of graphene—well-known to be exfoliable—which is found to be ~20 meV/$Å^2$ by both theory and experiment,[25,58,61] is also indicated. While for all binary systems in Figure 2a the exfoliation energy is considerably higher than for graphene, the value of 140 meV/$Å^2$ computed for hematene with PBE+U nicely fits to previously reported values (after accounting for the different normalization by a factor of 2),[40,44] employing slightly different computational parameters. Considering that hematene has been realized experimentally, all other systems are also likely exfoliable with Al_2O_3 being a potential exception. The systems with the lowest calculated exfoliation energies are close to the limit deemed "potentially exfoliable" (upper bound for ΔE_{exf} of 130 meV/$Å^2$) in ref 25, albeit in this study vdW bonded materials were considered. A limit of ~200 meV/atom for exfoliability has also been proposed,[23] which corresponds to about 2/3 of the value calculated for hematene.

As evident from Figure 2b, the ternaries show in general smaller exfoliation energies in part even close to the graphene reference, suggesting the feasibility of mechanical peel-off. Importantly, the value becomes particularly small when the element at the surface of the slab is in a low oxidation state as indicated most prominently by $AgBiO_3$, $BiNaO_3$, and $CuVO_3$, where the surface Ag, Na, and Cu are in state +1. This pattern can be understood from the fact that smaller surface charges lead to weaker Coulomb-like interactions between facets. Also Zn- and Fe-termination is energetically favorable, while Mg-termination leads to the highest ΔE_{exf} among the investigated ternaries, albeit smaller than for hematene, for which exfoliation was achieved experimentally. This general behavior has a strong effect on the magnetic properties, since it results in the magnetic ions Mn^{2+}, Fe^{2+}, Co^{2+}, and Ni^{2+} terminating the 2D materials.

In conclusion, when comparing the results for the whole set, the exfoliation energies vary by about an order of magnitude: The highest value is obtained for Al_2O_3 as 200 (250) meV/$Å^2$ from PBE+U (SCAN), whereas the lowest is calculated for $AgBiO_3$ as 18 (34) meV/$Å^2$. Thus, there is a pronounced difference in the (mechanical) effort to exfoliate these systems.
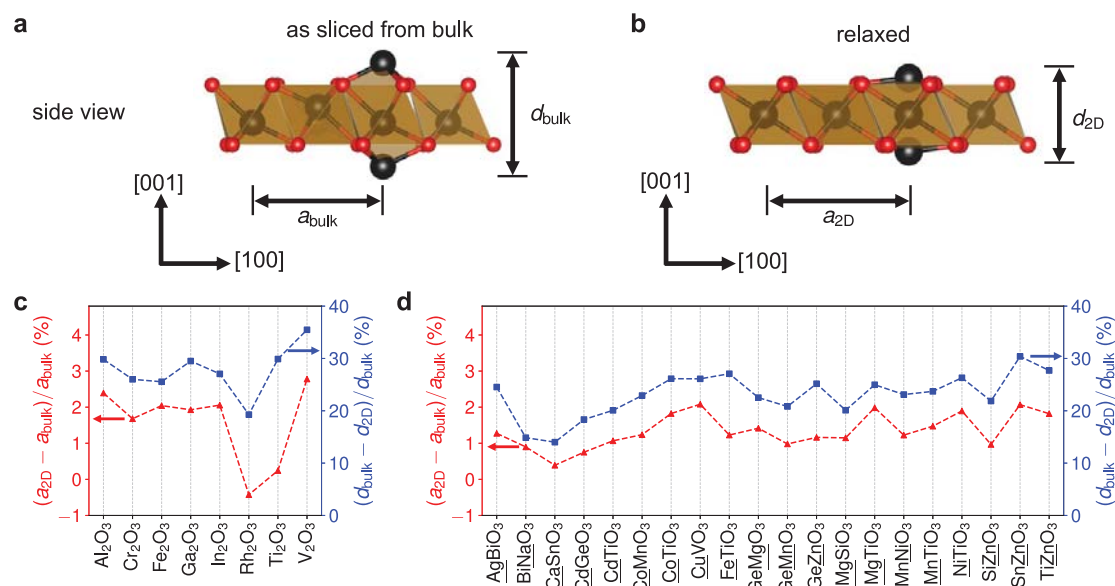
Figure 3. Modification of structural parameters. Side views of the (a) initial and (b) relaxed unit cells of [001] hematene. Fe coordination polyhedra are visualized in brown. Change of structural parameters for (c) binary and (d) ternary non-vdW materials upon exfoliation. The modification of the in-plane lattice parameter is indicated by the red curves (left y-axis), while the thickness change is given by the blue curves (right y-axis). The ternary data are for the energetically preferred slab termination. The dashed lines connecting the data points are visual guides.

While low surface energies for other compounds[62] might also suggest exfoliability, this is a necessary, but not sufficient, condition. The bonding between the atoms after the exfoliation and the reconstruction of the obtained sheets defining its stability is also critical. As an example, NaCl appears to have a very small surface energy[63] but is strictly unstable as a freestanding 2D system. To verify the dynamic stability of the outlined candidates in a high-throughput fashion, 2×2 in-plane supercells are generated from the relaxed structures with the atomic coordinates randomized (Gaussian distribution, standard deviation 50 mÅ)[64,65] and reoptimized. In each case, the systems relax back to the previously found structures, confirming their stability.

▪ STRUCTURAL PROPERTIES

The investigated non-vdW 2D materials show pronounced structural modifications as compared to their bulk parents. In general, systems compress laterally upon confinement into 2D to compensate for the loss in the out-of-plane bonding by stronger in-plane bonds. The present compounds, however, expand. Figure 3a,b shows side views of the initial (as sliced from bulk) and relaxed structures for hematene. The in-plane lattice constants (thickness of the slab) as sliced from the bulk a_{bulk} (d_{bulk}) and for the relaxed 2D systems a_{2D} (d_{2D}) are also indicated. The relative change of a_{2D} with respect to a_{bulk} is depicted in Figure 3c,d (red curves) for PBE+U. An equivalent plot for SCAN showing very similar trends and magnitudes is included in Figure S4. For all systems, a strong expansion of up to $\sim$3% for V_2O_3 is observed. The only exception is Rh_2O_3, for which a small contraction of $\sim$−0.5% is found.

The expansion correlates well with a corresponding vertical contraction of the systems from d_{bulk} to d_{2D} (blue curves in Figure 3c,d), which ranges up to $\sim$35% for V_2O_3. The mechanism of this behavior can be understood from Figure 3a,b. In order to compensate for the dangling bonds created at the surface cations upon exfoliation, the outer atoms move toward the center of the slab during the relaxation, reducing

the slab thickness. As a consequence, this exerts a stress onto the plane of oxygen anions, causing the structures to stretch laterally. For Rh_2O_3, the structure compensates for the (smaller) vertical contraction by a twist of the coordination polyhedra rather than a lateral expansion.

▪ ELECTRONIC PROPERTIES

A detailed presentation of all band structures and densities of states is located in the Supporting Information (Figures S5 to S32), and here the main focus shall be on the band gaps. Figure 4 shows the calculated band gap energies E_{gap} for all bulk and 2D systems. While it is well-known that DFT—even in the employed PBE+U scheme—in general has problems predicting absolute gap values, the overall trends and differences between similar systems are often still reliable. We thus believe that the observed distribution of the gaps over a wide range (from below 1 eV to almost 6 eV) is noteworthy, pointing to the potential usefulness of these systems in, e.g., optoelectronics. For Al_2O_3, Cr_2O_3, Fe_2O_3, Rh_2O_3, and $MgSiO_3$, the 2D gap is considerably smaller than that in the bulk parent system, which can be assigned to the emergence of surface states in the gap upon exfoliation. For the other systems, however, the two gaps are similar or the trend is reversed; i.e., the 2D gap is significantly larger than the bulk one as observed for $AgBiO_3$, $FeTiO_3$, and $SnZnO_3$. This is likely associated with the strong structural relaxation described earlier. When the outer cations relax toward the planes of oxygen anions, Figure 3a,b, the electronic interaction is intensified, leading to larger level splittings and thus an opening of the gap. This interpretation is corroborated by the fact that for these three systems according to Figure 3d a particularly large out-of-plane contraction is found.

It shall also be highlighted that interesting linear band crossings, i.e., Dirac-like points, are observed in the band structures of 2D $AgBiO_3$ and $BiNaO_3$ at the high-symmetry K-point (see Figures S13 and S14), warranting further
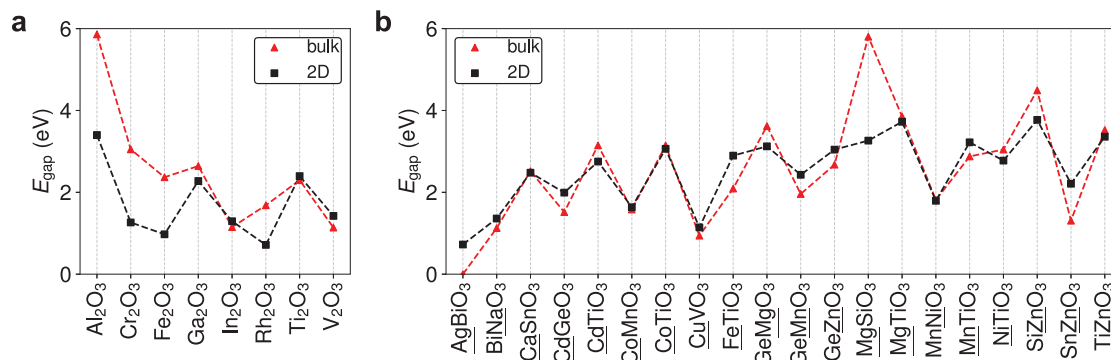
Figure 4. Band gap changes upon exfoliation. Comparison of the calculated band gaps of the bulk and 2D systems for the (a) binary and (b) ternary compounds.
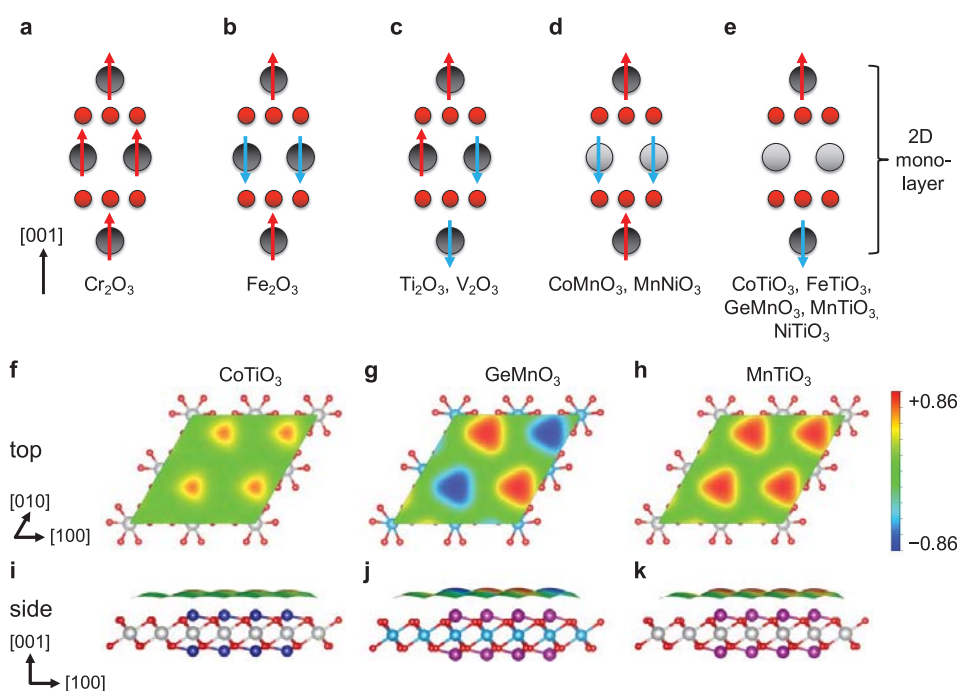
Figure 5. Magnetic configurations and surface spin polarizations. Schematic representation of the magnetic configurations for (a−c) binary and (d and e) ternary 2D systems. The compositions for which the specific configuration applies are indicated at the bottom. Cations are visualized by black and light gray spheres, whereas oxygen anions are in red. Surface spin polarization on an isosurface of the charge density for (f and i) $CoTiO_3$, (g and j) $GeMnO_3$, and (h and k) $MnTiO_3$ in the top and side views, respectively. The isovalue for the charge density is 3×10^{-4} $e/\text{Å}^3$. The scale bar indicates the degree of spin polarization. Colors: Co, dark blue; Ti, light gray; Ge, light blue; Mn, magenta; and O, red.

investigations on the potential topological nature of these systems and other non-vdW 2D materials.

■ MAGNETISM

These mainly transition metal based 2D systems are especially interesting in terms of their magnetic properties as already reported for hematene and ilmenene.[29,30] Table 1 also indicates for which of the bulk parent systems a finite magnetic moment is reported in the AFLOW database. Hence, 4 (7) of 8 (20) binary (ternary) systems are found to be magnetic. While the standard workflow[66] of AFLOW might be biased toward ferromagnetic (FM) configurations with small magnetic moments, we have further investigated the preferred magnetic ordering according to the algorithm developed within the coordination corrected enthalpies (CCE) method[67,68] (see Methods section for details). This ansatz reliably finds the

antiferromagnetic (AFM) configurations of hematite and hematene reported previously.[40] Note that, for the 2D systems, the size of the surface moments (outer moments) is generally not equal to the ones within the slab (inner moments), and hence the AFM configuration might have a small net moment. This is particularly evident for ternary systems with two different magnetic ions such as $CoMnO_3$ and $MnNiO_3$.

The spin configurations found are indicated in Figure 5a−e, and additional results including the energy difference $\Delta E = E_{AFM} - E_{FM}$ between the lowest energy AFM and FM ordering and magnetic moments also including bulk reference data are summarized in Table 2. Results for SCAN are included in Section VI in the Supporting Information. The 2D materials are primarily AFM with the exception of Cr_2O_3, which becomes FM (Figure 5a) upon confinement to 2D as noted previously,[46] albeit for oxygen terminated slabs. For Fe_2O_3, the

Table 2. Magnetic Properties[a]

formula	mag. order type bulk	2D	ΔE bulk	2D	μ_{bulk}	μ_{2D} inner	outer	formula	mag. order type bulk	2D	ΔE bulk	2D	μ_{bulk} A el.	B el.	μ_{2D} inner	outer
Cr_2O_3	AFM	FM	−0.044	0.013	2.91	2.97	3.04	$\underline{Co}MnO_3$	AFM	AFM	−0.024	−0.062	2.77	3.07	3.12	2.72
Fe_2O_3	AFM	AFM	−0.489	−0.479	4.18	4.20	4.01	$\underline{Co}TiO_3$	FM	AFM	0.004	−0.011	2.79	0.06	0.00	2.74
Ti_2O_3	AFM	AFM	−0.893	−0.094	0.87	0.89	0.74	$\underline{Fe}TiO_3$	FM	AFM	0.003	−0.007	3.72	0.08	0.00	3.69
V_2O_3	AFM	AFM	−0.013	−0.090	1.83	1.84	1.67	$Ge\underline{Mn}O_3$	AFM	AFM	−0.041	−0.014	0.01	4.61	0.00	4.57
								$Mn\underline{Ni}O_3$	AFM	AFM	−0.054	−0.147	3.07	1.73	3.13	1.69
								$\underline{Mn}TiO_3$	AFM	AFM	−0.027	−0.018	4.60	0.02	0.00	4.55
								$\underline{Ni}TiO_3$	FM	AFM	0.001	−0.001	1.75	0.07	0.00	1.73

[a]Energetically preferred magnetic ordering type, energy difference $\Delta E = E_{AFM} - E_{FM}$ between lowest energy AFM and FM ordering in eV/formula unit, and absolute magnetic moments for the inner and outer magnetic ions of the slab in μ_B for the bulk and corresponding [001] facets. For ternaries, the A element is the first cation species in the formula while the B element corresponds to the second. The terminating elements of the slabs (outer ions) are underlined.

moments of the inner ions are antialigned to the ones at the bottom and top, Figure 5b. On the contrary, for Ti_2O_3 and V_2O_3 also the inner moments show AFM ordering, resulting in the top and bottom moments being antialigned (Figure 5c). For ternaries, only two types of magnetic configurations are observed (Figures 5d,e). If two magnetic species are present as for $CoMnO_3$ and $MnNiO_3$, the inner moments are AFM to the outer ones. For the other cases with only one magnetic species, the spins at the top and bottom are AFM. The surface moments generally reduce by up to ~0.2 μ_B when compared to their bulk references. The only exception is Cr_2O_3, for which they are slightly enhanced.

Even with most systems being AFM, the preferred termination of the 2D materials by the species in the lower oxidation state causes the magnetic ions of the ternary systems, i.e., Mn^{2+}, Fe^{2+}, Co^{2+}, and Ni^{2+}, to be at the surface. This outlines an ideal playground for spintronics since the spin polarization at surfaces can be accessed by techniques such as spin-polarized scanning tunneling microscopy (STM) and tuned by, e.g., adsorbates.[40,69] While the 2D systems themselves are found to be insulating, it has already been demonstrated that, due to weak interactions, the electronic and magnetic properties of hematene were well preserved on $Au(111)$[45]—a prototypical substrate in surface science.

To underscore this point, Figure 5f−k presents the surface spin polarization on an isosurface of the charge density for $CoTiO_3$, $GeMnO_3$, and $MnTiO_3$. We decided to use the total charge density to clearly indicate that the whole density is strongly spin-polarized and not just a part of it within a certain energy interval (as sampled by STM). For this, we have studied the FM and AFM alignment of the surface spins in a 2 × 2 supercell, as the interplane couplings (see Figure 5a−e) are regarded to be reliably determined from the study of the structural unit cell. For $GeMnO_3$, the surface moments couple antiferromagnetically, whereas for the other systems FM order is observed. As indicated in Figure 5, for $CoTiO_3$, a positive polarization reaching up to ~70% in a narrow region above the Co centers is found. $GeMnO_3$ depicts a strong spatial variation of the polarization from −86% to +86% due to the AFM in-plane coupling. Finally, $MnTiO_3$ shows high positive values extending over a larger spatial range above the Mn ions compared to $CoTiO_3$, also reaching a maximum of +86%. These examples showcase the versatile degree of surface spin polarization that can be expected from non-vdW 2D materials offering great potential for spintronic applications.

CONCLUSIONS

We have outlined a new set of non-vdW 2D materials by employing data-driven concepts and extensive calculations. By filtering the AFLOW-ICSD database according to the structural prototype of the two first systems realized experimentally, we have obtained 8 binary and 20 ternary candidates. The oxidation number of the cations at the surface of the 2D slab is identified as a suitable descriptor for exfoliability, i.e., indicating easy exfoliation in the case of a low oxidation state—a principle of likely high value for future 2D materials discovery. In terms of the structure, the 2D systems show a strong vertical contraction and lateral expansion as compared to the bulk parents. The band gaps are distributed over a large range, and potential topological features are exhibited by several candidates. The magnetic properties are especially appealing: while most spin-polarized systems show AFM ordering, the magnetic ions are at the surface, which leads to a very diverse set of surface spin polarizations, foreshadowing potential applications in spintronics. Eventually, surface functionalization by appropriate molecular adsorbates can be a fruitful future direction to selectively enhance the properties of the outlined compounds. We thus anticipate that our study will prove useful for the discovery of new non-vdW 2D systems and will unravel the potential of this class of novel materials.

METHODS

The *ab initio* calculations for the exchange-correlation functionals LDA,[70,71] PBE,[72] SCAN,[73] and PBE+U[74−76] are performed with AFLOW[77,78] and the Vienna *Ab-initio* Simulation Package (VASP)[79−81] with settings according to the AFLOW standard[66] and the internal VASP precision set to ACCURATE. For calculations with SCAN, projector-augmented-wave (PAW) pseudopotentials[82] of VASP version 5.4 are used, and nonspherical contributions to the gradient of the density in the PAW spheres are explicitly included for SCAN and PBE+U. The [001] monolayer 2D facets are constructed from the bulk standard conventional unit cell with the respective AFLOW commands,[83] resulting in structures with 10 atoms, and at least 20 Å of vacuum perpendicular to the slabs are included. For the facets, both the ionic positions and the cell shape are allowed to relax unless stated otherwise. The AFLOW internal automatic determination of k-point sets is used, and for the calculations of the 2D facets, the setting for the number of k-points per reciprocal atom[66] is reduced to 1000, resulting in Γ-centered 10 × 10 × 1 grids.

The bulk and 2D candidate systems containing potentially magnetic elements such as Ti, V, Cr, Mn, Fe, Co, Ni, and Rh are rigorously checked for magnetism, using the algorithm developed within the CCE method,[67,68] i.e., investigating all possible FM and AFM configurations in the structural unit cell for five different sizes of induced magnetic moments each. The analysis is only applied to other systems when the standard workflow of AFLOW[66] resulted in finite magnetic moments after the relaxation. Ferrimagnetic configurations, i.e., having one moment antialigned to the other three in the unit cell, are only checked for the bulk binary systems but never resulted in the lowest energy configuration; hence, they are not considered for the 2D facets and ternary systems. In each case, the lowest energy magnetic state is used for the further calculations.

The exfoliation energy is computed as

$$\Delta E_{\mathrm{exf}} = \frac{E_{\mathrm{slab}} - E_{\mathrm{bulk}}}{A} \tag{1}$$

where E_{slab} and E_{bulk} indicate the total energies of the relaxed 2D material and bulk, respectively, and A is the in-plane surface area according to the relaxed bulk unit cell. As pointed out in ref 59, the exfoliation energy from the surface of the material is exactly equal to the binding energy between layers/facets in the bulk.

The spin polarization is defined as

$$P = \frac{n_\uparrow - n_\downarrow}{n_\uparrow + n_\downarrow} \tag{2}$$

where $n_\uparrow$ and $n_\downarrow$ correspond to up spin and down spin densities, respectively. For the relaxed 2D systems, a static electronic calculation on 2×2 supercells was carried out. FM and AFM in-plane magnetic ordering was considered with the size of the magnetic moments induced according to the lowest energy magnetic configuration found for the structural unit cell. In each case, due to the weak in-plane magnetic coupling, the forces on the atoms and stress on the supercell were found to be negligibly small in each case.

Numerical data for the exfoliation energies, structural parameters, and magnetic properties are included in Section VI in the Supporting Information.

ASSOCIATED CONTENT

ⓈⒾ Supporting Information

The Supporting Information is available free of charge at https://pubs.acs.org/doi/10.1021/acs.nanolett.1c03841.

Exfoliation energies for additional functionals and from relaxing different degrees of freedom, exfoliation energies for different terminations for ternaries, change of structural parameters for SCAN, band structures for all binaries and ternaries, and tables with numerical data. (PDF)

AUTHOR INFORMATION

Corresponding Author

Rico Friedrich − *Institute of Ion Beam Physics and Materials Research, Helmholtz-Zentrum Dresden-Rossendorf, 01328 Dresden, Germany; Center for Autonomous Materials Design, Duke University, Durham, North Carolina 27708, United States;* ⓞ orcid.org/0000-0002-4066-3840; Email: r.friedrich@hzdr.de

Authors

Mahdi Ghorbani-Asl − *Institute of Ion Beam Physics and Materials Research, Helmholtz-Zentrum Dresden-Rossendorf, 01328 Dresden, Germany;* ⓞ orcid.org/0000-0003-3060-4369

Stefano Curtarolo − *Center for Autonomous Materials Design, Duke University, Durham, North Carolina 27708, United States; Materials Science, Electrical Engineering, and Physics, Duke University, Durham, North Carolina 27708, United States;* ⓞ orcid.org/0000-0003-0570-8238

Arkady V. Krasheninnikov − *Institute of Ion Beam Physics and Materials Research, Helmholtz-Zentrum Dresden-Rossendorf, 01328 Dresden, Germany; Department of Applied Physics, Aalto University, Aalto 00076, Finland;* ⓞ orcid.org/0000-0003-0074-7588

Complete contact information is available at:
https://pubs.acs.org/10.1021/acs.nanolett.1c03841

Notes

The authors declare no competing financial interest.

REFERENCES

(1) Novoselov, K. S.; Geim, A. K.; Morozov, S. V.; Jiang, D.; Zhang, Y.; Dubonos, S. V.; Grigorieva, I. V.; Firsov, A. A. Electric Field Effect in Atomically Thin Carbon Films. *Science* **2004**, *306*, 666−669.

(2) Cao, Y.; Fatemi, V.; Fang, S.; Watanabe, K.; Taniguchi, T.; Kaxiras, E.; Jarillo-Herrero, P. Unconventional superconductivity in magic-angle graphene superlattices. *Nature* **2018**, *556*, 43−50.

(3) Campi, D.; Kumari, S.; Marzari, N. Prediction of Phonon-Mediated Superconductivity with High Critical Temperature in the Two-Dimensional Topological Semimetal W_2N_3. *Nano Lett.* **2021**, *21*, 3435−3442.

(4) Butler, S. Z.; Hollen, S. M.; Cao, L.; Cui, Y.; Gupta, J. A.; Gutiérrez, H. R.; Heinz, T. F.; Hong, S. S.; Huang, J.; Ismach, A. F.; et al. Progress, Challenges, and Opportunities in Two-Dimensional Materials Beyond Graphene. *ACS Nano* **2013**, *7*, 2898−2926.

(5) Chhowalla, M.; Shin, H. S.; Eda, G.; Li, L.-J.; Loh, K. P.; Zhang, H. The chemistry of two-dimensional layered transition metal dichalcogenide nanosheets. *Nat. Chem.* **2013**, *5*, 263−275.

(6) Manzeli, S.; Ovchinnikov, D.; Pasquier, D.; Yazyev, O. V.; Kis, A. 2D transition metal dichalcogenides. *Nat. Rev. Mater.* **2017**, *2*, 17033.

(7) Burch, K. S.; Mandrus, D.; Park, J.-G. Magnetism in two-dimensional van der Waals materials. *Nature* **2018**, *563*, 47−52.

(8) Gibertini, M.; Koperski, M.; Morpurgo, A. F.; Novoselov, K. S. Magnetic 2D materials and heterostructures. *Nat. Nanotechnol.* **2019**, *14*, 408−419.

(9) Huang, Y. L.; Chen, W.; Wee, A. T. S. Two-dimensional magnetic transition metal chalcogenides. *SmartMat* **2021**, *2*, 139−153.

(10) Kou, L.; Ma, Y.; Sun, Z.; Heine, T.; Chen, C. Two-Dimensional Topological Insulators: Progress and Prospects. *J. Phys. Chem. Lett.* **2017**, *8*, 1905−1919.

(11) Wang, Q. H.; Kalantar-Zadeh, K.; Kis, A.; Coleman, J. N.; Strano, M. S. Electronics and optoelectronics of two-dimensional transition metal dichalcogenides. *Nat. Nanotechnol.* **2012**, *7*, 699−712.

(12) Lemme, M. C.; Li, L.-J.; Palacios, T.; Schwierz, F. Two-dimensional materials for electronic applications. *MRS Bull.* **2014**, *39*, 711−718.

(13) Deng, D.; Novoselov, K. S.; Fu, Q.; Zheng, N.; Tian, Z.; Bao, X. Catalysis with two-dimensional materials and their heterostructures. *Nat. Nanotechnol.* **2016**, *11*, 218−230.

(14) Wang, Y.; Mao, J.; Meng, X.; Yu, L.; Deng, D.; Bao, X. Catalysis with Two-Dimensional Materials Confining Single Atoms: Concept, Design, and Applications. *Chem. Rev.* **2019**, *119*, 1806−1854.

(15) Anasori, B.; Lukatskaya, M. R.; Gogotsi, Y. 2D metal carbides and nitrides (MXenes) for energy storage. *Nat. Rev. Mater.* **2017**, *2*, 16098.

(16) Wang, J.; Malgras, V.; Sugahara, Y.; Yamauchi, Y. Electro-chemical energy storage performance of 2D nanoarchitectured hybrid materials. *Nat. Commun.* **2021**, *12*, 3563.

(17) Chepkasov, I. V.; Ghorbani-Asl, M.; Popov, Z. I.; Smet, J. H.; Krasheninnikov, A. V. Alkali metals inside bi-layer graphene and MoS₂: Insights from first-principles calculations. *Nano Energy* **2020**, *75*, 104927.

(18) Novoselov, K. S.; Jiang, D.; Schedin, F.; Booth, T. J.; Khotkevich, V. V.; Morozov, S. V.; Geim, A. K. Two-dimensional atomic crystals. *Proc. Natl. Acad. Sci. U. S. A.* **2005**, *102*, 10451−10453.

(19) Nicolosi, V.; Chhowalla, M.; Kanatzidis, M. G.; Strano, M. S.; Coleman, J. N. Liquid Exfoliation of Layered Materials. *Science* **2013**, *340*, 1226419.

(20) Penev, E. S.; Marzari, N.; Yakobson, B. I. Theoretical Prediction of Two-Dimensional Materials, Behavior, and Properties. *ACS Nano* **2021**, *15*, 5959−5976.

(21) Lebègue, S.; Björkman, T.; Klintenberg, M.; Nieminen, R. M.; Eriksson, O. Two-Dimensional Materials from Data Filtering and Ab Initio Calculations. *Phys. Rev. X* **2013**, *3*, 031002.

(22) Rasmussen, F. A.; Thygesen, K. S. Computational 2D Materials Database: Electronic Structure of Transition-Metal Dichalcogenides and Oxides. *J. Phys. Chem. C* **2015**, *119*, 13169−13183.

(23) Choudhary, K.; Kalish, I.; Beams, R.; Tavazza, F. High-throughput Identification and Characterization of Two-dimensional Materials using Density functional theory. *Sci. Rep.* **2017**, *7*, 5179.

(24) Cheon, G.; Duerloo, K.-A. N.; Sendek, A. D.; Porter, C.; Chen, Y.; Reed, E. J. Data Mining for New Two- and One-Dimensional Weakly Bonded Solids and Lattice-Commensurate Heterostructures. *Nano Lett.* **2017**, *17*, 1915−1923.

(25) Mounet, N.; Gibertini, M.; Schwaller, P.; Campi, D.; Merkys, A.; Marrazzo, A.; Sohier, T.; Castelli, I. E.; Cepellotti, A.; Pizzi, G.; et al. Two-dimensional materials from high-throughput computational exfoliation of experimentally known compounds. *Nat. Nanotechnol.* **2018**, *13*, 246−252.

(26) Besse, R.; Lima, M. P.; Da Silva, J. L. F. First-Principles Exploration of Two-Dimensional Transition Metal Dichalcogenides Based on Fe, Co, Ni, and Cu Groups and Their van der Waals Heterostructures. *ACS Appl. Energy Mater.* **2019**, *2*, 8491−8501.

(27) Núñez, M.; Weht, R.; Núñez-Regueiro, M. Searching for electronically two dimensional metals in high-throughput ab initio databases. *Comput. Mater. Sci.* **2020**, *182*, 109747.

(28) Schleder, G. R.; Acosta, C. M.; Fazzio, A. Exploring Two-Dimensional Materials Thermodynamic Stability via Machine Learning. *ACS Appl. Mater. Interfaces* **2020**, *12*, 20149−20157.

(29) Puthirath Balan, A.; Radhakrishnan, S.; Woellner, C. F.; Sinha, S. K.; Deng, L.; Reyes, C. d. l.; Rao, B. M.; Paulose, M.; Neupane, R.; Apte, A.; et al. Exfoliation of a non-van der Waals material from iron ore hematite. *Nat. Nanotechnol.* **2018**, *13*, 602−609.

(30) Puthirath Balan, A.; Radhakrishnan, S.; Kumar, R.; Neupane, R.; Sinha, S. K.; Deng, L.; de los Reyes, C. A.; Apte, A.; Rao, B. M.; Paulose, M.; et al. A Non-van der Waals Two-Dimensional Material from Natural Titanium Mineral Ore Ilmenite. *Chem. Mater.* **2018**, *30*, 5923−5931.

(31) Yadav, T. P.; Shirodkar, S. N.; Lertcumfu, N.; Radhakrishnan, S.; Sayed, F. N.; Malviya, K. D.; Costin, G.; Vajtai, R.; Yakobson, B. I.; Tiwary, C. S.; et al. Chromiteen: A New 2D Oxide Magnetic Material from Natural Ore. *Adv. Mater. Interfaces* **2018**, *5*, 1800549.

(32) Puthirath, A. B.; Shirodkar, S. N.; Gao, G.; Hernandez, F. C. R.; Deng, L.; Dahal, R.; Apte, A.; Costin, G.; Chakingal, N.; Balan, A. P.; et al. Scale-Enhanced Magnetism in Exfoliated Atomically Thin Magnetite Sheets. *Small* **2020**, *16*, 2004208.

(33) Kaur, H.; Tian, R.; Roy, A.; McCrystall, M.; Horvath, D. V.; Lozano Onrubia, G.; Smith, R.; Ruether, M.; Griffin, A.; Backes, C.; et al. Production of Quasi-2D Platelets of Nonlayered Iron Pyrite (FeS₂) by Liquid-Phase Exfoliation for High Performance Battery Electrodes. *ACS Nano* **2020**, *14*, 13418−13432.

(34) Puthirath, A. B.; Balan, A. P.; Oliveira, E. F.; Sreepal, V.; Robles Hernandez, F. C.; Gao, G.; Chakingal, N.; Sassi, L. M.; Thibeorchews, P.; Costin, G.; et al. Apparent Ferromagnetism in Exfoliated Ultrathin Pyrite Sheets. *J. Phys. Chem. C* **2021**, *125*, 18927−18935.

(35) Moinuddin, M. G.; Srinivasan, S.; Sharma, S. K. Probing Ferrimagnetic Semiconductor with Enhanced Negative Magneto-resistance: 2D Chromium Sulfide. *Adv. Electron. Mater.* **2021**, *7*, 2001116.

(36) Hu, L.; Cao, L.; Li, L.; Duan, J.; Liao, X.; Long, F.; Zhou, J.; Xiao, Y.; Zeng, Y.-J.; Zhou, S. Two-dimensional magneto-photo-conductivity in non-van der Waals manganese selenide. *Mater. Horiz.* **2021**, *8*, 1286−1296.

(37) Yousaf, A.; Gilliam, M. S.; Chang, S. L. Y.; Augustin, M.; Guo, Y.; Tahir, F.; Wang, M.; Schwindt, A.; Chu, X. S.; Li, D. O.; et al. Exfoliation of Quasi-Two-Dimensional Nanosheets of Metal Diborides. *J. Phys. Chem. C* **2021**, *125*, 6787−6799.

(38) Guo, Y.; Gupta, A.; Gilliam, M. S.; Debnath, A.; Yousaf, A.; Saha, S.; Levin, M. D.; Green, A. A.; Singh, A. K.; Wang, Q. H. Exfoliation of boron carbide into ultrathin nanosheets. *Nanoscale* **2021**, *13*, 1652−1662.

(39) Gibaja, C.; Rodríguez-San-Miguel, D.; Paz, W. S.; Torres, I.; Salagre, E.; Segovia, P.; Michel, E. G.; Assebban, M.; Ares, P.; Hernández-Maldonado, D.; et al. Exfoliation of Alpha-Germanium: A Covalent Diamond-Like Structure. *Adv. Mater.* **2021**, *33*, 2006826.

(40) Wei, Y.; Ghorbani-Asl, M.; Krasheninnikov, A. V. Tailoring the Electronic and Magnetic Properties of Hematene by Surface Passivation: Insights from First-Principles Calculations. *J. Phys. Chem. C* **2020**, *124*, 22784−22792.

(41) Zhang, B. Y.; Xu, K.; Yao, Q.; Jannat, A.; Ren, G.; Field, M. R.; Wen, X.; Zhou, C.; Zavabeti, A.; Ou, J. Z. Hexagonal metal oxide monolayers derived from the metal−gas interface. *Nat. Mater.* **2021**, *20*, 1073−1078.

(42) Wei, Y.; Liu, C.; Wang, T.; Zhang, Y.; Qi, C.; Li, H.; Ma, G.; Liu, Y.; Dong, S.; Huo, M. Electronegativity regulation on opt-electronic properties of non van der Waals two-dimensional material: Ga₂O₃. *Comput. Mater. Sci.* **2020**, *179*, 109692.

(43) Jin, C.; Kou, L. Two-dimensional non-van der Waals magnetic layers: functional materials for potential device applications. *J. Phys. D: Appl. Phys.* **2021**, *54*, 413001.

(44) Padilha, A. C. M.; Soares, M.; Leite, E. R.; Fazzio, A. Theoretical and Experimental Investigation of 2D Hematite. *J. Phys. Chem. C* **2019**, *123*, 16359−16365.

(45) Gonzalez, R. I.; Mella, J.; Díaz, P.; Allende, S.; Vogel, E. E.; Cardenas, C.; Munoz, F. Hematene: a 2D magnetic material in van der Waals or non-van der Waals heterostructures. *2D Mater.* **2019**, *6*, 045002.

(46) Bandyopadhyay, A.; Frey, N. C.; Jariwala, D.; Shenoy, V. B. Engineering Magnetic Phases in Two-Dimensional Non-van der Waals Transition-Metal Oxides. *Nano Lett.* **2019**, *19*, 7793−7800.

(47) Chahal, S.; Kauzlarich, S. M.; Kumar, P. Microwave Synthesis of Hematene and Other Two-Dimensional Oxides. *ACS Materials Lett.* **2021**, *3*, 631−640.

(48) Mohapatra, J.; Ramos, A.; Elkins, J.; Beatty, J.; Xing, M.; Singh, D.; La Plante, E. C.; Ping Liu, J. Ferromagnetism in 2D α-Fe₂O₃ nanosheets. *Appl. Phys. Lett.* **2021**, *118*, 183102.

(49) Momma, K.; Izumi, F. *VESTA3* for three-dimensional visualization of crystal, volumetric and morphology data. *J. Appl. Crystallogr.* **2011**, *44*, 1272−1276.

(50) Liu, S.; Xie, L.; Qian, H.; Liu, G.; Zhong, H.; Zeng, H. Facile preparation of novel and active 2D nanosheets from non-layered and traditionally non-exfoliable earth-abundant materials. *J. Mater. Chem. A* **2019**, *7*, 15411−15419.

(51) Curtarolo, S.; Setyawan, W.; Wang, S.; Xue, J.; Yang, K.; Taylor, R. H.; Nelson, L. J.; Hart, G. L. W.; Sanvito, S.; Buongiorno Nardelli, M.; et al. AFLOWLIB.ORG: A distributed materials properties repository from high-throughput *ab initio* calculations. *Comput. Mater. Sci.* **2012**, *58*, 227−235.

(52) Hicks, D.; Oses, C.; Gossett, E.; Gomez, G.; Taylor, R. H.; Toher, C.; Mehl, M. J.; Levy, O.; Curtarolo, S. *AFLOW-SYM*: platform for the complete, automatic and self-consistent symmetry analysis of crystals. *Acta Crystallogr., Sect. A* **2018**, *74*, 184−203.

(53) Hicks, D.; Toher, C.; Ford, D. C.; Rose, F.; De Santo, C.; Levy, O.; Mehl, M. J.; Curtarolo, S. AFLOW-XtalFinder: a reliable choice to identify crystalline prototypes. *npj Comput. Mater.* **2021**, *7*, 30.

(54) Taylor, R. H.; Rose, F.; Toher, C.; Levy, O.; Yang, K.; Buongiorno Nardelli, M.; Curtarolo, S. A RESTful API for exchanging materials data in the AFLOWLIB.org consortium. *Comput. Mater. Sci.* **2014**, *93*, 178−192.

(55) Rose, F.; Toher, C.; Gossett, E.; Oses, C.; Buongiorno Nardelli, M.; Fornari, M.; Curtarolo, S. AFLUX: The LUX materials search API for the AFLOW data repositories. *Comput. Mater. Sci.* **2017**, *137*, 362−370.

(56) Mehl, M. J.; Hicks, D.; Toher, C.; Levy, O.; Hanson, R. M.; Hart, G. L. W.; Curtarolo, S. The AFLOW Library of Crystallographic Prototypes: Part 1. *Comput. Mater. Sci.* **2017**, *136*, S1−S828.

(57) Backes, C.; Campi, D.; Szydlowska, B. M.; Synnatschke, K.; Ojala, E.; Rashvand, F.; Harvey, A.; Griffin, A.; Sofer, Z.; Marzari, N.; et al. Equipartition of Energy Defines the Size−Thickness Relationship in Liquid-Exfoliated Nanosheets. *ACS Nano* **2019**, *13*, 7050−7061.

(58) Zacharia, R.; Ulbricht, H.; Hertel, T. Interlayer cohesive energy of graphite from thermal desorption of polyaromatic hydrocarbons. *Phys. Rev. B* **2004**, *69*, 155406.

(59) Jung, J. H.; Park, C.-H.; Ihm, J. A Rigorous Method of Calculating Exfoliation Energies from First Principles. *Nano Lett.* **2018**, *18*, 2759−2765.

(60) Sun, J.; Remsing, R. C.; Zhang, Y.; Sun, Z.; Ruzsinszky, A.; Peng, H.; Yang, Z.; Paul, A.; Waghmare, U.; Wu, X.; et al. Accurate first-principles structures and energies of diversely bonded systems from an efficient density functional. *Nat. Chem.* **2016**, *8*, 831.

(61) Mohanty, B.; Wei, Y.; Ghorbani-Asl, M.; Krasheninnikov, A. V.; Rajput, P.; Jena, B. K. Revealing the defect-dominated oxygen evolution activity of hematene. *J. Mater. Chem. A* **2020**, *8*, 6709−6716.

(62) Navrotsky, A.; Ma, C.; Lilova, K.; Birkner, N. Nanophase Transition Metal Oxides Show Large Thermodynamically Driven Shifts in Oxidation-Reduction Equilibria. *Science* **2010**, *330*, 199−201.

(63) Kvashnin, A. G.; Kvashnin, D. G.; Oganov, A. R. Novel Unexpected Reconstructions of (100) and (111) Surfaces of NaCl: Theoretical Prediction. *Sci. Rep.* **2019**, *9*, 14267.

(64) Bahn, S. R.; Jacobsen, K. W. An object-oriented scripting interface to a legacy electronic structure code. *Comput. Sci. Eng.* **2002**, *4*, 56−66.

(65) Hjorth Larsen, A.; Jørgen Mortensen, J. J.; Blomqvist, J.; Castelli, I. E.; Christensen, R.; Dułak, M.; Friis, J.; Groves, M. N.; Hammer, B.; Hargus, C.; et al. The atomic simulation environment—a Python library for working with atoms. *J. Phys.: Condens. Matter* **2017**, *29*, 273002.

(66) Calderon, C. E.; Plata, J. J.; Toher, C.; Oses, C.; Levy, O.; Fornari, M.; Natan, A.; Mehl, M. J.; Hart, G. L. W.; Buongiorno Nardelli, M.; et al. The AFLOW standard for high-throughput materials science calculations. *Comput. Mater. Sci.* **2015**, *108*, 233−238.

(67) Friedrich, R.; Usanmaz, D.; Oses, C.; Supka, A.; Fornari, M.; Buongiorno Nardelli, M.; Toher, C.; Curtarolo, S. Coordination corrected ab initio formation enthalpies. *npj Comput. Mater.* **2019**, *5*, 59.

(68) Friedrich, R.; Esters, M.; Oses, C.; Ki, S.; Brenner, M. J.; Hicks, D.; Mehl, M. J.; Toher, C.; Curtarolo, S. Automated coordination corrected enthalpies with AFLOW-CCE. *Phys. Rev. Mater.* **2021**, *5*, 043803.

(69) Heß, V.; Friedrich, R.; Matthes, F.; Caciuc, V.; Atodiresei, N.; Bürgler, D. E.; Blügel, S.; Schneider, C. M. Magnetic subunits within a single molecule−surface hybrid. *New J. Phys.* **2017**, *19*, 053016.

(70) Kohn, W.; Sham, L. J. Self-consistent equations including exchange and correlation effects. *Phys. Rev.* **1965**, *140*, A1133.

(71) von Barth, U.; Hedin, L. A local exchange-correlation potential for the spin polarized case: I. *J. Phys. C: Solid State Phys.* **1972**, *5*, 1629.

(72) Perdew, J. P.; Burke, K.; Ernzerhof, M. Generalized Gradient Approximation Made Simple. *Phys. Rev. Lett.* **1996**, *77*, 3865−3868.

(73) Sun, J.; Ruzsinszky, A.; Perdew, J. P. Strongly Constrained and Appropriately Normed Semilocal Density Functional. *Phys. Rev. Lett.* **2015**, *115*, 036402.

(74) Dudarev, S. L.; Botton, G. A.; Savrasov, S. Y.; Humphreys, C. J.; Sutton, A. P. Electron-energy-loss spectra and the structural stability of nickel oxide: An LSDA + U study. *Phys. Rev. B* **1998**, *57*, 1505−1509.

(75) Liechtenstein, A. I.; Anisimov, V. I.; Zaanen, J. Density-functional theory and strong interactions: Orbital ordering in Mott-Hubbard insulators. *Phys. Rev. B* **1995**, *52*, R5467−R5470.

(76) Anisimov, V. I.; Zaanen, J.; Andersen, O. K. Band theory and Mott insulators: Hubbard U instead of Stoner I. *Phys. Rev. B* **1991**, *44*, 943−954.

(77) Levy, O.; Chepulskii, R. V.; Hart, G. L. W.; Curtarolo, S. The New Face of Rhodium Alloys: Revealing Ordered Structures from First Principles. *J. Am. Chem. Soc.* **2010**, *132*, 833−837.

(78) Curtarolo, S.; Setyawan, W.; Hart, G. L. W.; Jahnátek, M.; Chepulskii, R. V.; Taylor, R. H.; Wang, S.; Xue, J.; Yang, K.; Levy, O.; et al. AFLOW: An automatic framework for high-throughput materials discovery. *Comput. Mater. Sci.* **2012**, *58*, 218−226.

(79) Kresse, G.; Hafner, J. *Ab initio* molecular dynamics for liquid metals. *Phys. Rev. B* **1993**, *47*, 558−561.

(80) Kresse, G.; Furthmüller, J. Efficient iterative schemes for *ab initio* total-energy calculations using a plane-wave basis set. *Phys. Rev. B* **1996**, *54*, 11169−11186.

(81) Kresse, G.; Furthmüller, J. Efficiency of *ab-initio* total energy calculations for metals and semiconductors using a plane-wave basis set. *Comput. Mater. Sci.* **1996**, *6*, 15−50.

(82) Kresse, G.; Joubert, D. From ultrasoft pseudopotentials to the projector augmented-wave method. *Phys. Rev. B* **1999**, *59*, 1758−1775.

(83) Chepulskii, R. V.; Curtarolo, S. First principles study of Ag, Au, and Cu surface segregation in FePt-L1$_0$. *Appl. Phys. Lett.* **2010**, *97*, 221908.

nature communications

Wafer-scale nanofabrication of telecom single-photon emitters in silicon

Michael Hollenbach [1,2] ✉, **Nico Klingner**[1], **Nagesh S. Jagtap**[1,2], **Lothar Bischoff**[1], **Ciarán Fowley**[1], **Ulrich Kentsch**[1], **Gregor Hlawacek** [1], **Artur Erbe** [1], **Nikolay V. Abrosimov**[3], **Manfred Helm**[1,2], **Yonder Berencén** [1] ✉ & **Georgy V. Astakhov** [1] ✉

A highly promising route to scale millions of qubits is to use quantum photonic integrated circuits (PICs), where deterministic photon sources, reconfigurable optical elements, and single-photon detectors are monolithically integrated on the same silicon chip. The isolation of single-photon emitters, such as the G centers and W centers, in the optical telecommunication O-band, has recently been realized in silicon. In all previous cases, however, single-photon emitters were created uncontrollably in random locations, preventing their scalability. Here, we report the controllable fabrication of single G and W centers in silicon wafers using focused ion beams (FIB) with high probability. We also implement a scalable, broad-beam implantation protocol compatible with the complementary-metal-oxide-semiconductor (CMOS) technology to fabricate single telecom emitters at desired positions on the nanoscale. Our findings unlock a clear and easily exploitable pathway for industrial-scale photonic quantum processors with technology nodes below 100 nm.

Quantum technologies based on the generation and state manipulation of single photons enable demanding applications[1,2]. A prime example of this is linear optical quantum computation using boson sampling, which requires only single photons and linear optical components[3–5]. The front-runner demonstration is Gaussian boson sampling with 50 single-mode squeezed states[6]. A general-purpose photonic quantum processor can be built using fusing, cluster states, and nonlinear units[7,8]. The latter can be implemented through photon scattering by a two-level quantum system (i.e., a single-photon emitter) coupled to an optical cavity. State of the art for deterministic single-photon sources corresponds to boson sampling with 20 photons using quantum dots (QDs)[9]. To ensure indistinguishability, the same QD routes several photons into a delay line. Delay lines up to 27 m can be realized on a single silicon chip[10], which allows the interference of about 100 deterministic photons. However, the scalability of millions of qubits is not realistic with this approach.

Deterministic single-photon sources monolithically integrated with silicon quantum PIC represent a new tool in quantum photonics[11], complementing heralded probabilistic sources[12] and offering very-large-scale integration (VLSI)[13]. The strategic, long-term goal is the implementation of a photonic quantum processor compatible with present-day silicon technology. Most of the necessary components for cryogenic quantum PICs are available nowadays, including superconducting single-photon detectors[14], delay lines[10], modulators[15], and phase shifters[16]. The practical implementation of this concept has been largely hampered by the lack of controllable fabrication of single-photon emitters in silicon[11,17].

Recently, a broad variety of single-photon emitters have been isolated in commercial silicon-on-insulator (SOI) wafers, including G centers[11,17], W centers[18], T centers[19], some other unidentified damage centers[20], and erbium dopants[21].

Particularly single G centers are carbon-related color centers emitting in the telecom O-band[11,17]. The atomic configuration of the G

[1]Helmholtz-Zentrum Dresden-Rossendorf, Institute of Ion Beam Physics and Materials Research, 01328 Dresden, Germany. [2]Technische Universität Dresden, 01062 Dresden, Germany. [3]Leibniz-Institut für Kristallzüchtung (IKZ), 12489 Berlin, Germany. ✉e-mail: m.hollenbach@hzdr.de; y.berencen@hzdr.de; g.astakhov@hzdr.de

center (Fig. 1a) has been revised several times. According to the latest density functional theory calculations[22], it consists of two substitutional carbon atoms and one interstitial silicon atom in the configuration $C_s - Si_i - C_s$ distorted from the $\langle 111 \rangle$ bond axis (Fig. 1a). The spectroscopic fingerprint of the G center is a spectrally narrow zero-phonon line (ZPL) at $\lambda_G = 1278$ nm in the photoluminescence (PL) spectrum[23]. Another single-photon emitter in silicon is the W center (Fig. 1a), which is ascribed to a tri-interstitial Si complex I_3[18]. Like the aforementioned G center, it also possesses a single dipole emission, which has been shown to be polarized along the $\langle 111 \rangle$ crystal axis, revealing a ZPL at $\lambda_W = 1218$ nm in the PL spectrum[23].

Ensembles of the G and W centers in isotopically purified ^{28}Si crystals reveal extremely narrow linewidths of their ZPLs exceeding the Fourier limit by a factor of two only, which implies marginal spectral diffusion[24]. This makes the G and W centers very promising candidates for the implementation of spatially separated emitters of indistinguishable photons, where the fine-tuning of the emission wavelength can be implemented through the Stark effect or strain control[25,26].

To date, the protocols for the creation of single-photon emitters in silicon consist of either broad-beam implantation of carbon ions at a low fluence ($\Phi \sim 10^9$ cm^{-2})[11] or medium-fluence implantation ($\Phi \sim 10^{12}$ cm^{-2})[17] followed by rapid thermal annealing (RTA)[17]. In both approaches, the process of creating single-photon emitters is not controllable, resulting in emitters being created at random locations. This poses a major obstacle to the realization of wafer-scale quantum PICs with monolithically integrated and on-demand single-photon sources at desired locations.

Here, we use a focused ion beam (FIB)[27–30] to create single G and W centers with a precision better than 100 nm. This concept is illustrated in Fig. 1a. Confirmed by the PL spectra, we unambiguously find that in the case of carbon-rich Si wafers, the Si implantation results in the preferable formation of G centers (the left side of Fig. 1a). For ultrapure silicon wafers and a larger number of Si ions per implantation spot, interstitial complexes rather than G centers are formed, among which are the optically active W centers (the right side of Fig. 1a). In addition to that, we demonstrate large-scale, CMOS-compatible fabrication of single G and W centers using broad-beam Si implantation through lithographically defined nanoholes[31].

Results

Creation of single G centers on the nanoscale

To create G centers in a commercial SOI wafer (IceMOS tech.), we perform FIB implantation with double-charged Si^{2+} ions (Fig. 1a). The residual carbon concentration is estimated to be in the range of 10^{16} cm^{-3}[11]. The Si ions with a kinetic energy of 40 keV are focused to a spot size of about 50 nm. Using the Stopping and Range of Ions in Matter (SRIM) software[32], we calculate the lateral straggling to be ±25 nm and the mean implantation depth to be $R_p = 60$ nm. The overall spatial resolution is better than 100 nm, both in-depth and laterally (Supplementary Fig. 1).

We generate a FIB pattern consisting of a frame with a dimension of 200×200 μm^2 and 15×16 individual spots. The frame is created by implanting Si ions at a fluence $\Phi = 1 \times 10^{11}$ cm^{-2}. The average number of implanted Si ions per spot is the same in each row and increases logarithmically from $\overline{n}_{Si} = 6$ Si ions for row 1 to $\overline{n}_{Si} = 570$ Si ions for row 15. A detailed list of the averaged number of implanted Si ions ($\overline{n}_{Si}$) per spot is given in Supplementary Table 1. We use the chess notation to label each implanted spot.

After creating the FIB pattern, the samples are measured in a home-built confocal scanning microscope at $T = 6.3$ K under a continuous wave (CW) laser excitation at 637 nm (Supplementary Fig. 2).
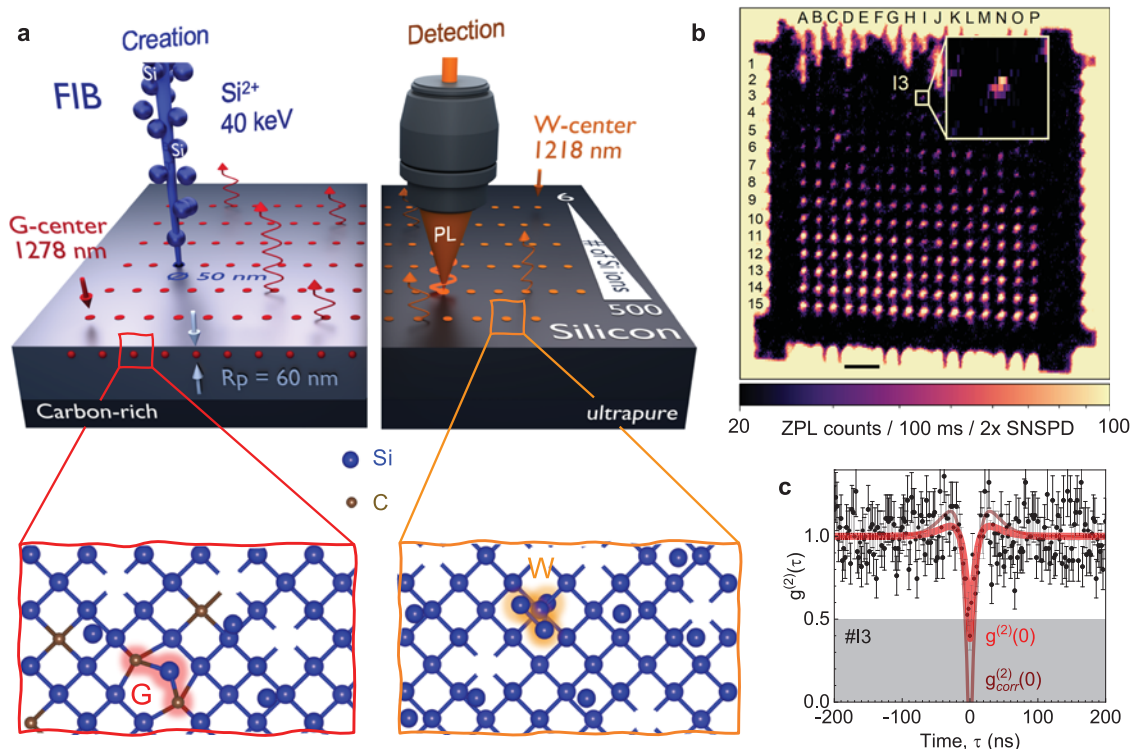
Fig. 1 | Creation and detection of single G and W centers in silicon. a Schematic of FIB implantation with Si^{2+} ions and PL collection from single centers. The kinetic energy of 40 keV corresponds to an average implantation depth $R_p = 60$ nm. Si implantation into a carbon-rich and an ultrapure silicon wafer results in the formation of the G and W centers, respectively. **b** Confocal ZPL (1278 nm) intensity map of locally created G centers on an SOI wafer. The number of ions per spot increases logarithmically from nominally 6 (row 1) to 570 (row 15). The pattern frame is created with a fluence $\Phi = 1 \times 10^{11}$ cm^{-2}. The scale bar is 20 μm. The inset shows photon emission from a single G center. The color scale is different from the main panel to increase visibility. **c** Second-order autocorrelation function $g^{(2)}(\tau)$ obtained with no BG correction (#I3). The red solid line is a fit to Eq. (1), yielding $g^{(2)}(0) = 0.36 \pm 0.06$. The thin solid line is $g^{(2)}_{corr}(\tau)$ calculated according to Eq. (2). The error bars represent standard deviation (SD).

Fig. 2 | Scalable fabrication of single G centers with sub-100-nm precision in an SOI wafer. a Statistics histogram representing the probability distribution of the G centers depending on the number of implanted Si ions. **b** The occurrence probability of G centers for FIB implantation (on average 25 Si ions per spot) and Si broad-beam implantation (fluence 1×10^{12} cm^{-2}) through PMMA holes (nominal diameter 40 nm). The solid line represents the sub-Poisson distribution with $\mu = 4$, as described in the text. **c** Confocal PL intensity map of locally created G centers in an SOI wafer through a PMMA mask using broad-beam Si implantation. The nominal hole diameter increases from 30 nm (row 1) to 400 nm (row 20). The PL is collected using a BP filter $\Delta\lambda = 50$ nm at $\lambda = 1275$ nm. The scale bar is 20 µm. The inset shows four implanted spots with single and no G centers. **d** Second-order autocorrelation function $g^{(2)}(\tau)$ obtained with no BG correction (#M3). The purple solid line is a fit to Eq. (1), yielding $g^{(2)}(0) = 0.22 \pm 0.08$. The thin solid line is $g^{(2)}_{\text{corr}}(\tau)$ calculated according to Eq. (2). The error bars represent SD.

Figure 1b shows a confocal ZPL map. To attenuate the background (BG) contribution, which may be related to the presence of defect states in the bandgap, we use a long pass (LP) filter ($\lambda > 1250$ nm) in combination with a narrow bandpass (BP) filter ($\Delta\lambda = 1$ nm) whose central wavelength coincides with the ZPL of the G center $\lambda_G = 1278$ nm.

To determine the number of G centers in the implanted spots, we measured the second-order autocorrelation function $g^{(2)}(\tau)$ using Hanbury–Brown–Twiss interferometry (Supplementary Fig. 2). The collected photons are coupled to a single-mode fiber and split with a 50/50 fiber beam splitter. The photons are then detected with two superconducting-nanowire single-photon detectors (SNSPDs) with an efficiency >90% in the telecom O-band. The photon detection statistics are recorded with a time-tagging device. An example of such a second-order autocorrelation function from spot #I3 is shown in Fig. 1c with no BG corrections. It is fitted[33]

$$g^{(2)}(\tau) = \frac{N-1}{N} + \frac{1}{N}\left[1 - (1+a)e^{-\left|\frac{\tau}{\tau_1}\right|} + ae^{-\left|\frac{\tau}{\tau_2}\right|}\right]. \quad (1)$$

Here, N corresponds to the number of single-photon emitters. The fit to Eq. (1) yields $g^{(2)}(0) = 0.36 \pm 0.08 < 0.5$ ($N < 2$). From the best fit, we obtain the characteristic antibunching time $\tau_1 \approx 10$ ns. Because of nearly negligible bunching in Fig. 1c, the parameters $\tau_2 \gtrsim \tau_1$ and $a > 0$ cannot be determined with reasonable accuracy.

To increase the photon count rate and consequently decrease the recording time of $g^{(2)}(\tau)$ in Fig. 1c, we use a BP filter with $\Delta\lambda = 50$ nm at $\lambda = 1275$ nm instead of the narrow-band filter as in Fig. 1b. This results in an additional BG contribution to the signal. The autocorrelation function can be corrected due to the presence of the BG as[34]

$$g^{(2)}_{\text{corr}}(\tau) = \frac{g^{(2)}(\tau) - (1 - \rho^2)}{\rho^2}. \quad (2)$$

The constant factor $\rho = (I - B)/I$ takes into account the count rate from an implanted spot (I) and the BG, i.e., the count rate from the location in the immediate surrounding the implanted spots (B). According to the recent theoretical analysis, the single photon nature of the emission is unambiguously confirmed if the second-order autocorrelation function is zero after the BG and time-jitter corrections[35,36]. The correction due to time jitter (40 ps for the SNSPDs and 14 ps for the time-tagging device) is negligible in Fig. 1c, as it is by more than two orders of magnitude shorter than the τ_1 time. After the BG correction to

Eq. (2), we obtain $g^{(2)}_{\text{corr}}(0) \approx 0$ for spot #I3 (thin solid line in Fig. 1c), which unambiguously points to a single G center ($N = 1$). Remarkably, this G center demonstrates stable operation over hours, with no indication of instability of either the ZPL intensity or the spectrally integrated photon count rate (Supplementary Fig. 3). We note that the spectral resolution is limited by our spectrometer and therefore no conclusions about the ZPL spectral stability can be made. Using this approach, we determine the number of single G centers in other implanted spots.
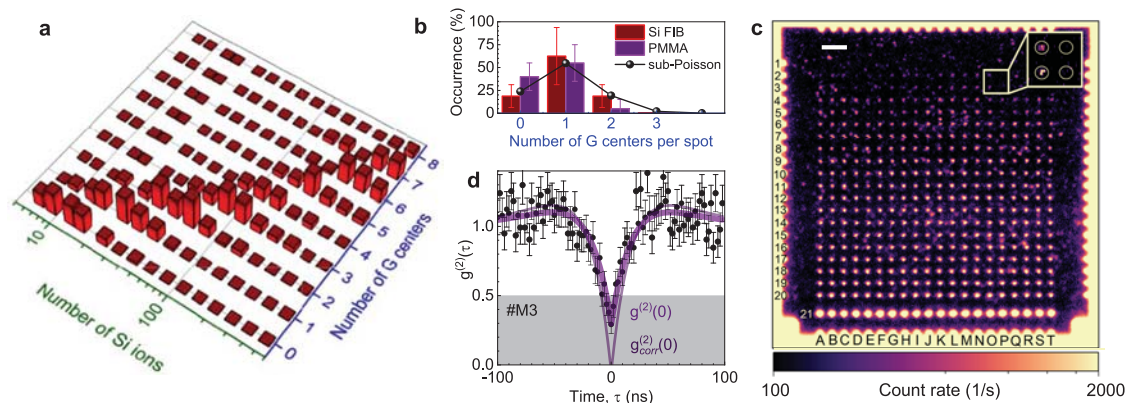
Fabrication statistics

The emission from single G centers is linearly polarized and equivalently distributed across four subgroups in the (001) plane[17]. As the excitation energy (1.9 eV) is far above the Si bandgap (1.1 eV), the PL is expected to be independent of the weak elliptical polarization of the excitation. As we collect PL without linear polarizers, we assume the same detection efficiency for all four possible dipole orientations. We assume that the count rate scales linearly with the number of color centers[31] per implantation spot. To estimate an average count rate from the single G center, we use

$$I_G = \frac{\sum_i (I_i - B)}{\sum_i N_i}. \quad (3)$$

Here, I_i is the count rate at the spot i in Fig. 1b obtained from a Gaussian fit (Supplementary Fig. 3) and N_i is the number of G centers established from the BG-corrected autocorrelation function following Eq. (2). We then estimate the number of the G centers in all implanted spots as $N_i = \text{round}\left[(I_i - B)/I_G\right]$. For instance, all spots with a count rate in the range from $0.5I_G$ to $1.5I_G$ are ascribed to single G centers.

Figure 2a summarizes the statistical distribution of the number of G centers (N) depending on the average number of implanted Si ions ($\overline{n}_{\text{Si}}$). The mean value of N increases with $\overline{n}_{\text{Si}}$ following a sublinear dependence as expected[11]. The reason is that higher implantation fluence leads to higher crystal damage and, consequently, to a decrease in available crystallographic sites suitable for the formation of G centers. According to the statistics histogram of Fig. 2a, the optimal number of Si ions required to create a single G center is $\overline{n}_{\text{Si}} = 25$ (row 5). The occurrence probability for a different number of G centers, in this case, is presented in Fig. 2b (the red histogram data Si FIB). The probability to create a single G center is as high as $(62 \pm 31)\%$, while there is a lower but nonzero probability of creating multiple or no G centers at the implantation spots. Though within the error bars, the
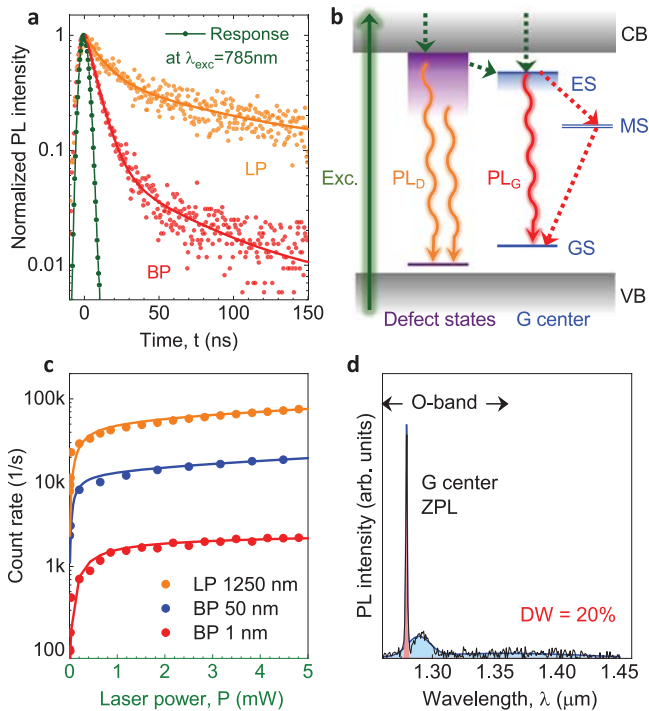
Article

Fig. 3 | Photoexcitation of G centers. a PL decay of the locally created G centers obtained with an LP filter $\lambda > 1250$ nm (orange) and a BP filter $\Delta\lambda = 1$ nm at $\lambda_G = 1278$ nm, corresponding to the ZPL of the G center (red). The solid lines are fits to a bi-exponential decay. The excitation laser pulse at $\lambda_{exc} = 785$ nm is also shown for comparison (green). **b** Schematic representation of the excitation and recombination processes of the G center (PL$_G$) in the vicinity of bandgap defect states (PL$_D$). **c** Count rate of a single G center as a function of the excitation power in the presence of BG obtained with different optical filters: LP filter $\lambda > 1250$ nm (orange), BP filter $\Delta\lambda = 50$ nm at $\lambda = 1275$ nm (blue) and BP filter $\Delta\lambda = 1$ nm at $\lambda_G = 1278$ nm (red). The solid lines are fits to Eq. (4). **d** PL spectrum of a single G center, obtained at $P = 100$ μW. A multi-Gauss fit over the ZPL and PSB's (blue solid line) yields a Debye–Waller factor DW = 20%.

distributions of Fig. 2a, b can be described by the Poisson function, there is a strong indication that the experimental data deviate from it. Considering that the G center is a composite defect consisting of three atoms, we can reproduce the sub-Poisson statistics shown by the solid line in Fig. 2b (Supplementary Fig. 4). The real formation process of the G centers is much more complex than in our simplified model based on a multi-step Si implantation process (Supplemental Material) and beyond the scope of this work.

To analyze the BG contribution, we perform time-resolved PL measurements with an LP and a narrow BP filter (Fig. 3a). The PL spectrum, together with the filter transmission wavelengths, is shown in Supplementary Fig. 5. The PL decay is fitted to a bi-exponential function. The fast PL decay with a time constant of about 10 ns dominates when the narrow BP filter is tuned to the ZPL[37]. Therefore, this is associated with the G center. For the spectrally integrated decay, i.e., with the LP filter only, there is a slow contribution with a time constant of about 70 ns. This is ascribed to the presence of defect states in the bandgap, which are created during the fabrication of the SOI wafer. The excitation and recombination processes involving the defect states and G centers are schematically presented in Fig. 3b. This explanation is also confirmed by the excitation power (P) dependence of the PL count rate (I) for three different filter configurations (Fig. 3c). It is fitted to

$$I(P) = \frac{I_G(\lambda)}{1 + P_0/P} + S_D(\lambda)P, \quad (4)$$

where $I_G(\lambda)$ is the saturation count rate and $S_D(\lambda)$ is a spectrally-dependent slope describing the BG contribution. The fit of $I(P)$ integrated over the ZPL and the phonon sideband (PSB), i.e., with a BP filter 50 nm, gives $I_G = 13 \times 10^3$ counts per second. We find the saturation excitation power for this case $P_0 = 110$ μW, which can be reduced using an optimum excitation wavelength according to the PL excitation spectrum[17,37] (Supplementary Fig. 5).

Wafer-scale fabrication of single G centers

To reduce the BG in our commercial SOI wafers, a series of RTA and furnace annealing (FA) experiments were performed (Supplementary Fig. 6). We find that the most efficient reduction is obtained with RTA processing at 1000 °C for 60 s. After optimizing the implantation and annealing parameters, we demonstrate the controllable creation of single G centers using a CMOS-compatible protocol. We first fabricate a PMMA mask with lithographically defined arrays of nanoholes (Supplementary Fig. 1) having different diameters (Supplementary Table 2). Then, we perform a broad-beam implantation with Si ions at a fluence $\Phi = 1 \times 10^{11}$ cm^{-2} and with the same kinetic energy of 40 keV as in the FIB experiments.

A confocal map of the G centers created in 20×20 nanoholes is depicted in Fig. 2c. The PL count rate is spectrally integrated over the ZPL and PSBs. As an illustration, we show the autocorrelation function recorded at the spot #M3 with no BG correction (thick solid line in Fig. 2d). The fit to Eq. (1) yields $g^{(2)}(0) = 0.22 \pm 0.08$ and after BG correction to Eq. (2) $g_{corr}^{(2)}(0) \approx 0$ (the thin solid line in Fig. 2d), pointing to a single-photon emission. Some other $g^{(2)}(\tau)$ measurements of single G centers at different implanted spots are shown in Supplementary Fig. 7. Based on the $g^{(2)}(\tau)$ measurements and calibrated count rate, we find that more than 50% of the nanoholes with nominal diameters of 35 and 40 nm (rows 2 and 3, respectively) contain single G centers (Fig. 2b).

Figure 3d shows a PL spectrum from the spot with a nominal diameter of 40 nm (#M3). It consists of the ZPL at $\lambda_G = 1278$ nm and the PSB with a maximum at around 1290 nm[17]. The Debye–Waller (DW) factor, i.e., the probability of coherently emitting into the ZPL, is an important characteristic of single-photon emitters for their applications in photonic quantum technologies. We find DW = 19 ± 1%. This is the largest value reported to date for individual G centers and is comparable with a DW factor of an ensemble of G centers with an optimized creation protocol[37].

Creation of single W centers on the nanoscale

Finally, we turn to the controlled creation of W center emitters with the ZPL at $\lambda_W = 1218$ nm. In order to locally write W centers, we use the same procedure as for G centers in SOI, with the difference that the substrates are now ultrapure Si wafers with negligible carbon content (Fig. 1a). After implantation, the sample is annealed at 225 °C for 300 s[24,38]. Figure 4a shows a confocal PL map of this pattern. A 50-nm BP filter at 1225 nm is used to selectively collect the PL emission from the ZPL and the first PSB of W centers. We optically resolve all the implanted spots in row 15 (on average, 570 Si ions per spot) down to only a few implanted spots in row 10 (on average, 113 Si ions per spot).

We show an autocorrelation measurement at a spot irradiated with, on average, 384 Si ions (#I14) with no BG correction (Fig. 4b). The dip at $\tau = 0$ indicates a countable number of W centers ($N \leqslant 5$). We observe a relatively high BG (Supplementary Fig. 8). A possible reason is that we use an established annealing protocol optimized for a dense ensemble of W centers[38], which might not be optimum for the creation of individual W centers. Applying the BG correction procedure of Eq. (2), we obtain $g_{corr}^{(2)}(0) = 0.13_{-0.13}^{+0.35}$, which indicates that, in fact, we have single-photon emission from this spot. To find the power dependence of the photon count rate from a single W center of Fig. 4c, we subtract the BG contribution taken from the non-implanted area between the nearest spots. A fit to Eq. (4) gives $I_W = 3600$ counts per second and
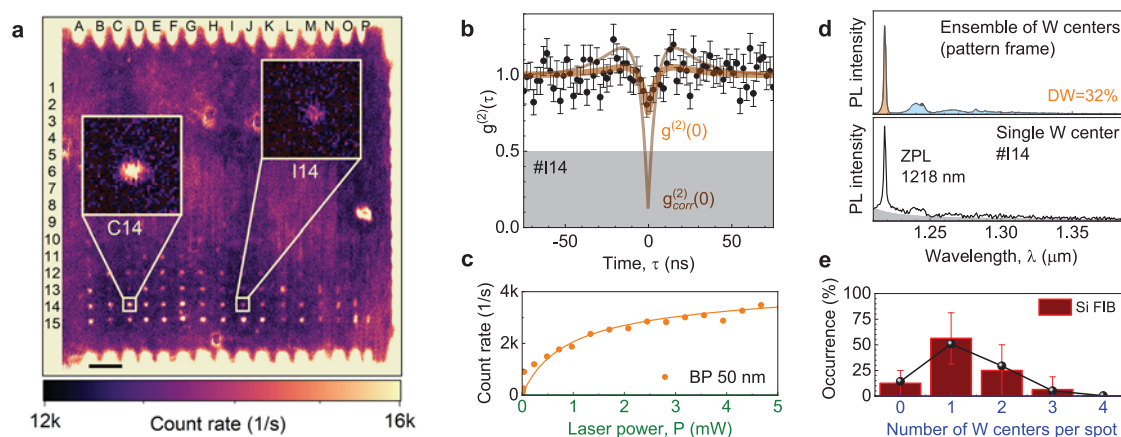
Fig. 4 | Single W centers in ultrapure silicon. a Confocal PL intensity map of locally created W centers. The pattern frame is created with a fluence $\Phi = 1 \times 10^{11}$ cm^{-2}. The PL is collected using a BP filter $\Delta\lambda = 50$ nm at $\lambda = 1225$ nm. The scale bar is 20 μm. The insets show the PL from two W centers (#C14) and a single W center (#I14). **b** Second-order autocorrelation function $g^{(2)}(\tau)$ obtained at the spot #I14 with no BG correction. The BG correction (thin solid line) gives $g^{(2)}_{corr}(0) = 0.13^{+0.35}_{-0.13}$. **c** Count rate of a single W center after BG subtraction as a function of the excitation power, which is measured with a BP filter $\Delta\lambda = 50$ nm at $\lambda = 1225$ nm. The solid line is a fit to Eq. (4). **d** PL spectrum from the frame and a single W center (#I14). Integration over the ZPL and PSB yields a Debye–Waller factor DW = 32%. The BG contribution is schematically shown by the shaded area. **e** The occurrence probability of W centers for FIB implantation with, on average, 384 Si ions per spot. The solid line represents the sub-Poisson distribution with $\mu = 4.8$, as described in the text. The error bars represent SD.

$P_0 = 810$ μW (Supplementary Fig. 8), which is lower than the saturation count rate of the G centers.

A PL spectrum from a single W center is shown in the lower panel of Fig. 4d, which is similar to the PL spectrum of an ensemble of W centers (upper panel of Fig. 4d). We find a DW = 32%, which is significantly larger than that for the G center. For low excitation powers ($P \ll P_0$), the PL spectrum and photon count rate remain stable over one day of operation (Supplementary Fig. 8). For high excitation powers ($P > P_0$), we observe blinking of the ZPL. The origin of this optical instability is beyond the scope of this work.

Two spots with implantation $\bar{n}_{Si} = 384$ (row 14) show a difference in count rate, after the BG correction, of a factor of two, indicating that one contains a single center (#I14) and one contains two single centers (#C14). This is in agreement with the corrected $g^{(2)}_{corr}(0) = 0.52 \pm 0.15$ indicating two-photon emission (Supplementary Fig. 9). The emission from the W centers is linearly polarized either along the [110] or [1$\bar{1}$0] direction[18] and, similar to the G centers, we assume the same detection efficiency for both directions. Based on the $g^{(2)}(\tau)$ and the photon count rate analysis of the implanted row 14, we find that, in a similar way to Fig. 2b, the creation probability of a single W center is $(56 \pm 28)\%$ (Fig. 4e). Thus, the analysis indicates that the W centers are created with sub-Poisson statistics, as explained in Supplementary Fig. 4.

To demonstrate the wafer-scale fabrication of single W centers, we use broad-beam Si implantation through nanoholes in a PMMA mask. The implantation parameters (Si^{2+} with a kinetic energy of 40 keV, $\Phi = 1 \times 10^{12}$ cm^{-2}) and mask design (Supplementary Table 2) are similar to those optimized for the fabrication of single G centers. A confocal map of the W centers created in 20×20 nanoholes is depicted in Fig. 5a. The PL count rate is spectrally integrated over the ZPL and the first PSB. Because post-implantation annealing at 225 °C leads to a high BG in Fig. 4a, no annealing is performed. Indeed, the BG in the confocal map of Fig. 5a is significantly lower.

As an illustration, we show the autocorrelation function recorded at spot #C13 (nanohole with a nominal diameter of 300 nm) without BG correction (Fig. 5b). The fit to Eq. (1) yields $g^{(2)}(0) = 0.48 \pm 0.27$. With BG correction to Eq. (2), we obtain $g^{(2)}_{corr}(0) \approx 0$ demonstrating single-photon emission. We note that the absence of annealing also leads to a lower count rate from single W centers because the lattice damage after implantation is not removed. The optimization of the annealing conditions for the local creation of single W centers with a high photon
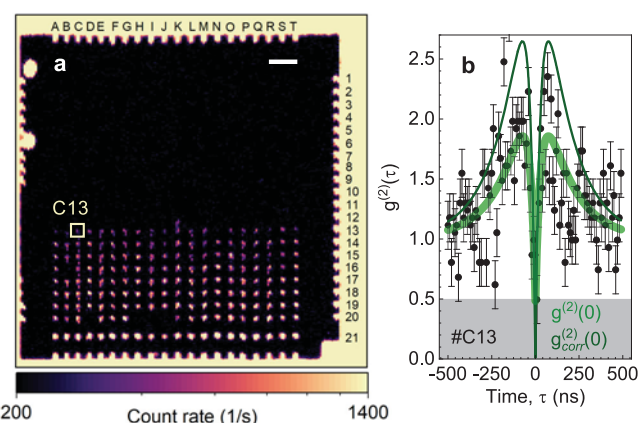
Fig. 5 | Scalable fabrication of single W centers in ultrapure silicon. a Confocal PL intensity map of locally created W centers through a PMMA mask using broad-beam Si implantation. The nominal hole diameter increases from 30 nm (row 1) to 400 nm (row 20). The PL is collected using a BP filter $\Delta\lambda = 50$ nm at $\lambda = 1225$ nm. No annealing is performed. The scale bar is 20 μm. **b** Second-order autocorrelation function $g^{(2)}(\tau)$ obtained with no BG correction from the spot #C13. The green solid line is a fit to Eq. (1), yielding $g^{(2)}(0) = 0.48 \pm 0.27$. The thin solid line is $g^{(2)}_{corr}(\tau)$ calculated according to Eq. (2). The error bars represent SD.

emission rate and low BG contribution is a technologically challenging task and is beyond the scope of this work.

Discussion

In summary, we unambiguously demonstrate the controllable creation of quantum telecom emitters based on single silicon-interstitial- and carbon-related color centers in silicon wafers. These single-photon emitters are created with a spatial resolution better than 100 nm and a probability exceeding 50%. Using broad-beam implantation through lithographically defined nanoholes, we demonstrate the wafer-scale nanofabrication of telecom single-photon emitters compatible with CMOS technology for VLSI. Our results enable the direct realization of quantum PICs with monolithically integrated single-photon sources with electrical control[11]. These findings also provide a route for the quasi-deterministic creation of single G and W centers at desired

locations of photonic structures[39], tunable cavities[40], and SOI waveguides[41]. Furthermore, our approach can potentially be applied for the controllable creation of other color centers in silicon, including T centers with optically-interfaced spins[19].

Methods

Samples

Two different sets of p-type silicon wafers are utilized for the experiments. In the case of G centers, we performed our experiments on a commercially available Czochralski (CZ)-grown ⟨110⟩-oriented SOI wafer purchased from IceMOS Technology. This wafer consists of a 12-μm-thick Si device layer separated by a 1-μm-thick silicon dioxide (SiO_2) layer from the bulk silicon substrate. The double-side polished 315-μm-thick substrate is cleaved into $5 \times 5\ mm^2$ pieces. The as-grown concentration of carbon impurities for this type of wafers is specified to be higher than $10^{16}\ cm^{-3}$ [11]. To decrease the natural BG contribution, we perform either FA or RTA in an N_2 atmosphere.

To investigate W centers, we use ⟨100⟩-oriented single-side polished, 525-μm-thick, ultrapure silicon substrates grown by the float zone (FZ) technique. The residual concentration of carbon and oxygen impurities is less than $5 \times 10^{14}\ cm^{-3}$ and $1 \times 10^{14}\ cm^{-3}$, respectively, whereas the concentration of boron and phosphorous dopants falls below $7 \times 10^{12}\ cm^{-3}$. To create the optically active W center, we performed FA at 225 °C for 300 s in an N_2 atmosphere following fabrication protocols optimized for an ensemble of W centers[24,38].

FIB implantation

We used a customized Orsay Physics CANION Z31Mplus FIB system with a liquid metal alloy ion source (LMAIS). The FIB system is equipped with an in-house-fabricated $Au_{82}Si_{18}$ ion source, which provides a focused ion beam with a diameter of roughly 50 nm[42]. The small focal spot of the FIB offers fast, flexible, maskless, and spatially resolved targeted positioning of the implanted ions at the nanoscale. Additionally, the system is equipped with a Wien ExB mass filter to block different ion species and charge states emerging from the ion source. The double-charged Si^{2+} ions with a nominal beam current between 1 and 2.5 pA have a kinetic energy of 40 keV (at 20 kV acceleration potential).

For the FIB implantation of single G and W centers, a custom patterning file is created for both the frame and the single dot arrays, respectively. The frame is implanted with a constant fluence $\Phi \sim 10^{11}\ cm^{-2}$ to intentionally create a dense ensemble of color centers for reference and alignment purposes. For the individual single dot arrays with 15×16 irradiation spots (vertical and horizontal spacing 10 μm), the number of ions per spot is targeted to be between 6 to 570 with logarithmic incremental steps. The implanted number of Si ions is controlled by the dwell time, such that the desired dose of Si ions is reached.

Broad-beam implantation

SOI wafers are processed using an RTA at 1000 °C for 3 min under an N_2 atmosphere, 15 min of piranha (3 parts H_2SO_4 : 1 part H_2O_2) cleaning is performed to remove residual carbon- and oxygen-terminate the sample surface. Prior to resist spin coating, the samples are ultrasonically cleaned in acetone, rinsed in IPA, and blown dry with N_2. Next, a layer of positive micro resist (PMMA, 950K A6) with a nominal thickness of $t = 324$ nm is spin-coated on the wafer as an implantation mask. Subsequently, the sample is baked on a hot plate for 5 min at 150 °C. The nanohole patterns, containing 20×20 of variable diameters d ranging from 30 to 400 nm, were transferred to the photoresist by electron beam lithography (EBL) utilizing a Raith 150TWO system. To tune the number of implanted Si ions through different nanoholes, we vary the nominal nanohole diameter while keeping the EBL dose constant. The overall design, including the lateral 10 μm pitch between all nanoholes, was chosen for comparison and consistency with the irradiation pattern used for the FIB writing. During the EBL process, the following parameters are used: 20 kV acceleration voltage, 0.25 nA current, 30 μm aperture with a base dose of 820 μC · cm^{-2}. After the EBL, the PMMA is developed with a mixture of DI-water and isopropyl alcohol (3:7) for 30 s followed by an isopropyl alcohol stopper for 30 s, the samples are then dried with pressurized nitrogen. To create single G centers for VLSI, we use broad-beam implantation with Si^{2+} ions (energy 40 keV) through the micro resist mask with a fluence of $\Phi = 1 \times 10^{12}\ cm^{-2}$ at $\theta = 7°$ tilt to avoid ion channeling. After the lift-off process, ultrasonication in acetone for 3 min is applied to remove the residuals of PMMA, followed by washing in isopropyl alcohol and blow-drying under a stream of nitrogen gas.

According to SRIM calculations[32], the R_p of 40 keV Si^{2+} in PMMA is ~100 nm. Therefore, ions only reach the substrate through the holes in the mask. To prevent the unwanted creation of other types of emitting color centers, no post-irradiation annealing treatment was performed.

Data availability

The experimental data are available upon request.

References

1. O'Brien, J. L., Furusawa, A. & Vučković, J. Photonic quantum technologies. *Nat. Photonics* **3**, 687–695 (2009).
2. Aharonovich, I., Englund, D. & Toth, M. Solid-state single-photon emitters. *Nat. Photonics* **10**, 631–641 (2016).
3. Knill, E., Laflamme, R. & Milburn, G. J. A scheme for efficient quantum computation with linear optics. *Nature* **409**, 46–52 (2001).
4. Walther, P. et al. Experimental one-way quantum computing. *Nature* **434**, 169–176 (2005).
5. O'Brien, J. L. Optical Quantum Computing. *Science* **318**, 1567–1570 (2007).
6. Zhong, H.-S. et al. Quantum computational advantage using photons. *Science* **370**, 1460–1463 (2020).
7. Bartolucci, S. et al. Fusion-based quantum computation. Preprint at arXiv:2101.09310 (2021).
8. Yan, X. et al. Silicon photonic quantum computing with spin qubits. *APL Photonics* **6**, 070901 (2021).
9. Wang, H. et al. Boson sampling with 20 input photons and a 60-mode interferometer in a 1014-dimensional Hilbert space. *Phys. Rev. Lett.* **123**, 250503 (2019).
10. Lee, H., Chen, T., Li, J., Painter, O. & Vahala, K. J. Ultra-low-loss optical delay line on a silicon chip. *Nat. Commun.* **3**, 867 (2012).
11. Hollenbach, M., Berencén, Y., Kentsch, U., Helm, M. & Astakhov, G. V. Engineering telecom single-photon emitters in silicon for scalable quantum photonics. *Opt. Express* **28**, 26111 (2020).
12. Rudolph, T. Why I am optimistic about the silicon-photonic route to quantum computing. *APL Photonics* **2**, 030901 (2017).
13. Uppu, R., Midolo, L., Zhou, X., Carolan, J. & Lodahl, P. Quantum-dot-based deterministic photon-emitter interfaces for scalable photonic quantum technology. *Nat. Nanotechnol.* **16**, 1308–1317 (2021).
14. Pernice, W. et al. High-speed and high-efficiency travelling wave single-photon detectors embedded in nanophotonic circuits. *Nat. Commun.* **3**, 1325 (2012).
15. Gyger, S. et al. Reconfigurable photonics with on-chip single-photon detectors. *Nat. Commun.* **12**, 1408 (2021).
16. Tian, Y. et al. Experimental demonstration of a reconfigurable electro-optic directed logic circuit using cascaded carrier-injection micro-ring resonators. *Sci. Rep.* **7**, 6410 (2017).
17. Redjem, W. et al. Single artificial atoms in silicon emitting at telecom wavelengths. *Nat. Electron.* **3**, 738–743 (2020).
18. Baron, Y. et al. Detection of single W-centers in silicon. *ACS Photonics* **9**, 2337–2345 (2022).
19. Higginbottom, D. B. et al. Optical observation of single spins in silicon. *Nature* **607**, 266–270 (2022).
20. Durand, A. et al. Broad diversity of near-infrared single-photon emitters in silicon. *Phys. Rev. Lett.* **126**, 083602 (2021).

Article

21. Weiss, L., Gritsch, A., Merkel, B. & Reiserer, A. Erbium dopants in nanophotonic silicon waveguides. *Optica* **8**, 40–41 (2021).

22. Udvarhelyi, P., Somogyi, B., Thiering, G. & Gali, A. Identification of a telecom wavelength single photon emitter in silicon. *Phys. Rev. Lett.* **127**, 196402 (2021).

23. Davies, G. The optical properties of luminescence centres in silicon. *Phys. Rep.* **176**, 83–188 (1989).

24. Chartrand, C. et al. Highly enriched Si-28 reveals remarkable optical linewidths and fine structure for well-known damage centers. *Phys. Rev. B* **98**, 195201 (2018).

25. Lukin, D. M. et al. Spectrally reconfigurable quantum emitters enabled by optimized fast modulation. *npj Quantum Inf.* **6**, 80 (2020).

26. Wan, N. H. et al. Large-scale integration of artificial atoms in hybrid photonic circuits. *Nature* **583**, 226–231 (2020).

27. Kraus, H. et al. Three-dimensional proton beam writing of optically active coherent vacancy spins in silicon carbide. *Nano Lett.* **17**, 2865–2870 (2017).

28. Ohshima, T. et al. Creation of silicon vacancy in silicon carbide by proton beam writing toward quantum sensing applications. *J. Phys. D Appl. Phys.* **51**, 333002 (2018).

29. Jakob, A. M. et al. Deterministic shallow dopant implantation in silicon with detection confidence upper?Bound to 99.85% by ion-solid interactions. *Adv. Mater.* **34**, 2103235 (2021).

30. Titze, M. et al. In situ ion counting for improved implanted ion error rate and silicon vacancy yield uncertainty. *Nano Lett.* https://doi.org/10.1021/acs.nanolett.1c04646 (2022).

31. Sangtawesin, S., Brundage, T. O., Atkins, Z. J. & Petta, J. R. Highly tunable formation of nitrogen-vacancy centers via ion implantation. *Appl. Phys. Lett.* **105**, 063107 (2014).

32. Ziegler, J. F., Ziegler, M. & Biersack, J. SRIM - The stopping and range of ions in matter (2010). *Nucl. Instrum. Methods Phys. Res. Sect. B: Beam Interact. Mater. At.* **268**, 1818–1823 (2010).

33. Fuchs, F. et al. Engineering near-infrared single-photon emitters with optically active spins in ultrapure silicon carbide. *Nat. Commun.* **6**, 7578 (2015).

34. Brouri, R., Beveratos, A., Poizat, J.-P. & Grangier, P. Photon anti-bunching in the fluorescence of individual color centers in diamond. *Opt. Lett.* **25**, 1294 (2000).

35. Fishman, R. E. K., Patel, R. N., Hopper, D. A., Huang, T.-Y. & Bassett, L. C. Photon emission correlation spectroscopy as an analytical tool for quantum defects. Preprint at arXiv:2111.01252 (2021).

36. Gardill, A. et al. Super-resolution airy disk microscopy of individual color centers in diamond. *ACS Photonics* https://doi.org/10.1021/acsphotonics.2c00713 (2022).

37. Beaufils, C. et al. Optical properties of an ensemble of G-centers in silicon. *Phys. Rev. B* **97**, 035303 (2018).

38. Buckley, S. M. et al. Optimization of photoluminescence from W centers in silicon-on-insulator. *Opt. Express* **28**, 16057 (2020).

39. Hollenbach, M. et al. Metal-assisted chemically etched silicon nanopillars hosting telecom photon emitters. *J. Appl. Phys.* **132**, 033101 (2022).

40. Wachter, G. et al. Silicon microcavity arrays with open access and a finesse of half a million. *Light Sci. Appl.* **8**, 37 (2019).

41. Prabhu, M. et al. Individually addressable artificial atoms in silicon photonics. Preprint at arXiv:2202.02342 (2022).

42. Bischoff, L., Mazarov, P., Bruchhaus, L. & Gierak, J. Liquid metal alloy ion sources – An alternative for focussed ion beam technology. *Appl. Phys. Rev.* **3**, 021101 (2016).

Author contributions

M.Ho., Y.B., and G.V.A. conceived and designed the experiments. M.Ho. performed the single-photon spectroscopy experiments under the supervision of G.V.A. M.Ho., N.K., and L.B. designed the FIB layout. N.K. and L.B. performed FIB implantation and in situ annealing. M.Ho., N.S.J., Y.B., C.F., and G.V.A. designed the PMMA mask. N.S.J. fabricated the PMMA mask. M.Ho., U.K., Y.B., and G.V.A. conceived and performed the broad-beam silicon implantation. C.F. and Y.B. carried out the RTA processing. N.V.A. grew the ultrapure silicon substrates. M.Ho. and G.V.A. wrote the manuscript. All authors, together with G.H., A.E., and M.H. discussed the results and contributed to the manuscript preparation.

Competing interests

The authors declare no competing interest.

Additional information

Supplementary information The online version contains supplementary material available at https://doi.org/10.1038/s41467-022-35051-5.

Correspondence and requests for materials should be addressed to Michael Hollenbach, Yonder Berencén or Georgy V. Astakhov.

Peer review information *Nature Communications* thanks Adam Gali, and the other, anonymous, reviewers for their contribution to the peer review of this work. Peer reviewer reports are available.

Reprints and permissions information is available at http://www.nature.com/reprints

Publisher's note Springer Nature remains neutral with regard to jurisdictional claims in published maps and institutional affiliations.

Spin-wave frequency combs 🔓

T. Hula,[1,2] 🆔 K. Schultheiss,[1] 🆔 F. J. T. Gonçalves,[1] 🆔 L. Körber,[1,3] 🆔 M. Bejarano,[1,4] 🆔 M. Copus,[5] L. Flacke,[6,7] 🆔
L. Liensberger,[6,7] A. Buzdakov,[1] 🆔 A. Kákay,[1] 🆔 M. Weiler,[6,7,8] 🆔 R. Camley,[5] 🆔 J. Fassbender,[1,3] 🆔
and H. Schultheiss[1,a)] 🆔

AFFILIATIONS

[1]Helmholtz-Zentrum Dresden-Rossendorf, Institute of Ion Beam Physics and Materials Research, Dresden, Germany
[2]Institut für Physik, Technische Universität Chemnitz, 09107 Chemnitz, Germany
[3]Fakultät Physik, Technische Universität Dresden, Dresden, Germany
[4]Fakultät Elektrotechnik und Informationstechnik, Technische Universität Dresden, Dresden, Germany
[5]Center for Magnetism and Magnetic Nanostructures, University of Colorado, Colorado Springs, Colorado 80918, USA
[6]Walther-Meißner-Institut, Bayerische Akademie der Wissenschaften, Garching, Germany
[7]Physik-Department, Technische Universität München, Munich, Germany
[8]Fachbereich Physik and Landesforschungszentrum OPTIMAS, Technische Universität Kaiserslautern, Kaiserslautern, Germany

[a)]Author to whom correspondence should be addressed: h.schultheiss@hzdr.de

ABSTRACT

We experimentally demonstrate the generation of spin-wave frequency combs based on the nonlinear interaction of propagating spin waves
in a microstructured waveguide. By means of time- and space-resolved Brillouin light scattering spectroscopy, we show that the simultaneous
excitation of spin waves with different frequencies leads to a cascade of four-magnon scattering events, which ultimately results in well-
defined frequency combs. Their spectral weight can be tuned by the choice of amplitude and frequency of the input signals. Furthermore, we
introduce a model for stimulated four-magnon scattering, which describes the formation of spin-wave frequency combs in the frequency and
time domain.

Published under an exclusive license by AIP Publishing. https://doi.org/10.1063/5.0090033

Frequency combs have been attracting interest in multiple fields of research in the last few decades. For example, optical frequency combs have had great impact on metrology, as they have led to a significant enhancement in the precision of frequency measurements.[1–3] In solid state magnetism, several mechanisms are known to cause frequency spectra with equidistantly spaced spin-wave (SW) modes, by means of nonlinear interactions known as modulation instabilities.[4–10] These were often discussed in the time domain, as they were found to cause soliton formation. In addition, frequency mixing of two independently excited quasi-uniform modes has been studied in magnetic thin films leading to the generation of additional equidistantly spaced modes.[11–13] Very recently, micromagnetic simulations have shown the generation of magnonic frequency combs by nonlinear three-magnon scattering of spin waves interacting with the intrinsic modes of magnetic skyrmions.[14]

In microstructured magnetic waveguides, the process of four-magnon scattering (4MS) has been reported to populate a continuum of SW states in frequency ranges of up to several GHz around a strongly driven mode.[15–17] 4MS commonly describes the decay of two initial magnons, the quanta of SWs, into a pair of secondary magnons with different energies and momenta while conserving total energy and momentum.[17,18] 4MS is often considered parasitic and undesirable,[19–21] since it leads to additional damping of a strongly populated SW mode by coupling to the continuum of thermally populated states within the SW band.[16,17,22]

In this Letter, we take the active control of 4MS in order to create tunable SW frequency combs. Those have significant impact on both fundamental and applied physics, as the superposition of frequencies and associated wavevectors allows one to create specific high-wavevector magnons, which could not be readily created with typical geometries. In terms of applications, this frequency comb creates a series of microwave pulses in the time domain, where the width of each pulse can be significantly adjusted by changing the amplitude of the initial signals. Furthermore, our results experimentally demonstrate the efficient downconversion of spin-wave frequencies, which is important for the integration of magnonic devices into different environments, an

issue currently addressed by multiple complex approaches including the modulation of optical frequency combs,[23] superconducting qubits in cavities,[24] and electronic circuits.[25] Finally, we explore the timescale of the nonlinear responses, a topic not substantially addressed in earlier works.

We experimentally demonstrate the generation of such a frequency comb by exciting SWs in a $Co_{25}Fe_{75}$ microconduit[26–28] with a width of 3 μm, a length of 60 μm, and a thickness of 30 nm, as shown in Fig. 1(a).[29] Two 1 μm wide microwave antennas, referred to as RF1 and RF2, are patterned on top of the magnetic waveguide. Connecting the antennas to two microwave sources allows for the independent excitation of SWs at potentially different power levels P_{RF1} and P_{RF2}. In the following, SWs generated by RF1 (RF2) will be referred to as mode a_1 (a_2) with frequency f_{RF1} (f_{RF2}) and wave vector k_1 (k_2). In all measurements, an external in-plane magnetic field of $B = 46$ mT is applied, which is not sufficient to fully saturate the waveguide perpendicular to the transport direction but still yields long SW decay lengths, as reported for a similar geometry in.[15,26] Note, however, that the non-collinearity at the edges of the sample is not essential for the emergence of 4MS, which is possible also in fully saturated specimens.[30] The green dot in Fig. 1(a) indicates the position of the probing laser spot of the utilized Brillouin light scattering microscope (μBLS) on the sample.[31] All spin-wave spectra were obtained from the same position. The inelastically scattered laser light, obtained at the measurement position, was analyzed using a tandem Fabry–Pérot interferometer.

Figure 1(b) shows the dispersion relation of the lowest order waveguide mode (n = 0) of the investigated sample, calculated
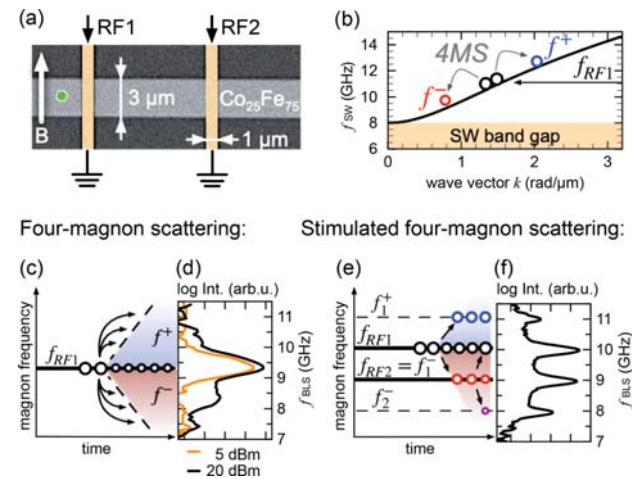
FIG. 1. (a) Scanning electron micrograph of the SW waveguide. SWs with frequencies f_{RF1} and f_{RF2} were excited by the antennas RF1 and RF2, respectively. All measurements were performed in 1 μm distance to the left edge of RF1 as indicated by the green dot. (b) Dispersion relation of the lowest order waveguide mode in the investigated sample. Circles and arrows illustrate a four-magnon scattering process: two excited magnons with f_{RF1} scatter into a pair of secondary magnons with f^- and f^+. (c) Energy-time diagram illustrating how spontaneous 4MS populates the SW band. (d) μBLS spectra measured in the SW waveguide only exciting with RF1 (CW) at two different powers. (e) Energy-time diagram for stimulated 4MS. (f) μBLS spectrum measured when exciting with RF1 and RF2 (both CW) simultaneously.

according to the formalism of Kalinikos and Slavin.[32] The SW bandgap for the investigated sample was found to occur below a frequency of 8 GHz.

Additionally, Fig. 1(b) illustrates the process of spontaneous 4MS,[15–17] which causes the parametric generation of pairs of secondary magnons above a critical SW amplitude. Using the notation of nonlinear SW theory,[18,30] we describe the current state (phase and oscillation magnitude) of a SW mode as a time-dependent complex amplitude variable $a_\nu(t)$ (with some mode index ν), classical analog to bosonic creation, and annihilation operators $\hat{a}_\nu$ in second quantization. When a mode a_i is excited above a certain threshold amplitude, its energy redistributes within the SW band via scattering of two initial magnons a_i characterized by $f_i = f_{RF1}$ and k_i into a pair of secondary magnons a_+ (f^+, k^+) and a_- (f^-, k^-) under the conservation of energy and momentum. The states a_+ and a_- can be located all across the respective SW sub-bands f^+ and f^- as schematically shown for spontaneous four-magnon scattering in Fig. 1(c).

The rates da_k/dt for these scattering processes describe the change in amplitudes of the participating modes a_k over time and can be derived using the Hamiltonian formalism for nonlinear SW dynamics,[18,30]

$$\frac{da_k}{dt} = -i\omega(\mathbf{k})a_k - \Gamma(\mathbf{k})(a_k - a_{k,\text{th}}) + i\gamma b_{\text{RF},k} \cdot e^{-i\omega_{\text{RF},k}t} - i\frac{\partial \mathcal{H}_{\text{int}}}{\partial a_k^*}. \quad (1)$$

In Eq. (1), the SW dispersion $\omega(\mathbf{k})$, the linear damping $\Gamma(\mathbf{k}) = \alpha\omega(\mathbf{k})$ with $\alpha = 0.004$ typical for $Co_{25}Fe_{75}$, a phenomenological term for thermal population $a_{k,\text{th}} = i\sqrt{N_{k,\text{th}}}e^{-i\omega(k)t}$, the pump field $b_{\text{RF},k}$, and the interaction Hamiltonian $\mathcal{H}_{\text{int}}$ are included. Since in our experiments $f_i/2 = f_{RF1}/2$ is located in the SW bandgap, resonant three-magnon scattering is prohibited and is, thus, excluded.[17,18] Therefore, the lowest order of interaction to be considered for our calculations is the decay of a_i into the final states a_+ and a_-, and the corresponding Hamiltonian is written as

$$\mathcal{H}_{\text{int}} \simeq \mathcal{H}^{(4)} = \sum_{i+-} W_{ii,+-}a_i a_i a_+^* a_-^*. \quad (2)$$

The rates given in Eq. (1) depend on the coupling coefficients $W_{ii,+-}$ between the different modes as well as the amplitudes of the three modes a_i, a_+, and a_-.[18] As the coupling coefficients are inversely proportional to the wave-vector mismatch of the participating modes,[15,18] the delay time for populating secondary modes via 4MS scales with the frequency spacing $\Delta f = |f^\pm - f_{RF1}|$, as illustrated by dashed lines in Fig. 1(c). This delay time can be understood as the time needed to compensate for the intrinsic damping of the secondary states.

Figure 1(d) shows the anti-Stokes side of μBLS spectra that was measured when exciting SWs with antenna RF1 at a fixed frequency $f_{RF1} = 9.25$ GHz using two different pumping powers. At low powers (orange line), the SW spectrum shows a single symmetric peak at f_{RF1}. When increasing the pumping power above the threshold for 4MS (black line), a broadening of the peak is measured as a consequence of the energy redistribution caused by spontaneous 4MS.

For the generation of a SW frequency comb with a well-defined frequency spectrum, we need to actively increase the scattering rate into one specific scattering channel f_1^+ or f_1^-, which has to be located in the scattering ranges f^+ or f^-, respectively. Using antenna RF2, a

second magnon state can be populated at $f_{RF2} \neq f_{RF1}$ as shown in Fig. 1(e), which acts as a seed mode. Considering $f_{RF1} = f(a_i)$ and $f_{RF2} = f(a_-) = f_1^-$, the nonlinear coupling between both states increases according to Eq. (2). Hence, the rate for f_{RF1} magnons to scatter into the f_{RF2} state is enhanced as indicated by the red circles in Fig. 1(e). Furthermore, a third mode is generated at $f(a_+) = f_1^+ = f_{RF1} + \Delta f$ with $\Delta f = |f_{RF1} - f_{RF2}|$ [blue circles in Fig. 1(e)] in order to conserve the energy of the two initial magnons at f_{RF1}.

By actively populating the seed mode (a_-), we control all frequency channels of the scattering process. We refer to this process as stimulated 4MS, similar to the process of stimulated three-magnon scattering as shown in Ref. 33.

As depicted in Fig. 1(e), higher order scattering processes then lead to the formation of a SW frequency comb. The secondary modes a_- and a_+ at f_1^- and f_1^+ take the role of initial and seed modes in new scattering events. Therefore, higher order processes are stimulated, e.g., with two magnons at f_1^- scattering into the states at f_{RF1} and f_2^-. In Fig. 1(e), this is illustrated by an additional mode at f_2^- (violet circle) that appears with equidistant frequency spacing but at a later time. The higher order processes need to compensate the intrinsic damping of the participating states, which causes an increasing delay time, as indicated by the slope of the dashed line.

One example of a measured SW frequency comb is shown in Fig. 1(f). The initial mode is pumped at $f_{RF1} = 10$ GHz using antenna RF1 while the seed mode is provided by antenna RF2 at $f_{RF2} = f_1^- = 9$ GHz. In addition to those two frequencies, the BLS spectrum shows very distinct peaks at $f_1^+ = 11$ GHz and $f_2^- = 8$ GHz.

In order to demonstrate the high degree of tunability of SW frequency combs, we measured μBLS spectra with a fixed frequency of the initial mode $f_{RF1} = 10$ GHz but varying frequency of the seed mode f_{RF2} between 8 and 12 GHz. The microwave powers of RF1 and RF2 were kept at constant values of $P_{RF1} = P_{RF2} = 10$ dBm. The resulting BLS spectra are plotted in Fig. 2(a), with the SW intensity color coded on a logarithmic scale. The horizontal and diagonal white dashed lines indicate the applied frequencies f_{RF1} and f_{RF2}. As f_{RF2} is

varied continuously to cross f_{RF1}, the frequency gap $\Delta f = |f_{RF1} - f_{RF2}|$ decreases up to $f_{RF2} = f_{RF1} = 10$ GHz and then increases again. Depending on the value of Δf, different numbers of indirectly excited SW modes are measured. All detected intensities appear above a frequency of 7 GHz, which is in qualitative agreement with the obtained SW bandgap in Fig. 1(b). Figure 2(a) demonstrates that the additional frequencies, observed in our experiments, strictly follow the spacing of the two driving frequencies f_1 and f_2 (dashed lines).

Figure 2(b) shows individual BLS spectra measured for $f_{RF2} = 9.5$ GHz (red) and $f_{RF2} = 11$ GHz (blue), highlighting the different frequency spacing between neighboring modes of 0.5 and 1 GHz, respectively. In addition to the SW frequency combs, we measure a continuous background from the SW band between 8 and 12 GHz, as depicted by dashed lines. This demonstrates that both mechanisms of spontaneous and stimulated 4MS take place at the same time. We note that, in addition to the coupling efficiency discussed earlier, the experimental observation of the continuum of SW states is limited toward lower frequencies by the SW bandgap (in our case between 7 and 8 GHz) and toward higher frequencies by the scattering geometry of the μBLS setup.[15,16,31]

According to Eqs. (1) and (2), the population rate of secondary states via 4MS increases with increasing driving powers or amplitudes. In order to investigate the power dependence of stimulated 4MS, we fix the excitation frequencies of a_1 and a_2 at $f_{RF1} = 10$ GHz and $f_{RF2} = 9.5$ GHz, respectively. In addition, we fix the pumping power of mode a_1 at $P_{RF1} = 4.6$ dBm, whereas mode a_2 is pumped with varying microwave powers P_{RF2} ranging from 4.6 to 23 dBm. The measured μBLS spectra as a function of P_{RF2} are shown in Fig. 3(a) with the BLS intensity color coded on a logarithmic scale. As expected, the intensity of a_2 at f_{RF2} continuously grows with increasing pumping power P_{RF2} whereas only a minor increase in the intensity of a_1 (f_{RF1}) can be observed. In addition to the increase in the intensity of a_2,

FIG. 2. (a) μBLS spectrum plotted as a function of the input frequency of RF2 (CW) while the frequency of RF1 (CW) was fixed at 10 GHz. Both antennas were set to a constant input power of 10 dBm. The frequency of RF2 was swept from 8 to 12 GHz. (b) Examples of the BLS spectrum measured for RF2 set to 9.5 GHz (red) and 11 GHz (blue). The dashed lines indicate the continuum of states excited by 4MS.
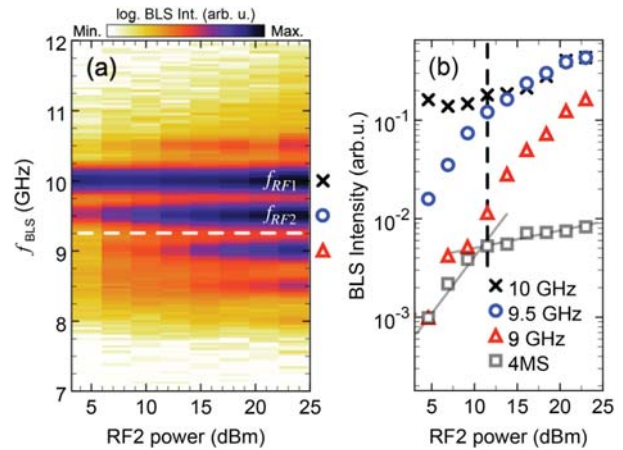
FIG. 3. (a) μBLS spectra measured as a function of the microwave power P_{RF2} pumping mode a_2 at a constant frequency $f_{RF2} = 9.5$ GHz (CW). Mode a_1 is excited at a constant power $P_{RF1} = 4.6$ dBm and constant frequency $f_{RF1} = 10$ GHz (CW). (b) Power dependent intensities evaluated for the different modes at 9 GHz (triangles), 9.5 GHz (circles), and 10 GHz (crosses). The intensity of the continuum of spontaneous 4MS (squares) is extracted for 9.25 GHz (dashed line in a). Lines are just a guide to the eye to highlight different slopes measured below and above 12 dBm.

additional modes at 8.5, 9, and 10.5 GHz appear in the spectra, especially for larger values of P_{RF2}.

The dependence of the SW spectra with respect to P_{RF2} is discussed further with Fig. 3(b), where the intensities extracted at 10 (a_1, crosses), 9.5 (a_2, circles), 9 (triangles), and 9.25 GHz (4MS, squares) are plotted. The signal at 9.25 GHz represents states in the continuum of the SW band that are only excited by spontaneous 4MS.

Interestingly, the intensity of mode a_1 (crosses) is not constant despite its fixed excitation power of $P_{RF1} = 4.6$ dBm. Its intensity remains on the same level up to $P_{RF2} = 11.5$ dBm and then increases to values larger than those initially measured for $P_{RF2} = 4.6$ dBm. This development of the intensity of a_1 shows that we can distinguish different scattering regimes.

For $P_{RF2} < 11.5$ dBm, spontaneous 4MS of both modes a_1 and a_2 into the continuum of the SW band is the dominant scattering channel. Since a_2 is provided with more and more energy by the increasing microwave power, its intensity rises rapidly, which directly leads to a strong increase in the intensity of the continuum of the SW band [squares in Fig. 3(b)].

For $P_{RF2} > 11.5$ dBm, stimulated 4MS is the pronounced scattering channel, and spontaneous 4MS plays a minor role only. Since mode a_2 [circles in Fig. 3(b)] is pumped much stronger than a_1 (crosses), a_2 can be assigned as the initial mode and a_1 the seed mode. As a result, two magnons at $f_i = f_{RF2} = 9.5$ GHz scatter in one magnon at $f_1^+ = f_{RF1} = 10$ GHz and one at $f_1^- = 9$ GHz (triangles). This not only leads to a rapid increase in the intensity at 9 GHz above the level of 4MS but also to an increase in the intensity of a_1 (f_{RF1}). Even though the intensity of a_2 continues to increase due to the larger pumping powers, it never exceeds the intensity of mode a_1. This is quite remarkable since at $P_{RF2} = 23$ dBm, a_2 is pumped significantly stronger than a_1 ($P_{RF1} = 4.6$ dBm) and still their intensities remain on the same level. This demonstrates the high efficiency of stimulated 4MS: most of the energy of mode a_2 is redistributed within the modes of the SW frequency comb. Hence, spontaneous 4MS is less pronounced as for $P_{RF2} < 11.5$ dBm and the intensity of the continuum [squares in Fig. 3(b)] increases at a much lower rate.

The mechanism of stimulated 4MS, outlined in Fig. 1(e), generates a SW frequency comb in terms of a temporal cascade of 4MS events that populate discrete modes in the SW band. To experimentally investigate this temporal evolution, we use time-resolved BLS microscopy (TR μBLS).[31]

First, we investigated the temporal response of the system to a single microwave pulse at $f_{RF1} = 8.5$ GHz. The pulse width was set to 150 ns with a rise time of 3 ns and a repetition period of 200 ns. The first 40 ns of the measurement are shown in Fig. 4(a). The microwave pulse sets in after 17 ns, accompanied by the characteristic frequency broadening of 4MS. Interestingly, it takes up to 6 ns after the onset of the SW pulse for the frequency distribution to reach a dynamic equilibrium and fill states of the continuum with frequencies ranging from 7 to almost 10 GHz. The diagonal dashed lines highlight that modes in the continuum with smaller frequency spacing to the directly excited mode are populated much faster than modes with larger frequency spacing [also see Fig. 1(c)].

Figure 4(b) shows a TR μBLS spectrum measured for a continuously excited initial mode at $f_{RF1} = f_i = 8$ GHz and a pulsed seed mode at $f_{RF2} = f_1^+ = 8.5$ GHz starting at 15 ns with respect to the displayed time window. Here, the additional secondary mode a_- at
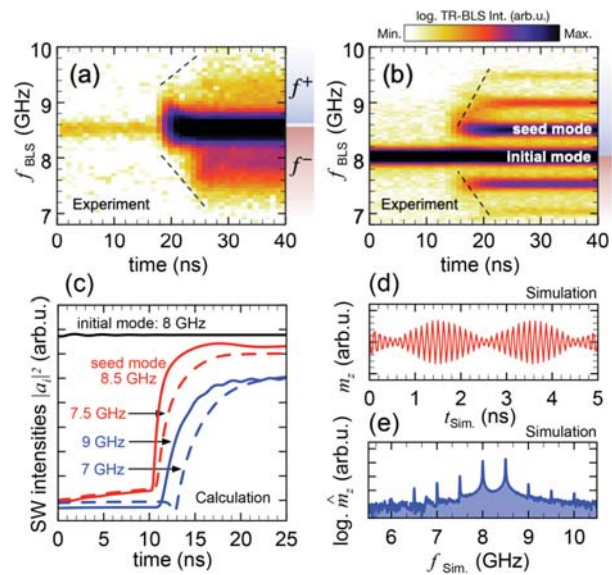
FIG. 4. (a) TR μBLS spectrum measured when exciting SWs with a single RF pulse at $f_1 = 8.5$ GHz (only the first 40 ns are shown). (b) TR μBLS spectrum measured when pumping the initial mode at $f_{RF1} = 8$ GHz (CW) and exciting the seed mode at $f_{RF2} = 8.5$ GHz by a microwave pulse. (c) Temporal profiles of modes of the frequency comb obtained by the analytic model in Eq. (1). (d) First 5 ns of the 150 ns-long time profile of m_z and (e) FFT showing the simulated SW frequency comb.

7.5 GHz is measured simultaneously to the seed mode. Higher order modes at 7, 9, and 9.5 GHz are measured with larger time delays, depending on their frequency spacing to the initial mode.

These measurements demonstrate that in both cases, a certain time is needed to populate additional states via nonlinear interactions. The observed time delay is in agreement with nonlinear SW theory[18] and has also been reported in previous experimental studies.[34] The experimental findings in Fig. 4(b) indicate an increase in nonlinear mode coupling for the case of stimulated four-magnon scattering compared to spontaneous four-magnon scattering.

Figure 4(c) shows the results of the calculations based on Eq. (2) for a continuously driven initial mode at 8 GHz (black line) and a pulsed secondary mode at 8.5 GHz setting in after 10 ns. A set of seven rate equations was solved, referring to SW modes ranging from 6.5 to 9.5 GHz in 0.5 GHz steps. For simplicity, only five of these modes are shown by the modulus square $|a_i|^2$, which corresponds to the SW intensity and is proportional to the photon counts in our time-resolved BLS experiments. We note that the delay times obtained analytically are in qualitative agreement with those obtained experimentally in Fig. 4(b).

In the time domain, a superposition of several modes translates into a time-modulated amplitude, which enables, e.g., optical frequency combs to bridge the gap between optical and microwave frequencies.[1,3] In order to demonstrate a similar behavior for the observed magnon frequency combs, we investigated the temporal evolution of the magnetization in micromagnetic simulations using MuMax3[11,35] with material parameters and grid size listed in Ref. 36.

In the simulations, the excitation field was strictly localized to the area of the two antennas in order to investigate the interaction of

propagating waves and avoid any far-field excitations of the antennas. The excitation frequencies of RF1 and RF2 were set to 8 and 8.5 GHz, respectively, with field amplitudes of 1 mT. The temporal representation of the simulated SW frequency comb is displayed in Fig. 4(d) in form of the amplitude of the dynamic component of the magnetization, $m_z(t)$. Here, we confirm a temporal modulation of the amplitude by 80% with a 2 ns period, which corresponds to the inverse of the 0.5 GHz frequency spacing between the two input frequencies. Figure 4(e) shows the fast Fourier transform (FFT) of $m_z(t)$. The resulting spectrum exhibits multiple SW modes in addition to the directly excited modes at 8 and 8.5 GHz, resembling the measured SW frequency comb.

In conclusion, we observed the formation of spin-wave frequency combs generated by the nonlinear interaction of propagating spin waves excited at two different frequencies in a magnon conduit. A variety of spin-wave modes can be observed, whose frequency spacing and amplitudes were exemplarily manipulated by varying the frequency and power of one of the applied microwave currents. The underlying mechanism can be understood in terms of stimulated four-magnon scattering, which was found to be the dominant process in the performed experiments. We propose that this effect can be utilized in any magnetic material and/or geometry as long as four-magnon scattering occurs.

AUTHOR DECLARATIONS
Conflict of Interest

The authors have no conflicts to disclose.

Author Contributions

T. Hula: Conceptualization (equal); Data curation (lead); Formal analysis (lead); Investigation (lead); Writing – original draft (equal); Writing – review & editing (equal). **A. Kakay:** Resources (supporting); Supervision (supporting); Visualization (supporting); Writing – review & editing (supporting). **M. Weiler:** Resources (supporting); Validation (supporting); Writing – original draft (supporting); Writing – review & editing (supporting). **R. E. Camley:** Conceptualization (supporting); Resources (supporting); Writing – original draft (supporting); Writing – review & editing (supporting). **J. Fassbender:** Resources (supporting); Supervision (supporting). **H. Schultheiss:** Conceptualization (lead); Writing – original draft (equal); Writing – review & editing (equal). **K. Schultheiss:** Visualization (supporting); Writing – original draft (supporting); Writing – review & editing (supporting). **F. J. T. Gonçalves:** Visualization (supporting); Writing – original draft (equal); Writing – review & editing (equal). **L. Körber:** Formal analysis (equal); Investigation (supporting); Writing – review & editing (supporting). **M. Bejarano:** Investigation (supporting); Software (supporting); Writing – review & editing (supporting). **M. Copus:** Formal analysis (supporting); Writing – original draft (supporting); Writing – review & editing (supporting). **L. Flacke:** Methodology (supporting); Resources (supporting); Writing – review & editing (supporting). **L. Liensberger:** Methodology (supporting); Resources (supporting); Writing – review & editing (supporting). **A. Buzdakov:** Investigation (supporting); Writing – review & editing (supporting).

DATA AVAILABILITY

The data that support the findings of this study are available from the corresponding author upon reasonable request.

REFERENCES

[1] M. Bellini and T. W. Hänsch, "Phase-locked white-light continuum pulses: Toward a universal optical frequency-comb synthesizer," Opt. Lett. **25**(14), 1049–1051 (2000).

[2] T. Fortier and E. Baumann, "20 years of developments in optical frequency comb technology and applications," Commun. Phys. **2**(1), 153 (2019).

[3] D. J. Jones, S. A. Diddams, M. S. Taubman, S. T. Cundiff, L.-S. Ma, and J. L. Hall, "Frequency comb generation using femtosecond pulses and cross-phase modulation in optical fiber at arbitrary center frequencies," Opt. Lett. **25**(5), 308–310 (2000).

[4] H. Benner, B. A. Kalinikos, N. G. Kovshikov, and M. P. Kostylev, "Observation of spin-wave envelope dark solitons in ferromagnetic films," JETP Lett. **72**(4), 213–216 (2000).

[5] J. W. Boyle, S. A. Nikitov, A. D. Boardman, and K. Xie, "Observation of cross-phase induced modulation instability of travelling magnetostatic waves in ferromagnetic films," J. Magn. Magn. Mater. **173**(3), 241–252 (1997).

[6] B. A. Kalinikos, N. G. Kovshikov, and A. N. Slavin, "Envelope solitons of highly dispersive and low dispersive spin waves in magnetic films," J. Appl. Phys. **69**, 5712 (1991).

[7] A. N. Slavin, "Thresholds of envelope soliton formation in a weakly dissipative medium," Phys. Rev. Lett. **77**, 4644–4647 (1996).

[8] R. A. Staudinger, P. Kabos, H. Xia, B. T. Faber, and C. E. Patton, "Calculation of the formation time for microwave magnetic envelope solitons," IEEE Trans. Magn. **34**(4), 2334–2338 (1998).

[9] M. A. Tsankov, M. Chen, and C. E. Patton, "Forward volume wave microwave envelope solitons in yttrium iron garnet films: Propagation, decay, and collision," J. Appl. Phys. **76**(7), 4274–4289 (1994).

[10] M. Wu, B. A. Kalinikos, and C. E. Patton, "Generation of dark and bright spin wave envelope soliton trains through self-modulational instability in magnetic films," Phys. Rev. Lett. **93**(15), 157207 (2004).

[11] Y. Khivintsev, J. Marsh, V. Zagorodnii, I. Harward, J. Lovejoy, P. Krivosik, R. E. Camley, and Z. Celinski, "Nonlinear amplification and mixing of spin waves in a microstrip geometry with metallic ferromagnets," Appl. Phys. Lett. **98**(4), 042505 (2011).

[12] J. Marsh and R. E. Camley, "Two-wave mixing in nonlinear magnetization dynamics: A perturbation expansion of the Landau–Lifshitz–Gilbert equation," Phys. Rev. B **86**(22), 224405 (2012).

[13] J. Marsh, V. Zagorodnii, Z. Celinski, and R. E. Camley, "Nonlinearly generated harmonic signals in ultra-small waveguides with magnetic films: Tunable enhancements of 2nd and 4th harmonics," Appl. Phys. Lett. **100**(10), 102404 (2012).

[14] Z. Wang, H. Y. Yuan, Y. Cao, Z.-X. Li, R. A. Duine, and P. Yan, "Magnonic frequency comb through nonlinear magnon-skyrmion scattering," Phys. Rev. Lett. **127**, 037202 (2021).

[15] T. Hula, K. Schultheiss, A. Buzdakov, L. Körber, M. Bejarano, L. Flacke, L. Liensberger, M. Weiler, J. M. Shaw, H. T. Nembach, J. Fassbender, and H. Schultheiss, "Nonlinear losses in magnon transport due to four-magnon scattering," Appl. Phys. Lett. **117**(4), 042404 (2020).

[16] H. Schultheiss, K. Vogt, and B. Hillebrands, "Direct observation of nonlinear four-magnon scattering in spin-wave microconduits," Phys. Rev. B **86**(5), 054414 (2012).

[17] H. Suhl, "The theory of ferromagnetic resonance at high signal powers," J. Phys. Chem. Solids **1**, 209–227 (1957).

[18] P. Krivosik and C. E. Patton, "Hamiltonian formulation of nonlinear spin-wave dynamics: Theory and applications," Phys. Rev. B **82**(18), 184428 (2010).

[19] H. G. Bauer, P. Majchrak, T. Kachel, C. H. Back, and G. Woltersdorf, "Nonlinear spin-wave excitations at low magnetic bias fields," Nat. Commun. **6**, 8274 (2015).

[20] V. E. Demidov, J. Jersch, K. Rott, P. Krzysteczko, G. Reiss, and S. O. Demokritov, "Nonlinear propagation of spin waves in microscopic magnetic stripes," Phys. Rev. Lett. **102**(17), 177207 (2009).

[21] M. M. Scott, C. E. Patton, M. P. Kostylev, and B. A. Kalinikos, "Nonlinear damping of high-power magnetostatic waves in yttrium–iron–garnet films," J. Appl. Phys. **95**(11), 6294–6301 (2004).

[22] A. Venugopal, T. Qu, and R. H. Victora, "Nonlinear parallel-pumped FMR: Three and four magnon processes," IEEE Trans. Microwave Theory Tech. **68**(2), 602–610 (2020).

[23] K. Moon and S. M. Girvin, "Theory of microwave parametric down-conversion and squeezing using circuit QED," Phys. Rev. Lett. **95**, 140504 (2005).

[24] X. Fang, M. Bai, X. Ye, J. Miao, and Z. Zheng, "Ultra-broadband microwave frequency down-conversion based on optical frequency comb," Opt. Express **23**(13), 17111 (2015).

[25] C. I. Yeh, W. S. Feng, and C. Y. Hsu, "0.9–10.6 GHz UWB mixer using current bleeding for multi-band application," Electron. Lett. **50**(3), 186–187 (2014).

[26] L. Flacke, L. Liensberger, M. Althammer, H. Huebl, S. Geprägs, K. Schultheiss, A. Buzdakov, T. Hula, H. Schultheiss, E. R. J. Edwards, H. T. Nembach, J. M. Shaw, R. Gross, and M. Weiler, "High spin-wave propagation length consistent with low damping in a metallic ferromagnet," Appl. Phys. Lett. **115**(12), 122402 (2019).

[27] H. S. Korner, M. A. W. Schoen, T. Mayer, M. M. Decker, J. Stigloher, T. Weindler, T. N. G. Meier, M. Kronseder, and C. H. Back, Appl. Phys. Lett. **111**(13), 132406 (2017).

[28] M. A. Schoen, D. Thonig, M. L. Schneider, T. J. Silva, H. T. Nembach, O. Eriksson, O. Karis, and J. M. Shaw, "Ultra-low magnetic damping of a metallic ferromagnet," Nat. Phys. **12**(9), 839–842 (2016).

[29] The stripe of $Co_{25}Fe_{75}$ was processed on Si/SiO_2 using electron beam lithography, magnetron sputtering, and subsequent lift-off. The metallic thin film was deposited with a thickness of 30 nm. Two shorted-CPW gold antennas, processed via e-beam lithography, thermal evaporation, and lift-off, were used as the microwave inputs RF1 and RF2.

[30] V. S. L'vov, *Wave Turbulence under Parametric Excitation* (Springer-Verlag, New York, 1994).

[31] T. Sebastian, K. Schultheiss, B. Obry, B. Hillebrands, and H. Schultheiss, "Micro-focused Brillouin light scattering: Imaging spin waves at the nanoscale," Front. Phys. **3**, 35 (2015).

[32] B. A. Kalinikos and A. N. Slavin, "Theory of dipole-exchange spin wave spectrum for ferromagnetic films with mixed exchange boundary conditions," J. Phys. C: Solid State Phys. **19**(35), 7013–7033 (1986).

[33] L. Körber, K. Schultheiss, T. Hula, R. Verba, J. Fassbender, A. Kákay, and H. Schultheiss, "Nonlocal stimulation of three-magnon splitting in a magnetic vortex," Phys. Rev. Lett. **125**(20), 207203 (2020).

[34] T. Brächer, P. Pirro, and B. Hillebrands, "Parallel pumping for magnon spintronics: Amplification and manipulation of magnon spin currents on the micron-scale," Phys. Rep. **699**, 1–34 (2017).

[35] A. Vansteenkiste, J. Leliaert, M. Dvornik, M. Helsen, F. Garcia-Sanchez, and B. Van Waeyenberge, "The design and verification of MuMax3," AIP Adv. **4**(10), 107133 (2014).

[36] We modeled the conduit using 4096 cells along the long axis, 64 cells along the short axis, and 1 cell along the film normal. For excitation, we defined two rectangular regions across the stripe where dynamic out-of-plane fields could be applied. The position of these areas was similar to the fabricated sample. The following material parameters were used: $A_{ex} = 26 \times 10^{-12}$ J/m^3, $M_{sat} = 1700 \times 10^3$ A/m, and $\alpha = 0.01$.

Article

Epitaxial Lateral Overgrowth of Tin Spheres Driven and Directly Observed by Helium Ion Microscopy

Nico Klingner,* Karl-Heinz Heinig, David Tucholski, Wolfhard Möller, René Hübner, Lothar Bischoff, Gregor Hlawacek, and Stefan Facsko

ACCESS | 📊 Metrics & More | 📄 Article Recommendations | 🔲 Supporting Information

ABSTRACT: Enhanced interstitial diffusion in tin is a phenomenon often observed during ion-beam irradiation and in lead-free solders. For the latter, this not very well understood, strain-driven mechanism results in the growth of whiskers, which can lead to unwanted shorts in electronic designs. In ion-beam physics, this phenomenon is often observed as a result of the enhanced formation of Frenkel pairs in the energetic collision cascade. Here, we show how epitaxial growth of tin extrusions on tin-oxide-covered tin spheres can be induced and simultaneously observed by implanting helium using a helium ion microscope. Calculations of collision cascades based on the binary collision approximation and 3D-lattice-kinetic Monte Carlo simulations show that the implanted helium will occupy vacancy sites, leading to a tin interstitial excess. Sputtering and phase separation of the tin oxide skin, which is impermeable for tin atoms, create holes and will allow the epitaxial overgrowth to start. Simultaneously, helium accumulates inside the irradiated spheres. Fitting the simulations to the experimentally observed morphology allows us to estimate the tin to tin-oxide interface energy to be 1.98 J m^{-2}. Our approach allows the targeted initiation and in situ observation of interstitial diffusion-driven effects to improve the understanding of the tin-whisker growth mechanism observed in lead-free solders.
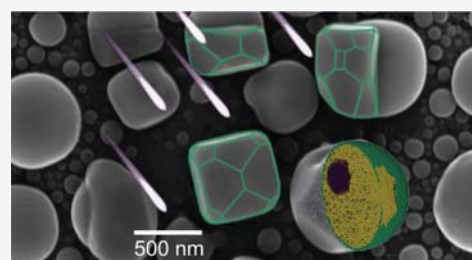
1. INTRODUCTION

The growth of tin whiskers has been extensively studied over the last 70 years and has increased even more in recent years due to the ban on lead-containing solder.[1,2] One reason is that alternative solder formulations are prone to whisker formation.[3,4] The detailed mechanisms of whisker growth are still under discussion, especially the source of point defects and their kinetics.[5−7] At room temperature, tin whisker growth takes weeks or even months, which makes experimental studies time-consuming. Point defect creation by ion irradiation can considerably accelerate the kinetics of the growth of extrusions. On the other hand, high-fluence helium implantation into semiconductor materials and metals causes bubble and blister formation,[8−13] serving valuable insights for first wall fusion reactor materials research.[14] Furthermore, ion irradiation of nano-objects can considerably change their shape due to mechanisms like ion-beam hammering,[15] ion-induced shaping of buried particles,[16] or ion-induced viscous flow of nano-pillars.[17] These shape changes are mainly driven by the kinetics of defects generated by collisions of atoms with energetic ions and recoils. Defect generation by electron irradiation can also cause shape changes of nanoobjects.[18]

Here, we report on an interesting observation during medium-fluence He$^+$ irradiation of micrometer-sized tin spheres. The experiments were carried out with gas-field-ion-source-based focused He$^+$ irradiation using helium ion microscopy (HIM). This approach enables the in situ observation of the ion-induced shape transformation of Sn micro-spheres with sufficiently high resolution. To explain the observed shape changes, one needs to consider He implantation into the Sn micro-spheres, causing ion-beam mixing and the production of Frenkel pairs, as well as the subsequent He nano-bubble formation. To better understand the He$^+$-irradiation-induced morphology changes of Sn spheres caused by the kinetics of point defects (He-interstitials, tin interstitials, and tin vacancies), we have developed an appropriate diffusion-reaction model and employed 3D-lattice-kinetic Monte Carlo (3DlkMC) simulations. These simulations provide detailed information on the nucleation and growth mechanisms of the observed Sn extrusion. It is shown that the growth starts at holes in the SnO skin of the spheres formed by ion erosion, followed by epitaxial lateral overgrowth (ELO) fed by Sn interstitials coming from the interior of the Sn spheres. The presented combination of experimental studies and atomistic simulations will improve the understanding of point defect kinetics in tin, which controls the whisker growth too.

2. EXPERIMENTAL RESULTS

The experiments were performed with tin spheres on a carbon substrate—a widely used resolution test specimen for scanning electron microscopy (SEM) and manufactured by vapor deposition.[19] Tin has very low wettability on the carbon substrate and forms, due to its high surface tension, almost perfect spheres with sizes ranging from a few nanometers to several tens of micrometers. This type of sample allows an easy and fast inspection and correction of astigmatism over a wide magnification range in SEM, focused ion beam (FIB), or HIM devices. Commercially, the tin sphere test specimen is available from various suppliers.[20−22] The sample used in our experiments contains particles with sizes ranging from <5 nm to 30 μm.[23]

The ion-beam exposure of the tin spheres was performed with a helium ion microscope. HIM is well known for imaging, modification, and for material analysis on the nanometer scale.[24−29] It is best suited to perform a local He or Ne exposure with a very high fluence due to the small beam spot size (1 nm for He and 4 nm for Ne) and the possibility of in situ observation of the irradiated area using the same beam. The irradiation was performed by scanning the beam in line-by-line mode over a small subset of tin spheres. The so-obtained high-resolution images of the nanostructures were then analyzed with respect to the observed geometric changes of the tin spheres. The fluence typically applied per image was chosen to be below 1×10^{16} ions cm^{-2} to track small ion-induced modifications.

In Figure 1, snapshots of typical irradiation with 28 keV helium ions are shown.

After a homogeneously distributed fluence of 2×10^{17} ions cm^{-2}, small pyramidal extrusions form preferentially at the equator of the irradiated spheres, where the north pole points to the ion source (Figure 1b). With increasing fluence, these extrusions become bigger in size and begin to overgrow the surface (Figure 1c). Later on, the extrusions become more and more faceted (Figure 1d−g). In Figure 1h, a larger field of view (FOV) including parts of the non-irradiated surface is presented. Extrusions from tin spheres form only in the irradiated area or only a few tens of nanometers from its rim. Above a fluence of 5×10^{17} to 7×10^{17} ions cm^{-2}, helium bubbles seem to emerge on the surface. The collapsed surface locations are indicated by blue arrows in Figure 1f,g. Once this fluence is exceeded, no further extrusion growth was observed on these spheres, and the edges of the facets become rounded.

Images of several irradiation experiments were recorded as videos and are published in RODARE.[30] The noise-level of the videos was improved by a recursive prediction/correction algorithm based on the Kalman-Filter.[31]

Irradiations with various beam parameters were performed. Primary ion energies from 10 to 30 keV, ion currents from 0.1 to 8 pA, and different FOV from 0.6 to 4 μm were adjusted—all He$^+$ irradiations led to the described phenomena with only slight variations. Tin spheres smaller than about 150 nm do not show any extrusion; they only shrink due to erosion by ion sputtering. Simulations with the TRIM program[32] show that the projected He$^+$ range at 30 keV is (149 ± 67) nm, which coincidences with the threshold radius of the smallest spheres forming extrusions, which was determined to be (150 ± 50) nm for 28 keV helium ions.

We did not observe any flux dependence within the range of 2.6×10^{13} to 4.1×10^{15} ions cm^{-2} s^{-1}. Once extrusions are
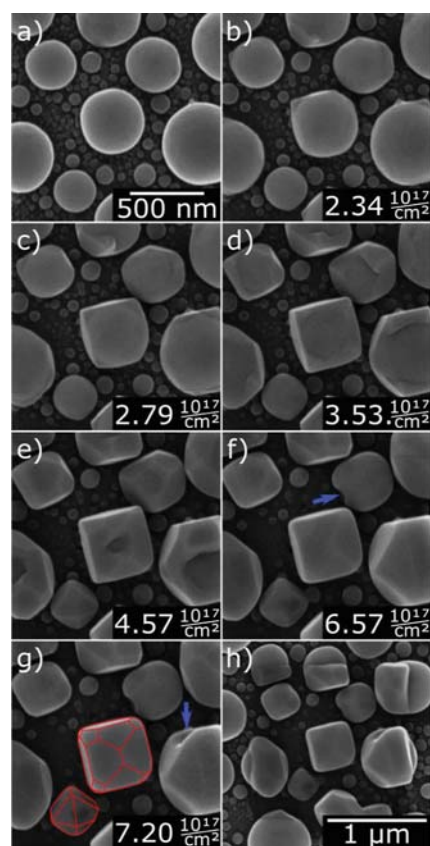
Figure 1. HIM images of (a) pristine, not irradiated tin spheres on carbon. (b−g) Same sample region after the irradiation of various fluencies, as indicated in the images. FOV of (a−g) is 1.4 μm (cropped from 2.0 μm). (h) Image of the irradiated area captured on a larger FOV of 2.2 μm (cropped from 4.0 μm). No morphological changes of the tin spheres are visible outside the irradiated area. Collapsed bubbles are indicated by blue arrows in (f) and (g).

formed, they are stable over time and grow, provided they are not destroyed by emanating He bubbles or sputtering due to continuous He$^+$ ion irradiation.

A similar tin sphere evolution was observed under Ne$^+$ ion irradiation in HIM, but the extrusions formed were much smaller in size before the process stopped due to neon gas bubbles reaching the particle surface. The data for 28 keV Ne$^+$ ion irradiation is openly available in RODARE.[30]

A large tin sphere with a diameter of 4.7 μm has been irradiated only partly in an area of 2 μm × 2 μm. In Figure 2, snapshots from the irradiation are shown.

As shown in Figure 2a, extrusions are not yet visible on the large sphere, while the smaller one at the right edge of the image already shows clear facets. As shown in Figure 2b, a small extrusion becomes visible at the equator of the large sphere, where the ion beam hits the surface nearly tangentially. The small extrusion grows slowly with increasing fluence (see Figure 2c). As shown in Figure 2d, a second extrusion with an equal-facet orientation appears close to the first one. As shown in Figure 2e, both extrusions have merged into a larger one. Gaps between both extrusions have been filled and show clear merged facets keeping the initial orientation, and the extrusions on the smaller spheres start rounding. The final size of the described extrusions on the sphere on the bottom right side of the image is nearly reached, as shown in Figure 2f.
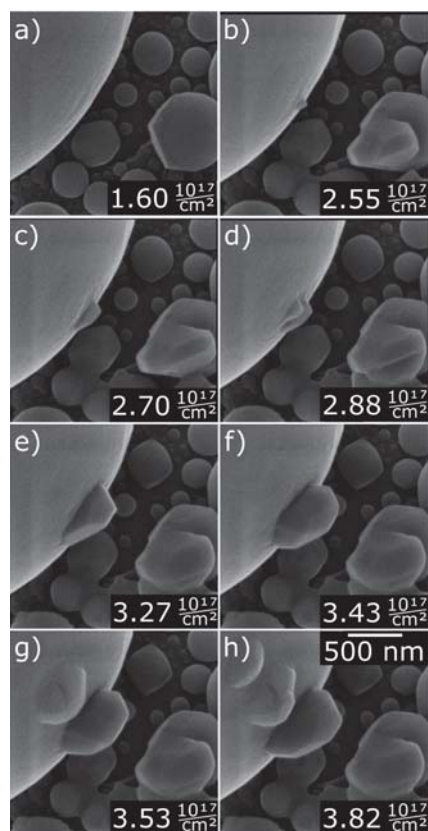
Figure 2. a−h) HIM snapshots of the irradiation of tin spheres for increasing fluencies. A partially irradiated larger tin sphere with a diameter of around 4.7 μm can be seen in the top left corner. The field of view is 1.9 μm cropped from an irradiated area of 2.0 μm.

In contrast to the growth of the crystal-like facets in Figure 2a−f, the extrusion appearing in Figure 2g has a more rounded bubble-like shape. This feature is popping up within just two consecutive single image scans, equivalent to a fluence difference of only 7×10^{14} ions cm^{-2}. Finally, after 3.82×10^{17} ions cm^{-2} (see Figure 2h), another more spherical extrusion appears above the older extrusions after only a small amount of additional fluence. The process seems to be different for the extrusions appearing in Figure 2a−f than for the features shown in Figure 2g,h. For a better presentation of the evolution of the extrusions, the process can be seen as a movie in RODARE.[30]

For transmission electron microscopy (TEM) analysis, pristine tin spheres were mechanically removed from the surface onto carbon-coated copper grids. In the high-resolution TEM (HRTEM) images presented in Figure 3a,b, the crystallinity of a 80 nm small unirradiated tin sphere passivated by a 3 to 5 nm oxide layer is visible. While the spheres possess the well-known single-crystalline tetragonal β-tin structure (Figure 3a−c), the amorphous outer shell layer was proven to be a Sn oxide, using energy-dispersive X-ray spectroscopy (EDXS) analysis. More TEM and EDXS data of a tin sphere can be found in RODARE[30] and in the supporting information. Additional X-ray photoelectron spectroscopy (XPS) analysis confirmed a tin-to-oxygen ratio of 47−53 at. %. We therefore conclude that the layer consists of meta-stable tin(II) oxide SnO (stannous oxide). We assume that this oxide layer is a native oxide layer that forms under air exposure and that it covers all tin spheres homogeneously.[33]
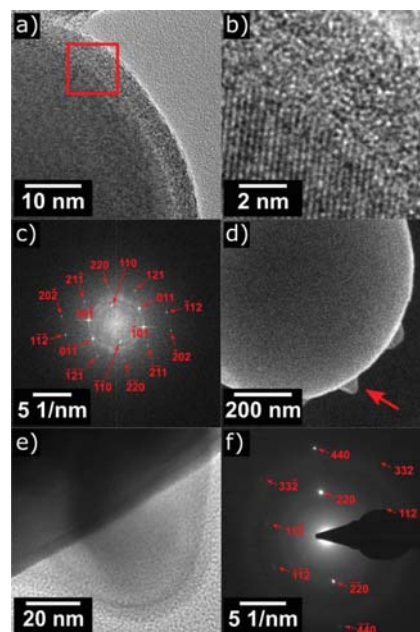
Figure 3. a) HRTEM image of a small, pristine tin sphere (FOV 37.9 nm); the square indicates the area that is shown at higher magnification in (b). (c) Fast Fourier transform image of a HRTEM image (FOV of 37.9 nm) of the inner crystalline part of the tin sphere shown in (a). Indexing was done based on the β-tin structure in the $\overline{1}1\overline{1}$ zone axis geometry. (d) HIM image of the irradiated sphere on a carbon-coated TEM grid and (e) overgrown crystalline extrusion, indicated by an arrow in (d). (f) Selected-area electron diffraction pattern of the extrusion shown in (d). Indexing was done based on the β-tin structure in the $\overline{1}10$ zone axis geometry.

In Figure 3d, a HIM image of a tin sphere is presented that was irradiated with a fluence of 2.4×10^{17} ions cm^{-2}. The growth of several extrusions on the equator of the sphere was monitored during the helium irradiation process. The irradiation was stopped after the first extrusions appeared to later obtain TEM images of this stage in the formation process.

The crystal orientation of all extrusions was investigated by TEM analysis. A TEM image of the extrusion indicated in Figure 3d is presented in Figure 3e. Selected-area electron diffraction analysis of all extrusions and the tin sphere shows identical diffraction patterns, which can be indexed with the β-Sn structure (Figure 3f). This result gives strong evidence that the tin sphere is mono-crystalline and that the extrusions have grown epitaxially.

The tin spheres were also analyzed after gallium FIB cross-sectioning to gain information on the internal structure. For this purpose, unirradiated and irradiated spheres were cut in half with a Ga-FIB, and the resulting cross-sections were imaged at 54° tilt, using SEM (see Figure 4).

The internal structure of an unirradiated tin sphere is presented in Figure 4a. In Figure 4b,c, HIM images of the same area before and after 30 keV helium ion irradiation are shown. The irradiation was stopped when clear extrusions appeared. The sample area visible in Figure 4c was imaged by HIM, using the minimal necessary fluence (short dwell times and low currents) to not further irradiate the tin spheres during imaging and therefore does not reflect the best possible image quality. The sample was transferred—and thereby exposed to air—to the dual beam tool (Ga FIB, SEM), and the exposed area was identified using SEM imaging. A cross-section has
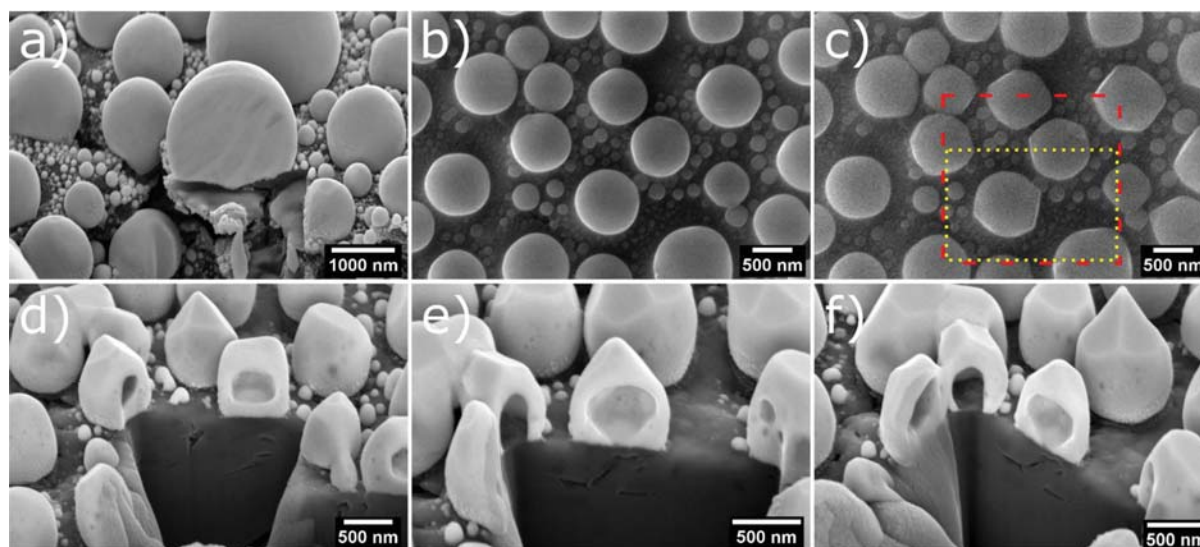
Figure 4. (a) SEM image of unirradiated tin spheres. The largest sphere was cut-opened with a gallium FIB. The SEM image was taken at 54° tilt angle. (b−f) show the same area of the sample at various points of the analysis process. (b) HIM image before irradiation. (c) HIM image after irradiation with visible extrusions. The yellow, dotted rectangle is a guide to the eye, indicating the gallium-FIB-milled region shown in (d). The red, dashed region indicates the milled area visible in (e) and (f). (d−f) SEM images under 54° tilt of tin spheres with extrusions that were opened by FIB milling. Cavities are visible that were probably filled with helium bubbles. In (f), the sample was rotated clockwise to image the inside of all three opened tin spheres, simultaneously.
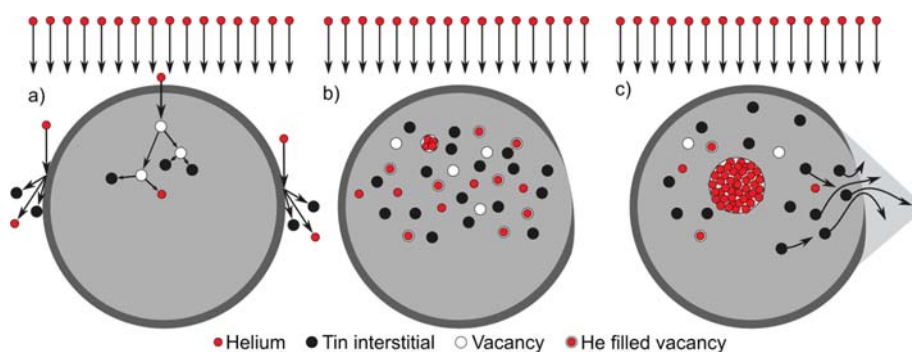
Figure 5. Schematic representation of the proposed model for the formation of extrusions and bubbles in tin spheres of typical size (500 nm) by 30 keV helium ion irradiation. (a) Initial state of the irradiation process. Implantation of helium leads directly and also indirectly via the collision cascade to about 70 interstitial-vacancy pairs per implanted ion. About half of the helium is implanted, while the other half is scattered out of the sphere or is transmitted in the outer, thinner region of the sphere. The schematic exaggerates the number of sputtered atoms at the outer shell (black circles). The following simulations show that each helium atom sputters 0.2 atoms on average, with higher sputtering rates at the rim of the spheres. (b) Further implantation leads to increasing helium, interstitial, and vacancy densities. Vacancies can be reoccupied by tin interstitials or filled by helium atoms. Sputter erosion and phase separation will cause somewhere a local exposure of the tin core. (c) Epitaxial lateral overgrowth of the tin sphere by escaping tin interstitials and formation of helium bubbles inside the sphere.

been prepared from several irradiated spheres, using Ga-FIB milling. The first milled area is indicated in Figure 4c as a dotted yellow box, and the result is presented in Figure 4d. Due to sample tilting toward the FIB column, the sputtered region appears as a trapezoid in the SEM image. Small spheres, as shown in Figure 4d, show a large cavity in their center. The sample was further milled, as indicated in Figure 4c, by a dashed, red box, and the resulting cross-section is shown in Figure 4e. For larger spheres, several smaller He bubbles in a depth corresponding to the projected range of the 30 keV helium beam were observed (see e.g., the sphere on the right side of Figure 4e). The sample was rotated clockwise by 45° to be able to look into all three milled structures, and the resulting image is presented in Figure 4f. All cross-section tin spheres which showed crystal-like extrusions have the same kind of cavity-like internal structure. We will see later that this

finding is essential for the understanding of the observed effect and the proposed model.

Localized pre-irradiation of the tin spheres could cause weak points in the SnO skin, allowing the location of faceted extrusions formed upon further broad-beam-like irradiation to be determined in advance. Due to surface sputtering and ion-beam mixing, the oxide layer could potentially be pre-thinned at these locations.

3. MODELING, SIMULATIONS, AND DISCUSSION

The observed ion-irradiation-induced growth of extrusions on tin spheres can be roughly divided into three stages:

(i) Collisions of the energetic He$^+$ ions with tin atoms of the spheres create Frenkel pairs of interstitial atoms and vacancies in the tin lattice. Additionally, such collisions

can erode the SnO skin of the tin spheres by sputtering and by ion-beam mixing of the Sn−SnO interface, resulting in sub-stoichiometric SnO_x (x < 1) (Figure 5a). As sputtering is the strongest for small incident angles (in respect to the surface), the SnO skin becomes damaged most severely near the equator.

(ii) With increasing He$^+$ ion fluence, the number of deposited He atoms and the number of interstitials and vacancies increase within the tin spheres (Figure 5b). The SnO skin is assumed to be impermeable for He atoms, vacancies, and interstitials.[34,35] Due to ion erosion of SnO, a contact of the tin core with the external vacuum can form first somewhere along the equator.

(iii) Through the hole in the SnO skin, Sn interstitials and vacancies can escape from the core of the tin particle (Figure 5c). As the tin particle is crystalline, the extrusions also become crystalline due to ELO (see e.g., ref 36). The only difference with conventional ELO is the source of the atoms: Here, interstitial atoms come from the interior of the spheres through the oxide openings, as compared to atoms delivered by a chemical vapor source. Some of the vacancies capture a helium atom and can therefore not annihilate with an interstitial. In an extreme case, one could consider a situation in which all but one of the interstitial-vacancy pairs—which are created by an incoming He$^+$ ion—annihilate. The vacancy of the remaining Frenkel-pair is filled with the implanted helium atom, and one interstitial atom per implanted He$^+$ ion remains in the lattice. For phosphorus and boron implantation into silicon, this very successful approach is called the "+1"-model.[37] The He-filled vacancies diffuse slowly and will unlikely escape through the hole in the SnO skin. They become enriched and form, due to their low nucleation barrier, He nano-bubbles that later coalesce to larger He bubbles within the tin sphere. The creation of helium bubbles was confirmed by FIB cross-sectioning and is observed for other material systems too.[8,9,13,38−41]

For stage (i), the spatial distributions of point defects and of implanted He$^+$ ions were calculated with the program TRI3DST[42] which is based on the binary collision approximation (BCA). As the projected range of (156 ± 70) nm for 30 keV He$^+$ ions in tin (simulated with TRIM[43]) is of the order of the size of the tin spheres, a truly 3D program like TRI3DST is indispensable. The simulation of the impact of 1 × 10^{10} He$^+$ ions onto a tin sphere of 500 nm diameter having a 5 nm tin oxide skin resulted in an average sputter yield of 0.20 atoms per incident ion and a He deposition efficiency of 49%. As is evident from the simulation results, 30 keV He$^+$ ions become deposited mostly in the upper half of the sphere (Figure 6a). For spheres with a diameter smaller than 150 nm, most of the helium will be transmitted and not implanted.

On average, about 70 Frenkel pairs are formed per incoming He$^+$ ion, and their spatial distribution (calculated with TRI3DST) is closer to the north pole than the distribution of the implanted He atoms shown in Figure 6a. However, as only one of the interstitials of a Frenkel pair survives, whose nearby vacancy is filled by a He atom, the relevant Sn interstitial generation is approximated by the spatial distribution of implanted He atoms, as shown in Figure 6a. Figure 6b shows that the strongest ion erosion of the tin oxide skin takes
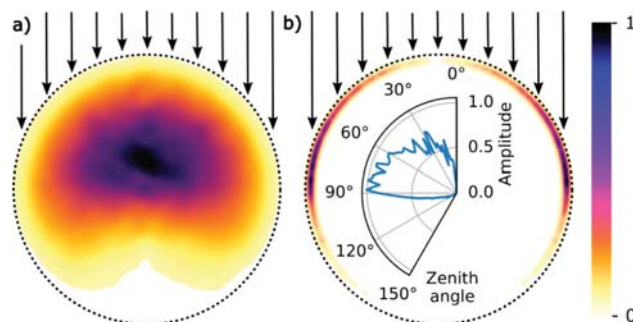
Figure 6. TRI3DST BCA simulation of a nanosphere with 500 nm diameter, consisting of a Sn core and a 5 nm tin oxide shell irradiated with 30 keV He$^+$. 1 × 10^{10} He$^+$ ion impacts were simulated. (a) Normalized He$^+$ ion implantation profile, (b) normalized sputter ejection profile (thin colored area below the dashed circle). The color represents the relative implantation and sputter yield amplitude normalized from 0 to 1. In the inset, the sputter profile of the sphere is plotted in polar coordinates. For angles smaller than 90°, the polar angle also corresponds to the angle of incidence of the ions. For angles larger than 90°, the ions must first enter the sphere and can then sputter particles from the surface during the projectile exit. Most particles are sputtered for angles between 75 and 90°.

place at the equator of the sphere between 75 and 90°. There, the SnO skin will be removed, as regrowth due to tin oxidation under the used high-vacuum conditions is negligible. Tin extrusions are observed at fluencies slightly above 2 × 10^{17} ions cm^{-2} (see Figure 2b). According to TRI3DST, a hole in the SnO skin is not yet opened by sputtering. However, besides sputtering, there is ion-beam-induced mixing at the Sn−SnO interface, and the resulting SnO_x (x < 1) decays into Sn and SnO regions of the nm size. Thus, a contact of the tin core with the vacuum can form also without sputtering, just by ion-beam mixing and ion-assisted phase separation of SnO_x. A detailed investigation of how far sputtering alone or to which extent the ion beam-induced phase separation is responsible for the formation of the extrusions has not been performed and is beyond the scope of this article. Quantitative statements cannot be made based on the data of TEM measurements and therefore remain an important subject of future investigations.

The results of the TRI3DST simulations serve as input data for 3DlkMC simulations[44] of the diffusion-reaction kinetics of the He atoms, interstitials, and vacancies. Simulations were performed on a body-centered tetragonal (bct) crystal structure which is close to the A5 lattice structure of β-tin. The A5 structure of β-tin is in fact a double-bct structure,[45] which differs energetically only slightly from the simpler bct structure. In our model system, initially, all bct sites inside the sphere are occupied by tin. The sphere is surrounded by a skin of lattice sites which are not reachable by diffusion jumps (dark gray atoms in Figure 5a and green atoms in Figure 7).

This skin is a few lattice sites thick and imitates the inert properties of the SnO shell with respect to the diffusion[34,35] of the species considered here. To emulate the holes in the SnO formed by sputtering and ion-beam mixing, the SnO shell is removed locally at the equator (see Figure 7a), that is, at this position tin atoms are in contact with the vacuum. Here, a tin interstitial atom can become a surface adatom, and a tin vacancy can become a surface vacancy.

The interatomic interaction of tin atoms is described by a Rosato, Guillopé, and Legrand (RGL) potential[46] fitted to the {200} surface energy and the energy of cohesion of β-tin.[47]
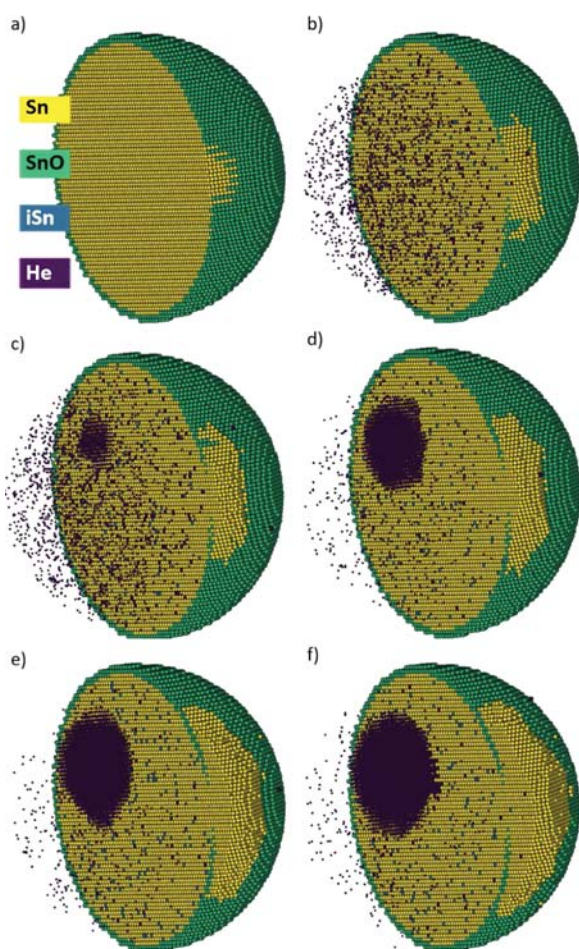
Figure 7. Snapshots of a simulation of He$^+$ irradiation of a SnO-covered tin sphere of 500 nm diameter after different equivalent fluencies: To show interior evolution, the spheres are cut in half, and all species but He are hidden in one-half. Purple points: deposited He atoms, yellow points: bct sites occupied with Sn atoms, green points: SnO species, and blue points: Sn atoms on interstitial sites. (a) Initial sphere with a hole in the SnO skin. After an equivalent fluence of (b) 4.3×10^{15} ions cm^{-2}, (c) 5.3×10^{15} ions cm^{-2}, (d) 6.4×10^{15} ions cm^{-2}, (e) 1.2×10^{16} ions cm^{-2}, and (f) 1.7×10^{16} ions cm^{-2}, the He$^+$ ion is coming from the top, and the long axis of the bct lattice is oriented vertically.

Other than standard Ising-like kinetic Monte Carlo (kMC) simulations, with the RGL potential, the energy of a tin atom is no longer linearly dependent on the number of occupied nearest neighboring sites but shows a square-root-like behavior. Thus, the RGL potential allows a more appropriate description of the kinetics in metals, especially of the formation of the correct crystal facets and the nucleation of voids. The interaction of a Sn atom with a SnO species is assumed to depend linearly on the number of nearest neighboring SnO species. This Sn−SnO bond strength is a free parameter in our model. It could be derived from the Sn−SnO interface energy which is unfortunately unknown. Therefore, we modified it until the experimentally found features of extruded tin on the SnO-covered tin sphere were reproduced, resulting in a value of 1.98 J m^{-2}. It is assumed that there is neither He−Sn nor He−SnO interaction.

The used interatomic tin potential describes suitably the nucleation of voids/He bubbles and the formation of facets on the extrusions and at the surface of bubbles. However, the kinetics additionally depends on the migration energy of the species, that is, the saddle point energy of diffusion jumps. The migration energies of vacancies (empty or He-filled) and tin interstitials could be derived with the Einstein−Smoluchovski equation from their diffusion coefficients which, unfortunately, are not available. It is known, however, that energetic electron irradiation of metals like copper accelerates point-defect-driven microstructure shape changes strongly.[18] He$^+$ ion irradiation is expected to assist diffusion even more efficiently. Figure 1h shows further evidence for this as the wetting of the SnO skin is restricted to highly irradiated areas only. Thus, in our model, we implemented the following reasonable approximation which corresponds to the "+1"-model discussed above: from the ≈70 Frenkel pairs per He$^+$ ion impact, just one Sn interstitial and one He-filled vacancy survive. For our problem, the validity of the "+1"-model approximation was confirmed by a comparison with a long-lasting 3DlkMC simulation taking into account the full generation of 70 Frenkel pairs per He impact. A similar assumption on He$^+$-ion-created defects was quite successfully used in the simulation of He$^+$ ion irradiation of intermetallic compounds.[48] Possibly more than one He atom can fit into a tin vacancy; this number is a parameter in the 3DlkMC simulations.

Despite all the approximations made, the computation time for realistic sphere diameters is prohibitive; thus, simulations were carried out for scaled-down spheres, accompanied by also scaling the projected range of the He$^+$ ions and the fluence per volume to be equivalent to that of a 500 nm sphere irradiated with 10^{17} ions cm^{-2}. Independent of the scaling, the thickness of the SnO shell is fixed to the minimum value necessary to act as a diffusion barrier. The scaling factor of the sphere diameter in the simulations presented here is roughly 13. Snapshots of a 3DlkMC simulation (see Figure 7) show the formation of a faceted tin extrusion on a tin sphere and the formation of a He bubble within the tin sphere. The complete simulated tin sphere evolution under He$^+$ ion irradiation is available as a movie in the Supporting Information.[30] The extrusion grows epitaxially from the hole in the SnO skin at the equator and overgrows the SnO surface, driven by the tin interstitials diffusing out of the sphere. The He bubbles in the simulation are rhomboidal rather than spherical.

Pressure has not been taken into account in our simulations; thus, the shapes of the extrusions and of the He bubbles are controlled by the surface energies and the point defect kinetics. In longer-running simulations (not shown here), an escape of He bubbles from the interior of the sphere through the extrusion into the vacuum was observed, similar to experimental findings.

4. SUMMARY

We report on the effects of high-fluence He$^+$ ion implantation into tin spheres within a HIM. The spheres were characterized and analyzed by SEM, XPS, and TEM to be single-crystalline β-tin spheres with a few-nm-thick oxide skin. Under He$^+$ irradiation, faceted ELO of tin on the SnO skin starts from holes in the SnO skin, and it forms small-edged extrusions on the outside of the spheres, which was observed in situ in the HIM for different irradiation parameters. BCA-based simulations of collision cascades show that high-fluence 30 keV He$^+$ irradiation leads to the implantation of nearly half of the supplied helium into a depth of ≈150 nm below the north poles of 500 nm spheres. In addition, the energetic He particles

lead to the creation of ≈70 Frenkel-pairs per ion and enhanced sputtering of SnO under tangential impact conditions at the equator of the sphere. In the framework of the "+1"-model, for each He^+ impact, all but one of the Frenkel pairs annihilate due to He occupation of one vacancy; thus, one Sn interstitial atom remains. In the course of He^+ implantation, the helium-vacancy complexes accumulate, and He bubbles nucleate and grow. Sn interstitial atoms accumulate too, but due to the increasing pressure in the SnO-covered tin spheres, the nucleation of Sn dislocations is hampered. Upon creation of an opening in the SnO skin at the equator due to sputtering and ion-beam mixing, the dense Sn interstitial gas can emanate through that hole, leading to ELO on the SnO, that is, the formation of an extrusion. This behavior was observed experimentally and is qualitatively reproduced by modeling and atomistic simulations of the defect generation and the reaction-diffusion kinetics of the defects. Thus, the observed phenomenon becomes a well-understood mechanism of point-defect-driven nanostructure formation. The He^+-irradiation-induced defect generation is intense, which allows short experimental studies, and there is a good theoretical understanding of the defect generation. This is quite different for the tin whisker growth which is detrimental for electronics. There, the defect generation rate is very low (and not well understood, e.g., pressure-induced), leading to very long-lasting experiments. Thus, our study of point defect kinetics in tin can help to get a better understanding of tin whisker growth.

As such, the process is not restricted to Sn spheres and He but might also be relevant for many other examples. It is also of importance for a wide range of irradiation conditions that lead to a large number of interstitials and where a passivating surface layer prevents the surface from acting as an effective sink for point defects.

5. METHODS

5.1. HIM Irradiation. The ion beam exposure of the tin spheres was performed in the Carl Zeiss NanoFAB using helium and neon ions, the latest generation of HIM devices. Stage drift and sample drift were compensated by manually adjusting the irradiation window position and by post-aligning of the recorded image stack using the scale-invariant feature transform algorithm[49] in ImageJ.[50]

For the irradiation shown in Figure 1, a primary ion current of (6.6 ± 1.0) pA was applied, utilizing a 10 μm aperture, 5.2×10^{-6} mbar helium gas pressure in the ion source, and a crossover position of −193 mm (spotcontrol 3). The dwell time per pixel was chosen to be 10 μs, capturing (512×512) pixel images on a FOV of 2.0 μm. This equals to 2.6 s irradiation time per image, a fluence of 2.7×10^{15} ions cm^{-2} per scan, and a flux of 1×10^{15} ions cm^{-2} s^{-1}. After 301 images, the resulting total implantation fluence was 8.3×10^{17} ions cm^{-2}, resulting in a total irradiation time of approximately 13 min. The chamber pressure during the irradiation was below 2.0×10^{-7} mbar.

The irradiation shown in Figure 2 was performed with (0.2 ± 0.1) pA of 30 keV He^+ using a 10 μm aperture, 4.5×10^{-6} mbar helium gas pressure in the ion source, and a crossover position of −246 mm (spotcontrol 6). The dwell time per pixel was chosen to be 5 μs, capturing (1024×1024) pixel images at a FOV of 2.0 μm, while every scan line was averaged 4 times. With an irradiation time per image of 21 s and a fluence of 7.3×10^{14} ions cm^{-2} per scan, we calculate a flux of 3.5×10^{13} ions cm^{-2} s^{-1}. 521 images equal a total irradiation fluence of $3.8 \times$

10^{17} ions cm^{-2} and a total irradiation time of 3 h. Including the time for saving the individual images and correction for drift, the irradiation was done in 9 h in total and split in two sessions.

In Figure 3d, a tin sphere is shown that was irradiated with 2.0 pA of 30 keV He^+ by using a 10 μm aperture, 5.6×10^{-6} mbar helium gas pressure in the ion source, and a crossover position of −229 mm (spotcontrol 5). 5 μs dwell time per pixel was used to capture (1024×1024) pixel images on a FOV of 1.4 μm without line averaging. The irradiation time per image was 5.2 s, resulting in a fluence of 3.3×10^{15} ions cm^{-2} per scan and a flux of 6.4×10^{14} ions cm^{-2} s^{-1}. 71 image scans equal a total implantation fluence of 2.4×10^{17} ions cm^{-2}. Videos of the irradiation process can be found in RODARE.[30]

5.2. TEM and SEM Analyses. Smaller tin spheres were analyzed by TEM. Selected-area electron diffraction and HRTEM imaging were performed with an image-C_s-corrected Titan 80−300 microscope (FEI) operated at an accelerating voltage of 300 kV. Additionally, spectrum imaging analysis based on EDXS was done in scanning TEM mode at 200 kV with a Talos F200X microscope (FEI) equipped with a Super-X EDX detector system (FEI). XPS measurements were performed using a Microlab 310-F from Thermo Scientific. A Zeiss NVision 40 CrossBeam Workstation was used to perform Ga FIB cross-sectioning and SEM imaging.

■ ASSOCIATED CONTENT

ⓢ Supporting Information

The Supporting Information is available free of charge at https://pubs.acs.org/doi/10.1021/acs.jpcc.2c03707.

Additional TEM and EDXS data (PDF).

■ AUTHOR INFORMATION

Corresponding Author

Nico Klingner − Helmholtz—Zentrum Dresden—Rossendorf e.V., 01328 Dresden, Germany; ⓞ orcid.org/0000-0001-9539-5874; Email: n.klingner@hzdr.de

Authors

Karl-Heinz Heinig − Helmholtz—Zentrum Dresden—Rossendorf e.V., 01328 Dresden, Germany

David Tucholski − Helmholtz—Zentrum Dresden—Rossendorf e.V., 01328 Dresden, Germany

Wolfhard Möller − Helmholtz—Zentrum Dresden—Rossendorf e.V., 01328 Dresden, Germany

René Hübner − Helmholtz—Zentrum Dresden—Rossendorf e.V., 01328 Dresden, Germany; ⓞ orcid.org/0000-0002-5200-6928

Lothar Bischoff − Helmholtz—Zentrum Dresden—Rossendorf e.V., 01328 Dresden, Germany

Gregor Hlawacek − Helmholtz—Zentrum Dresden—Rossendorf e.V., 01328 Dresden, Germany; ⓞ orcid.org/0000-0001-7192-716X

Stefan Facsko − Helmholtz—Zentrum Dresden—Rossendorf e.V., 01328 Dresden, Germany; ⓞ orcid.org/0000-0003-3698-3793

Complete contact information is available at:
https://pubs.acs.org/10.1021/acs.jpcc.2c03707

Author Contributions

N.K. performed HIM experiments. K.-H.H, did modeling and DT performed 3DlkMC simulations. W.M. delivered BCA

simulations. R.H. carried out all TEM-based experiments. L.B. did FIB cross-sectioning. S.F. was responsible for XPS analysis. K.-H.H., W.M., N.K., and G.H. developed the theoretical model. All authors contributed to the data analysis and co-wrote the manuscript.

Notes

The authors declare no competing financial interest.

■ REFERENCES

(1) Furuta, N.; Hamamura, K. Growth Mechanism of Proper Tin-Whisker. *Jpn. J. Appl. Phys.* **1969**, *8*, 1404−1410.

(2) Galyon, G. Annotated tin whisker bibliography and anthology. *IEEE Trans. Electron. Packag. Manuf.* **2005**, *28*, 94−122.

(3) LeBret, J. B.; Norton, M. G. Electron microscopy study of tin whisker growth. *J. Mater. Res.* **2003**, *18*, 585−593.

(4) Fadil, N. A.; Yusof, S. Z.; Abu Bakar, T. A. A.; Ghazali, H.; Mat Yajid, M. A. M.; Osman, S. A.; Ourdjini, A. Tin Whiskers' Behavior under Stress Load and the Mitigation Method for Immersion Tin Surface Finish. *Materials* **2021**, *14*, 6817.

(5) Liu, S. H.; Chen, C.; Liu, P. C.; Chou, T. Tin whisker growth driven by electrical currents. *J. Appl. Phys.* **2004**, *95*, 7742−7747.

(6) Smetana, J. Theory of Tin Whisker Growth: "The End Game. *IEEE Trans. Electron. Packag. Manuf.* **2007**, *30*, 11−22.

(7) Jain, N.; Wang, X.; Jagtap, P.; Bower, A.; Chason, E. Analysis of Pressure-Induced Whisker Nucleation and Growth in Thin Sn Films. *J. Electron. Mater.* **2021**, *50*, 6639−6653.

(8) Livengood, R.; Tan, S.; Greenzweig, Y.; Notte, J.; McVey, S. Subsurface damage from helium ions as a function of dose, beam energy, and dose rate. *J. Vac. Sci. Technol., B: Microelectron. Nanometer Struct.* **2009**, *27*, 3244.

(9) Veligura, V.; Hlawacek, G.; Berkelaar, R. P.; van Gastel, R.; Zandvliet, H. J. W.; Poelsema, B. Digging gold: keV He$^+$ ion interaction with Au. *Beilstein J. Nanotechnol.* **2013**, *4*, 453−460.

(10) Bergner, F.; Hlawacek, G.; Heintze, C. Helium-ion microscopy, helium-ion irradiation and nanoindentation of Eurofer 97 and ODS Eurofer. *J. Nucl. Mater.* **2018**, *505*, 267.

(11) Shan, G.; Chen, Y.; Liang, N.; Dong, H.; Zhang, W.; Suo, T.; Liu, F. Irradiation resistance of a thermally stable nanocrystalline Fe-1 at. alloy. *Mater. Lett.* **2019**, *238*, 261−263.

(12) Allen, F. I.; Hosemann, P.; Balooch, M. Key mechanistic features of swelling and blistering of helium-ion-irradiated tungsten. *Scr. Mater.* **2020**, *178*, 256−260.

(13) Wang, Z.-J.; Allen, F. I.; Shan, Z.-W.; Hosemann, P. Mechanical behavior of copper containing a gas-bubble superlattice. *Acta Mater.* **2016**, *121*, 78−84.

(14) Bolt, H.; Barabash, V.; Federici, G.; Linke, J.; Loarte, A.; Roth, J.; Sato, K. Plasma facing and high heat flux materials − needs for ITER and beyond. *J. Nucl. Mater.* **2002**, *307−311*, 43−52.

(15) Snoeks, E.; van Blaaderen, A.; van Dillen, T.; van Kats, C. M.; Velikov, K.; Brongersma, M. L.; Polman, A. Colloidal assemblies modified by ion irradiation. *Nucl. Instrum. Methods Phys. Res. B* **2001**, *178*, 62−68.

(16) Schmidt, B.; Heinig, K.-H.; Mücklich, A.; Akhmadaliev, C. Swift-heavy-ion-induced shaping of spherical Ge nanoparticles into disks and rods. *Nucl. Instrum. Methods Phys. Res. B* **2009**, *267*, 1345−1348.

(17) Xu, X.; Heinig, K.-H.; Möller, W.; Engelmann, H.-J.; Klingner, N.; Gharbi, A.; Tiron, R.; Borany, J.; Hlawacek, G. Morphology modification of Si nanopillars under ion irradiation at elevated temperatures: plastic deformation and controlled thinning to 10 nm. *Semicond. Sci. Technol.* **2020**, *35*, 015021.

(18) Toimil-Molares, M. E.; Röntzsch, L.; Sigle, W.; Heinig, K.-H.; Trautmann, C.; Neumann, R. Pipetting Nanowires: In Situ Visualization of Solid-State Nanowire-to-Nanoparticle Transformation Driven by Surface Diffusion-Mediated Capillarity. *Adv. Funct. Mater.* **2012**, *22*, 695−701.

(19) Carson, K. R.; Rudee, M. L. An improved standard specimen for alignment of electron microscopes. *J. Sci. Instrum.* **1967**, *44*, 1036−1037.

(20) https://www.tedpella.com/calibration_html/SEM_Resolution_Test_Specimens_Tin_on_Carbon.htm#600 (accessed 12 April 2022).

(21) https://www.emsdiasum.com/microscopy/products/calibration/sem_resolution.aspx#79515 (accessed 12 April 2022).

(22) https://www.2spi.com/item/02863-ab/sem-tin-carbon/ (accessed 12 April 2022).

(23) https://www.plano-em.de/testobjekte/zinn-auf-kohle-universal?number=S1937 (accessed 12 April 2022).

(24) Ward, B. W.; Notte, J. A.; Economou, N. P. Helium ion microscope: A new tool for nanoscale microscopy and metrology. *J. Vac. Sci. Technol., B: Microelectron. Nanometer Struct.* **2006**, *24*, 2871.

(25) Notte, J.; Hill, R.; Ward, B. W.; Economou, N. P.; Hill, R.; Percival, R.; Farkas, L.; McVey, S. An Introduction to the Helium Ion Microscope. *AIP Conf. Proc.* **2007**, *931*, 489−496.

(26) Hlawacek, G.; Veligura, V.; van Gastel, R.; Poelsema, B. Helium ion microscopy. *J. Vac. Sci. Technol., B: Microelectron. Nanometer Struct.* **2014**, *32*, 020801.

(27) *Helium Ion Microscopy*; Hlawacek, G., Gölzhäuser, A., Eds.; Springer International Publishing, 2016.

(28) Klingner, N.; Heller, R.; Hlawacek, G.; Borany, J.; Notte, J.; Huang, J.; Facsko, S. Nanometer scale elemental analysis in the helium ion microscope using time of flight spectrometry. *Ultramicroscopy* **2016**, *162*, 91−97.

(29) Klingner, N.; Heller, R.; Hlawacek, G.; Facsko, S.; von Borany, J. Time-of-flight secondary ion mass spectrometry in the helium ion microscope. *Ultramicroscopy* **2019**, *198*, 10−17.

(30) Klingner, N.; Heinig, K.-H.; Tucholski, D.; Möller, W.; Hübner, R.; Bischoff, L.; Hlawacek, G.; Facsko, S. Data publication: Epitaxial lateral overgrowth of tin spheres driven and directly observed by helium ion microscopy [Data set]. *RODARE* **2022**, DOI: 10.14278/rodare.1540.

(31) https://imagej.nih.gov/ij/plugins/kalman.html (accessed 12 April 2022).

(32) Ziegler, J. F.; Ziegler, M.; Biersack, J. SRIM − The stopping and range of ions in matter. *Nucl. Instrum. Methods Phys. Res. B* **2010**, *268*, 1818−1823.

(33) Leitner, J.; Sedmidubský, D. Thermodynamic Modeling of Oxidation of Tin Nanoparticles. *J. Phase Equilib. Diffus.* **2019**, *40*, 10−20.

(34) Tu, K. N. Irreversible processes of spontaneous whisker growth in bimetallic Cu-Sn thin-film reactions. *Phys. Rev. B: Condens. Matter Mater. Phys.* **1994**, *49*, 2030−2034.

(35) Togo, A.; Oba, F.; Tanaka, I.; Tatsumi, K. First-principles calculations of native defects in tin monoxide. *Phys. Rev. B: Condens. Matter Mater. Phys.* **2006**, *74*, 195128.

(36) Kim, S.-H.; Lee, S. H.; Park, J.-W.; Roh, T. M.; Suh, D. In situ implementation of silicon epitaxial layer on amorphous SiO2 using reduced-pressure chemical vapor deposition. *Appl. Mater. Today* **2021**, *24*, 101143.

(37) Giles, M. D. Transient Phosphorus Diffusion Below the Amorphization Threshold. *J. Electrochem. Soc.* **1991**, *138*, 1160−1165.

(38) Wilson, W. D.; Baskes, M. I.; Bisson, C. L. Atomistics of helium bubble formation in a face-centered-cubic metal. *Phys. Rev. B: Solid State* **1976**, *13*, 2470−2478.

(39) Evans, J. The role of implanted gas and lateral stress in blister formation mechanisms. *J. Nucl. Mater.* **1978**, *76−77*, 228−234.

(40) Trinkaus, H. Energetics and formation kinetics of helium bubbles in metals. *Radiat. Eff.* **1983**, *78*, 189−211.

(41) Donnelly, S. E. The density and pressure of helium in bubbles in implanted metals: A critical review. *Radiat. Eff.* **1985**, *90*, 1−47.

(42) Nietiadi, M. L.; Sandoval, L.; Urbassek, H. M.; Möller, W. Sputtering of Si nanospheres. *Phys. Rev. B: Condens. Matter Mater. Phys.* **2014**, *90*, 045417.

(43) Ziegler, J. F.; Biersack, J. P.; Ziegler, M. D. SRIM—The Stopping and Range of Ions in Matter. *Nucl. Instrum. Methods Phys. Res., Sect. B* **2008**, *268*, 1818.

(44) Strobel, M.; Heinig, K.-H.; Möller, W. Three-dimensional domain growth on the size scale of the capillary length: Effective growth exponent and comparative atomistic and mean-field simulations. *Phys. Rev. B: Condens. Matter Mater. Phys.* **2001**, *64*, 245422.

(45) Mukherjee, D.; Joshi, K. D.; Gupta, S. C. Pressure induced phase transition in tin:Ab-initiocalculations. *J. Phys.: Conf. Ser.* **2010**, *215*, 012106.

(46) Rosato, V.; Guillope, M.; Legrand, B. Thermodynamical and structural properties of f.c.c. transition metals using a simple tight-binding model. *Philos. Mag. A* **1989**, *59*, 321−336.

(47) Eckold, P.; Sellers, M.; Niewa, R.; Hügel, W. The surface energies of β-Sn — A new concept for corrosion and whisker mitigation. *Microelectron. Reliab.* **2015**, *55*, 2799−2807.

(48) Bernas, H.; Attané, J.-P.; Heinig, K.-H.; Halley, D.; Ravelosona, D.; Marty, A.; Auric, P.; Chappert, C.; Samson, Y. Ordering Intermetallic Alloys by Ion Irradiation: A Way to Tailor Magnetic Media. *Phys. Rev. Lett.* **2003**, *91*, 077203.

(49) Lowe, D. G. Distinctive Image Features from Scale-Invariant Keypoints. *Int. J. Comput. Vis.* **2004**, *60*, 91−110.

(50) Schneider, C. A.; Rasband, W. S.; Eliceiri, K. W. NIH Image to ImageJ: 25 years of image analysis. *Nat. Methods* **2012**, *9*, 671−675.

nature communications

Flexomagnetism and vertically graded Néel temperature of antiferromagnetic Cr$_2$O$_3$ thin films

Pavlo Makushko[1,8], Tobias Kosub[1,8], Oleksandr V. Pylypovskyi [1,2]✉, Natascha Hedrich[3], Jiang Li[1], Alexej Pashkin [1], Stanislav Avdoshenko[4], René Hübner [1], Fabian Ganss[1], Daniel Wolf [5], Axel Lubk [5,6], Maciej Oskar Liedke [7], Maik Butterling [7], Andreas Wagner [7], Kai Wagner[3], Brendan J. Shields[3], Paul Lehmann[3], Igor Veremchuk[1], Jürgen Fassbender [1], Patrick Maletinsky [3] & Denys Makarov [1]✉

Antiferromagnetic insulators are a prospective materials platform for magnonics, spin superfluidity, THz spintronics, and non-volatile data storage. A magnetomechanical coupling in antiferromagnets offers vast advantages in the control and manipulation of the primary order parameter yet remains largely unexplored. Here, we discover a new member in the family of flex-effects in thin films of Cr$_2$O$_3$. We demonstrate that a gradient of mechanical strain can impact the magnetic phase transition resulting in the distribution of the Néel temperature along the thickness of a 50-nm-thick film. The inhomogeneous reduction of the antiferromagnetic order parameter induces a flexomagnetic coefficient of about 15 μ_B nm^{-2}. The antiferromagnetic ordering in the inhomogeneously strained films can persist up to 100 °C, rendering Cr$_2$O$_3$ relevant for industrial electronics applications. Strain gradient in Cr$_2$O$_3$ thin films enables fundamental research on magnetomechanics and thermodynamics of antiferromagnetic solitons, spin waves and artificial spin ice systems in magnetic materials with continuously graded parameters.

A standard micromagnetic approach for the description of thin films relies on the effective parameters being homogeneously distributed along the film thickness. Accounting for the magnetomechanical coupling makes the picture more complex, yet promises technological advantages: the cross-coupling between elastic, magnetic and electric subsystems opens additional degrees of freedom in the control of the respective order parameters[1–3]. The family of magnetomechanical effects includes piezo- and flexomagnetic responses, which determine the modification of the magnetic order parameter(s) due to

homogeneous or inhomogeneous strain, respectively. Piezomagnetic effects are well addressed in literature both for ferro- and antiferromagnetic materials including emergent anisotropy of material parameters when samples are exposed to uniaxial strain[4], change of material parameters in samples of different thickness[5], magnetoelasticity[6], transport effects in homogeneously strained films[7]. Despite the fact that flexomagnetism[8–13] is allowed for in the majority of bulk magnetic classes and enforced by boundaries[14], it is hardly addressed in the literature compared to the case of

[1]Helmholtz-Zentrum Dresden-Rossendorf e.V., Institute of Ion Beam Physics and Materials Research, 01328 Dresden, Germany. [2]Kyiv Academic University, 03142 Kyiv, Ukraine. [3]Department of Physics, University of Basel, 4056 Basel, Switzerland. [4]Institute for Solid State Research, Leibniz Institute for Solid State and Materials Research Dresden, 01069 Dresden, Germany. [5]Leibniz Institute for Solid State and Materials Research, IFW Dresden, Helmholtzstr. 20, 01069 Dresden, Germany. [6]Institute of Solid State and Materials Physics, TU Dresden, 01069 Dresden, Germany. [7]Helmholtz-Zentrum Dresden-Rossendorf e.V., Institute of Radiation Physics, 01328 Dresden, Germany. [8]These authors contributed equally: Pavlo Makushko, Tobias Kosub. ✉e-mail: o.pylypovskyi@hzdr.de; d.makarov@hzdr.de

piezomagnetism[15–19]. This situation is surprising considering that flexomagnetism is relevant for multiferroics and antiferromagnets, where magnetomechanical couplings lead to the control of the anisotropy and spontaneous magnetization[20–22]. Flexomagnetism can be found in magnets of 69 out of 90 bulk symmetry classes[14]. This includes the lowest symmetry groups 1 and $\bar{1}$ (54 nontrivial independent tensor components out of 81), which makes flexomagnetism to be readily expected even in Permalloy[10]. A higher symmetry of the lattice reduces number of independent components of the flexomagnetic tensor, e.g., leaving 10 independent components among 37 non-trivial ones for crystals of $\bar{3}'m'$ symmetry, or 5 independent components among non-trivial 18 ones for $\bar{6}'m2'$ crystals (e.g., ThMn$_2$). Lowering the symmetry at the surface allows the flexomagnetic effect in 19 surface magnetic classes, e.g., $(0\bar{1}10)$ surface cut of CrSb, which belongs to $6'/m'mm'$ bulk class[14].

The current understanding of the physics of flexomagnetism is limited to the prediction of the emergent ferromagnetic order parameter in the interior of an inhomogeneously strained antiferromagnetically ordered material. It is to be expected that the presence of the flexomagnetism-induced spontaneous ferromagnetic moment can provide novel but as-of-yet unexplored means for the manipulation of the antiferromagnetic order parameter, which could open new avenues for the design of non-volatile memory[23–25]. The fundamental understanding of the impact of flexomagnetism on thermodynamics of magnetic materials, as well as spin-reorientation and phase transitions, is missing at the moment. This lack in the fundamental knowledge of magnetomechanics in antiferromagnetic oxides hinders their application in prospective low-energy and high speed spintronic and spinorbitronic devices.

Here, we discover the presence of unconventional flexomagnetic effects in Cr$_2$O$_3$. Usually, flexomagnetism results in the magnetic moment induced by the strain gradient. For Cr$_2$O$_3$, we estimate this contribution to be 12 μ_B nm^{-2} for the unit strain gradient. In contrast, we demonstrate another mechanism in the family of flexomagnetic effects, which originates in the impact of the strain gradient on thermodynamic properties, namely on the Néel temperature. The presence of the gradient of the Néel temperature across the thickness of Cr$_2$O$_3$ films results in an induced magnetic moment per unit strain gradient as high as 15 μ_B nm^{-2}. The distinct feature of this induced moment is that it follows the direction of the Néel vector. By combining magnetotransport and Nitrogen vacancy (NV) microscopy characterization data, we experimentally determine the presence of the gradient of the Néel temperature in 30-nm and 50-nm-thick Cr$_2$O$_3$ thin films. Accessing this magnetization is crucial for the proper description of the physics of antiferromagnetic solitons, including domain walls, skyrmions, and disclinations. In addition to these fundamental discoveries, we show that the inhomogeneously strained Cr$_2$O$_3$ thin films can have magnetic transition temperature of about 100 °C, which is about 60 °C higher than the transition temperature of the bulk Cr$_2$O$_3$. Due to good oxide-oxide heteroepitaxy, the Néel temperature in Cr$_2$O$_3$ thin films can be enhanced persistently and no sign of degradation of the Néel temperature is observed after 1.5 years. The physics discussed here is not specific to the Cr$_2$O$_3$. Based on the crystal symmetry and on the magnetic symmetry groups, this effect should also be observable in other relevant antiferromagnetic samples including CuMnAs and Mn$_2$Au. In this respect, the results of our work motivate further research on antiferromagnetic thin films, where magneto-mechanical coupling can play a key role in the design of material and device responses for ultrafast spintronics and magnonics[26–28] and applications in data storage[23,24,29].

Results

Inhomogeneously strained thin films

We prepared a series of Cr$_2$O$_3$ thin films of different thickness ranging from 30 to 250 nm on $(0\,0\,0\,1)$ oriented Al$_2$O$_3$ substrates using magnetron sputtering (Supplementary Fig. 1). The samples are capped with a Pt layer to enable magnetotransport characterization (Fig. 1a). Regardless of the film thickness, Cr$_2$O$_3$ samples adopt the same orientation as the substrate and exhibit excellent crystallinity (Supplementary Figs. 2–8). Due to a wide deposition angle of the magnetron sputter source, the Cr$_2$O$_3$ films are dense and smooth (Supplementary Note 1, Supplementary Figs. 2–6). This is a major difference with respect to prior studies focused on thermally evaporated thin films[24,30], featuring columnar growth with clear grain boundaries going through the entire film thickness. The real space structure of the films is shown in the transmission electron microscopy (TEM) images in Fig. 1b,c for a 30-nm-thick film (Supplementary Figs. 4 and 5). A high-resolution TEM image (Fig. 1c) reveals that the misfit dislocations in such thin Cr$_2$O$_3$ films form several nanometers away from the interface with the Al$_2$O$_3$ substrate, leaving a significant amount of the film in a highly strained state that is pseudomorphic to Al$_2$O$_3$. The presence of the pseudomorphic Cr$_2$O$_3$ layer with a thickness of about 5 nm is also evidenced by the X-ray diffraction (XRD) characterization of 30- and 50-nm-thick samples (Supplementary Note 2, Supplementary Figs. 9–14). Thicker films do not reveal the presence of a pseudomorphic layer, but approach the bulk values of the lattice parameters (Supplementary Figs. 15–19).

Considering the absence of grain boundaries in the thin samples (Supplementary Note 1), we identify that the dominant strain relaxation mechanism in our samples is due to vacancy formation, their agglomeration and misfit dislocations. To access open volume defects, we perform the positron annihilation spectroscopy (PAS), revealing a change in the prevailing defect type from monovacancy-dislocation complexes to independent dislocations with the increase in the film thickness from 30 to 250 nm (Supplementary Note 3, Supplementary Figs. 20, 21). The size of the vacancy clusters at the top and bottom regions of the Cr$_2$O$_3$ film, which is linked to the measured positron annihilation time τ_2 (Supplementary Fig. 22, Supplementary Table 1), decreases for thicker films suggesting decrease in strain (Fig. 1d). The size of agglomerated vacancies is found to be substantially smaller in the bottom part of the film compared to the top region. The difference between the vacancy cluster size at the top and bottom regions (nVac), normalized to the film thickness (t), can be used as a qualitative measure of the strain gradient in the film. These data are shown in Fig. 1e, suggesting a sizable strain gradient in 30-nm- and 50-nm-thick Cr$_2$O$_3$ films (Supplementary Fig. 23).

We utilize the c/a ratio of the out-of-plane (c) and in-plane (a) lattice parameters as a measure of strain in Cr$_2$O$_3$ films. The lattice parameters averaged over the entire film thickness (Fig. 1f–h) are quantified relying on the analysis of the XRD data (Supplementary Note 2) and Raman spectroscopy characterization (Supplementary Note 4, Supplementary Figs. 24, 25). The thin film samples have developed compressive in-plane strain and show an extended c-axis. XRD data provide insights into the strain distribution along the thickness of the Cr$_2$O$_3$ film (Supplementary Note 2, Supplementary Figs. 10, 12–14, 16, 18). With increasing distance from the substrate, the strain gradually relaxes, resulting in a strain gradient along the film thickness, i.e. along the direction normal to the film interface (Fig. 1i, j, Supplementary Table 2 and Supplementary Fig. 26).

Strain modifies magnetic and thermodynamic properties of Cr$_2$O$_3$[16,19,31]. To evaluate the impact of the strain and strain gradient on the Néel temperature in thin films of sputter-deposited Cr$_2$O$_3$, we apply two complementary experimental methods. The Néel temperature at the top surface of the films, T_N^{top}, is assessed using magnetotransport measurements (Fig. 2). By monitoring the temperature evolution of the antiferromagnetic domain pattern using nitrogen vacancy (NV) scanning magnetometry, we evaluate the Néel temperature of the interior of the Cr$_2$O$_3$ films (Fig. 3).

Magnetic state of the top surface

To assess the surface Néel temperature, we measure the transverse resistance of the Pt electrode (R_{Tr}) using the Zero-Offset Hall technique[24,32] (Supplementary Note 5). This property is modified by the magnetic state of the underlying Cr_2O_3 as a result of the transverse spin Hall magnetoresistance, which is a local probe of the magnetic ordering in the sample area adjacent to the Pt electrode[33–36]. Figure 2a, b shows the dependence of the transverse resistance on the out-of-plane applied magnetic field H, $R_{Tr}(H,T)$, for Cr_2O_3 thin film samples at selected temperatures (see also Supplementary Fig. 27): below (blue) and above (red) the transition temperature and in its vicinity (green). The $R_{Tr}(H,T)$ contains the

temperature dependent contribution from the antiferromagnetic Cr_2O_3 ($R_0(T)$, Supplementary Fig. 28), which we determine based on the $R_{Tr}(H,T)$ data (Fig. 2a). $R_0(T)$ is used for the evaluation of the Néel temperature at the top surface T_N^{top} (Supplementary Note 5, Supplementary Figs. 29, 30), see Fig. 2c. For the 30-nm-thick film, T_N^{top} is estimated to be higher than 75 °C (Fig. 2d). This is a major increase in the Néel temperature compared to the bulk value of Cr_2O_3, which is measured on a single crystal to be 35 °C (Fig. 2c, d). Thin films with a thickness of 250 nm reveal a Néel temperature similar to the single crystal value, confirming the relaxed state of the sample. The enhancement of the Néel temperature correlates with the average strain in the samples and is in line with earlier theoretical
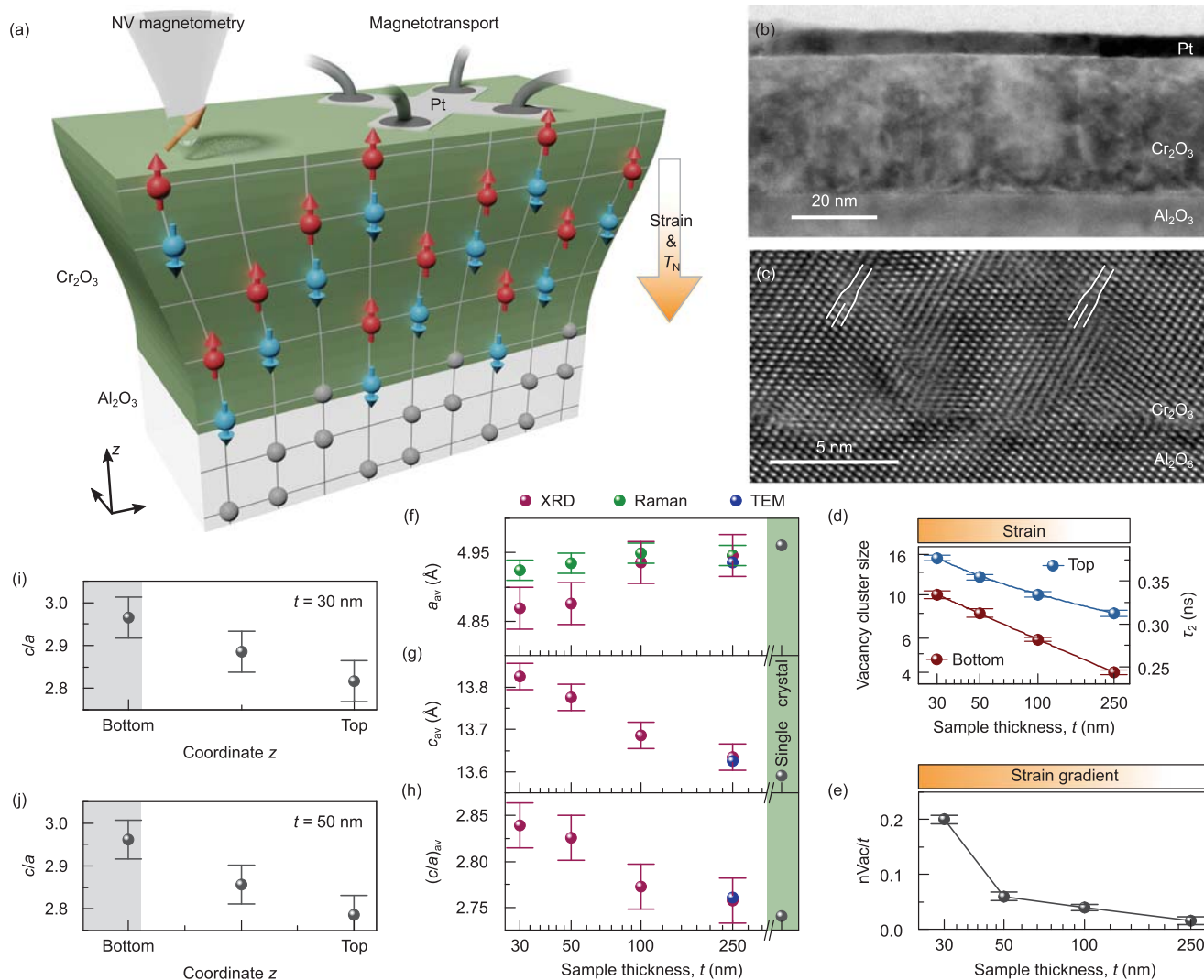
Fig. 1 | Thin films of Cr_2O_3 with a strain gradient. a Schematic of a Cr_2O_3 thin film prepared on a Al_2O_3 substrate. The film experiences a strain gradient along its thickness that leads to a gradient of the Néel temperature. The Néel temperature at the top surface is probed via magnetotransport relying on the transversal spin Hall magnetoresistance in a Pt electrode adjacent to the Cr_2O_3 film. The Néel temperature in the interior of the film is probed via NV magnetometry. **b** Cross-sectional bright-field TEM image showing the $Al_2O_3/Cr_2O_3/Pt$ stack for a 30-nm-thick sample. The sample does not reveal the presence of grain boundaries (see also Supplementary Note 1). **c** High-resolution TEM of the Al_2O_3/Cr_2O_3 interface. Two misfit dislocations are indicated in white. The dislocations are located about 5 nm away from the Al_2O_3/Cr_2O_3 interface. **d** Positron lifetime component τ_2 and the corresponding calculated vacancy cluster size (assuming spherical geometry) in the top and bottom regions of the Cr_2O_3 films of different thickness t. The vacancy cluster size increases for thinner samples, indicating larger strain. Error bars

correspond to the standard deviations of the fit. **e** The gradient of the vacancy cluster size along the film thickness (nVac/t) for the samples of different thickness. This parameter is a qualitative measure of the strain gradient across the sample thickness. The error bars correspond to the standard deviations of the fit. Average values of the in-plane (a; (**f**)) and out-of-plane (c; (**g**)) lattice parameters and the respective c/a ratio (**h**) estimated based on the XRD, Raman spectroscopy and TEM measurements of Cr_2O_3 samples of different thickness. Error bars of the lattice parameters obtained from XRD and Raman measurements are estimated from instrumental precision of the diffractometer and from the uncertainty of the Raman spectra peak fitting accordingly.(**I, j**) Change of the c/a ratio along the film thickness estimated for the 30-nm-thick (**i**) and 50-nm-thick (**j**) samples. The c/a ratio for the pseudomorpic layer is highlighted with the gray background. Error bars of the lattice parameters are estimated from instrumental precision of the diffractometer and from the uncertainty of the peak fitting.
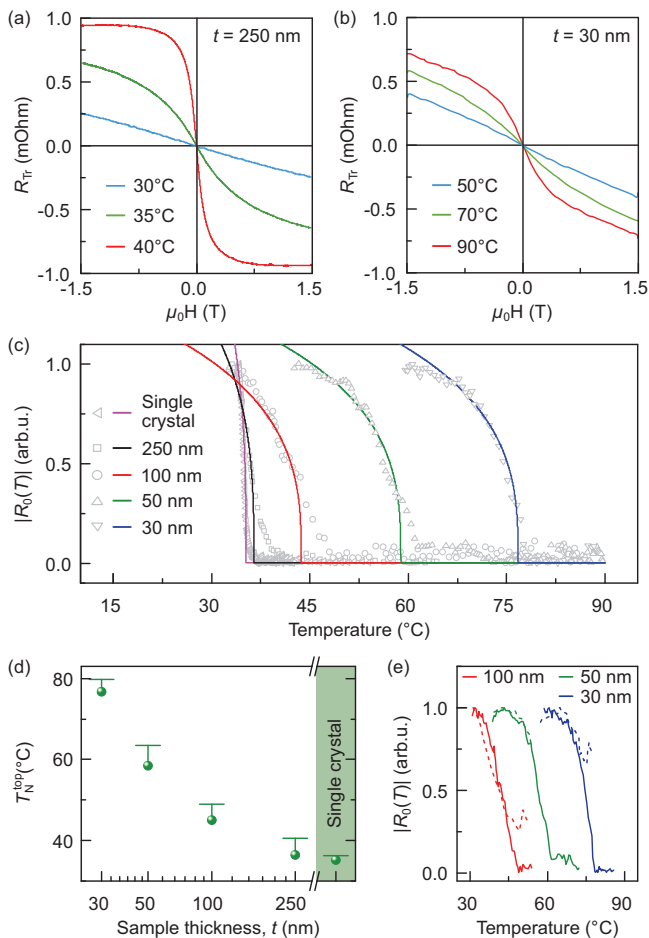
Fig. 2 | Assessment of the Néel temperature T_N^{top} at the top surface of Cr_2O_3 films. a, b Transverse resistance R_{Tr} of the Pt electrode vs out-of-plane magnetic field at temperatures below (blue), in the vicinity of (green) and above (red) the phase transition to the paramagnetic state for the samples of different thicknesses. **c** Temperature dependence of the antiferromagnetic contribution from the Cr_2O_3 (Supplementary Note 5) is shown with symbols. The fit used to determine the Néel temperature at the top surface of the sample is shown with solid lines. **d** Top surface Néel temperature T_N^{top} vs sample thickness. The Néel temperature measured on a single crystal is shown as well. Error bars arise from the smooth decay of the $|R_0(T)|$ to the noise level in the vicinity of antiferromagnet-paramagnet transition. **e** Temperature evolution of the antiferromagnetic contribution from the Cr_2O_3 taken right after sample fabrication (dashed lines) and after 18 months (solid lines).

predictions[16,19,31]. Because the lateral strain relaxation is suppressed in sputter-deposited samples, they are persistently strained, assuring a long-term enhancement of the Néel temperature. This is evidenced by the close-to-identical magnetotransport responses taken directly following the sample fabrication and 18 months later (Fig. 2e, Supplementary Fig. 31).

Magnetic state of the Cr_2O_3 films interior

We utilize NV magnetometry to assess the transition temperature within the interior of the films by following the temperature-induced decay of the magnetic contrast from the antiferromagnetic domain pattern, i.e., difference $\widetilde{B}$ between the strength of stray fields measured within oppositely magnetized domains. This approach is similar to the detection of the Néel temperature using X-ray magnetic linear dichroism (XMLD) contrast in in-plane metallic antiferromagnets[37-40]. For the case of strain-free (250-nm-thick film, Supplementary Fig. 32) and strained (100-nm-thick film, Supplementary Fig. 33) samples, the

domain pattern in NV measurements disappears at temperatures similar to the Néel temperatures determined in magnetotransport studies, see Fig. 3a, b. We note that the surface and interior Néel temperatures assessed by magnetotransport and NV magnetometry do agree for the case of the strain-free Cr_2O_3 single crystal[29] and for thermally evaporated thin films[30]. In contrast, in thin-film samples with an inhomogeneous strain (50- and 30-nm-thick films, Supplementary Figs. 34, 35, respectively, see also Supplementary Figs. 5, 23 and Supplementary Note 1), the domain contrast remains clearly visible even at $T \gtrsim 85$ °C, see Fig. 3c, d. This is the highest temperature accessible in the setup. Thus, the Néel temperature measured with NV magnetometry is substantially larger than the respective value of T_N^{top} (Supplementary Fig. 36). The observed difference in the transition temperature measured with the two methods is evidence for the gradient of the Néel temperature along the film thickness that arises from the inhomogeneous strain distribution (Fig. 1a, g, h, Supplementary Fig. 23).

Flexomagnetism of Cr_2O_3 thin films

The discussion above suggests that gradient of the strain tensor $u_{ij}(z)$, where z is the coordinate along the sample thickness, can impact antiferromagnetic materials not only via the emergence of ferromagnetism[14], but also by influencing the distribution of the transition temperature $T_N[u_{ij}(z)]$ along the thin film's thickness. This effect was not addressed before. For the phenomenological analysis, we assume that the strain varies linearly along the film thickness, $u_{ij} = u_{ij}^0 + w_{ij}z$ with u_{ij}^0 being the base level of strain and w_{ij} being the strain gradient. In line with the study by Kota et al. [16] and multiscale modeling (Supplementary Note 6), this leads to a linear coordinate dependence of the Néel temperature $T_N(z) = T_N^{top} + \zeta \times (t - z)$, where ζ parameterizes the strain distribution in the film (Fig. 1i, j). In the vicinity of the antiferromagnet-paramagnet phase transition, the gradient of $T_N(z)$ enables a fundamentally new type of ferromagnetic contribution, which originates from the local variation of the length of the sublattice magnetization at $T = const$, $\mathbf{M}_\zeta \propto \partial \mathbf{L}[T/T_N(z)]/\partial z$ (Supplementary Note 7, Supplementary Figs. 37, 38). This leads to the following form of the total flexomagnetic effect close to the phase transition $M = \mu \times \partial u/\partial z$, where $u = \langle u_{ij} \rangle$ is the average strain, $\mu = \mu^g + \mu^\zeta$ is the flexomagnetic coefficient. The first term, $\mu^g \sim 10$ μ_B nm^{-2}, originates from the gradient of g-tensor components due to the strain gradient (Supplementary Note 6, Supplementary Fig. 39). It leads to a constant magnetization along z in 50- and 30-nm-thick Cr_2O_3 films, independent of the orientation of the Néel vector in antiferromagnetic domains. The second term, μ^ζ, is responsible for the appearance of $\mathbf{M}_\zeta$ with the spatial distribution following the order parameter $\mathbf{L}$ (Supplementary Note 7, Supplementary Fig. 38).

To perform quantitative estimations of the Néel temperature distribution and μ^ζ, we access the ferromagnetism of the sample (Supplementary Note 7) relying on the analysis of the strength of stray fields measured using NV magnetometry. The uncompensated surface spins (Supplementary Fig. 40) constitute the dominant contribution to the stray fields, and are linked to the direction of $\mathbf{L}$ in antiferromagnetic domains[29,30,41]. We model the strength of measured stray fields as a sum of contributions from the top and bottom film surfaces, complemented by $\mathbf{M}_\zeta$. The fit of the experimental data (Fig. 3b, d) then allows for an estimate of the transition temperature at the bottom interface, T_N^{bot} (Supplementary Table 3). For the sample with a thickness of 100 nm, we find that $T_N^{bot} \approx T_N^{top}$. This is an expected behavior for thicker samples, as they do not reveal the presence of pseudomorphic layer or sizable strain gradient along the thickness. For the inhomogeneously strained film with the thickness of 50 nm, T_N^{bot} is estimated to be about 100 °C, which is substantially higher than T_N^{top} of 59 °C. This analysis leads to a value of μ^ζ on the order of 15 μ_B nm^{-2} at $T = 20$ °C.
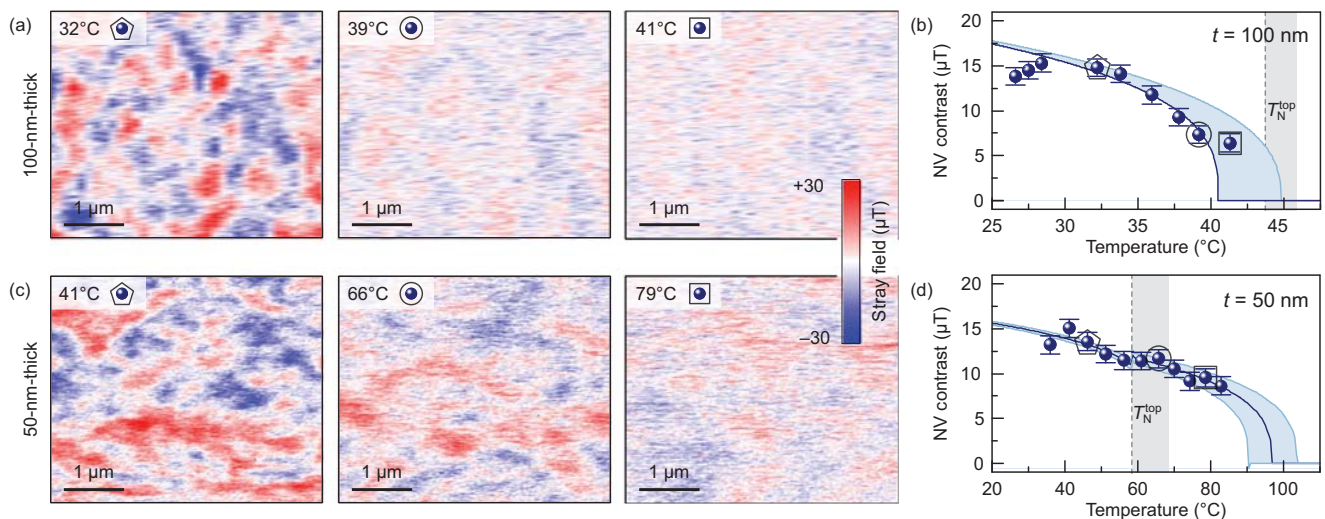
Fig. 3 | Néel temperature of the interior of thin Cr$_2$O$_3$ films. Temperature evolution of the antiferromagnetic domain pattern measured using NV magnetometry of (**a**) 100-nm-thick and (**c**) 50-nm-thick Cr$_2$O$_3$ samples. The strength of the measured stray fields decays upon approaching the transition temperature. Estimation of the phase transition temperature at the bottom interface, T_N^{bot}, of the (**b**) 100-nm-thick and (d) 50-nm-thick samples. The blue-shaded region in (**b** and **d**) corresponds to the uncertainty in the determination of the T_N^{bot}. The Néel temperature measured at the top surface via magnetotransport (Fig. 2) is shown for comparison in (**b** and **d**). A gray-shaded region indicates the uncertainty in the determination of the T_N^{top}. For the 50-nm-thick sample, a clear domain contrast is present even at temperature, which substantially higher than T_N^{top}. The strength of the stray field for scans shown in (**a** and **c**) are highlighted in (**b** and **d**) with corresponding symbols and error bars correspond to the half-width of the distribution.

Vertically graded Néel temperature

The control of magnetic parameters of Cr$_2$O$_3$ via homogeneous strain (piezoeffect) is well established. In contrast, we demonstrate, that the flexomagnetic contribution is comparable in strength with the piezo-magnetism and enhances even further the operation temperature of the devices based on technologically relevant Cr$_2$O$_3$ thin films. Due to the gradient of the Néel temperature along the sample thickness, different slices of the thin film experience the magnetic phase transition at different temperatures. Schematics of the phase transition for an inhomogeneously strained Cr$_2$O$_3$ film are shown in Fig. 4a–c. Far below T_N^{top} (Fig. 4a), the length of the Néel vector L is almost the same along the entire sample thickness (brown curve in Fig. 4d). Approaching T_N^{top}, the antiferromagnetic order parameter at the top surface becomes smaller and eventually vanishes at T_N^{top} (Fig. 4b and red curve in Fig. 4d). At higher temperatures, the boundary between the antiferromagnetic and paramagnetic phases progresses towards the bottom surface of the Cr$_2$O$_3$ film (Fig. 4c and orange curve in Fig. 4d). The coexistence of para- and antiferromagnetic phases within the interior of the 50-nm-thick film is shown in Fig. 4e. We note that the continuously graded Néel temperature allows the magnetic nature of part of the film to be turned off and on.

Based on our results, the Néel temperature T_N of inhomogeneously strained Cr$_2$O$_3$ thin films consists of the following contributions (Fig. 4f, Supplementary Note 7). The first term in T_N is the bulk Néel temperature of Cr$_2$O$_3$ (green colored bar). The second contribution comes from the base level of strain u_{ij}^0 (orange colored bar). We note that to plot Fig. 4f, we set u_{ij}^0 to be equal to the smallest level of strain for each sample which is achieved at the top surface. This piezoeffect-driven increase in the Néel temperature determines T_N^{top} and can be as high as 20 °C, in line with earlier theoretical predictions[16,19] (Supplementary Fig. 41). The third contribution is related to the increase of strain towards the bottom film surface (blue shaded bar refers to the maximal strain in the film). Due to the slow relaxation of strain along the film thickness, we see the pronounced and continuous increase in the Néel temperature towards the bottom interface. This results in the further increase in the transition temperature, reaching a remarkable 100 °C for 30- and 50-nm-thick Cr$_2$O$_3$ films. We note that despite

higher transition temperatures estimated for the 30-nm-thick film (Fig. 4f), the flexomagnetic effect in this sample can be reduced in comparison with the 50-nm-thick one because of lower gradient at smaller thickness.

Discussion

In summary, we show that thin films of undoped Cr$_2$O$_3$ with inhomogeneously distributed strain possess a flexomagnetic response, which we probe by means of magnetotransport and NV scanning magnetometry measurements. The key enabler of the flexomagnetism is the proper design of the sample, revealing a persistent and pronounced strain gradient along the sample thickness, which is a result of (i) the chemical adhesion to the substrate due to the oxide-oxide hetero-epitaxy and (ii) a grain boundary-free growth of thin films realized through a large magnetron sputter source. The latter prevents the formation of the interfacial misfit dislocations and an excessive strain relaxation into grain boundaries during the cool-down process. We note that the effect is not specific to Al$_2$O$_3$ substrates. Any substrate, which is isostructural to Cr$_2$O$_3$ (like V$_2$O$_3$) and can provide coherent epitaxy for Cr$_2$O$_3$ thin films should enable the discussed here flex-omagnetic effect. In this respect, other substrates could offer further advantages. For instance, V$_2$O$_3$ is conducting and when growing Cr$_2$O$_3$ thin films can act as a gate enabling magnetoelectric characterization of the strained samples. Still, high miscibility of Cr$_2$O$_3$ and V$_2$O$_3$ should be be taken into account while preparing these samples.

From the fundamental point of view, our findings enable the experimental access to a subtle and still unexplored magnetomechanical coupling in thin films of antiferromagnetic insulator Cr$_2$O$_3$ but is also applicable for other antiferromagnetic materials including CuMnAs, Mn$_2$Au (magnetic symmetry group mmm') and NiO (magnetic symmetry group $2/m'$)[14]. Although the $\bar{3}'m'$ bulk symmetry of the Cr$_2$O$_3$ and its boundary (0 0 0 1) allow for flexomagnetic effects[14], they have never been addressed for this material. Still, flexomagnetic effect is not generic. For instance, it is not expected in other well studied antiferromagnetic materials Mn$_3$Ir ($\bar{3}m'$ magnetic symmetry group) and MnF$_2$ ($4'/mmm'$ magnetic symmetry group)[14]. A spatial change of the material parameters along the thickness of thin films raises

Article   https://doi.org/10.1038/s41467-022-34233-5
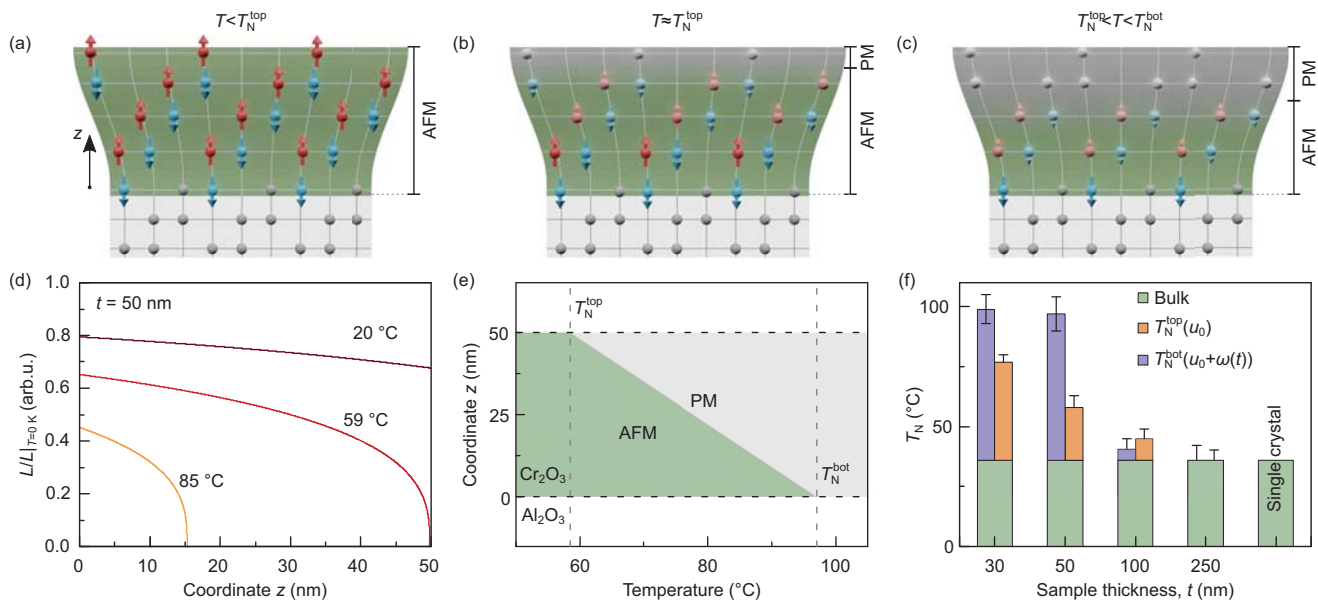
Fig. 4 | Impact of the strain gradient on the antiferromagnet-paramagnet phase transition in Cr₂O₃ thin films. a–c Schematics of the antiferromagnet-paramagnet phase transition. **a** At temperatures below T_N^{top}, the entire sample is antiferromagnetically ordered. **b** With the increase in temperature to about T_N^{top}, the less strained part of the sample (top region) undergoes a phase transition into the paramagnetic state. The bottom part of the sample remains antiferromagnetically ordered. **c** The portion of the sample in the ordered state is determined by the temperature. The sample turns into the paramagnetic state for $T > T_N^{bot}$. **d** The change of the length of the antiferromagnetic order parameter L along the film thickness for a 50-nm-thick Cr₂O₃ thin film. The brown/red/orange curves correspond to the states shown in (**a–c**), respectively. **e** The portion of the 50-nm-thick film, which remains in the antiferromagnetic state, dependent on the measurement temperature. In the temperature range between T_N^{top} and T_N^{bot}, only the part of the sample closer to the bottom interface remain in the ordered state. Green and gray shaded area represent regions in antiferromagnetic (AFM) and paramagnetic (PM) states, respectively. **f** Different contributions to the Néel temperature for Cr₂O₃ samples. The green shaded bar represents the bulk Néel temperature, which is measured for a single crystal and strain-free thin film (250-nm-thick in our study). The presence of a compressive strain in a Cr₂O₃ thin film leads to the increase in the Néel temperature. The value of T_N at the top surface ($z = t$) which is determined by the smallest strain u_0 is indicated by the orange shaded bar. T_N at the bottom surface (blue shaded bar) is larger according to the larger strain value $u_0 + wt$ at $z = 0$. Error bars on the T_N^{top} and T_N^{bot} correspond to uncertaininity of the fit of the magnetotransport and NV data, respectively.

questions about the applicability of the classical definition of the magnetic length as a universal characteristic of a magnetic thin film material. The community of high-resolution microscopies (X-ray- and electron-based techniques) can provide further unique insights into the spatially inhomogeneous antiferromagnet-paramagnet phase transition at the nanoscale, which can broaden our understanding of the physics of phase transitions in condensed matter. In addition to the spontaneous magnetization of flexomagnetic origin **M**, the symmetry of Cr₂O₃ allows a ferromagnetic moment to be produced by the gradient of the antiferromagnetic order parameter[14,42,43], for instance at the location of domain walls. This effect is not addressed in the present work, although we anticipate that NV magnetometry of thin films of Cr₂O₃ should be able to provide insight into this physics. Accessing this magnetization is crucial for the proper description of the physics of antiferromagnetic solitons, including domain walls, skyrmions, and disclinations[44,45]. Furthermore, our work poses questions on the magnetoelectric responses of these inhomogeneously strained thin films of Cr₂O₃. If confirmed experimentally, inhomogeneously strained magnetoelectric Cr₂O₃ thin films will become a game changer, enabling low-energy and high-speed spintronic and spin-orbitronic memory devices where magnetism is controlled by electric fields. The emergent flexomagnetism-driven ferromagnetic order parameter in antiferromagnetic thin films offers more flexibility in the design of spintronic and magnonic devices. In this respect, temperature becomes a useful tool for enabling the realization of reconfigurable racetracks and waveguides, given the unique possibility to deterministic turn off/on of the magnetism in less strained parts of the sample. For instance, a magnonic crystal can be designed as a stripe with modulated thickness. With the distribution of the Néel temperature along the stripe's normal, the relevant thickness of the magnetically

ordered interior of the sample can be controlled by temperature. The crystal's bandgap can be tuned, or its presence itself can be turned on or off by means of temperature. Furthermore, in contrast to statics, we anticipate that the magnetization of flexomagnetic origin should interact with spin waves in thin films due to the presence of stray fields[46–48]. Depending on the amplitude, it can be of relevance for spin Seebeck effect[49,50] and antiferromagnetic magnonics relying on antiferromagnetic insulators.

Methods
Sample preparation
Cr₂O₃ thin films were grown on *c*-cut single crystalline Al₂O₃(0001) substrates by RF magnetron sputtering (base pressure: below 10^{-7} mbar; Ar sputter pressure: 10^{-3} mbar; deposition rate: 1.72 nm min⁻¹; target size: 100 mm; sample to target separation: 10 cm) of a pure Cr₂O₃ target material (Robeko GmbH & Co. KG). Prior to the deposition of Cr₂O₃ the substrates were heated up to 750 °C for about 15 min to remove adsorbates from the surface and initiate the crystallization of Cr₂O₃ (Supplementary Fig. 1). Cr₂O₃ thin films of nominal thicknesses ranging from 30 to 250 nm were deposited at 700 °C. The high deposition temperature ensures a coherent epitaxial growth of Cr₂O₃ thin films. After the deposition, the substrate is cooled down by the heat dissipation through the sample mounting structure. The maximum cooling rate is 30 °C min⁻¹, resulting in a high level of thermally induced strain. To enable magnetotransport characterization, the samples were capped with a Pt layer in situ at room temperature (base pressure: 10^{-7} mbar; Ar sputter pressure: 8×10^{-4} mbar; deposition rate: 0.15 nm s⁻¹). A 1-mm-thick Cr₂O₃ single crystal (MaTecK, lattice parameters $a_0 = 4.96$ Å, $c_0 = 13.59$ Å) with (0 0 0 1) surface orientation was used as a reference sample. We note that the thickness of Pt capping

was different for Cr_2O_3 samples of different thickness: single crystal and 250-nm-thick Cr_2O_3 samples are capped with 3-nm-thick Pt; Cr_2O_3 films of other thickness are capped with 5-nm-thick Pt layer.

To address the absence of finite size effects in Cr_2O_3 samples with a thickness larger than 30 nm, we prepared an additional 15-nm-thick sample following the same growth protocol as discussed above. Due to the different criticality behavior (Supplementary Fig. 42), the 15-nm-thick Cr_2O_3 sample is not used for the analysis of the flexomagnetic effect and the flexomagnetism is discussed only for the samples with the thickness in the range between 30 and 250 nm.

The thickness of the Cr_2O_3 film affects the structural properties of the films due to a different strain state, which also affects the structure of the Al_2O_3/Cr_2O_3 interface. These two materials are isostructural with about 4% lattice mismatch within (0 0 0 1) plane. At the initial stages, Cr_2O_3 grows preudomorphically reproducing in-plane lattice parameters of the sapphire substrate. The pseudomorphic state is metastable. By forming this state, the chemical free energy competes with the strain free energy, which determines the critical thickness of the pseudomorphic layer[51]. During the growth, at some thickness of the film, it is energetically favorable to form dislocations, which are the limiting factor of the thickness of the pseudomorphic layer. Further, the film grows in non-pseudomorphic but highly strained state[52]. The location of the dislocation determines the thickness of the pseudomorphic layer (from the substrate to the plane with dislocations; Fig. 1 taken of a 30-nm-thick sample). With the increase in the total thickness of the Cr_2O_3 film, dislocations tend to diffuse towards the interface with the Al_2O_3 substrate. The pseudomorphic layer disappears when dislocations reach the interface with the substrate, while the coherent epitaxial relation of Cr_2O_3 and Al_2O_3 remains (Supplementary Fig. 2 taken of a 250-nm-thick sample).

The high-temperature high-field slope of R_{Tr} in Supplementary Fig. 27 is strongly dependent on the thickness of the Pt electrode. The reduction of the thickness of the Pt layer resulted in a decrease of χ_{Pt} contribution to the measured transversal resistance. We note that the change in slope due to the normal Hall effect in Pt does not change the conclusion about the phase transition temperature. Indeed, for our analysis of the Néel temperature, we subtract this linear contribution as it is not dependent on the transition temperature of Cr_2O_3.

We checked that our thin films do not have ferromagnetic signal as was reported in[51,53-55] (Supplementary Fig. 43).

Electron microscopy characterization

Cross-sectional bright-field and high-resolution TEM measurements were performed using an image-C_s-corrected Titan 80-300 microscope (FEI) operated at an accelerating voltage of 300 kV. High-angle annular dark-field scanning transmission electron microscopy (HAADF-STEM) imaging combined with spectrum imaging analysis based on energy-dispersive X-ray spectroscopy (EDX) were performed at 200 kV with a Talos F200X microscope equipped with an X-FEG electron source and a Super-X EDX detector system (FEI). Prior to (S)TEM analysis, the specimen was mounted in a double-tilt low-background holder and placed for 8 s into a Model 1020 Plasma Cleaner (Fischione) to remove possible contaminations. Classical TEM cross-sections, glued together in face-to-face geometry using G2 epoxy glue (Gatan), were prepared by sawing (Wire Saw WS 22, IBS GmbH), grinding (MetaServ 250, Bühler), polishing (Minimet 1000, Bühler), dimpling (Dimple Grinder 656, Gatan), and final Ar ion milling (Precision Ion Polishing System PIPS 691, Gatan). The TEM study was applied to understand the mechanism behind the persistent strain in magnetron-sputter-deposited Cr_2O_3 thin films and to confirm the high quality and coherent epitaxy of Cr_2O_3 thin films (Supplementary Note 1, Supplementary Fig. 2-6). TEM imaging revealed sharp and high-quality interfaces of Cr_2O_3 with the Al_2O_3 substrate and the Pt electrode. Fast Fourier transformation performed at the region of the Cr_2O_3/Al_2O_3 interface confirmed the coherent epitaxial growth of the thin films on Al_2O_3 (Supplementary Figs. 3a, b and 5a, 6a, b for the 250-nm-thick and 30-nm-thick films, respectively). Furthermore, EDX analysis confirmed the phase purity of the thin films and the absence of intermixing at the Cr_2O_3/Pt and Cr_2O_3/Al_2O_3 interfaces (Supplementary Figs. 3c, d and 6c, d for the 250-nm-thick and 30-nm-thick films, respectively).

High-resolution scanning TEM (HR-STEM) was performed on an FEI Titan[3] 80–300 probe-corrected instrument (ThermoFisher Company, US) operated at 300 kV. To this end, scan images were recorded with a high-angle annular dark-field (HAADF) detector at a camera length of 115 mm (collection angle 40–200 mrad) and a probe semi-convergence angle of 21.5 mrad.

X-ray diffraction analysis

XRD studies were carried out using a Rigaku SmartLab 3 kW with a parallel beam of Cu-$K_{\alpha 1}$ radiation, $\lambda = 1.54056$ Å (using a Ge (2 2 0) two-bounce monochromator). The reflection positions obtained by the profile deconvolution were corrected using the Al_2O_3 substrate. Lattice parameter refinement was performed with WinCSD[56].

Raman spectroscopy

The Raman measurements were performed using a JY Horiba LabRAM HR Evolution Raman Spectrometer in the backscattering geometry. The excitation wavelength was 532 nm. The power of the incident beam was <1 mW. The radiation was focused and collected by a $100 \times$ long working distance objective and the laser spot size was around 2 μm. The Rayleigh length for the beam divergence in the microscope is about 5 μm. As this is about 20 times larger than the thickness of our thickest film, we do not expect inhomogenieties along the film thickness. Besides multiple sharp peaks from the Al_2O_3 substrate, the Raman spectra of the Cr_2O_3 films are dominated by three relatively broad peaks (Supplementary Figs. 24, 25). The Cr_2O_3 spectra were fitted using a set of Lorentzian functions to obtain the phonon frequency dependence on the sample thickness. The variation of the lattice parameter has been estimated by comparing the observed phonon frequencies with literature data on pressure-induced phonon shift and the lattice compression[57]. All three phonon peaks demonstrate the frequency shift corresponding to the lattice compression. This agrees with the fact that the eigenvectors of the observed Raman-active phonons mainly involve the in-plane motion of the ions[58]. Correspondingly, they are mostly affected by the *in-plane compressive strain* of the Cr_2O_3 films. Using the XRD data on the strain-induced deformation and the pressure-induced shift of Raman modes[57], we estimate the variation of the averaged in-plane unit cell parameter a_{av} with film thickness (Fig. 1f). We note that if the growth morphology results in a non-uniform strain, that produces a shoulder in the Raman peak. This behavior is well established for semiconductor nanostructures, see e.g. Bernardi et al. [59] for the case of Ge nanodots.

Positron annihilation spectroscopy

Being implanted at a well-defined depth in the sample, positrons annihilate with electrons after localization in vacancy-like defects and their agglomerations (the so-called vacancy clusters or complexes; here voids) allowing for depth and concentration-dependent defect microstructure analysis. The positron annihilation lifetime experiments were carried out at the mono-energetic positron spectroscopy (MePS) beamline, the end station of the radiation source ELBE (Electron Linac for beams with high Brilliance and low Emittance) at HZDR[60]. Signals were processed by a digital data acquisition system using a $CrBr_3$ scintillator detector coupled to a Hamamatsu R13089-100 photomultiplier tube. The data were analyzed using a custom software rooted at a SPDevices ADQ14DC-2X digitizer with 14 bit vertical resolution and 2 GS s^{-1} horizontal resolution[61]. The overall measurement time resolution was not worse than 0.21 ns. A typical lifetime spectrum $N(t)$ is described by $N(t) = \sum (1/\tau_i) I_i \exp(-t/\tau_i)$, where τ_i and

I_i are the positron lifetime and relative intensity of the i-th component, respectively ($\sum I_i = 1$). All the spectra were deconvoluted using the non-linearly least-squared based package PALSfit fitting software[62] into three discrete lifetime components, which provides evidence for two different defect types and a surface ortho-Positronium annihilation state. The second lifetime component τ_2, representing vacancy agglomeration, is shown in Fig. 1d. The resolution function utilized for the spectrum analysis required two Gaussian functions with distinct intensities and shifts depending on the positron implantation energy E_p. All spectra contained at least 10^7 counts. Further discussion on the positron annihilation spectroscopy studies is in Supplementary Note 3, see also Supplementary Fig. 20,21 and Supplementary Table 1. Theoretical calculations of positron lifetimes for the delocalized states (bulk lifetime) and for positrons trapped at defects states were obtained using the atomic superposition (ATSUP) method within two-component density functional theory (DFT) ab initio calculations[63]. For the electron-positron correlation, the generalized gradient approximation (GGA) scheme was used[64]. The calculated positron lifetimes corresponding to specific spherical-shaped void sizes (vacancy cluster sizes) are plotted in Supplementary Fig. 22.

Magnetotransport measurements

Magnetotransport is a well-established technique to determine the phase transition temperature[65-68]. According to Wang et al. [69], the spin decay length in typical antiferromagnetic insulators including Cr_2O_3 is less than 10 nm (for Cr_2O_3 the spin decay length might be even smaller in the range of several nm only). This provides the upper bound on the depth from which we collect the information in the magnetotransport studies. Due to this surface sensitivity of the method, we refer to the transition temperature measured via magnetotransport as to the one measured at the top surface of the Cr_2O_3 film, T_N^{top}. We measured the magnetic field dependence of the transverse resistance, $R_{Tr}(H,T)$, of a Pt thin film deposited on Cr_2O_3 samples. The magnetotransport measurements were carried out using the Zero-Offset Hall preset of a Tensormeter measurement device[70], which provides the absolute transverse resistance without any offset due to undetermined sample geometry. Typical current amplitudes were on the order of 500 μA. For every sample, the $R_{Tr}(H,T)$ dependencies were measured for up to 100 different sample temperatures in the range from 15 °C up to 90 °C (this is the highest temperature, which is accessible in the setup), as shown in Fig. 2a, b and Supplementary Fig. 27. At low temperatures well in the antiferromagnetic state of the sample, the magnetic field dependence of the transversal resistance is a straight line. This behavior is given by the normal Hall effect of the Pt thin film (Supplementary Fig. 45). In the vicinity of the antiferromagnet-paramagnet transition temperature, the antiferromagnetic ordering is weakened and the contribution of the antiferromagnetic Cr_2O_3 to the measured transport signal becomes discernible (the slope of the $R_{Tr}(H,T)$ dependence taken at zero field increases). With further increase in the measurement temperature, the contribution from the Cr_2O_3 transforms the measured $R_{Tr}(H,T)$ dependence from a line to a Langevin-like function. By subtracting the normal Hall effect in Pt and the paramagnetic contribution from the Cr_2O_3 (Supplementary Note 5 and Supplementary Fig. 29), we access the temperature dependence of the contribution to the $R_{Tr}(H,T)$ from the antiferromagnetic Cr_2O_3. This is the $R_0(T)$ data shown in Fig. 2c. In a small temperature range close to the transition temperature, R_0 can be assumed to be proportional to the primary order parameter. Therefore, the dependencies $R_0(T)$ are used to determine the Néel temperature (Fig. 2c and Supplementary Fig. 29, 30, 42). Using this analysis method, we correctly capture the transition temperature of the single crystal to be 35 °C[71], see Supplementary Fig. 29a.

The $R_0(T)$ dependence for Cr_2O_3 thin films with the thickness of 30–250 nm can be described with the critical exponent $\beta \approx 0.3$, which is the same as for the reference Cr_2O_3 single crystal. This indicates the

absence of finite size effects in these samples. On the contrary, a 15-nm-thick sample reveals the critical exponent β of 0.67 (Supplementary Fig. 42), indicating the onset of finite size effects in this sample.

The magnetic polarization of Pt can be safely excluded from the consideration. In this respect, it is already established that Pt in proximity to antiferromagnetic insulators is not polarized[72-76]. This statement is also valid for Cr_2O_3/Pt interfaces, where it was experimentally confirmed that the measured transversal resistance is not an anomalous Hall effect but a spin-Hall magnetoresistance effect[35,77]. Here, we performed magnetotransport measurements of a 5-nm-thick Pt electrode deposited directly on a Al_2O_3 substrate (Supplementary Fig. 44). Besides a normal Hall effect due to paramagnetism of Pt, we do not observe any specific feature on the temperature and field dependence of the transversal resistance in the studied temperature range.

Alternatively, the change of the magnetic state at the Cr_2O_3/Pt interface can be detected by evaluating the change of the slope of the dependence $R_{Tr}(H=0,T)$. The transition of the $R_{Tr}(H=0,T)$ function from the linear to the Langevin-like shape upon the transition of the Cr_2O_3 to the paramagnetic state is accompanied by a pronounced change of the slope $\partial R_{Tr}/\partial H|_{H=0}$ at low (<100 mT) magnetic fields (see lines in Supplementary Fig. 45a). We analyze the variation of this parameter as a function of temperature according to $f_s(T) = \tanh T$ (Supplementary Fig. 45b). We correlate the transition temperature to the inflection point of the hyperbolic tangent function. The obtained values of the Néel temperature are summarized in Supplementary Fig. 45c. We note that the Néel temperatures estimated accordingly to these two methods of the analysis of the magnetotransport data are similar within the measurement error.

Growth of 30- and 250-nm-thick Cr_2O_3 films on a Pt seed layer leads to the relaxation of strain (Supplementary Figs. 46, 47, respectively) and low Néel temperature (Supplementary Fig. 30b).

Nitrogen-vacancy magnetic microscopy

NV magnetometry makes use of the electronic spin triplet ground state of the atomic NV defect in diamond to measure stray fields at the nanoscale[78]. Scanning NV magnetometry was performed with a tip fabricated from single-crystal, ⟨100⟩-oriented diamond that was implanted with ^{14}N ions at 12 keV and annealed to form NV centers. A small bias field (<60 Oe) is applied along the NV axis (54° from the sample normal) to split the $m_s = |\pm 1\rangle$ states of the NV. The magnetic stray field along the NV axis is then proportional to the Zeeman splitting of the $m_s = |\pm 1\rangle$ states, allowing us to achieve quantitative nanoscale imaging. For imaging, a single NV center is located at the tip of an all-diamond scanning probe[79] to provide scanning magnetometry capabilities with ~50 nm spatial resolution. The imaging is performed using feedback to lock to one of the NV resonances[80], thereby extracting the local stray field. We note that NV magnetometry is sensitive to non-collinear magnetic textures only. The texture should provide magnetic stray fields, which are detected by the NV magnetometer. Thus, any homogeneous magnetization also the one coming from the saturated surface with uncompensated moments will not influence the measured signal. Furthermore, for the analysis of the T_N^{bot} we follow the decay of the domain contrast

$$\widetilde{B} = B_{NV}^{red} - B_{NV}^{blue} \tag{1}$$

with B_{NV}^{red} and B_{NV}^{blue} being signed values of the average stray field strength measured on the oppositely ordered antiferromagnetic domains (red and blue areas in Fig. 3a, c). When the contrast (1) vanishes, we interpret this as the transition to the paramagnetic regime. No further assumptions are made for the determination of the Néel temperature in these measurements. This is determined by the detection limit of the setup, which provides $\widetilde{B} \sim 5\,\mu$T in the vicinity and above the phase transition. In this respect, the reported Néel

temperature is a lower bound and can be slightly higher. This means that the difference between the transport and NV estimates for the Néel temperature might be even higher, and the flexomagnetic contribution can be larger.

To build Fig. 3b, d and Supplementary Fig. 36, we average the measured stray field values from oppositely oriented domains separately. These average values were used to calculate B_{NV}. The measurements were carried out between room temperature and 85 °C, which is a hardware limitation for the setup. The temperature evolution of the antiferromagnetic domain pattern taken of the Cr_2O_3 samples of different thicknesses are shown in Supplementary Figs. 32–35. The NV contrast error bars of $2\,\mu T$ correspond to the halfwidth of the distribution.

Furthermore, we note that the presence of the Pt(3 nm) electrode does not affect the NV measurement of antiferromagnetic contrast $\tilde{B}$ (Supplementary Fig. 48).

Multiscale modeling

Molecular dynamics modeling of a Cr_2O_3 block containing 14,050 atoms ($60 \times 60 \times 100$ Å³ simulation box) was done using the LAMMPS package[81] (Supplementary Note 6). The systems were parameterized with reactive force field Cr–Al–O[82]. We found that parameters for Al_2O_3 have a better agreement between theory and experiment. Therefore, instead of using the parameters of the Cr_2O_3 system and straining them down to the Al_2O_3 geometry at the bottom interface by 4%, we used parameters of Al_2O_3 and strained further by 4% to mimic the same relative geometric transformations. The structure optimization protocol includes quick NVT quenching down to $T = 10$ K with an overall time of 5000 fs following quick annealing at $T = 10$ K. An example of the LAMMPS protocol is provided in Supplementary Note 6. The first-principles CASSCF calculations were done at the DKH2/CAS(3,5)/RASSI-SO/ANO-RCC-MB level of theory using OpenMolcas[83]. In the complete active space (CAS) model, the total spin of the 3d-shell populated with three electrons is $S = 3/2$. Having solved the spin-free CAS problem, all 10 roots were used in further state interaction modeling using the spin–orbit coupling (SOC)-Hamiltonian. Finally, for all doubly degenerate SOC-states of the g-tensors were computed using first-order perturbation theory.

We used the D value fit in ruby as a standard for our ab initio anisotropy model in the distorted polyhedra of the strained Cr_2O_3. That is independent modeling for CrO_6-polyhedron as found in the Al_2O_3 structure. Then, we employed the ReaxFF model to predict a possible geometry of the asymmetrically loaded Cr_2O_3 fragment. This modeling produces a local polyhedra distortion along the c-axis and in the ab-pane. For each CrO_6-polyhedron in the predicted Cr_2O_3 structure, the D-value and μ_g was estimated. The limitations of the ReaxFF model are summarized in[82]. Also, for a given geometry, the local anisotropy can be predicted rather well, according to CASSCR/RASSI-SO literature[83].

We stress that the zero-field splitting is a function of all three lattice parameters for each Chromium ion and, in the general case, cannot be considered as a function of c value only. The parameter $c = c(z)$ is computed as the equilibrium value for the given strain and geometry. Thus, both distributions $D(z)$ and $c(z)$ reflect the actual state of the Cr_2O_3 epitaxially grown at Al_2O_3.

Model of strained film

Typically, thin films are considered as homogeneous materials and variations of the micromagnetic parameters along the film thickness are neglected. In this approach, physical properties of epitaxial thin films (magnetic, electric, etc.) are linked to the average values of structural parameters like lattice constants or stress/strain state, which are often presented as functions of the overall film thickness. The primary focus of the manuscript is on the fact that thin film samples reveal variation of structural parameters along the normal direction of the film, which results in peculiar magnetic effects. Only within this assumption that magnetic parameters change across the film thickness for the same sample, flexomagnetic effects can emerge in Cr_2O_3.

To describe inhomogeneously strained thin antiferromagnetic films (Supplementary Note 7), first we expand the Néel temperature into a power series as the function of the c/a ratio. Having numerical evidence of a linear behavior of T_N in a wide range of strain values[16] and considering thin films, we limit our description to the linear term only. In this way, we determine the expression (Supplementary Equation (S20)) for the position of the boundary between the paramagnetic and antiferromagnetically ordered regions of the thin film, which is used to calculate the curves in Fig. 4d,e. For quantitative analysis, we need to determine sources of the magnetic moment in the samples. We take into account the following contributions, which are written for the local density of magnetic moments per unit area of the film surface:

$$\sigma = \sigma_{surf} + \sigma_{dis} + \sigma_{flex} + \sigma_{d-l} + \sigma_\zeta. \tag{2}$$

(i) Uncompensated spins at the top and bottom surfaces[29,30,41] (Supplementary Fig. 40). This contribution gives the surface magnetization σ_{surf} of about 2.2 μ_B nm⁻² for a single crystal[29] and a 200-nm-thick Cr_2O_3 film[30] at room temperature, which is several K below the transition temperature. We note that for a relaxed sample, the surface magnetization is the same at the top and bottom surfaces. For the following discussion, we define the direction of **L** to be associated with the direction of magnetic moments at the top surface.

(ii) Uncompensated spins at dislocations located close to the bottom film surface[24] (Supplementary Fig. 49). This contribution gives the surface magnetization of about $\sigma_{dis} = 0.45\ \mu_B$ nm⁻² for a 200-nm-thick Cr_2O_3 film[24] close to the bottom interface with Al_2O_3. Recent studies carried out for Cr_2O_3 films of 250 nm thickness prepared under different protocols to reveal different defect nanostructure exhibit the Néel temperature close to single crystals[84]. Furthermore, even SPS-sintered polycrystalline Cr_2O_3 samples with random orientation of the easy axis across the volume of the sample reveal the bulk value of the Néel temperature of 307.5 ± 2 K[85]. This allows us to conclude that the local magnetic ordering and direction of the easy axis are not of importance for the determination of the Néel temperature.

(iii) Ferromagnetism induced by the strain gradient (the inverse flexomagnetic effect)[14] (Supplementary Fig. 50). The estimations of the strain gradient in our samples and flexomagnetic coefficient via multiscale modeling (Supplementary Note 6, Supplementary Fig. 39) gives the respective magnetic moment per unit area of the film of order of 0.7 μ_B nm⁻² (Supplementary Table 4).

(iv) Dzyaloshinskii-like coupling between the ferro- and antiferromagnetic order parameters at non-collinear textures results in $\sigma_{d-l} \neq 0$ (Supplementary Fig. 51). There are two mechanisms which lead to the appearance of magnetization with the effective surface density σ_{d-l} induced by the gradients of the Néel vector in Cr_2O_3[42,43]. In the approach by Andreev [42], the spatial orientation of magnetization is determined by the spatial derivatives of **L** yet it is not necessarily aligned with **L**. The magnetization due to the flexoantiferromagnetic term introduced by Kabychenkov and Lisovskii [43] is mainly determined by the spatial derivatives of the in-plane components of **L**. The volume magnetization caused by this term is about 0.01 μ_B nm⁻³ (see Supplementary Note 7).

In case of Cr_2O_3, the DMI links the antiferromagnetic order parameter $\mathbf{n} = \mathbf{m}_1 - \mathbf{m}_2 + \mathbf{m}_3 - \mathbf{m}_4$ with the secondary antiferromagnetic order parameter $\mathbf{n}_1 = \mathbf{m}_1 + \mathbf{m}_2 - \mathbf{m}_3 - \mathbf{m}_4$, where $\mathbf{m}_i$ denote magnetic moments of Cr ions within the unit cell[19,86]. This leads to the spin canted state with $\mathbf{m}_1 = -\mathbf{m}_4$ and $\mathbf{m}_2 = -\mathbf{m}_3$ resulting in a zero total magnetic moment. This situation is different for α-Fe_2O_3, where $\mathbf{m}_1 = \mathbf{m}_4$ and $\mathbf{m}_2 = \mathbf{m}_3$ leads to the phenomenon of weak ferromagnetism[86]. Thus, even if spin canting is present in our samples, it cannot be detected via the NV magnetometry measurements.

(v) The spatially inhomogeneous reduction of the length of sublattice magnetizations (Supplementary Fig. 37) along the film thickness (and reduction of **L** as well) due to the inhomogeneous profile of the Néel temperature leads to the uncompensated magnetization

$$\mathbf{M}_\zeta \propto \frac{\mathbf{L}}{|\mathbf{L}|} \frac{\partial f(T/T_\mathrm{N})}{\partial z} \propto \frac{\partial u_{ij}}{\partial z}, \qquad (3)$$

where the function f determines the temperature dependence of the sublattice magnetization and the Néel temperature is a function of strain tensor components u_{ij}. We estimate its strength using the temperature dependence of the sublattice magnetization. At $T = T_\mathrm{N}^\mathrm{top}$, the respective surface density $\sigma_\zeta = \int_0^t (\mathbf{M}_\zeta)_z \mathrm{d}z \sim 2\,\mu_\mathrm{B}/\mathrm{nm}^2$.

The strength of the aforementioned contributions is summarized in Supplementary Table 5. Piezomagnetism of Cr_2O_3 is not taken into account in our discussion, as it is forbidden in center-antisymmetric magnetic materials[87].

The inhomogeneous magnetic texture in the film plane leads to the appearance of stray fields, which can be detected using NV magnetometry. In our analysis, we rely on the numerical value of the NV contrast (1), which can be compared with the theoretical model we discuss in the following. The average stray field above the top surface reads

$$B_\mathrm{NV} = \langle B_\mathrm{top} \rangle + \langle B_\mathrm{bot} \rangle + \langle B_\zeta \rangle. \qquad (4)$$

Here, $\langle \cdot \rangle$ means average over the NV scan area, $\langle B_\mathrm{top} \rangle$ arises from the domains pattern at the top surface (contribution (i) discussed above), $\langle B_\mathrm{bot} \rangle$ contains the signal from antiferromagnetic domains at the bottom film surface (contribution (i)) and contribution from dislocations (contribution (ii)), and $\langle B_\zeta \rangle$ contains the contribution from the magnetization (v). It is reasonable to assume that defects-induced moments are randomly distributed in the film. Therefore, their explicit net contribution is averaged to zero. Hence, we cannot detect this contribution relying on the analysis of the NV contrast (1). In this way, we model the NV signal as a function of temperature as

$$B_\mathrm{NV}(T) = \underbrace{b_1 \left[1 - \left(\frac{T}{T_\mathrm{N}^\mathrm{bot}} \right)^3 \right]^{1/3}}_{\text{bottom surface}} + \underbrace{b_2 \left[1 - \left(\frac{T}{T_\mathrm{N}^\mathrm{bot}} \right)^3 \right]^{1/3}}_{\text{top surface}}$$
$$+ \underbrace{b_3 \int_0^{t_\mathrm{AFM}} |\mathrm{M}_\zeta(T,z)| \mathrm{d}z}_{\text{via reduction of L}}, \qquad (5)$$

where the parameters $b_{1,2,3}$ incorporate characteristics of the setup, t_AFM is the thickness of the antiferromagnetic layer and $T_\mathrm{N}^\mathrm{bot} = T_\mathrm{N}(0)$. The first two parameters $b_{1,2}$ contain information on the uncompensated surface magnetization; b_3 determines the average scale of the contribution from the interior of the film (Supplementary Fig. 52). There is a constraint on b_1 and b_2 that they should have opposite signs because they come from the oppositely oriented spins at the top and bottom surfaces[88]. The signal amplitude b_3 by definition consists of uncompensated sublattice magnetizations along the film thickness, which are scaling from the saturation magnetization of one sublattice to zero. Therefore, by magnitude, it should not exceed the signal from the bottom film surface where the magnetization length is maximal. We note that upon approaching the transition temperature, the magnetic length, which determines the domain wall width, diverges rendering the antiferromagnetic domains as effectively small ones. This explains why the stray field B is measured not only at the domain walls,

but at the domains as well. In Equation (4), stray fields arising from contributions (iii) and (iv) are absent. The contribution (iii) induces magnetization with out-of-plane and in-plane components[14]. The out-of-plane component is homogeneous along the film thickness and, hence, it does not produce stray fields. The in-plane components are averaged to zero over the film area. The strength of the magnetization due to the mechanism (iv) is small and can be hardly detected in our measurements (Supplementary Note 7). We note that uncompensated moments located at point defects of arbitrary nature do not contribute to the value of (5) being averaged to zero.

Our theory is not directly applicable the region in the vicinity of T_N, where the renormalization group theory should be used to describe thermal fluctuations of magnetization and smooth transition from finite sublattice magnetization to the paramagnetic state. Taking the latter into account, will make the dependency $B_\mathrm{NV}(T)$ a smoother function of temperature as well. We note that within our approach, the kinks in the temperature dependence of the NV contrast (Supplementary Fig. 36) is of the order of 2 μT. Although irregularities in the NV contrast could be found in the relevant temperature range, the observed change is close to the resolution of our NV setup and is not discussed further.

The strength and direction of the magnetic moment, which is induced by the flexomagnetic effect is determined by the direction of the strain gradient with respect to crystallographic axes. In the absence of shear, the strain gradient along the c-axis can result in the magnetic moment, which is collinear with this axis. The strain gradient along the selected axis within the c plane can result in the magnetic moment, inclined with respect to this axis, see Eliseev [14] and Eqns. (26) and (27) in Supplementary Notes of the manuscript. However, the thermally induced magnetic moment, $\mathbf{M}_\zeta$, is generated along the gradient of $\mathbf{L}$ only. The uncompensated magnetic moment of thermal origin is aligned along the Néel vector (see schematics in Supplementary Fig. 37).

Data availability

The data supporting the findings of this study are available within the main text of this article and its Supplementary Information. Further information on this study is available from the corresponding authors upon reasonable request. Source data are provided with this paper.

References

1. Glinchuk, M., Ragulya, A. & Stephanovich, V. A. *Nanoferroics* (Springer Netherlands, 2013).
2. Bukharaev, A. A., Zvezdin, A. K., Pyatakov, A. P. & Fetisov, Y. K. Straintronics: a new trend in micro- and nanoelectronics and materials science. *Phys.—Usp.* **61**, 1175 (2018).
3. Lee, D. Flexoelectricity in thin films and membranes of complex oxides. *APL Mater.* **8**, 090901 (2020).
4. Gusev, N. S., Sadovnikov, A. V., Nikitov, S. A., Sapozhnikov, M. V. & Udalov, O. G. Manipulation of the Dzyaloshinskii-Moriya interaction in Co/Pt multilayers with strain. *Phys. Rev. Lett.* **124**, 157202 (2020).
5. Ceballos, A. et al. Effect of strain and thickness on the transition temperature of epitaxial FeRh thin-films. *Appl. Phys. Lett.* **111**, 172401 (2017).
6. Barra, A. et al. Effective strain manipulation of the antiferromagnetic state of polycrystalline NiO. *Appl. Phys. Lett.* **118**, 172408 (2021).
7. Jin, Q. et al. Strain-mediated high conductivity in ultrathin antiferromagnetic metallic nitrides. *Adv. Mater.* **33**, 2005920 (2021).
8. Eliseev, E. A., Morozovska, A. N., Glinchuk, M. D. & Blinc, R. Spontaneous flexoelectric/flexomagnetic effect in nanoferroics. *Physical Review B* **79**, 165433 (2009).
9. Sidhardh, S. & Ray, M. C. Flexomagnetic response of nanostructures. *J. Appl. Phys.* **124**, 244101 (2018).

10. Belyaev, B. A., Izotov, A. V., Solovev, P. N. & Boev, N. M. Strain-gradient-induced unidirectional magnetic anisotropy in nanocrystalline thin permalloy films. *Phys. Status Solidi (RRL)—Rapid Res. Lett.* **14**, 1900467 (2020).

11. Malikan, M. & Eremeyev, V. A. On nonlinear bending study of a piezo-flexomagnetic nanobeam based on an analytical-numerical solution. *Nanomaterials* **10**, 1762 (2020).

12. Cai, R., Antohe, V.-A., Nysten, B., Piraux, L. & Jonas, A. M. Thermally induced flexo-type effects in nanopatterned multiferroic layers. *Advanced Functional Materials* **30**, 1910371 (2020).

13. Shi, Y., Li, N., Ye, J. & Ma, J. Enhanced magnetoelectric response in nanostructures due to flexoelectric and flexomagnetic effects. *J. Magn. Magn. Mater.* **521**, 167523 (2021).

14. Eliseev, E. A. et al. Linear magnetoelectric coupling and ferroelectricity induced by the flexomagnetic effect in ferroics. *Phys. Rev. B* **84**, 174112 (2011).

15. Lukashev, P. & Sabirianov, R. F. Spin density in frustrated magnets under mechanical stress: Mn-based antiperovskites. *J. Appl. Phys.* **107**, 09E115 (2010).

16. Kota, Y., Imamura, H. & Sasaki, M. Strain-induced Néel temperature enhancement in corundum-type Cr_2O_3 and Fe_2O_3. *Appl. Phys. Express* **6**, 113007 (2013).

17. Kota, Y., Imamura, H. & Sasaki, M. Effect of lattice deformation on exchange coupling constants in Cr_2O_3. *J. Appl. Phys.* **115**, 17D719 (2014).

18. Kota, Y. & Imamura, H. Narrowing of antiferromagnetic domain wall in corundum-type Cr_2O_3 by lattice strain. *Appl. Phys. Express* **10**, 013002 (2016).

19. Mu, S. & Belashchenko, K. D. Influence of strain and chemical substitution on the magnetic anisotropy of antiferromagnetic Cr_2O_3: an ab-initio study. *Phys. Rev. Mater.* **3**, 034405 (2019).

20. Lukashev, P. & Sabirianov, R. F. Flexomagnetic effect in frustrated triangular magnetic structures. *Phys. Rev. B* **82**, 094417 (2010).

21. Zhang, J. X., Zeches, R. J., He, Q., Chu, Y.-H. & Ramesh, R. Nanoscale phase boundaries: a new twist to novel functionalities. *Nanoscale* **4**, 6196 (2012).

22. Lee, J. H. et al. Strain-gradient-induced magnetic anisotropy in straight-stripe mixed-phase bismuth ferrites: Insight into flexomagnetism. *Phys. Rev.* B **96**, 064402 (2017).

23. He, X. et al. Robust isothermal electric control of exchange bias at room temperature. *Nat. Mater.* **9**, 579 (2010).

24. Kosub, T. et al. Purely antiferromagnetic magnetoelectric random access memory. *Nat. Commun.* **8**, 13985 (2017).

25. Manipatruni, S. et al. Scalable energy-efficient magnetoelectric spin–orbit logic. *Nature* **565**, 35 (2018).

26. Li, J. et al. Observation of magnon polarons in a uniaxial antiferromagnetic insulator. *Phys. Rev. Lett.* **125**, 217201 (2020).

27. Yuan, W. Experimental signatures of spin superfluid ground state in canted antiferromagnet Cr_2O_3 via nonlocal spin transport. *Sci. Adv.* **4**, eaat1098 (2018).

28. Li, J. et al. Spin current from sub-terahertz-generated antiferromagnetic magnons. *Nature* **578**, 70 (2020).

29. Hedrich, N. et al. Nanoscale mechanics of antiferromagnetic domain walls. *Nat. Phys.* **17**, 574 (2021).

30. Appel, P. et al. Nanomagnetism of magnetoelectric granular thin-film antiferromagnets. *Nano Lett.* **19**, 1682 (2019).

31. Kota, Y., Yoshimori, Y., Imamura, H. & Kimura, T. Enhancement of magnetoelectric operating temperature in compressed Cr_2O_3 under hydrostatic pressure. *Appl. Phys. Lett.* **110**, 042902 (2017).

32. Kosub, T., Kopte, M., Radu, F., Schmidt, O. G. & Makarov, D. All-electric access to the magnetic-field-invariant magnetization of antiferromagnets. *Phys. Rev. Lett.* **115**, 097201 (2015).

33. Chen, Y.-T. et al. Theory of spin Hall magnetoresistance. *Phys. Rev. B* **87**, 144411 (2013).

34. Nakayama, H. et al. Spin Hall magnetoresistance induced by a nonequilibrium proximity effect. *Phys. Rev. Lett.* **110**, 206601 (2013).

35. Schlitz, R. et al. Evolution of the spin Hall magnetoresistance in Cr_2O_3/Pt bilayers close to the Néel temperature. *Appl. Phys. Lett.* **112**, 132401 (2018).

36. Kosub, T. et al. Anomalous Hall-like transverse magnetoresistance in Au thin films on $Y_3Fe_5O_{12}$. *Appl. Phys. Lett.* **113**, 222409 (2018).

37. Stöhr, J. et al. Images of the antiferromagnetic structure of a NiO(100) surface by means of X-ray magnetic linear dichroism spectromicroscopy. *Phys. Rev. Lett.* **83**, 1862 (1999).

38. Wadley, P. et al. Antiferromagnetic structure in tetragonal CuMnAs thin films. *Sci. Rep.* **5**, 17079 (2015).

39. Saidl, V. et al. Optical determination of the Néel vector in a CuMnAs thin-film antiferromagnet. *Nat. Photonics* **11**, 91 (2017).

40. Mandziak, A. et al. Tuning the Néel temperature of an antiferromagnet: the case of $Ni_xCo_{1-x}O$ microstructures. *Sci. Rep.* **9**, 13584 (2019).

41. Wörnle, M. S. et al. Coexistence of Bloch and Néel walls in a collinear antiferromagnet. *Phys. Rev. B* **103**, 094426 (2021).

42. Andreev, A. F. Macroscopic magnetic fields of antiferromagnets. *J. Exp. Theoretical Phys. Lett.* **63**, 758 (1996).

43. Kabychenkov, A. F. & Lisovskii, F. V. Flexomagnetic and flexoantiferromagnetic effects in centrosymmetric antiferromagnetic materials. *Techn. Phys.* **64**, 980 (2019).

44. Ivanov, B. A. & Kireev, V. E. Spin disclination in a layered antiferromagnet with a screw dislocation. *J. Exp. Theoretical Phys. Lett.* **73**, 188 (2001).

45. Galkina, E. G. & Ivanov, B. A. Dynamic solitons in antiferromagnets (review article). *Low Temp. Phys.* **44**, 618 (2018).

46. Stamps, R. L. & Camley, R. E. Bulk and surface spin waves in thin-film antiferromagnets. *J. Appl. Phys.* **56**, 3497 (1984).

47. Stamps, R. L. & Camley, R. E. Dipole-exchange spin-wave modes in very-thin-film antiferromagnets. *Phys. Rev. B* **35**, 1919 (1987).

48. Sharaevskaya, A., Kalyabin, D., Beginin, E., Fetisov, Y. & Nikitov, S. Surface spin waves in coupled easy-axis antiferromagnetic films. *J. Magn. Magn. Mat.* **475**, 778 (2019).

49. Seki, S. et al. Thermal generation of spin current in an antiferromagnet. *Phys. Rev. Lett.* **115**, 266601 (2015).

50. Wu, S. M. et al. Antiferromagnetic spin seebeck effect. *Phys. Rev. Lett.* **116**, 097204 (2016).

51. Vila, M. et al. Ferromagnetic epitaxial Cr_2O_3 thin films grown on oxide substrates by pulsed laser deposition. *Appl. Surf. Sci.* **534**, 147638 (2020).

52. Narayan, J. Recent progress in thin film epitaxy across the misfit scale (2011 acta gold medal paper). *Acta Materialia* **61**, 2703 (2013).

53. Punugupati, S., Narayan, J. & Hunte, F. Strain induced ferromagnetism in epitaxial Cr_2O_3 thin films integrated on Si(001). *Appl. Phys. Lett.* **105**, 132401 (2014).

54. Street, M. et al. Increasing the Néel temperature of magnetoelectric chromia for voltage-controlled spintronics. *Appl. Phys. Lett.* **104**, 222402 (2014).

55. Punugupati, S., Narayan, J. & Hunte, F. Room temperature ferromagnetism in epitaxial Cr_2O_3 thin films grown on r-sapphire. *J. Appl. Phys.* **117**, 193907 (2015).

56. Anwand, W., Brauer, G., Butterling, M., Kissener, H. R. & Wagner, A. Design and construction of a slow positron beam for solid and surface investigations. *Defect and Diffusion Forum* **331**, 25 (2012).

57. Shim, S.-H., Duffy, T. S., Jeanloz, R., Yoo, C.-S. & Iota, V. Raman spectroscopy and x-ray diffraction of phase transitions in Cr_2O_3 to 61 GPa. *Phys. Rev. B* **69**, 144107 (2004).

58. Iishi, K. Lattice dynamics of corundum. *Phys. Chem. Minerals* **3**, 1 (1978).

59. Bernardi, A. et al. Evolution of strain and composition during growth and capping of Ge quantum dots with different morphologies. *Nanotechnology* **18**, 475401 (2007).

60. Wagner, A., Butterling, M., Liedke, M. O., Potzger, K., & Krause-Rehberg, R. Positron annihilation lifetime and Doppler broadening spectroscopy at the ELBE facility. *AIP Conf. Proc.* **1970**, 040003 (2018).

61. Hirschmann, E. et al. A new system for real-time data acquisition and pulse parameterization for digital positron annihilation lifetime spectrometers with high repetition rates. *J. Instrumentation* **16**, P08001 (2021).

62. Olsen, J. V., Kirkegaard, P., Pedersen, N. J. & Eldrup, M. PALSfit: A new program for the evaluation of positron lifetime spectra. *Phys Status Solidi (c)* **4**, 4004 (2007).

63. Puska, M. J. & Nieminen, R. M. Theory of positrons in solids and on solid surfaces. *Rev. Mod. Phys.* **66**, 841 (1994).

64. Alatalo, M. et al. Theoretical and experimental study of positron annihilation with core electrons in solids. *Phys. Rev. B* **54**, 2397 (1996).

65. Qiu, Z. et al. Spin-current probe for phase transition in an insulator. *Nat. Commun.* **7**, 12670 (2016).

66. Asa, M. et al. Detecting antiferromagnetism in tetragonal Cr_2O_3 by electrical measurements. *Phys. Rev. B* **100**, 174423 (2019).

67. Hoogeboom, G. R., Aqeel, A., Kuschel, T., Palstra, T. T. M. & van Wees, B. J. Negative spin Hall magnetoresistance of Pt on the bulk easy-plane antiferromagnet NiO. *Appl. Phys. Lett.* **111**, 052409 (2017).

68. Oda, K., Moriyama, T., Kimata, M., Kasukawa, S. & Ono, T. Temperature dependence of spin Hall magnetoresistance across the Néel temperature of CoO. *Japan. J. Appl. Phys.* **59**, 010908 (2020).

69. Wang, H., Du, C., Hammel, P. C. & Yang, F. Spin transport in antiferromagnetic insulators mediated by magnetic correlations. *Phys. Rev. B* **91**, 220410 (2015).

70. HZDR Innovation GmbH, https://www.tensorinstruments.com/products, Tensormeter measurement device.

71. Brown, C. A. Magnetoelectric domains in single crystal chromium oxide (1969). https://spiral.imperial.ac.uk/bitstream/10044/1/15723/2/Brown-CA-1969-PhD-Thesis.pdf

72. Geprägs, S. et al. Investigation of induced Pt magnetic polarization in $Pt/Y_3Fe_5O_{12}$ bilayers. *Appl. Phys. Lett.* **101**, 262407 (2012).

73. Valvidares, M. et al. Absence of magnetic proximity effects in magnetoresistive $Pt/CoFe_2O_4$ hybrid interfaces. *Phys. Rev. B* **93**, 214415 (2016).

74. Collet, M. et al. Investigating magnetic proximity effects at ferrite/Pt interfaces. *Appl. Phys. Lett.* **111**, 202401 (2017).

75. Geprägs, S. et al. Static magnetic proximity effects and spin Hall magnetoresistance in $Pt/Y_3Fe_5O_{12}$ and inverted $Y_3Fe_5O_{12}/Pt$ bilayers. *Phys. Rev. B* **102**, 214438 (2020).

76. Moriyama, T. et al. Giant anomalous hall conductivity at the Pt/Cr_2O_3 interface. *Phys. Rev. Appl.* **13**, 034052 (2020).

77. Muduli, P. et al. Local and nonlocal spin seebeck effect in lateral $Pt-Cr_2O_3-Pt$ devices at low temperatures. *APL Mater.* **9**, 021122 (2021).

78. Rondin, L. et al. Magnetometry with nitrogen-vacancy defects in diamond. *Rep. Prog. Phys.* **77**, 056503 (2014).

79. Hedrich, N., Rohner, D., Batzer, M., Maletinsky, P. & Shields, B. J. Parabolic diamond scanning probes for single-spin magnetic field imaging. *Phys. Rev. Appl.* **14**, 064007 (2020).

80. Schoenfeld, R. S. & Harneit, W. Real time magnetic field sensing and imaging using a single spin in diamond. *Phys. Rev. Lett.* **106**, 030802 (2011).

81. Plimpton, S. Fast parallel algorithms for short-range molecular dynamics. *J. Comput. Phys.* **117**, 1 (1995).

82. Shin, Y. K., Kwak, H., Vasenkov, A. V., Sengupta, D. & van Duin, A. C. Development of a ReaxFF reactive force field for Fe/Cr/O/S and application to oxidation of butane over a pyrite-covered Cr_2O_3 catalyst. *ACS Catalysis* **5**, 7226 (2015).

83. Galván, I. F. et al. OpenMolcas: from source code to insight. *J. Chem. Theory Comput.* **15**, 5925 (2019).

84. Veremchuk, I. et al. Defect nanostructure and its impact on magnetism of α-Cr_2O_3 thin films. *Small* **18**, 2201228 (2022).

85. Veremchuk, I. et al. Magnetism and magnetoelectricity of textured polycrystalline bulk Cr_2O_3 sintered in conditions far out of equilibrium. *ACS Appl. Electron. Mater.* **4**, 2943 (2022).

86. Dzyaloshinsky, I. A thermodynamic theory of "weak" ferromagnetism of antiferromagnetics. *J. Phys. Chem. Solids* **4**, 241 (1958).

87. Turov, E. A. Can the magnetoelectric effect coexist with weak piezomagnetism and ferromagnetism? *Phys.—Usp.* **37**, 303 (1994).

88. Belashchenko, K. D. Equilibrium magnetization at the boundary of a magnetoelectric antiferromagnet. *Phys. Rev. Lett.* **105**, 147204 (2010).

Acknowledgements

Author contributions

T.K. and P.Mak. fabricated and characterized the samples with the support of I.V. R.H., A.L., D.W. performed TEM characterization and data analysis. M.O.L., A.W., P.Mak. and I.V. collected and analyzed the PAS data. M.B. conducted positron DFT-ATSUP simulations. F.G. carried out XRD characterization with the support of I.V. N.H., K.W., B.J.S., P.L., and P.Mal. carried out and analyzed NV microscopy measurements with the support of O.V.P. and P.Mak. J.L. and A.P. carried out and analyzed Raman measurements. O.V.P. developed the phonomenological model of flexomagnetism and applied it for the analysis of the experimental data with the support of P.Mak. and D.M. S.A. performed multiscale modeling to describe the strain propagation along the thickness of Cr_2O_3 films. P.Mak., T.K., O.V.P. and D.M. prepared the manuscript and organized figures. O.V.P. and D.M. developed the concept. J.F., P.Mal. and D.M. conceived the project. All authors contributed to discussions of the data and writing the manuscript.

Funding

Competing interests

The authors declare no competing interests.

Article

Additional information

Supplementary information The online version contains supplementary material available at
https://doi.org/10.1038/s41467-022-34233-5.

Correspondence and requests for materials should be addressed to Oleksandr V. Pylypovskyi or Denys Makarov.

Peer review information *Nature Communications* thanks the anonymous reviewer(s) for their contribution to the peer review of this work. Peer reviewer reports are available.

Reprints and permissions information is available at
http://www.nature.com/reprints

Publisher's note Springer Nature remains neutral with regard to jurisdictional claims in published maps and institutional affiliations.

Terahertz control of photoluminescence emission in few-layer InSe

T. Venanzi,[1,2,a)] M. Selig,[3] A. Pashkin,[1] S. Winnerl,[1] M. Katzer,[3] H. Arora,[1] A. Erbe,[1] A. Patanè,[4]
Z. R. Kudrynskyi,[4] Z. D. Kovalyuk,[5] L. Baldassarre,[2] A. Knorr,[3] M. Helm,[1,6] and H. Schneider[1]

AFFILIATIONS

[1]Helmholtz-Zentrum Dresden-Rossendorf, 01314 Dresden, Germany
[2]Dipartimento di Fisica, Università di Roma "Sapienza," 00185 Rome, Italy
[3]Institut für Theoretische Physik, Technische Universität Berlin, 10623 Berlin, Germany
[4]School of Physics and Astronomy, University of Nottingham, Nottingham NG7 2RD, United Kingdom
[5]Frantsevich Institute for Problems of Materials Science, The National Academy of Sciences of Ukraine, Chernivtsi Branch,
  58001 Chernivtsi, Ukraine
[6]Technische Universität Dresden, 01062 Dresden, Germany

[a)]Author to whom correspondence should be addressed: tommaso.venanzi@uniroma1.it

ABSTRACT

A promising route for the development of opto-electronic technology is to use terahertz radiation to modulate the optical properties of semi-conductors. Here, we demonstrate the dynamical control of photoluminescence (PL) emission in few-layer InSe using picosecond terahertz pulses. We observe a strong PL quenching (up to 50%) after the arrival of the terahertz pulse followed by a reversible recovery of the emission on the timescale of 50 ps at $T = 10$ K. Microscopic calculations reveal that the origin of the photoluminescence quenching is the terahertz absorption by photo-excited carriers: this leads to a heating of the carriers and a broadening of their distribution, which reduces the probability of bimolecular electron-hole recombination and, therefore, the luminescence. By numerically evaluating the Boltzmann equation, we are able to clarify the individual roles of optical and acoustic phonons in the subsequent cooling process. The same PL quenching mechanism is expected in other van der Waals semiconductors, and the effect will be particularly strong for materials with low carrier masses and long carrier relaxation time, which is the case for InSe. This work gives a solid background for the development of opto-electronic applications based on InSe, such as THz detectors and optical modulators.

The use of terahertz radiation to modulate the optical properties of van der Waals (vdW) semiconductors is a promising route for the development of opto-electronic technology.[1] Indeed, this class of materials offers unique engineering possibilities by controlling the material thickness down to monolayers and by making heterostructures without lattice matching constrains and with the additional twist-angle degree of freedom.[2–4] Among vdW materials, InSe is a III–VI semiconductor that has shown numerous promising properties for opto-electronic applications: it features a direct bandgap, low electron mass that leads to high electron mobility[5,6] and large bandgap tunability,[7–9] and very low Young's modulus that leads to high plasticity.[10,11] Therefore, InSe can be used as an active layer for various applications like photodetectors,[12,13] field-effect transistors,[6,14] and flexible electronics.[12,15,16]

It was recently shown that InSe is an appealing material for applications in the THz range, such as detectors and emitters. In fact,

intersubband electronic transitions in few-layer InSe were predicted and observed experimentally by means of electronic resonant tunneling.[17–19] However, the use of InSe in the infrared and terahertz range of the electromagnetic spectrum has not been intensively investigated so far. On the one hand, it is of fundamental interest to investigate the THz/infrared response of InSe,[20,21] which, in turn, could constitute a novel characterization technique for InSe quality testing to be employed in the more developed visible range technology. On the other hand, THz radiation can be employed to control the optical response of the material and the light-matter interaction.[22,23]

Here, we demonstrate the dynamical control of photoluminescence emission in InSe using picosecond terahertz pulses obtained with the free-electron laser (FEL) FELBE. To this end, we perform a two-color time-resolved photoluminescence (PL) experiment. After exciting an electron–hole population with picosecond visible (VIS)

pulses, a THz pulse arrives with a delay on the sample causing a transient quenching of the PL emission. For all the investigated temperatures, we observe a full recovery of the PL intensity, e.g., on the timescale of 50 ps at $T = 10$ K. Our microscopic analysis reveals that the transient quenching is due to the heating of the carriers after THz absorption: this leads to a broadening of the electron and hole distributions in the momentum space that reduces the rate of spontaneous emission. By monitoring the subsequent recovery of the PL, we are able to extract the effective cooling times. We accompany our experiment with a microscopic calculation of carrier cooling obtaining good agreement. The present study is important for the basic physics knowledge of the electron-phonon dynamics in InSe and for the development of THz and opto-electronic applications as ultrafast THz detectors, optical modulators, and ultrafast lasing switchers.

The InSe samples are fabricated via mechanical exfoliation and are transferred onto a diamond substrate. The thicknesses of the flakes are measured with atomic force microscopy, and the data are reported in the supplementary material. The InSe flakes under investigation have a thickness between 8 and 40 nm. If it is not stated differently, we show results from a 16.5 nm thick sample since the experimental results do not show any significant thickness dependence. This corresponds to about 20 atomic layers.[24] In this work, we focus on flakes thicker than 8 nm since they feature strong PL emission due to the direct bandgap.[24] For this thickness, the bandgap energy of InSe is of about 1.31 eV.

Time-resolved photoluminescence spectra are recorded with a streak camera coupled to a spectrometer. With this system, 5 ps time resolution and 1 meV spectral resolution are obtained. A mode-locked Ti:sapphire (TiSa) oscillator with a pulse length of 3 ps is used as excitation source at $\lambda = 770$ nm. The spot diameter is around 3 μm. The THz radiation is obtained with an infrared FEL (FELBE). The THz frequency is tuned from 5.5 to 26 THz (from 22 to 110 meV). The THz pulse length is of about 5 ps. The TiSa laser is reduced from 78 to 13 MHz by pulse-picking with a Pockels cell to match the FEL repetition rate.

Figure 1(a) shows the time-resolved photoluminescence spectrum without THz pumping. The visible radiation excites electrons well-above the bandgap. After the initial thermalization and relaxation of the photo-excited carriers, a long-living PL emission is observed at 1.31 eV. The PL emission is assigned to a combination of defect-assisted radiative recombination and band-to-band recombination.[25,26] Figure 1(b) shows the PL decay integrated over the photon energy. The PL decay time of the PL emission is longer than the time range of our setup, i.e., $\tau_D > 1$ ns.

Figure 1(c) shows the time-resolved PL spectrum with the additional THz pulse. The THz pulse arrives around 250 ps after the visible pulse and induces a PL quenching. Shortly after the quenching, the PL emission is recovered.

The time dependence of the spectrally integrated PL emission is shown in Fig. 1(d). The PL emission is quenched by about 35% by the
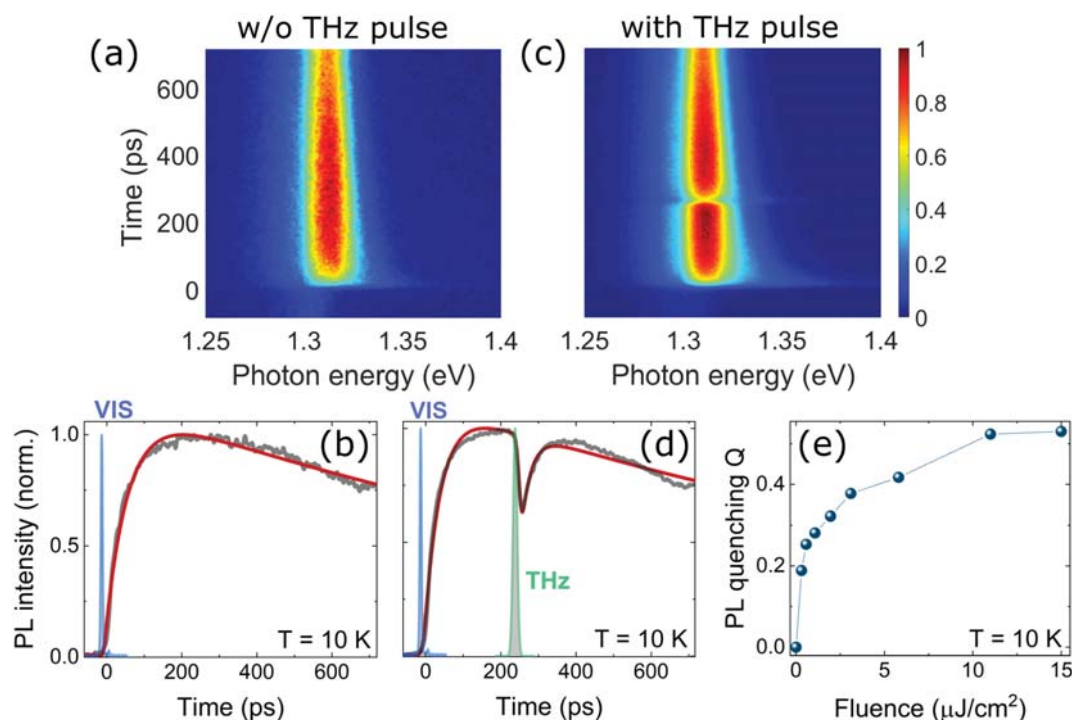
FIG. 1. (a) Time-resolved PL spectrum of a thin-flake of InSe at $T = 10$ K. (b) Time dependence of the PL signal integrated over the emission photon energy (dark gray curve). The red curve is a fit of the experimental data. (c) Time-resolved PL spectrum with additional THz pumping. The THz pulse arrives 250 ps after the optical pulse and induces a transient PL quenching. The FEL fluence is $\phi_{FEL} = 5\,\mu$J/cm^2 at 12 THz. (d) Time dependence of the integrated PL signal with THz radiation. (e) THz fluence dependence of the quenching parameter Q.

THz radiation at THz fluence $\phi_{FEL} = 5\,\mu J/cm^2$ and reaches values higher than 50% at higher fluences [see Fig. 1(e)]. The THz fluence dependence of the PL quenching parameter Q shows a saturation behavior at high fluences [Fig. 1(e)]. The quenching parameter Q is the fraction of PL quenching during the THz pulse arrival with respect to the PL just before the THz pulse. It ranges between 0 (no quenching) and 1 (full quenching).

In order to extract the PL decay constants, a system of rate equations is used containing the decay constants (τ_{rise}, τ_{PL}, and $\tau_{cooling}$) and the quenching parameter Q (all the details are given in SM). The fits of the PL time dependence are shown in Figs. 1(b) and 1(d). This way we extract a recovery time after the FEL pulse of $\tau_{cooling} = 40 \pm 10$ ps at 10 K of lattice temperature. The PL rise time is $\tau_{rise} = 50 \pm 10$ ps.

At this point, the most important question to answer concerns the mechanism responsible for the PL quenching. As discussed in the literature for quantum well and quantum dot semiconductor systems, various physical mechanisms can lead to a PL quenching.[27–32]

To investigate whether we observe a resonant effect, we repeated the experiment at different FEL photon energies, and we did not observe any significant dependence within our signal-to-noise ratio (see supplementary material). We conclude that we observe a broadband non-resonant effect, thus resonant effects such as phonon excitation,[33] resonant excitation of shallow impurities,[28] intra-excitonic transitions (e.g., 1s-to-2p),[27,34] and intersubband transitions[29] can be ruled out.

We also rule out exciton ionization as origin of the PL quenching since the fluence dependence of the PL quenching shows a saturation behavior that is in contradiction with an exciton ionization process.[30] Moreover, we observe a strong PL quenching at THz fields of the order of 1 kV/cm, which is much lower than the needed electric field for exciton ionization in InSe, since the exciton binding energy is of about 20 meV.[35–37]

Furthermore, lattice heating due to non-resonant absorption by the substrate could lead to a PL quenching, but (1) we do not expect this fast dynamics, (2) the substrate is transparent and has a very high thermal conductivity (no heat transfer from the substrate to the flake and good thermal dissipation), and (3) the PL emission shows a slight blueshift after the THz pulse arrival while an increase in lattice temperature would induce a redshift of the PL emission.[25,38]

The most probable origin of the PL quenching is THz absorption by photo-excited free carriers. To verify this interpretation, we analyze the spectral shape of the PL emission as a function of time [shown in Figs. 2(a) and 2(b)]. We fit the spectrum at any time with a convolution of an Urbach tail $U(E) \propto \exp\left(\frac{E}{E_u}\right)$ with the electronic density of state $D(E) \propto \Theta(E - E_g)$, where E_u is the Urbach energy, E_g is the bandgap energy, and Θ is the Heaviside step function.[26,39] The fitting function was then weighted with a Fermi–Dirac distribution $f \propto (1 + \exp(\frac{E-\mu}{k_B T}))^{-1}$. The resulting PL intensity reads as

$$I_{PL}(\omega) \propto \omega^2 (U(E) * D(E)) f(\omega, T), \quad (1)$$

where ω is the photon frequency. The complete analytic expression is given in supplementary material. We use Eq. (1) to fit the spectrum at any delay time using two free parameters: the carrier temperature and the density of carriers that contribute to the PL emission. Figure 2(a) shows the spectra with the fit at two delay times, i.e., just before and during the FEL pulse arrival. By comparing the two spectra, it can be seen that the FEL pulse induces a quenching and a broadening on the high-energy side of the peak [see Fig. 2(b)]. This latter effect is direct evidence of hot-carrier emission.[40] Figure 2(c) shows the time dependence of the carrier temperature as obtained from the fit. The carrier temperature shows a sharp increase after the visible pulse arrival due to the excitation of hot electron-hole pairs. A second sharp increase in the carrier temperature is observed at the THz pulse arrival. The increase in the carrier temperature is of about 50 K. From this value, we estimate a terahertz absorption of $A = 0.12\%$ by the photo-excited carriers (see supplementary material).

THz absorption by free carriers explains also the saturation behavior of the PL quenching at high THz fluences shown in Fig. 1(e). At high carrier temperatures, i.e., high THz fluences, the carrier cooling time becomes shorter and the electron heat capacity larger. The fast cooling of hot carriers via optical phonons leads to a limitation on the temperature that the carriers can reach, therefore a limitation on the maximum PL quenching. Similarly, at low temperature, the electron heat capacity increases linearly with the temperature, and this further reduces the heating of the carrier distribution at high THz fluences. A detailed discussion of these mechanisms is given in supplementary material alongside with another possible mechanism that leads to a saturation behavior at high THz fluences.
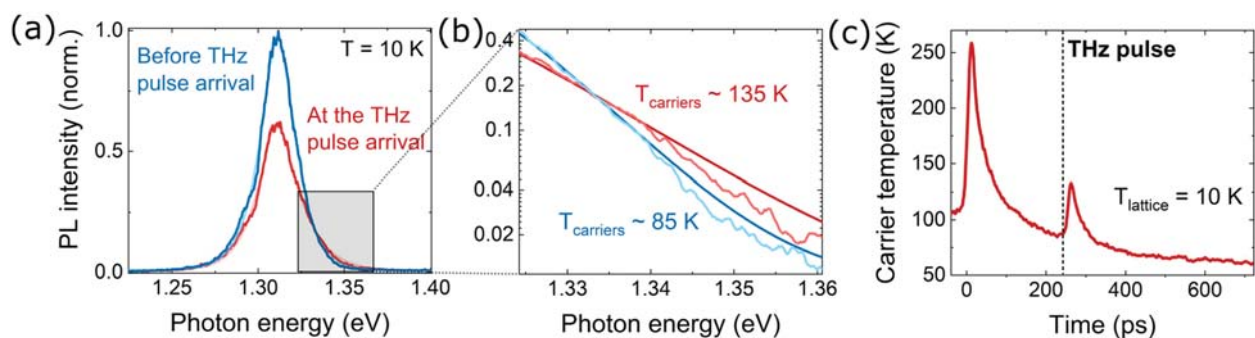
FIG. 2. (a) PL spectra before and during the arrival of the THz pulse. The PL emission is strongly quenched, and a broadening of the peak on the high-energy side is observed. (b) Zoom in of the high-energy tail of the PL spectra. The emission gets broader at higher effective carrier temperatures. (c) Time dependence of the carrier temperature. The FEL pulse heats the carrier system, and the radiative efficiency drops dramatically.

Now, we show how the heating of the photo-excited carriers by THz radiation leads to a PL quenching. To this end, we calculate the PL emission intensity with a microscopic theory assuming a quasi-stationary carrier distribution. Therefore, we calculate the luminescence in the free particle limit[41]

$$I(\Omega_{q_z}) \propto \text{Im}\left(d \sum_{\mathbf{k}} \frac{f_{\mathbf{k}}^e(t) f_{\mathbf{k}}^h(t)}{E_g + \frac{\hbar^2 \mathbf{k}^2}{2m} - \hbar\Omega_{q_z} - i\gamma} \right), \quad (2)$$

with the dipole strength d, carrier momentum $\mathbf{k}$, bandgap energy E_g, reduced mass of the electron-hole pair m, and a phenomenological chosen broadening γ. Note that we assume the optical dipole element d to be independent of the momentum, which is reasonable due to the negligible momenta of the photons.[41] $f_{\mathbf{k}}^e(t)$ and $f_{\mathbf{k}}^h(t)$ are the time-dependent electron and hole distribution after the heating process, respectively.

To obtain the luminescence from Eq. (2), we calculate the electron and hole distribution ($f_{\mathbf{k}}^e$ and $f_{\mathbf{k}}^h$) dynamics with the Boltzmann scattering equation in the low density limit

$$\frac{d}{dt} f_{\mathbf{q}}^{\lambda i} = \frac{2\pi}{\hbar} \sum_{\mathbf{k},j,\alpha,\pm} |g_{\mathbf{k}-\mathbf{q}}^{\lambda\alpha}|^2 \left(\frac{1}{2} \pm \frac{1}{2} + n_{\mathbf{k}-\mathbf{q}}^{\alpha} \right) \delta\left(\varepsilon_{\mathbf{q}}^i - \varepsilon_{\mathbf{k}}^j \pm \hbar\omega_{\mathbf{k}-\mathbf{q}}^{\alpha} \right) f_{\mathbf{k}}^{\lambda j}$$
$$- \frac{2\pi}{\hbar} \sum_{\mathbf{k},\alpha,\pm} |g_{\mathbf{k}-\mathbf{q}}^{\lambda\alpha}|^2 \left(\frac{1}{2} \pm \frac{1}{2} + n_{\mathbf{k}-\mathbf{q}}^{\alpha} \right) \delta\left(\varepsilon_{\mathbf{q}}^i - \varepsilon_{\mathbf{k}}^j \mp \hbar\omega_{\mathbf{k}-\mathbf{q}}^{\alpha} \right) f_{\mathbf{q}}^{\lambda i}.$$
$$(3)$$

The equation accounts for the thermalization of electrons to the lattice temperature, which is encoded in the phonon occupation $n_{\mathbf{q}}^{\alpha}$. The summation $\pm$ accounts for phonon emission ($+$) and phonon absorption ($-$) processes, which are involved in the scattering. $n_{\mathbf{q}}^{\alpha}$ accounts for the phonon occupation of the mode α with momentum $\mathbf{q}$. The Dirac delta function imposes the energy conservation during the electron-phonon scattering event. $\varepsilon_{\mathbf{k}}^{\lambda i} = \frac{\hbar^2 \mathbf{k}^2}{2m^{\lambda}}$ is the carrier dispersion as a function of the carrier momentum $\mathbf{k}$, band λ, and the electronic subband i. The intersubband spacing is calculated in supplementary material and is about 28 meV between the first and

second subband. The effective masses in the conduction and the valence band are $m^c = 0.12 m_0$ and $m^v = 0.73 m_0$, respectively.[24,42] $g_{\mathbf{q}}^{\alpha,\lambda}$ is the electron-phonon coupling element. Further details are given in supplementary material.

We solve the Boltzmann equation (Eq. 3) for lattice temperature $T_{lattice} = 10$ K and by setting an initial carrier temperature $T_{add} = 50$ K as obtained by the spectral fit of the PL emission just after the FEL pulse arrival. We note that we perform the calculation for different T_{add} and show in supplementary material that the results do not change qualitatively by varying this parameter. With this procedure, we are able to calculate the electron and hole cooling time as a function of carrier temperature and, therefore, the luminescence intensity as a function of time.

Figure 3(a) shows the calculated PL spectra for selected times after the FEL pulse arrival. A PL recovery is clearly observed as a consequence of the carrier cooling, while the carrier density is kept constant. The origin of the quenching relates to the broadening of the electron and hole distributions when the carrier temperature increases. This can be understood by considering Eq. (2): when the carrier temperature increases, the carrier distributions are broader in the momentum space, and the sum over $\mathbf{k}$ in the numerator strongly reduces leading to a PL quenching.

We stress that the denominator in Eq. (2) contributes to shift the PL emission to higher energies. This observation is in agreement with the experimental data. However, the denominator does not have a significant influence on the PL quenching that is instead ruled by the numerator. The following is the intuitive interpretation of the observed PL quenching: the band-to-band bimolecular recombination depends on the probability to find both an electron and a hole at $\mathbf{k}$, and this probability is strongly reduced when the electron and hole distributions become broader in the momentum space. Further details are given in supplementary material.

With this calculation, we can compare the time dependence of the PL recovery after the THz pulse arrival with the experimental data [see Fig. 3(b) for a lattice temperature of 10 K]. We note that in Fig. 3(b), we multiply the calculated curve by a multiplication factor to match the intensity of the PL quenching. In fact, we notice that from the theoretical calculation, we expect a PL quenching of about 70%
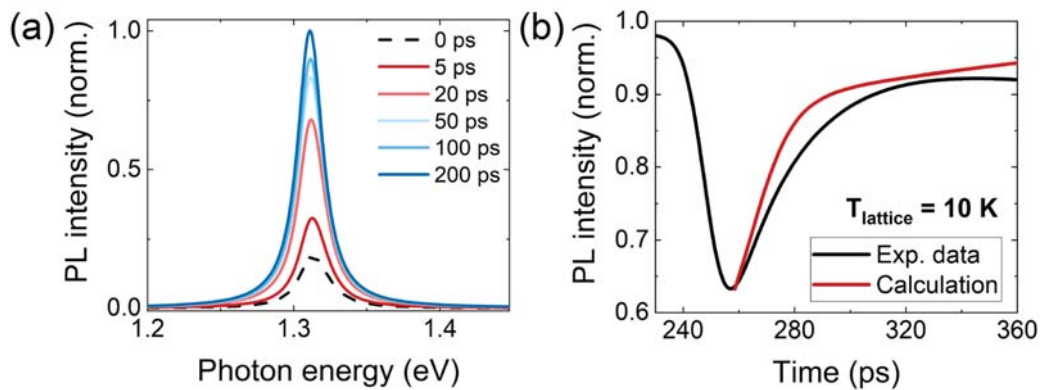
FIG. 3. (a) Calculated PL spectra as a function of delay time after the THz pulse arrival on the sample. After the initial quenching, the PL emission increases due to the relaxation of the heated electrons (holes) to the bottom (top) of the conduction (valence) band. (b) Comparison between experimental and calculated PL recovery after the THz pulse arrival at 10 K.

[Fig. 3(a)] differently from the experimentally observed quenching of 35%. The reasons for this quantitative disagreement are (1) the limited time resolution of the setup that smears out the dip in the recorded PL spectra and makes the experimental value of quenching smaller than the actual quenching; (2) in the calculation, we made the approximation of a quasi-stationary distribution, so that we could define a carrier temperature at any time. This approximation can be critical, especially during the arrival of the THz pulse, and can lead to a wrong value of the calculated PL quenching.

To further corroborate our results and to get more information on the material properties, we investigate the dependence of the PL quenching on the lattice temperature. Figure 4 shows the lattice temperature dependence of the PL recovery time (black dots). The error bars are calculated considering the time resolution of the setup and the error of the fitting procedure. The strength of the PL modulation decreases at high temperatures (data in supplementary material) as a consequence of higher electron heat capacity and shorter relaxation time. Figure 4 shows also the PL cooling times calculated with the microscopic theory (red line). By comparing the experimental and calculated PL recovery time, we find good agreement between calculation and data. This strongly suggests that our interpretation and our theory capture correctly the physics behind the modulation of the PL signal by the THz pulse.

Interestingly, the cooling time determined via a Boltzmann fitting of the electron occupation is one order of magnitude longer than the measured data (Fig. 4, blue line). This is connected to the missing momentum resolution in the simplification of the complex carrier relaxation under the influence of electron-phonon coupling to a single number (the cooling time). Differently from our full microscopic model, this method to obtain the relaxation time does not account for the fact that the PL emission arises mostly from occupied states with small momenta. In fact, electron–hole bimolecular luminescence is sensitive to the most densely populated regions, which are the low $\mathbf{q}$-regions because they are quickly populated via optical phonon scattering.

As discussed, we have used Eq. (3) to calculate, *ab initio*, the temperature dependence of the cooling times finding very good agreement with the experimental data. If we start from our calculation and leave

the electron-phonon coupling constant g as free parameter (not done in any plotted calculation), we find that the best fit is obtained for $g' = 0.88g$, a slightly smaller value of the coupling constant than what expected from DFT calculations.[43,44]

The temperature dependence of the cooling time can mainly be understood from the scattering of electrons by optical phonons. At low temperatures, optical phonons only have a minor impact on the relaxation because the optical phonon energy ($\hbar\omega_{ZO_1} = 12.4$ meV[43]) is too large to contribute effectively to the cooling of carriers with low kinetic energy.[45] Therefore, the cooling is mainly determined via acoustic phonon scattering at low temperatures. Increasing the lattice temperature increases the kinetic energies of electrons resulting in a larger impact of optical phonon scattering to the cooling dynamics. This leads to a speed-up of the cooling at high lattice temperatures.

Finally, we note that the strength of the PL quenching depends mostly on (1) THz absorption, (2) electron heat capacity, and (3) carrier relaxation time. In other words, it depends on how well the heating of the electron distribution via THz absorption works. In this regard, the low electron mass plays a central role since the THz absorption and the heat capacity depend on the electron mass ($A \sim \frac{n}{m}$ and $c \sim m$ in a two-dimensional electron gas, respectively). High absorption and low heat capacity lead to a high heating of the carrier distribution and, consequently, to a strong PL quenching. The carrier relaxation time plays also an important role and long time corresponds to high quenching. To conclude, the PL quenching is expected in other vdW semiconductors, and the effect will be particularly strong for materials that have low carrier masses and long relaxation time, which is the case for InSe.

In summary, we investigated the effects of THz radiation on the PL emission of few-layer InSe. We observe a transient quenching of the PL emission induced by heating of the photo-excited electron–hole system. The PL quenching reaches values up to 52%. The heating and cooling of the electron–hole system are modeled by Boltzmann equation, and the PL emission is calculated microscopically. With the microscopic theory, we are able to reproduce the experimental data corroborating the physical interpretation that THz free carrier absorption leads to a broader carrier distribution in the momentum space and, therefore, to a PL quenching. The increase in cooling time at low temperatures is attributed to the less efficient cooling via the emission of optical phonons because of their high energy with respect to the thermal energy of carriers. By comparing the experimental and theoretical results, we provide an experimental estimation of the electron-phonon coupling constants of 0.88 times of the expected values from DFT calculations.

All in all, we demonstrate the possibility to use terahertz radiation for the dynamic control of the photoluminescence emission in a van der Waals semiconductor. This work demonstrates a promising route for the realization of opto-electronic technology, such as terahertz detectors and optical modulators.

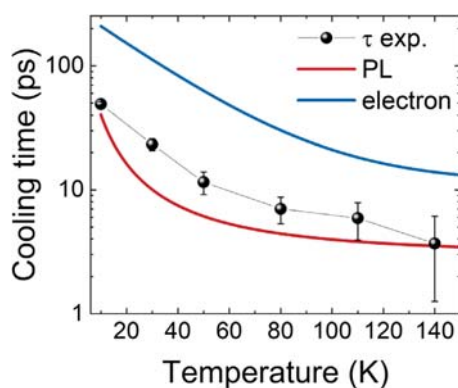See the supplementary material with further experiments and calculations is provided.

FIG. 4. Lattice temperature dependence of measured (black dots) and theoretically predicted (red line) PL recovery time. For comparison, we also show the electron cooling time (blue line), which is quite different from the calculated PL recovery time as explained in the main text. The measured temperatures are 10, 30, 50, 80, 110, and 140 K.

AUTHOR DECLARATIONS

Conflict of Interest

The authors have no conflict of interest to disclose.

DATA AVAILABILITY

The data that support the findings of this study are openly available in Rodare at https://rodare.hzdr.de/, Ref. 46.

REFERENCES

[1]F. Langer, S. Schlauderer, M. Gmitra, J. Fabian, T. Korn, J. T. Steiner, M. Kira, R. Huber, and U. Huttner, "Lightwave valleytronics in a monolayer of tungsten diselenide," Nature **557**, 76–80 (2018).

[2]A. K. Geim and I. V. Grigorieva, "Van der Waals heterostructures," Nature **499**, 419–425 (2013).

[3]N. Ubrig, E. Ponomarev, J. Zultak, D. Domaretskiy, V. Zólyomi, D. Terry, J. Howarth, I. Gutiérrez-Lezama, A. Zhukov, Z. R. Kudrynskyi, Z. D. Kovalyuk, A. Patané, T. Taniguchi, K. Watanabe, R. V. Gorbachev, V. I. Fal'ko, and A. F. Morpurgo, "Design of van der Waals interfaces for broad-spectrum optoelectronics," Nat. Mater. **19**, 299–304 (2020).

[4]Y. Liu, Y. Huang, and X. Duan, "Van der Waals integration before and beyond two-dimensional materials," Nature **567**, 323–333 (2019).

[5]D. A. Bandurin, A. V. Tyurnina, G. L. Yu, A. Mishchenko, V. Zólyomi, S. V. Morozov, R. K. Kumar, R. V. Gorbachev, Z. R. Kudrynskyi, S. Pezzini, Z. D. Kovalyuk, U. Zeitler, K. S. Novoselov, A. Patané, L. Eaves, I. V. Grigorieva, V. I. Fal'ko, A. K. Geim, and Y. Cao, "High electron mobility, quantum Hall effect and anomalous optical response in atomically thin InSe," Nat. Nanotechnol. **12**, 223–227 (2017).

[6]S. Sucharitakul, N. J. Goble, U. R. Kumar, R. Sankar, Z. A. Bogorad, F. C. Chou, Y. T. Chen, and X. P. A. Gao, "Intrinsic electron mobility exceeding 10^3 cm^2/(V s) in multilayer InSe FETs," Nano Lett. **15**, 3815–3819 (2015).

[7]G. W. Mudd, S. A. Svatek, T. Ren, A. Patanè, O. Makarovsky, L. Eaves, P. H. Beton, Z. D. Kovalyuk, G. V. Lashkarev, Z. R. Kudrynskyi, and A. I. Dmitriev, "Tuning the bandgap of exfoliated InSe nanosheets by quantum confinement," Adv. Mater. **25**, 5714–5718 (2013).

[8]Y. Li, T. Wang, M. Wu, T. Cao, Y. Chen, and R. Sankar, "Ultrasensitive tunability of the direct bandgap of 2D InSe flakes via strain engineering Ultrasensitive tunability of the direct bandgap of 2D InSe flakes via strain engineering," 2D Mater. **5**, 021002 (2018).

[9]C. Song, F. Fan, N. Xuan, S. Huang, G. Zhang, C. Wang, Z. Sun, H. Wu, and H. Yan, "Largely tunable band structures of few-layer InSe by uniaxial strain," ACS Appl. Mater. Interfaces **10**, 3994 (2018).

[10]Q. Zhao, R. Frisenda, T. Wang, and A. Castellanos-Gomez, "InSe: A two-dimensional semiconductor with superior flexibility," Nanoscale **11**, 9845–9850 (2019).

[11]T-r. Wei, M. Jin, Y. Wang, H. Chen, Z. Gao, K. Zhao, P. Qiu, Z. Shan, J. Jiang, R. Li, L. Chen, J. He, and X. Shi, "Exceptional plasticity in the bulk single-crystalline van der Waals semiconductor InSe," Science **369**, 542–545 (2020).

[12]S. R. Tamalampudi, Y. Y. Lu, R. Kumar U, R. Sankar, C. D. Liao, K. Moorthy B, C. H. Cheng, F. C. Chou, and Y. T. Chen, "High performance and bendable few-layered InSe photodetectors with broad spectral response," Nano Lett. **14**, 2800–2806 (2014).

[13]S. Lei, L. Ge, S. Najmaei, A. George, R. Kappera, J. Lou, M. Chhowalla, H. Yamaguchi, G. Gupta, R. Vajtai, A. D. Mohite, and P. M. Ajayan, "Evolution of the electronic band structure and efficient photo-detection in atomic layers of InSe," ACS Nano **8**, 1263–1272 (2014).

[14]W. Feng, W. Zheng, W. Cao, and P. Hu, "Back gated multilayer InSe transistors with enhanced carrier mobilities via the suppression of carrier scattering from a dielectric interface," Adv. Mater. **26**, 6587–6593 (2014).

[15]M. Dai, H. Chen, F. Wang, Y. Hu, S. Wei, J. Zhang, Z. Wang, T. Zhai, and P. A. Hu, "Robust piezo-phototronic effect in multilayer-InSe for high-performance self-powered flexible photodetectors," ACS Nano **13**, 7291–7299 (2019).

[16]L. Wu, J. Shi, Z. Zhou, J. Yan, A. Wang, C. Bian, J. Ma, R. Ma, H. Liu, J. Chen, Y. Huang, W. Zhou, L. Bao, M. Ouyang, S. T. Pantelides, and H. J. Gao, "InSe/hBN/graphite heterostructure for high-performance 2D electronics and flexible electronics," Nano Res. **13**, 1127–1132 (2020).

[17]S. J. Magorrian, A. Ceferino, V. Zólyomi, and V. I. Fal'ko, "Hybrid k · p tight-binding model for intersubband optics in atomically thin InSe films," Phys. Rev. B **97**, 165304 (2018).

[18]J. Zultak, S. J. Magorrian, M. Koperski, A. Garner, M. J. Hamer, E. Tóvári, K. S. Novoselov, A. A. Zhukov, Y. Zou, N. R. Wilson, S. J. Haigh, A. V. Kretinin, V. I. Fal'ko, and R. Gorbachev, "Ultra-thin van der Waals crystals as semiconductor quantum wells," Nat. Commun. **11**, 125 (2020).

[19]Z. R. Kudrynskyi, J. Kerfoot, D. Mazumder, M. T. Greenaway, E. E. Vdovin, O. Makarovsky, Z. D. Kovalyuk, L. Eaves, P. H. Beton, and A. Patanè, "Resonant tunnelling into the two-dimensional subbands of InSe layers," Commun. Phys. **3**, 16 (2020).

[20]J. Lauth, A. Kulkarni, F. C. Spoor, N. Renaud, F. C. Grozema, A. J. Houtepen, J. M. Schins, S. Kinge, and L. D. Siebbeles, "Photogeneration and mobility of charge carriers in atomically thin colloidal InSe nanosheets probed by ultrafast terahertz spectroscopy," J. Phys. Chem. Lett. **7**, 4191–4196 (2016).

[21]W. Lu, Z. Yang, J. Hao, and D. Sun, "Terahertz relaxation dynamics of a two-dimensional InSe multilayer," Phys. Rev. B **102**, 014314 (2020).

[22]T. Kampfrath, K. Tanaka, and K. A. Nelson, "Resonant and nonresonant control over matter and light by intense terahertz transients," Nat. Photonics **7**, 680–690 (2013).

[23]T. Venanzi, M. Selig, S. Winnerl, A. Pashkin, A. Knorr, M. Helm, and H. Schneider, "Terahertz-induced energy transfer from hot carriers to trions in a MoSe$_2$ monolayer," ACS Photonics **8**, 2931–2939 (2021).

[24]G. W. Mudd, M. R. Molas, X. Chen, V. Zólyomi, K. Nogajewski, Z. R. Kudrynskyi, Z. D. Kovalyuk, G. Yusa, O. Makarovsky, L. Eaves, M. Potemski, V. I. Fal'Ko, and A. Patanè, "The direct-to-indirect band gap crossover in two-dimensional van der Waals indium selenide crystals," Sci. Rep. **6**, 39619 (2016).

[25]G. W. Mudd, A. Patane, Z. R. Kudrynskyi, M. W. Fay, O. Makarovsky, L. Eaves, Z. D. Kovalyuk, and V. Falko, "Quantum confined acceptors and donors in InSe nanosheets," Appl. Phys. Lett. **105**, 221909 (2014).

[26]T. Venanzi, H. Arora, S. Winnerl, A. Pashkin, P. Chava, A. Patanè, Z. D. Kovalyuk, Z. R. Kudrynskyi, K. Watanabe, T. Taniguchi, A. Erbe, M. Helm, and H. Schneider, "Photoluminescence dynamics in few-layer InSe," Phys. Rev. Mater. **4**, 044001 (2020).

[27]W. D. Rice, J. Kono, S. Zybell, S. Winnerl, J. Bhattacharyya, H. Schneider, M. Helm, B. Ewers, A. Chernikov, M. Koch, S. Chatterjee, G. Khitrova, H. M. Gibbs, L. Schneebeli, B. Breddermann, M. Kira, and S. W. Koch, "Observation of forbidden exciton transitions mediated by Coulomb interactions in photoexcited semiconductor quantum wells," Phys. Rev. Lett. **110**, 137404 (2013).

[28]M. A. J. Klik, T. Gregorkiewicz, I. N. Yassievich, V. Y. Ivanov, and M. Godlewski, "Terahertz modulation of the blue photoluminescence in ZnSe," Phys. Rev. B **72**, 125205 (2005).

[29]S. Zybell, H. Schneider, S. Winnerl, M. Wagner, K. Köhler, and M. Helm, "Photoluminescence dynamics in GaAs/AlGaAs quantum wells under pulsed intersubband excitation," Appl. Phys. Lett. **99**, 041103 (2011).

[30]M. Brotons-Gisbert, R. Proux, and R. Picard, "Exciton fission in monolayer transition metal dichalcogenide semiconductors," Nat. Commun. **10**, 3913 (2019).

[31]J. Černe, J. Kono, M. S. Sherwin, M. Sundaram, A. C. Gossard, and G. E. W. Bauer, "Terahertz dynamics of excitons in GaAs/AlGaAs quantum wells," Phys. Rev. Lett. **77**, 1131–1134 (1996).

[32]S. Hughes and D. S. Citrin, "Ultrafast heating and switching of a semiconductor optical amplifier using half-cycle terahertz pulses," Phys. Rev. B **58**, R15969 (1998).

[33]F. Sekiguchi, H. Hirori, G. Yumoto, A. Shimazaki, T. Nakamura, A. Wakamiya, and Y. Kanemitsu, "Enhancing the hot-phonon bottleneck effect in a metal halide perovskite by terahertz phonon excitation," Phys. Rev. Lett. **126**, 077401 (2021).

[34]C. Poellmann, P. Steinleitner, U. Leierseder, P. Nagler, G. Plechinger, M. Porer, R. Bratschitsch, C. Schüller, T. Korn, and R. Huber, "Resonant internal quantum transitions and femtosecond radiative decay of excitons in monolayer WSe$_2$," Nat. Mater. **14**, 889–893 (2015).

[35]J. Černe, A. G. Markelz, M. S. Sherwin, S. J. Allen, M. Sundaram, A. C. Gossard, P. C. van Son, and D. Bimberg, "Quenching of excitonic

quantum-well photoluminescence by intense far-infrared radiation: Free-carrier heating," Phys. Rev. B **51**, 5253–5262 (1995).

[36] T. V. Shubina, W. Desrat, M. Moret, A. Tiberj, O. Briot, V. Y. Davydov, M. A. Semina, and B. Gil, "InSe as a case between 3D and 2D layered crystals for excitons," Nat. Commun. **10**, 3479 (2019).

[37] J. Felton, E. Blundo, S. Ling, J. Glover, Z. R. Kudrynskyi, O. Makarovsky, Z. D. Kovalyuk, E. Besley, G. Walker, A. Polimeni, and A. Patané, "The interaction of hydrogen with the van der Waals crystal γ-inse," Molecules **25**, 2526 (2020).

[38] D. Christiansen, M. Selig, G. Berghäuser, R. Schmidt, I. Niehues, R. Schneider, A. Arora, S. M. de Vasconcellos, R. Bratschitsch, E. Malic, and A. Knorr, "Phonon sidebands in monolayer transition metal dichalcogenides," Phys. Rev. Lett. **119**, 187402 (2017).

[39] J. K. Katahara and H. W. Hillhouse, "Quasi-fermi level splitting and sub-bandgap absorptivity from semiconductor photoluminescence," J. Appl. Phys. **116**, 173504 (2014).

[40] D. N. Purschke, M. Na, A. Longman, L. V. Titova, and F. A. Hegmann, "Enhancement of hot-carrier photoluminescence with intense terahertz pulses," Appl. Phys. Lett. **112**, 072105 (2018).

[41] M. Kira, F. Jahnke, W. Hoyer, and S. Koch, "Quantum theory of spontaneous emission and coherent effects in semiconductor microstructures," Prog. Quantum Electron. **23**, 189–279 (1999).

[42] C. Ferrer-Roca, A. Segura, M. Andrés, J. Pellicer, and V. Muñoz, "Investigation of nitrogen-related acceptor centers in indium selenide by means of photoluminescence: Determination of the hole effective mass," Phys. Rev. B **55**, 6981 (1997).

[43] L.-B. Shi, S. Cao, M. Yang, Q. You, K.-C. Zhang, Y. Bao, Y.-J. Zhang, Y.-Y. Niu, and P. Qian, "Theoretical prediction of intrinsic electron mobility of monolayer InSe: First-principles calculation," J. Phys.: Condens. Matter **32**, 065306 (2020).

[44] H. Wang, G. Qin, J. Yang, Z. Qin, Y. Yao, Q. Wang, and M. Hu, "First-principles study of electronic, optical and thermal transport properties of group III–VI monolayer MX (M = Ga, In; X= S, Se)," J. Appl. Phys. **125**, 245104 (2019).

[45] B. N. Murdin, W. Heiss, C. J. G. M. Langerak, S.-C. Lee, I. Galbraith, G. Strasser, E. Gornik, M. Helm, and C. R. Pidgeon, "Direct observation of the LO phonon bottleneck in wide GaAs/Al$_x$ Ga$_{1-x}$ As quantum wells," Phys. Rev. B **55**, 5171–5176 (1997).

[46] See https://rodare.hzdr.de/ "Rodare" to find the raw data of the experiment reported in this publication.

ROYAL SOCIETY
OF CHEMISTRY

Nanoscale

PAPER

Mid- and far-infrared localized surface plasmon resonances in chalcogen-hyperdoped silicon†

Mao Wang, [ID] *[a] Ye Yu, [ID] *[b] Slawomir Prucnal, [ID] [a] Yonder Berencén, [ID] [a]
Mohd Saif Shaikh, [ID] [a] Lars Rebohle, [ID] [a] Muhammad Bilal Khan, [ID] [a] Vitaly Zviagin,[c]
René Hübner, [ID] [a] Alexej Pashkin, [ID] [a] Artur Erbe, [ID] [a,d] Yordan M. Georgiev, [ID] [a,e]
Marius Grundmann, [ID] [c] Manfred Helm,[a,f] Robert Kirchner[b,d] and Shengqiang Zhou [ID] [a]

Plasmonic sensing in the infrared region employs the direct interaction of the vibrational fingerprints of molecules with the plasmonic resonances, creating surface-enhanced sensing platforms that are superior to traditional spectroscopy. However, the standard noble metals used for plasmonic resonances suffer from high radiative losses as well as fabrication challenges, such as tuning the spectral resonance positions into mid- to far-infrared regions, and the compatibility issue with the existing complementary metal−oxide-semiconductor (CMOS) manufacturing platform. Here, we demonstrate the occurrence of mid-infrared localized surface plasmon resonances (LSPR) in thin Si films hyperdoped with the known deep-level impurity tellurium. We show that the mid-infrared LSPR can be further enhanced and spectrally extended to the far-infrared range by fabricating two-dimensional arrays of micrometer-sized antennas in a Te-hyperdoped Si chip. Since Te-hyperdoped Si can also work as an infrared photodetector, we believe that our results will unlock the route toward the direct integration of plasmonic sensors with the on-chip CMOS platform, greatly advancing the possibility of mass manufacturing of high-performance plasmonic sensing systems.

[a]*Helmholtz-Zentrum Dresden-Rossendorf, Institute of Ion Beam Physics and Materials Research, Bautzner Landstraße 400, 01328 Dresden, Germany. E-mail: m.wang@hzdr.de*
[b]*Institute of Semiconductors and Microsystems, Technische Universität Dresden, 01062 Dresden, Germany. E-mail: ye.yu@tu-dresden.de*
[c]*Felix-Bloch-Institut für Festkörperphysik, Universität Leipzig, Linnéstraße 5, 04103 Leipzig, Germany*
[d]*Centre for Advancing Electronics Dresden (CfAED), Technische Universität Dresden, 01062 Dresden, Germany*
[e]*Institute of Electronics at the Bulgarian Academy of Sciences, 1784 Sofia, Bulgaria*
[f]*Institut für Angewandte Physik (IAP), Technische Universität Dresden, 01062 Dresden, Germany*
†Electronic supplementary information (ESI) available. See DOI: 10.1039/d1nr07274a

I.   Introduction

The field of plasmonics has elicited great attention and research efforts for potential applications as varied as enhanced sensing, waveguides for integrated optical interconnects, and nanoscale optoelectronic devices.[1–3] Surface plasmons generated by the coupling of collective charge oscillations with electromagnetic radiation at a conducting surface[4] offer effective light–matter interactions in nanoscale structures with sub-wavelength light confinement and large enhancement of the local electromagnetic field intensity.[5,6] In this framework, materials with a good crystalline quality and a small amount of plasmon losses are proposed for plasmonic applications that span a wide range of electromagnetic frequencies.[5,7,8] Particularly, the mid-infrared (MIR) spectral range that covers the frequency band from 3000 to 300 cm^{-1} is of high interest for chemical and biological molecular sensing,[9–11] since many molecules display unique spectral vibrational fingerprints in this range. Therefore, a plasmonic material platform that can be tailored to the frequency range of interest with strong subwavelength confinement is desired.[12]

It has been recently shown that hyperdoped semiconductors[10,13–18] provide a promising material system for the development of a plasmonic platform with inherent advantages in the mid-infrared (MIR) region.[19,20] Here, hyperdoping means a doping concentration well above the impurity solid solubility limit. Contrary to metals (Au, Ag, and Al), in which the density of free electrons is fixed and the resulting resonance frequencies are mainly located in the visible and near-infrared (VIS-NIR) spectral range,[11] the plasmon resonance in doped semiconductors can be tuned over a broad spectral window, ranging from NIR to far-infrared (FIR) by controlling the carrier concentration.[12,15,21–26] Among hyperdoped semiconductor materials, Si is the most desired material for plasmonic applications in the MIR spectral range, owing to its

compatibility with the complementary metal–oxide-semiconductor (CMOS) technology.[21,22,27–32] Moreover, a plasmonic material based on doped Si has certain advantages over other doped semiconductors, such as cost-effectiveness, environmental friendliness and the well-developed and versatile fabrication process. Importantly, compared to III–V semiconductors, the absence of optical phonon absorption in the FIR spectral range in Si will naturally reduce the plasmon losses since Si is a non-polar semiconductor.[15,33–35] Recently, Si hyperdoped with the chalcogen dopant Te has gained increasing attention in the development of room-temperature MIR photodetectors.[36] Also, Te-hyperdoped Si exhibits a high free-electron concentration with a reasonably high mobility,[37] as well as a better thermal stability as compared to other deep-level impurities.[33] This boosts the potential of Te-hyperdoped Si serving as a nanoscale MIR plasmonics platform with a broadly tunable plasma frequency. Such a platform could allow an easy integration with the current chip technology, providing room-temperature enhanced IR sensing.

In this work, we explore the potential of using Si hyperdoped with the deep-level dopant Te as an alternative for MIR-FIR plasmonic materials. A plasma frequency ω_p of around 1880–1630 cm^{-1} is obtained in the Te-hyperdoped Si material. In addition, micrometer-sized antenna arrays, which are fabricated from the Te hyperdoped-Si layer *via* electron-beam lithography and reactive ion etching, exhibit an enhanced localized plasmon resonance in the spectral range of 100 to 700 cm^{-1} compared to the non-patterned Te-hyperdoped Si material. This work points out the potential of Si hyperdoped with Te for plasmon-enhanced sensing applications such as the detection of the vibrational fingerprints of thin molecular films.

II. Methods

A. Experimental methods

A non-equilibrium approach combining ion implantation and flash lamp annealing (FLA) is used to achieve solid-phase epitaxial regrowth of hyperdoped-Si layers with a Te doping concentration several orders of magnitude above the equilibrium solid solubility. The electrical and optical properties of Si hyperdoped with Te have been systematically investigated previously.[36,37] It was found that the hyperdoped-Si layer with a Te concentration of 1.5% exhibits below-bandgap infrared absorption and yields high electron concentration. In this work, we used (100)-oriented double-side polished Si wafers (*p*-type, boron-doped, $\rho \approx$ 1–10 Ωcm) with a thickness of around 380 μm. A triple implantation with energies of 350 keV, 150 keV and 50 keV with a fluence ratio of 5.3 : 2.3 : 1 was applied to compensate the Gaussian distribution of Te dopants during the implantation process.[31] The dopant concentration and the doping depth can be increased by increasing implantation fluence and energy, respectively. The parameters can be simulated by using the software of the Stopping and Range of Ions in Matter (SRIM).[38–40] Note that, in our pre-

vious works,[36,37] we used pulsed laser melting to recrystallize Te-implanted Si with a thickness of about 100 nm. Here, milli-second-range FLA is applied to recrystallize the implanted layer.[41,42] The FLA was performed in nitrogen ambient with a pulse length of 3 ms along with an energy density of around 58 J cm^{-2}. This corresponds to a temperature in the range of around 1200 ± 50 °C at the sample surface. Further details on the FLA system employed in our experiments can be found in the ESI.† The optimal FLA parameters were obtained by inspecting the crystalline quality of the implanted layers using micro-Raman spectroscopy.

The antenna patterning was achieved by electron-beam lithography and reactive ion etching (see ESI† for more details). The geometrical details of the two-dimensional Te-hyperdoped Si antenna arrays are schematically depicted in Fig. 1. The rectangular antenna arms have a size of 2 μm (length) × 0.8 μm (width), and two equal arms featuring different gap sizes varied between 0.2 and 1 μm.

Structural characterization of the Te-hyperdoped Si layers and antenna arrays were performed by micro-Raman spectroscopy using a linearly polarized continuous 532 nm Nd:YAG laser for excitation and by scanning electron microscopy (SEM, S-4800, Hitachi). In addition, the microstructural properties of the FLA-treated Te-hyperdoped Si layer with a Te doping concentration of 1.5% were investigated by high-angle annular dark-field scanning transmission electron microscopy (HAADF-STEM) imaging coupled with spectrum imaging analysis based on energy-dispersive X-ray spectroscopy (EDXS) to obtain cross-sectional element distribution maps. Further details concerning the TEM techniques employed in our experiments can be found elsewhere.[40] The electrical properties were characterized using a Lake Shore Hall measurement system in a van der Pauw configuration. IR measurements were carried out at room temperature by Fourier-transform infrared spectroscopy (FTIR, Bruker Vertex 80v). A Deuterated L-Alanine doped Triglycine Sulphate (DLaTGS) detector was used for the detection of MIR (from 10 000 to 400 cm^{-1}) radiation, while a deuterated triglycine sulfate (DTGS) detector was used for FIR (from 700 to 10 cm^{-1}). FTIR
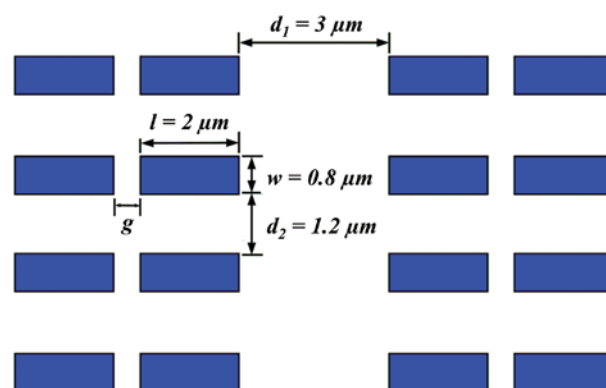
Fig. 1 A sketch of the geometry of the Te-hyperdoped Si antenna arrays. The geometrical details are indicated in the figure.

measurements were performed in vacuum to eliminate the infrared absorption lines of the atmosphere. A reflection geometry was employed to quantify the absolute reflectivity of FLA-performed Te-hyperdoped Si layers and the antenna arrays. The reflectance of a gold mirror was measured as a 100% reflectance standard for the FTIR data.

B. Theoretical methods

Electromagnetic simulations were carried out using finite-difference time domain (FDTD) methods (FDTD 3D Electromagnetic Simulator, DEVICE Multiphysics Simulation Suite, Lumerical Inc. version 8.22.2072).[43]

Before FDTD simulations, the broadband optical properties of the material, more specifically the real and imaginary part of permittivity need to be determined first. The permittivity of bulk highly doped semiconductors can be modeled approximatively across a wide frequency range using the Drude model:

$$\varepsilon(\omega) = \varepsilon_s \left(1 - \frac{\omega_p^2}{\omega^2 + i\omega\Gamma}\right), \quad \omega_p^2 = \frac{ne^2}{\varepsilon_s \varepsilon_0 m^*(n)} \qquad (1)$$

$$\varepsilon(\omega) = \varepsilon' + i\varepsilon'' = \varepsilon_s \left(1 - \frac{\omega_p^2}{\omega^2 + \Gamma^2}\right) + i\varepsilon_s \left(\frac{\Gamma \omega_p^2/\omega}{\omega^2 + \Gamma^2}\right) \qquad (2)$$

where the frequency-dependent permittivity $\varepsilon(\omega)$ is characterized by the screened plasma frequency ω_p, the scattering rate Γ, the background dielectric constant ε_s (for Si, $\varepsilon \approx 11.7$) and the permittivity of free space ε_0. The screened plasma frequency ω_p given above is characterized by the dielectric constant $\varepsilon_s \varepsilon_0$, the free-carrier density n, the charge of the electron e and the non-parabolic doping-dependent effective mass of the free carriers $m^*(n)$ ($0.27m_e$ for n-type heavily doped Si[26,44,45]). If Γ is small, ω_p marks the approximate spectral position where the sign of the real component of the semiconductor permittivity (ε') switches from positive to negative. Therefore, such kind of semiconductors can serve as an engineered MIR-FIR plasmonic material at frequencies (wavelengths, $\lambda_p = \frac{2\pi c}{\omega_p}$) lower (greater) than the plasma frequency of the material. Particularly, the plasma frequency can be accurately controlled by the doping concentration of the semiconductor.

III. Results and discussion

A. Material properties of the Te-hyperdoped Si layer

Raman spectroscopy and Hall measurements were performed in order to characterize the structural (Fig. 2(a)) and electrical properties (Fig. 2(c) and (d)), respectively (further data can be found in section D of the ESI†). The Raman spectrum of the as-implanted sample shows a very broad Raman band located at 460 cm^{-1}, which corresponds to a typical feature of the amorphous silicon layer created during the Te implantation process.[46,47] After FLA, only the sharp peaks at 520 cm^{-1} and 303 cm^{-1} are observed, which are ascribed to the transverse optical (TO) phonon mode and the second-order two trans-

verse acoustic phonon (2TA$_{Si}$) scattering, respectively. This indicates that the crystalline structure of the FLA-treated Te-hyperdoped Si layer is completely restored with comparable quality as the virgin Si wafer. A representative cross-sectional HAADF-STEM image superimposed with the corresponding EDXS-based element distributions is shown in Fig. 2(b). Apart from the native oxide layer at the surface, Te is found to be quite evenly distributed within the top ~120 nm of the Si wafer. However, the Te dopants show segregation with further increasing depth. In our previous work, we used pulsed laser annealing to melt Te-implanted Si, where the implanted layer is around 120 nm thick and the Te distribution is homogenous.[36] Here, we use a higher implantation energy along with flash lamp annealing to fabricate thicker hyperdoped samples, leading to some Te segregation at the interface between in the implanted layer and the Si substrate. In order to get a more homogenous Te distribution in thicker hyperdoped layers, the parameters for flash lamp annealing such as pulse duration and energy, pre-heating temperature and duration should be optimized.[48] As shown in Fig. 2(c) and (d), the Te-hyperdoped Si displays n-type and metal-like conductivity. The sheet carrier density and the carrier mobility measured at 300 K are 1.5×10^{15} cm^{-2} and 32 cm^2 V^{-1} s^{-1}, respectively (further data can be found in section D of the ESI†). As indicated in the cross-sectional STEM image (Fig. 2(b)), the Te impurities distribute within a depth of up to around 220 nm and the segregation occurs between 120 and 220 nm. Therefore, the estimated volume carrier density ranges from 1.25×10^{20} to 9.4×10^{19} cm^{-3} depending on the assumed effective thickness. This indicates an electrical activation efficiency of around 15% at room temperature. According to the theoretical Drude formalism (as shown in eqn (1) and (2)) and assuming our Te-hyperdoped Si layer as a bulk material, ω_p is calculated to be around 1880–1630 cm^{-1}, using the electrical transport data.

To cross-examine the accuracy of the plasma frequency of the bulk material obtained above with respect to the experimental values, we performed a further analysis of the reflection spectrum of the thin film using transfer matrix method (TMM). Fig. 2(c) displays the normal-incident reflectance (R/R_{Au}) spectra of the Te-hyperdoped Si layers measured by FTIR at room temperature. The spectrum of a Si wafer was also measured for comparison. The red dash-dotted line displays a three-layer system simulation of the reflectivity spectrum of Te-hyperdoped Si as described in the following. The approximated dielectric function of the implanted layer was constructed based on the multi-layer transfer matrix formalism with 20° incidence angle *via* VASE (vase-ellipsometer-liquid-prism-cell) software.[49] This model consists of two layers: (i) the implanted layer described by the Drude approximation function, and (ii) the Si substrate described by the tabulated optical constants of monocrystalline Si. The fitting gives a carrier concentration of 1.27×10^{20} cm^{-3} and plasma frequency is around 1900 cm^{-1} with the input free electron mass of $0.27m_e$, which is reasonable for n-type deep-level impurity heavily doped Si.[26,44,45] The extracted plasma frequency from
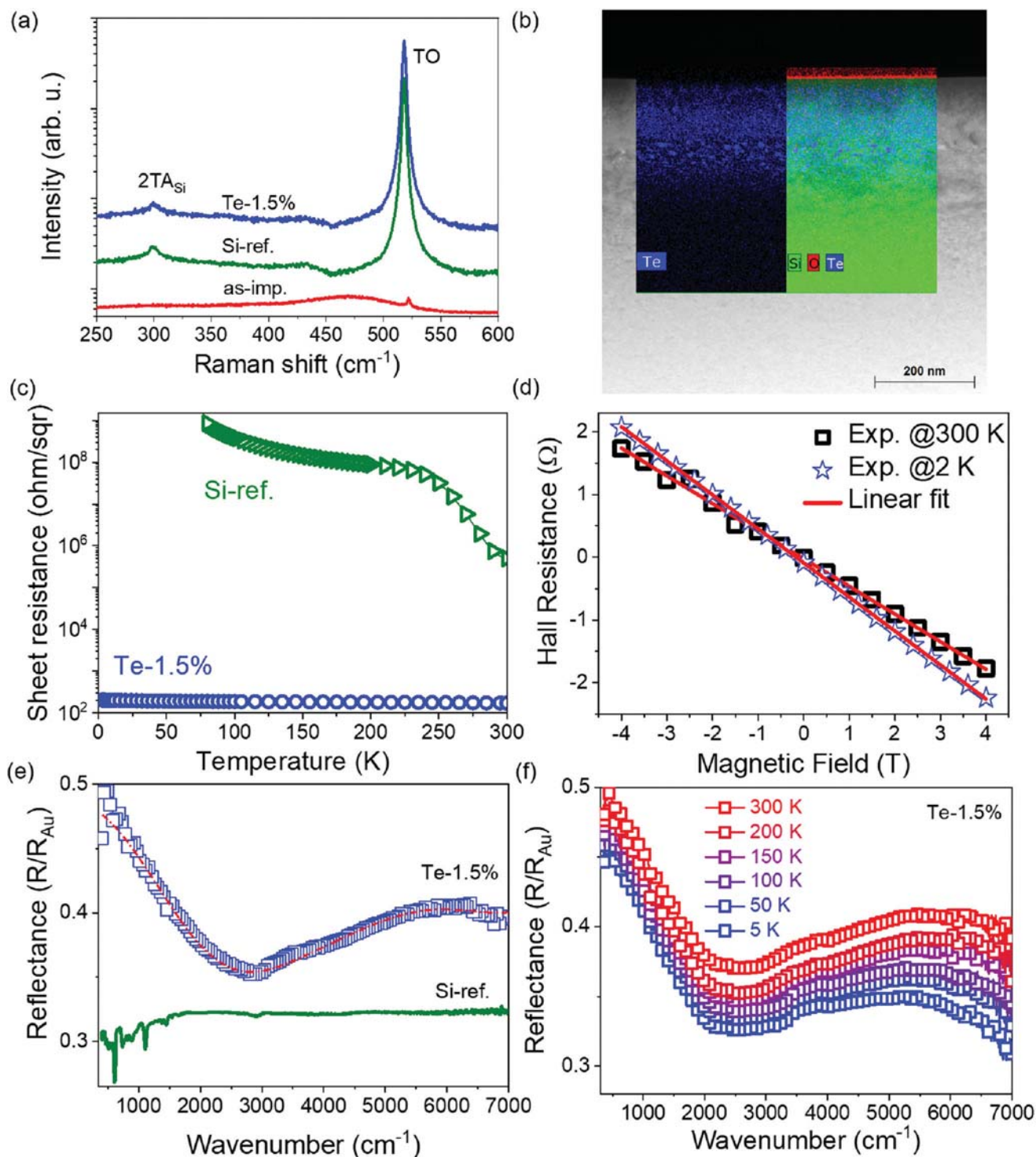
Fig. 2 Material characterization for FLA-treated Te-hyperdoped Si sample with the doping concentration of 1.5%. (a) Room-temperature micro-Raman spectra. The Raman spectra of the as-implanted sample as well as virgin Si (red and green solid lines, respectively) are also included for comparison. The spectra are stacked vertically with a constant offset for clarity. (b) Cross-sectional HAADF-STEM image superimposed with the corresponding EDXS element distributions (blue: tellurium, green: silicon, red: oxygen). Apart from the native oxide layer at the surface, Te is found to be quite evenly distributed within the top ~120 nm of the Si wafer. However, the Te dopants show segregation with further increasing depth. (c) The temperature-dependent sheet resistances. Also, the Si substrate is included as comparison. (d) The Hall resistance at 2 K and 300 K with a linear fit to experimental data. (e) Room-temperature reflectance spectra. The reflectivity of a bare Si wafer is included as a reference. (f) Reflectance measurements at different temperatures.

the fitting is shifted to a slightly higher wavenumber compared to the one obtained from the Drude formalism. The discrepancy may be related to the rather thin film thickness together with the graded doping; as a consequence, the fit allows many different solutions of similar quality, yet none could be found with optimal agreement. Besides, the line shape of the spectrum can be affected by the measurement conditions, such as the brilliance of the light source,[50,51] the maximum angle of acceptance of the detector.[52] One must carefully examine the experimental and instrumental conditions used during the measurement of the reflectance spectra, from which the broadband permittivity of the material is deduced. Fig. 2(d) displays the temperature-dependent spectral reflectance of the Te-hyperdoped layer. The reflectance spectrum at different temperatures exhibits similar behavior, which suggests that Te-hyperdoped Si can be used as a plasmonic material in a broad temperature range. In addition, the plasma frequency and optical response of Te-hyperdoped Si can be tuned by altering the doping concentration as well as the electrical and optical excitation.

B. LSPR in Te-hyperdoped Si: electromagnetic simulations

In order to understand and design the antenna response, we have performed FDTD simulations. We started with the simplest structure to simulate the spectral response of one

nanobar with an atomic Te doping concentration of 1.5% on a Si substrate in order to first analyze the possible range of plasmonic resonances. The dimensions of the antennas were set to be the same width (w) of 0.8 μm and thickness of 0.3 μm, as mentioned in the previous section, except the arm length (l) was varied from 0.5 to 3 μm. The corresponding extinction spectra and electric field intensity distribution are shown in Fig. 3. As displayed in Fig. 3(a), when the polarization is perpendicular to the long axis of the antenna, the spectral position of the resonance does not change as the antenna length increases. On the other hand, when the electric field polarization is parallel to the long antenna axis, the plasmon resonance shows a red shift (for a depiction in linear wavelength scale see ESI Fig. S1†) with increasing antenna length (Fig. 3(b)). The difference in the extinction cross-section shown in Fig. 3(a) and (b) indicates that the LSPR mode in Fig. 3(a) is much less intensive than that in Fig. 3(b). To understand the nature of these two modes, we further calculated the corresponding electric field intensity distributions at the resonance positions (at the wavelength of 25 μm), which is displayed in the top-down view in Fig. 3(c) and (d), respectively. As displayed in the coordinate, the antenna has a width of 0.8 μm and an arm length of 2 μm. As the polarization direction is perpendicular to the long axis of the antenna, shown in Fig. 3(c), the free electrons only accumulate along the longer
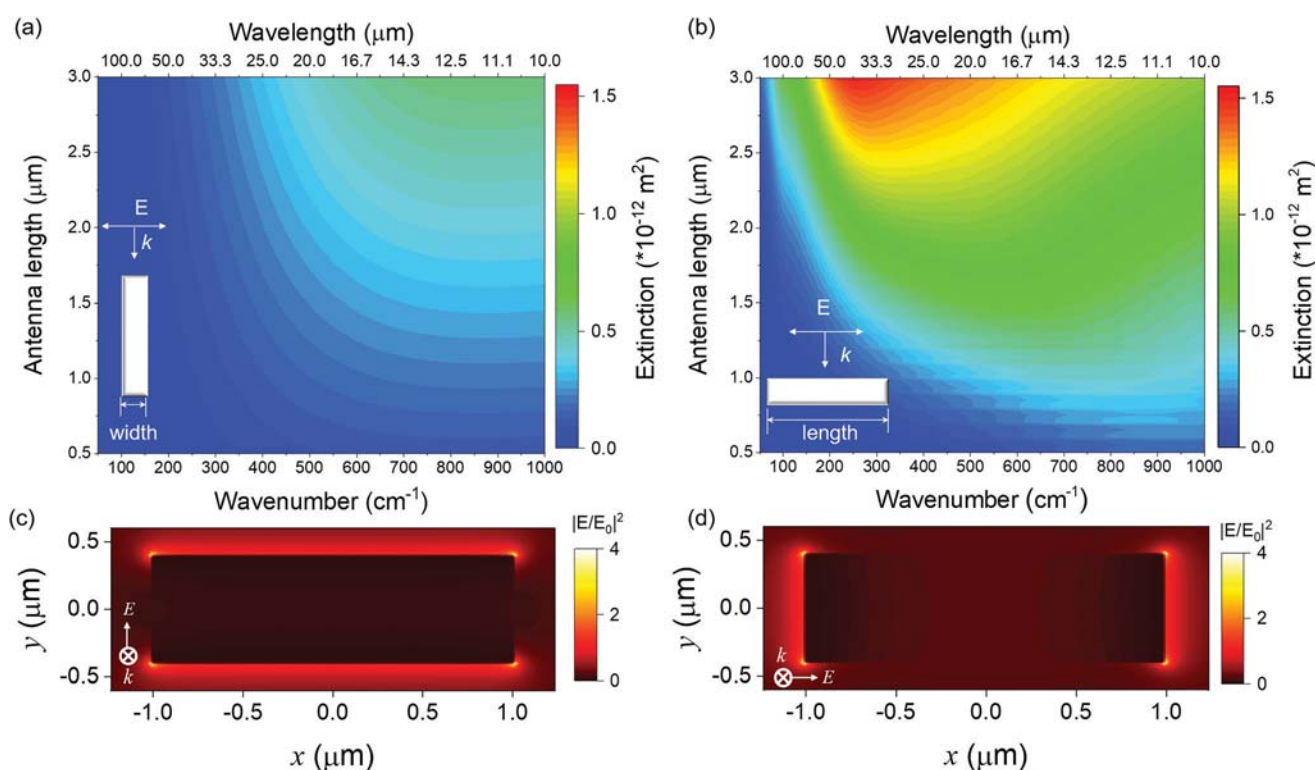
Fig. 3 The simulated extinction spectra as a function of the antenna length of a single antenna with the electric field polarization perpendicular to the long antenna axis (a) and parallel to the long antenna axis (b). The antenna length against wavelength is plotted in Fig. S1 in the ESI† for clarity. Top-down view of the electric field distribution map of single-arm antenna at the LSPR position (at the wavelength of 25 μm), the electric field polarization perpendicular to the long antenna axis (c) and parallel to the long antenna axis (d). The electric field enhancement is obtained by normalizing the electric field intensity to the incident plane wave amplitude E_0.

edge (length), indicating that this plasmonic resonance is a transverse mode. Whereas, in the case of Fig. 3(d), since the polarization direction is parallel to the long axis of the antenna, the free electrons in turn accumulate along the shorter edge (width), exciting the longitudinal mode at longer wavelength (Fig. 3(d)). This in general results in the strong near-field enhancement, which will be beneficial in surface-enhanced spectroscopies.

From the FDTD simulations of the single antenna in Fig. 3, we have successfully obtained the spectral range of the LSPRs for such a system. We then investigate the plasmonic properties of an array of coupled antennas, *i.e.* two nanoantennas placed very close to each other, forming a repeating structural unit, as illustrated in Fig. 1. The separations between units along the x and y axis were set to be 3 μm and 1.2 μm, respectively. The dimensions of the nanoantennas were kept constant: $l = 2$ μm; $w = 0.8$ μm; and $t = 0.3$ μm. Only the gap size between the two adjacent antennas was varied from 0.1 μm to 1 μm. However, since both periodicities are much smaller than the wavelength of the incident radiation resonant to the plasmon of Te-hyperdoped Si, we expect the diffractive far-field coupling not to interfere with the LSPRs. Fig. 4(a) reveals the broad-band spectral response of the coupled system, showing two reflection peaks sandwiching a reflection dip in between, indicating that the coupling between two adjacent nanoantennas is present. The presence of coupling is also corroborated by the fact that, as the gap size increases, the reflection peaks experience a slight blue shift due to the decreased near-field coupling strength. However, further careful examination is still needed, since the reflection intensity is expected to be consistent with the transmission intensity. Hence, the electric field intensity distribution, along with the corresponding charge distribution of the nanonantenna pair at both reflection peaks and valleys were plotted in the cross-section view, shown in Fig. 4(c) through (f), taking the structure with gap size $g = 0.2$ μm as an example. The spectral positions were all marked correspondingly in Fig. 4(b). Simulation reveals that at small wavenumbers, the system exhibits predominately the characteristics of a coupled dipolar resonance,[53,54] such as Fig. 4(c) and (d). This indicates that, an additional mode is created at a longer wavelength due to the coupling between the two adjacent nanoantennas. However, at shorter wavelength, the system exhibits briefly a quadrupolar resonance, shown in Fig. 4(e), and then transitions into non-coupled dipolar resonance (Fig. 4(f)). Note that the six-node charge distribution in Fig. 4(e) is because the energy level of the quadrupolar resonance is too close to the non-coupled dipolar resonance. This plasmonic behavior over the spectrum of interest suggests a classic plasmonic hybridization model, where the longitudinal dipolar resonances are treated as electric dipoles and the quadrupolar resonances as an electric dipole pair with opposite moment, the sketch of which is shown in Fig. S2 in ESI.†

Upon plasmonic hybridization, the dipolar resonances form a bonding mode, occupying a lower energy level, as well as an anti-bonding mode, occupying a higher energy level. At the same time, the quadrupolar resonances experience the same process, creating two additional energy levels. However, from FDTD simulations, only two energy levels were observed (Fig. 4(c)–(e)), indicating that the two anti-bonding modes are likely residing at the energy levels beyond the plasma frequency. On the other hand, we also observed that the non-coupled dipolar resonance remains prominent over a broad range of the spectrum, as evidenced in Fig. 4(f). This result indicates that even with a relatively small gap size that we simulated, the coupling strength is relatively low, which is corroborated by the small permittivity of the Te-hyperdoped Si material, as compared to the conventional plasmonic materials such as gold. It is safe to assume that, if a system with high coupling strength is needed, a much smaller gap size is generally required. However, this does not negate the value of plasmonic semiconductor materials. First, the "weak" confinement, despite the lower local field intensity, allows the plasmonic resonances to reach the bulk environment with a large interrogation volume. This could provide more stable detection performance at large distances from the semiconductor/dielectric interface, as well as potentially reducing the detection limit. Second, the propagation loss from the plasmonic semiconductor material is very low, since the imaginary part of the permittivity is a few orders of magnitude lower than that of plasmonic metals. While this is by no means the defining factor of a "better" material, it does provide a unique feature as compared to classic plasmonic metals. Additionally, the Te-hyperdoped Si material can result in an effective n-type doping with carrier density approaching 10^{21} cm^{-3},[37] which is only one order of magnitude lower than that of metal, in conjunction with a few comparative studies,[55,56] it would be reasonable to assume that the plasmonic performance from the Te-hyperdoped Si material could be on par with plasmonic metal structures.

C. LSPR in Te-hyperdoped Si: infrared spectral properties

The hyperdoped Si paired-arm antenna arrays with a Te doping concentration of 1.5% were designed based on the considerations of providing maximum coupling between the paired antenna arms and preserving the maximum coverage of the substrate. Therefore, the period for the antenna arrays is designed to be large enough to avoid significant near-field interactions between two neighboring paired antennas, where the near field coupling is only possible between the two nanobars within the same pair, as verified by the electromagnetic simulations (FDTD electric field intensity map) shown in Fig. 4. At the same time, the period for the antenna arrays should be smaller than the wavelength of the incident radiation resonant to the plasmon to avoid crosstalk between LSPR and diffractive far-field coupling. Thereby, with a small period, we can ensure that the spectral response is strong enough since more nanostructures will be measured in the same unit area. In this design, we can ensure that the plasmonic antennas provide spectral response strong enough to be detected. Moreover, the gap (g) between the two arms is varied from 0.2 μm to 1 μm, which aims at affecting the local intensity distribution, thereby further boosting the enhancement and con-
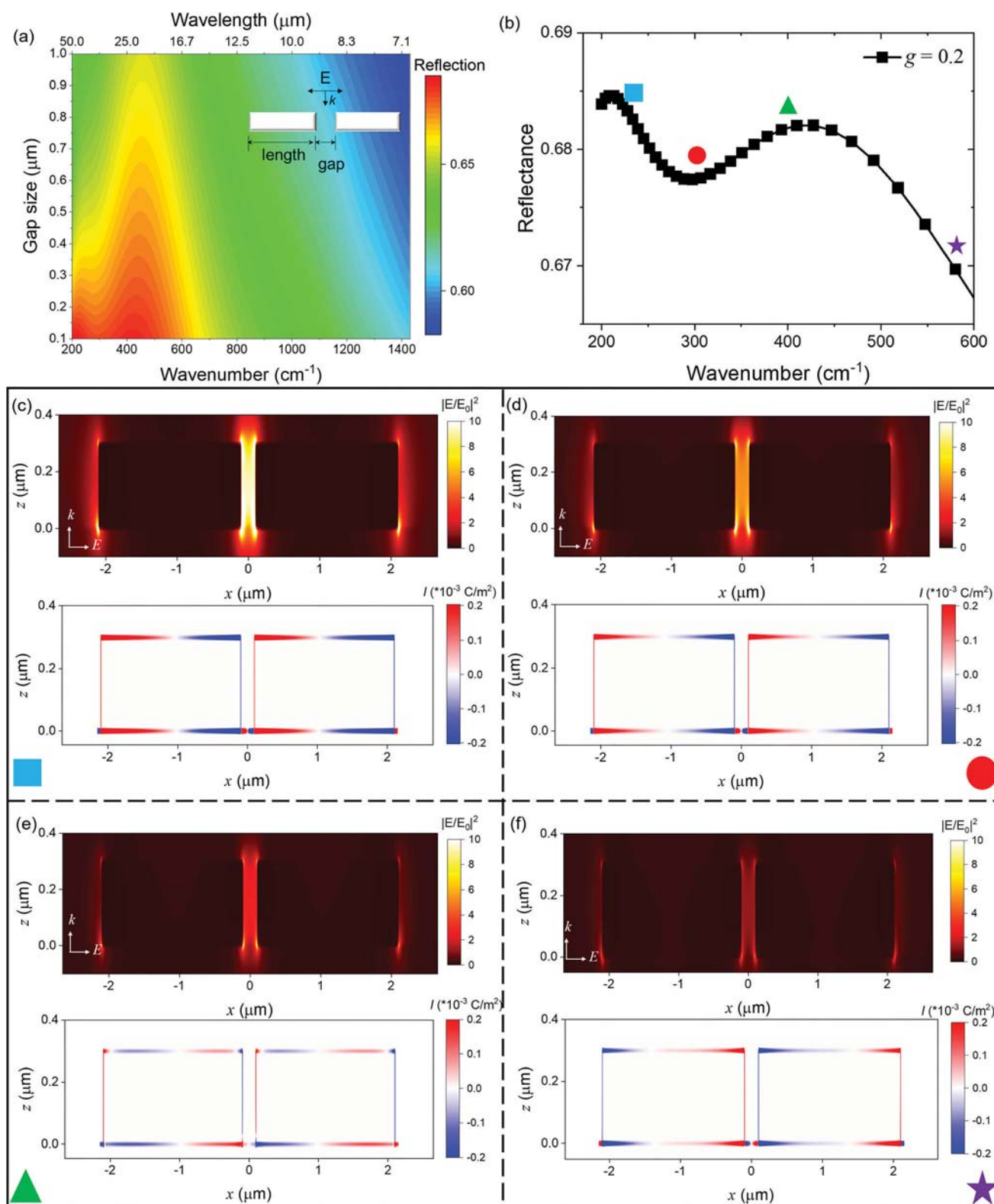
Fig. 4 The FDTD simulations for the paired-armed antennas. The simulated antenna has a width of 0.8 µm, a thickness of 0.3 µm and an arm length of 2 µm. (a) The simulated reflection spectra as a function of the gap size in an array of paired-arm antennas (antenna arm length, 2 µm) with the electric field polarization parallel to the long antenna axis. (b)–(f) are simulation results of a nanoantenna pair consisting of two identical nanobars with a gap size of 0.2 µm. (b) Simulated reflection spectrum and the cross section view of the electric field enhancement distribution (upper panels in c–f), as well as the charge distribution (lower panels in c–f) at the wavelengths of 44 µm (227 cm^{-1}) (c, marked with a blue solid square), 33 µm (303 cm^{-1}) (d, marked with a red circle), 25 µm (400 cm^{-1}) (e, marked with a green triangle), and 17 µm (588 cm^{-1}) (f, marked with a purple star), respectively. The electric field enhancement is obtained by normalizing the electric field intensity to the incident plane wave amplitude E_0.

finement of the field. Representative SEM images of Te-hyper-doped Si paired-arm antenna arrays are presented in Fig. 5, where the antennas have a width (w) of 0.8 μm, an arm length (l) of 2 μm and consist of two equal arms featuring a gap size of 0.2 μm (Fig. 5(a)), 0.3 μm (Fig. 5(b)), 0.4 μm (Fig. 5(c)), and 1.0 μm (Fig. 5(d)). In order to investigate the sensing appli-
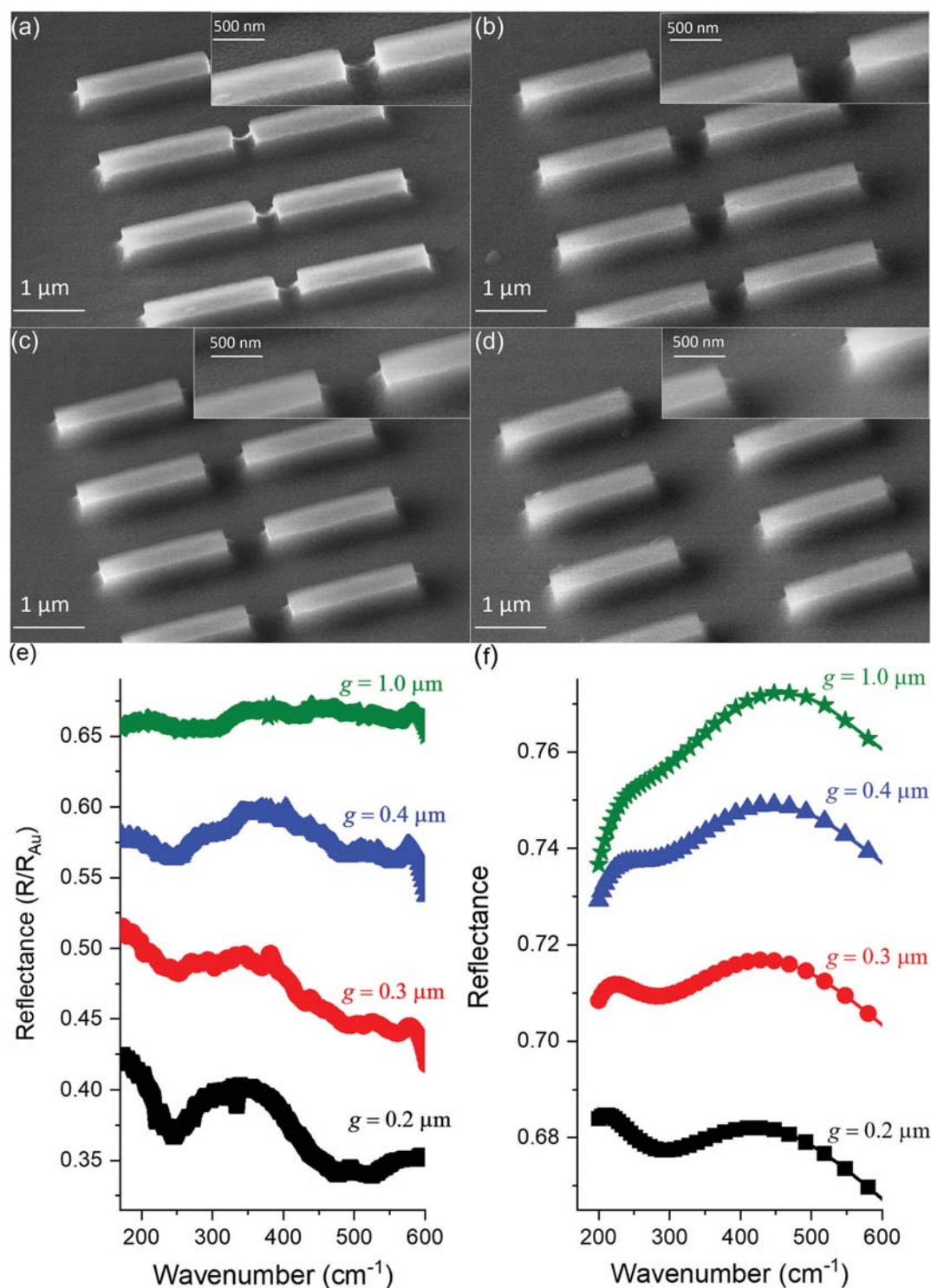
Fig. 5 Demonstration of MIR-FIR localized surface plasmon resonances in Te-hyperdoped Si antenna arrays. Bird's-eye SEM images of antenna arrays with an antenna width of 0.8 μm, an arm length of 2 μm and two equal arms featuring different gap sizes: (a) 0.2 μm, (b) 0.3 μm, (c) 0.4 μm and (d) 1.0 μm. (e) Representative reflection spectra for the antenna arrays shown in (a)–(d). The spectra are measured with the electric field polariz-ation parallel to the long antenna axis. (f) The simulated reflection spectra of the same antenna arrays in (e), which correspond to horizontal cuts through Fig. 4(a). The spectra in (e) and (f) have been vertically offset with a constant of 0.1 for clarity.

cations of Te-hyperdoped Si antenna arrays, it is worth discussing the antenna signal in reflection geometry. Particularly, it is important to use the reflectance spectrum in realistic MIR chemical sensing devices, since the aqueous solutions are not transparent at MIR frequencies.

Fig. 5(e) demonstrates the reflection spectra in the far-infrared range at normal incidence with the electric field polarization direction parallel to the long antenna axis. The spectra recorded in the mid-infrared range are shown in Fig. S3 in the ESI.† We conducted a comparison of the measured reflection spectra of the paired-arm antenna arrays with four different gap size of 0.2, 0.3, 0.4, and 1.0 µm, with l = 2.0 µm and w = 0.8 µm for an individual antenna arm. In order to extract the antenna optical response, the reflectance is displayed as R/R_{Au}, with R and R_{Au} being the reflection spectra acquired from the antenna array sample and from a gold mirror, respectively. The experimental results clearly display two sets of reflection peaks and valleys, shown in Fig. 5(e). In addition, these features barely observed when the excitation electric field is oriented perpendicular to the long antenna axis (shown in Fig. S4 in ESI†). This suggests that the line shape that we observe in Fig. 5(e) is indeed caused by the presence of longitudinal plasmonic modes. Furthermore, a blue shift of the features with increasing gap size is observed, indicating that the coupling between two adjacent nanobars is present. Fig. 5(f) presents the simulated reflection spectra for the same antenna arrays shown in Fig. 5(e). The line shapes of the two sets of spectra show reasonable resemblance to each other, indicating that our simulation can provide a good insight to the plasmonic behavior of the system. However, discrepancies are also noticeable. We believe, they mainly originate from the inhomogeneity of the Drude response, because the Te doping profile is not perfectly uniform along the depth, as shown in Fig. S5 in ESI.† One important aspect that should be noted, is that for plasmonic semiconductors, an accurate broadband permittivity ($\varepsilon(\lambda)$ and $\varepsilon'(\lambda)$) is the key to the quality of simulation, and has to be extracted properly. In our simulations, the permittivity of the Te-hyperdoped Si material was extracted from the classic Drude mode calculation, which only represents the theoretical values for the bulk material. In reality, the permittivity of the same material but in thin-film configuration often varies, which is partially evidenced by the discrepancies between the Drude model and the fitted data obtained *via* the TMM shown in Fig. 2. Moreover, the plasmon damping near the edges of the antenna structures may be much higher than in the inner part due to additional scattering by the roughly etched surfaces and nonideally shaped cuboid (as shown in the insets of Fig. 5(a)–(d)), which can be further minimized by optimizing the etching parameters.

IV. Conclusions

In summary, we have demonstrated that Si hyperdoped with the deep-level impurity Te is a promising material platform for MIR-FIR plasmonic applications. We have accomplished elec-

tron density of about 1.25×10^{20} to 9.4×10^{19} cm^{-3} in Te-hyperdoped Si, which gives rise to a plasma frequency ω_p of around 1880–1630 cm^{-1} (λ_p = 5.3–6.1 µm), ideal for surface-enhanced infrared absorption spectroscopy. By fabricating two-dimensional antenna arrays out of the Te-hyperdoped Si, multiple plasmon resonance modes are excited in the frequency range of 100–600 cm^{-1}. Since the whole manufacturing process of the Te-hyperdoped Si antennas is compatible with the CMOS technology, our result holds great promise for the realization of CMOS-compatible MIR-FIR devices for substance-specific molecular sensing, IR imaging, light detection, and energy harvesting.

Conflicts of interest

There are no conflicts to declare.

Acknowledgements

References

1 G. V. Naik, V. M. Shalaev and A. Boltasseva, Alternative plasmonic materials: beyond gold and silver, *Adv. Mater.*, 2013, **25**, 3264.

2 P. Biagioni, J. Frigerio, A. Samarelli, K. Gallacher, L. Baldassarre, E. Sakat, E. Calandrini, R. W. Millar, V. Giliberti, G. Isella, D. J. Paul and M. Ortolani, Group-IV midinfrared plasmonics, *J. Nanophotonics*, 2015, **9**, 093789.

3 S. Law, V. Podolskiy and D. Wasserman, Towards nanoscale photonics with micro-scale photons: the opportunities and challenges of mid-infrared plasmonics, *Nanophotonics*, 2013, **2**, 103–130.

4 S. A. Maier, *Plasmonics: fundamentals and applications*, Springer, 2007.

5 E. Ozbay, Plasmonics: merging photonics and electronics at nanoscale dimensions, *Science*, 2006, **311**, 189.

6 A. G. Curto, G. Volpe, T. H. Taminiau, M. P. Kreuzer, R. Quidant and N. F. van Hulst, Unidirectional emission of a quantum dot coupled to a nanoantenna, *Science*, 2010, **329**, 930.

7 V. Giannini, A. I. Fernandez-Dominguez, S. C. Heck and S. A. Maier, Plasmonic nanoantennas: fundamentals and their use in controlling the radiative properties of nanoemitters, *Chem. Rev.*, 2011, **111**, 3888.

8 F. K. Rezaie, C. Smith, J. Nath, N. Nader, M. Shahzad, J. Cleary, I. Avrutsky and R. Peale, Infrared surface polaritons on bismuth, *J. Nanophotonics*, 2015, **9**, 093792.

9 H. T. Lin, Z. Q. Luo, T. Gu, L. C. Kimerling, K. Wada, A. Agarwal and J. J. Hu, Mid-infrared integrated photonics on silicon: a perspective, *Nanophotonics*, 2018, **7**, 393.

10 S. Prucnal, F. Liu, M. Voelskow, L. Vines, L. Rebohle, D. Lang, Y. Berencén, S. Andric, R. Boettger, M. Helm, S. Zhou and W. Skorupa, Ultra-doped n-type germanium thin films for sensing in the mid-infrared, *Sci. Rep.*, 2016, **6**, 27643.

11 Y. Zhong, S. D. Malagari, T. Hamilton and D. Wasserman, Review of mid-infrared plasmonic materials, *J. Nanophotonics*, 2015, **9**, 093791.

12 A. Boltasseva and H. A. Atwater, Low-loss plasmonic metamaterials, *Science*, 2011, **331**, 290.

13 M. P. Fischer, A. Riede, K. Gallacher, J. Frigerio, G. Pellegrini, M. Ortolani, D. J. Paul, G. Isella, A. Leitenstorfer, P. Biagioni and D. Brida, Plasmonic mid-infrared third harmonic generation in germanium nanoantennas, *Light: Sci. Appl.*, 2018, **7**, 106.

14 M. P. Fischer, C. Schmidt, E. Sakat, J. Stock, A. Samarelli, J. Frigerio, M. Ortolani, D. J. Paul, G. Isella, A. Leitenstorfer, P. Biagioni and D. Brida, Optical Activation of Germanium Plasmonic Antennas in the Mid-Infrared, *Phys. Rev. Lett.*, 2016, **117**, 047401.

15 J. Frigerio, A. Ballabio, G. Isella, E. Sakat, G. Pellegrini, P. Biagioni, M. Bollani, E. Napolitani, C. Manganelli, M. Virgilio, A. Grupp, M. P. Fischer, D. Brida, K. Gallacher, D. J. Paul, L. Baldassarre, P. Calvani, V. Giliberti, A. Nucara and M. Ortolani, Tunability of the dielectric function of heavily doped germanium thin films for mid-infrared plasmonics, *Phys. Rev. B*, 2016, **94**, 085202.

16 M. J. Milla, F. Barho, F. Gonzalez-Posada, L. Cerutti, M. Bomers, J. B. Rodriguez, E. Tournie and T. Taliercio, Localized surface plasmon resonance frequency tuning in highly doped InAsSb/GaSb one-dimensional nanostructures, *Nanotechnology*, 2016, **27**, 425201.

17 M. Fehrenbacher, S. Winnerl, H. Schneider, J. Doring, S. C. Kehr, L. M. Eng, Y. Huo, O. G. Schmidt, K. Yao, Y. Liu and M. Helm, Plasmonic superlensing in doped GaAs, *Nano Lett.*, 2015, **15**, 1057.

18 S. Zhou, X. Pi, Z. Ni, Y. Ding, Y. Jiang, C. Jin, C. Delerue, D. Yang and T. Nozaki, Comparative study on the localized surface plasmon resonance of boron- and phosphorus-doped silicon nanocrystals, *ACS Nano*, 2015, **9**, 378.

19 S. Law, L. Yu, A. Rosenberg and D. Wasserman, All-semiconductor plasmonic nanoantennas for infrared sensing, *Nano Lett.*, 2013, **13**, 4569.

20 L. Baldassarre, E. Sakat, J. Frigerio, A. Samarelli, K. Gallacher, E. Calandrini, G. Isella, D. J. Paul, M. Ortolani and P. Biagioni, Midinfrared Plasmon-Enhanced Spectroscopy with Germanium Antennas on Silicon Substrates, *Nano Lett.*, 2015, **15**, 7225.

21 M. Shahzad, G. Medhi, R. E. Peale, W. R. Buchwald, J. W. Cleary, R. Soref, G. D. Boreman and O. Edwards, Infrared surface plasmons on heavily doped silicon, *J. Appl. Phys.*, 2011, **110**, 123105.

22 J. C. Ginn, R. L. Jarecki, E. A. Shaner and P. S. Davids, Infrared plasmons on heavily-doped silicon, *J. Appl. Phys.*, 2011, **110**, 043110.

23 S. Law, D. C. Adams, A. M. Taylor and D. Wasserman, Mid-infrared designer metals, *Opt. Express*, 2012, **20**, 12155.

24 T. Lewi, P. P. Iyer, N. A. Butakov, A. A. Mikhailovsky and J. A. Schuller, Widely Tunable Infrared Antennas Using Free Carrier Refraction, *Nano Lett.*, 2015, **15**, 8188.

25 D. J. Rowe, J. S. Jeong, K. A. Mkhoyan and U. R. Kortshagen, Phosphorus-doped silicon nanocrystals exhibiting mid-infrared localized surface plasmon resonance, *Nano Lett.*, 2013, **13**, 1317.

26 J. Salman, M. Hafermann, J. Rensberg, C. Wan, R. Wambold, B. S. Gundlach, C. Ronning and M. A. Kats, Flat Optical and Plasmonic Devices Using Area-Selective Ion-Beam Doping of Silicon, *Adv. Opt. Mater.*, 2018, **6**, 1701027.

27 W. Wei, J. Nong, X. Jiang, N. Chen, S. Luo and L. Tang, All-Semiconductor Plasmonic Resonator for Surface-Enhanced Infrared Absorption Spectroscopy, *Micromachines*, 2017, **8**, 6.

28 K. Gorgulu, A. Gok, M. Yilmaz, K. Topalli and A. K. Okyay, High-conductivity silicon based spectrally selective plasmonic surfaces for sensing in the infrared region, *J. Opt.*, 2017, **19**, 025002.

29 A. Hryciw, Y. C. Jun and M. L. Brongersma, Plasmonics: Electrifying plasmonics on silicon, *Nat. Mater.*, 2010, **9**, 3.

30 J. A. Dionne, L. A. Sweatlock, M. T. Sheldon, A. P. Alivisatos and H. A. Atwater, Silicon-Based Plasmonics for On-Chip Photonics, *IEEE J. Sel. Top. Quantum Electron.*, 2010, **16**, 295.

31 R. Soref, R. E. Peale and W. Buchwald, Longwave plasmonics on doped silicon and silicides, *Opt. Express*, 2008, **16**, 6507.

32 H. Zhang, R. Zhang, K. S. Schramke, N. M. Bedford, K. Hunter, U. R. Kortshagen and P. Nordlander, Doped silicon nanocrystal plasmonics, *ACS Photonics*, 2017, **4**, 963.

33 T. Taliercio and P. Biagioni, Semiconductor infrared plasmonics, *Nanophotonics*, 2019, **8**, 949.

34 T. Taliercio and P. Biagioni, Semiconductor infrared plasmonics, *Nanophotonics*, 2019, **8**, 949–990.

35 W. DiPippo, B. J. Lee and K. Park, Design analysis of doped-silicon surface plasmon resonance immunosensors in mid-infrared range, *Opt. Express*, 2010, **18**, 19396.

36 M. Wang, Y. Berencén, E. García-Hemme, S. Prucnal, R. Hübner, Y. Yuan, C. Xu, L. Rebohle, R. Böttger, R. Heller, H. Schneider, W. Skorupa, M. Helm and S. Zhou, Extended Infrared Photoresponse in Te-Hyperdoped Si at Room Temperature, *Phys. Rev. Appl.*, 2018, **10**, 024054.

37 M. Wang, A. Debernardi, Y. Berencén, R. Heller, C. Xu, Y. Yuan, Y. Xie, R. Böttger, L. Rebohle, W. Skorupa, M. Helm, S. Prucnal and S. Zhou, Breaking the Doping Limit in Silicon by Deep Impurities, *Phys. Rev. Appl.*, 2019, **11**, 054039.

38 S. Zhou, K. Potzger, J. von Borany, R. Grötzschel, W. Skorupa, M. Helm and J. Fassbender, Crystallographically oriented Co and Ni nanocrystals inside ZnO formed by ion implantation and postannealing, *Phys. Rev. B*, 2008, **77**, 035209.

39 K. Gao, S. Prucnal, R. Huebner, C. Baehtz, I. Skorupa, Y. Wang, W. Skorupa, M. Helm and S. Zhou, Ge$_{1-x}$Sn$_x$ alloys synthesized by ion implantation and pulsed laser melting, *Appl. Phys. Lett.*, 2014, **105**, 042107.

40 J. F. Ziegler, SRIM-2003, *Nucl. Instrum. Methods Phys. Res.*, 2004, **219**, 1027.

41 Y. Berencén, S. Prucnal, F. Liu, I. Skorupa, R. Hubner, L. Rebohle, S. Zhou, H. Schneider, M. Helm and W. Skorupa, Room-temperature short-wavelength infrared Si photodetector, *Sci. Rep.*, 2017, **7**, 43688.

42 S. Zhou, F. Liu, S. Prucnal, K. Gao, M. Khalid, C. Baehtz, M. Posselt, W. Skorupa and M. Helm, Hyperdoping silicon with selenium: solid vs. liquid phase epitaxy, *Sci. Rep.*, 2015, **5**, 8329.

43 F. Solutions, *Version 8.5. 3*, Lumerical Solutions. Inc., Vancouver, BC, Canada, 2013.

44 H. Van Driel, Optical effective mass of high density carriers in silicon, *Appl. Phys. Lett.*, 1984, **44**, 617.

45 M. Miyao, T. Motooka, N. Natsuaki and T. Tokuyama, Change of the electron effective mass in extremely heavily doped n-type Si obtained by ion implantation and laser annealing, *Solid State Commun.*, 1981, **37**, 605.

46 M. Lee, C. Huang, Y. Chang and Y. Chao, Double-resonance-enhanced Raman scattering in laser-recrystallized amorphous silicon film, *Phys. Rev. B: Condens. Matter Mater. Phys.*, 1989, **40**, 10420.

47 P. A. Temple and C. Hathaway, Multiphonon Raman spectrum of silicon, *Phys. Rev. B: Solid State*, 1973, **7**, 3685.

48 S. Prucnal, L. Rebohle and W. Skorupa, Doping by flash lamp annealing, *Mater. Sci. Semicond. Process.*, 2017, **62**, 115.

49 J. A. Woollam Co., Inc, Guide to using WVASE32, WexTech Systems, Inc 310 Madison Avenue, Suite 905 New York, Ny 10017 (212) 949-9595.

50 C. Chen, D. A. Mohr, H.-K. Choi, D. Yoo, M. Li and S.-H. Oh, Waveguide-integrated compact plasmonic resonators for on-chip mid-infrared laser spectroscopy, *Nano Lett.*, 2018, **18**, 7601.

51 E. Stankevičius, K. Vilkevičius, M. Gedvilas, E. Bužavaitė-Vertelienė, A. Selskis and Z. Balevičius, Direct Laser Writing for the Formation of Large–Scale Gold Microbumps Arrays Generating Hybrid Lattice Plasmon Polaritons in Vis–NIR Range, *Adv. Opt. Mater.*, 2021, **23**, 2100027.

52 Z. Geng, J. Theenhaus, B. K. Patra, J.-Y. Zheng, J. Busink, E. C. Garnett and S. R. Rodriguez, Fano lineshapes and Rabi splittings: Can they be artificially generated or obscured by the numerical aperture?, *ACS Photonics*, 2021, **8**, 1271.

53 R. Jiang, B. Li, C. Fang and J. Wang, Metal/semiconductor hybrid nanostructures for plasmon–enhanced applications, *Adv. Mater.*, 2014, **26**, 5274.

54 N. Li, P. Zhao and D. Astruc, Anisotropic gold nanoparticles: synthesis, properties, applications, and toxicity, *Angew. Chem., Int. Ed.*, 2014, **53**, 1756.

55 G. Pellegrini, L. Baldassare, V. Giliberti, J. Frigerio, K. Gallacher, D. J. Paul, G. Isella, M. Ortolani and P. Biagioni, Benchmarking the use of heavily doped Ge for plasmonics and sensing in the mid-infrared, *ACS Photonics*, 2018, **5**, 3601–3607.

56 W. T. Hsieh, P. C. Wu, J. B. Khurgin, D. P. Tsai, N. Liu and G. Sun, Comparative analysis of metals and alternative infrared plasmonic materials, *ACS Photonics*, 2018, **5**, 2541–2548.

Statistics

User facilities and services

Ion Beam Center (IBC)

The Ion Beam Center (IBC) at HZDR combines various machines (electrostatic accelerators, ion implanters, low-energy and focused ion beam systems) into a unique facility used for ion beam modification and ion beam analysis of materials. The available energy range spans from a few eV to 60 MeV with a respective interaction depth in solids between 0.1 nm to 10 µm. In addition to standard broad beams also focused (down to 1 nm) and highly-charged ion beams with charge states up to 45+ are available. In combination with an allocated ion beam experiment, users can also profit from structural analysis (electron microscopy and spectroscopy, X-ray scattering techniques) and sample or device processing under clean-room conditions. At the 6-MV tandem accelerator, the DREAMS (DREsden AMS = accelerator mass spectrometry) facility is used for the determination of long-lived radionuclides, like ^{7,10}Be, ^{26}Al, ^{36}Cl, ^{41}Ca, ^{55}Fe, ^{129}I, and others. A schematic overview of the IBC including the description of the main beam lines and experimental stations is given on page 87 of this Annual Report. In 2022, about 12,300 beam time hours were delivered for 155 proposals of 128 users from 16 countries worldwide, performing experiments at IBC or using the capabilities for ion beam services.
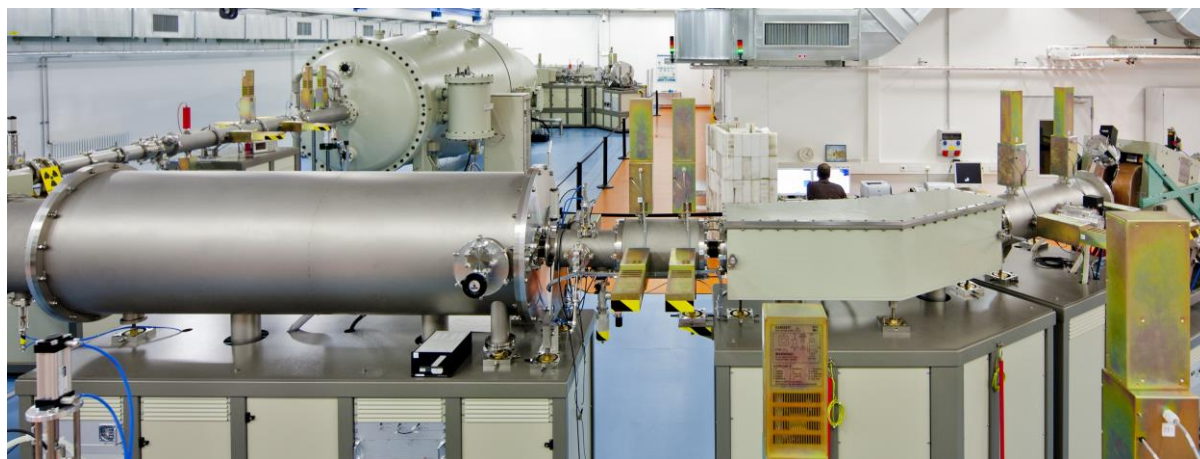
The IBC has provided ion beam technology as a user and competence center for ion beam applications for more than 30 years. With respect to user beam time hours, the IBC is internationally leading, and has been supported by numerous national and European grants, and by industry.

The research activities cover both ion beam modification and ion beam analysis (IBA), as well as rare isotope detection capabilities (accelerator mass spectrometry, AMS).

The operation of IBC is accompanied by a strong in-house research at the affiliated host "Institute of Ion Beam Physics and Materials Research", both in experiment and theory. Furthermore, the IBC strongly supports the commercial exploitation of ion beam technologies of partners from industry, which is essential for materials science applications. For ion beam services, the HZDR Innovation GmbH (spin-off of the HZDR) – www.hzdr-innovation.de – provides a direct and fast access to the IBC facilities based on individual contracts.

Quite recently, new ion beam tools and end stations have been commissioned which will attract new users by state-of-the-art experimental instrumentation. In a new end station for Rutherford-backscattering spectrometry (RBS), solid-liquid interfaces can now be investigated in-situ in an electrochemical cell. An ion microscope *ORION NanoFab* (He/Ne ions, 5 – 35 keV) provides unique possibilities for surface imaging, nano-fabrication, and for the first time, elemental analysis based on

ion beam techniques. The cluster tool at the 6-MV accelerator allows *in-situ* deposition and analysis investigations at temperatures of up to 800 °C. Medium-energy ion scattering (MEIS) is now available for investigation of elemental compositions and depth profiles of ultra-thin layers at the new 100-kV accelerator.

IBC activities are efficiently integrated into various Helmholtz programmes within the research field "Matter", but also in the Helmholtz cross-programme activities "Mineral Resources", "Materials Research for Energy Technologies", and "Helmholtz Energy Materials Foundry". Since 2013, the IBC has been recognized as a large-scale facility within the "BMBF Verbundforschung" promoting long-term collaborations with universities. In addition, as of 2019 the IBC is coordinating the EU Integrated Infrastructure Initiative (I3) project RADIATE, which provides trans-national access to the largest ion beam centers in Europe (www.ionbeamcenters.eu).

Following the rules of a European and national user facility, access for scientific experiments to IBC is provided on the basis of a proposal procedure (www.hzdr.de/IBC) via the common HZDR user facility portal **HZDR-GATE** (gate.hzdr.de), and for RADIATE via www.ionbeamcenters.eu. IBC users from EU countries are eligible to receive support through the RADIATE initiative. Due to the availability of multiple machines and versatile instrumentation, IBC proposals can be submitted continuously. The scientific quality of the proposals is evaluated and ranked by an external international User Selection Panel. For successfully evaluated proposals, users get free access to IBC facilities for their experiments. The use of the IBC facilities includes the scientific and technical support during planning, execution, and evaluation of the experiments. For AMS samples preparation, two chemistry laboratories are available.

For more detailed information, please contact Dr. Stefan Facsko (s.facsko@hzdr.de), or Dr. René Heller (r.heller@hzdr.de), for AMS enquiries Prof. Anton Wallner (a.wallner@hzdr.de), and visit the IBC webpage: www.hzdr.de/IBC.

Free Electron Laser FELBE

FELBE is an acronym for the free-electron laser (FEL) at the Electron Linear accelerator with high Brilliance and low Emittance (ELBE) located at the Helmholtz-Zentrum Dresden-Rossendorf. The heart of ELBE is a superconducting linear accelerator operating in continuous-wave (cw) mode with a pulse repetition rate of 13 MHz. The electron beam (40 MeV, 1 mA max.) is guided to several laboratories where secondary beams (particle and electromagnetic) are generated. Two free-electron lasers (U37-FEL and U100-FEL) produce intense, coherent electromagnetic radiation in the mid and far infrared,

which is tunable over a wide wavelength range (5 –250 µm) by changing the electron energy or the undulator magnetic field. Main parameters of the infrared radiation produced by FELBE are as follows:

Wavelength λ	5 – 40 µm	FEL with undulator U37
	18 – 250 µm	FEL with undulator U100
Pulse energy	0.1 – 2 µJ	depends on wavelength
Pulse length	1 – 25 ps	depends on wavelength
Repetition rate	13 MHz	3 modes: • cw
		• macropulsed (> 100 µs, < 25 Hz)
		• single pulsed (Hz … kHz)

In addition, there is the THz beamline TELBE that is run by the Institute of Radiation Physics. TELBE delivers high-power pulses (up to 10 µJ) in the low THz range (0.1 to 2.5 THz) at a repetition rate of 100 kHz.

Typical applications are picosecond pump-probe spectroscopy (also in combination with several other femtosecond lasers, which are synchronized to the FEL), near-field microscopy, and nonlinear optics. The FELBE facility also serves as a far-infrared source for experiments at the Dresden High Magnetic Field Laboratory (HLD) involving pulsed magnetic fields up to 70 T.

The statistics shows that the FEL used about 1000 hours beam time of the ELBE accelerator. This corresponds to 19 % of total beam time, which is again distributed among internal and external users.

For further information, please contact Prof. Manfred Helm (m.helm@hzdr.de) or visit the FELBE webpage www.hzdr.de/FELBE.

ELBE is a user facility and applications for beam time can be submitted twice a year, typically by April 15 and October 15.

Beamtime Distribution at ELBE 2022
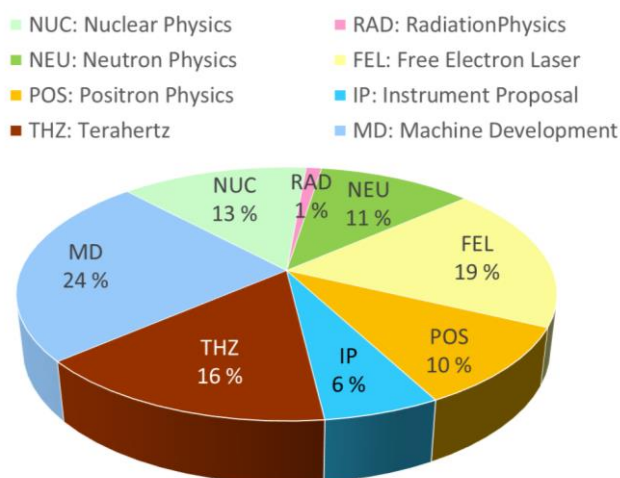
Experimental equipment

Accelerators, ion implanters, and other ion processing tools

Van de Graaff Accelerator (VdG)	2 MV	*TuR Dresden, DE*
Tandetron Accelerator (T1)	3 MV	*HVEE, NL*
Tandetron Accelerator (T2)	6 MV	*HVEE, NL*
Low-Energy Ion Implanter	40 kV	*Danfysik, DK*
Low-Energy Ion Platform (LEINEF)	100 kV	*HVEE, NL*
High-Energy Ion Implanter	500 kV	*HVEE, NL*
Mass-Separated Focused Ion Beam (FIB) (will be replaced in 2023)	10 – 30 keV, >10 A/cm^2	*Orsay Physics, FR*
ORION NanoFab HIM (including GIS, Nanopatterning, TOF-SIMS, µ-manipulators and heater)	He, Ne ions, 10 – 35 keV, Resolution ~ 0.5/1.8 nm	*Carl Zeiss Microscopy, DE*
ORION PLUS HIM modified for STIM	He ions, 10 – 35 keV, Resolution 0.35 nm	*Carl Zeiss Microscopy, DE*
Highly-Charged Ion Facility	25 eV – 6 keV $\times$ Q, Q = 1 … 45 (Xe)	*DREEBIT, DE; PREVAC, PL*
Surface Modifications by Low-Energy Ion Irradiation	200 – 1200 eV	*Home-built*
UHV Ion Irradiation (Ar, He, etc.)	0.2 – 5 keV, Scan 10 $\times$ 10 mm^2	*Cremer, DE; VG, USA*

Ion beam analysis (IBA)

A wide variety of advanced IBA techniques are available at the MV accelerators (see figure).

RBS	Rutherford-Backscattering Spectrometry	(A1), (A2), (5), (9), (11), (14)	*VdG, T1, T2, HIM*
RBS/C	RBS – Channeling	(A1)	*VdG, T1*
Liquid-RBS	Liquid Rutherford Backscattering Spectrometry	(A2)	*VdG*
MEIS	Medium Energy Ion Scattering	MEIS	*LEINEF*
ERDA	Elastic Recoil Detection Analysis	(2), (9)	*T2*
PIXE	Particle-Induced X-ray Emission	(A1), (A2), (5), (14)	*VdG, T1, T2*
PIGE	Particle-Induced gamma Emission	(5), (14)	*T1, T2*
NRA	Nuclear Reaction Analysis	(1), (14)	*T1, T2*
NMP	Nuclear Microprobe	(14)	*T1*

Some stations are equipped with additional process facilities enabling *in-situ* IBA investigations during ion irradiation, sputtering, deposition, annealing, investigations at solid-liquid interfaces, etc.
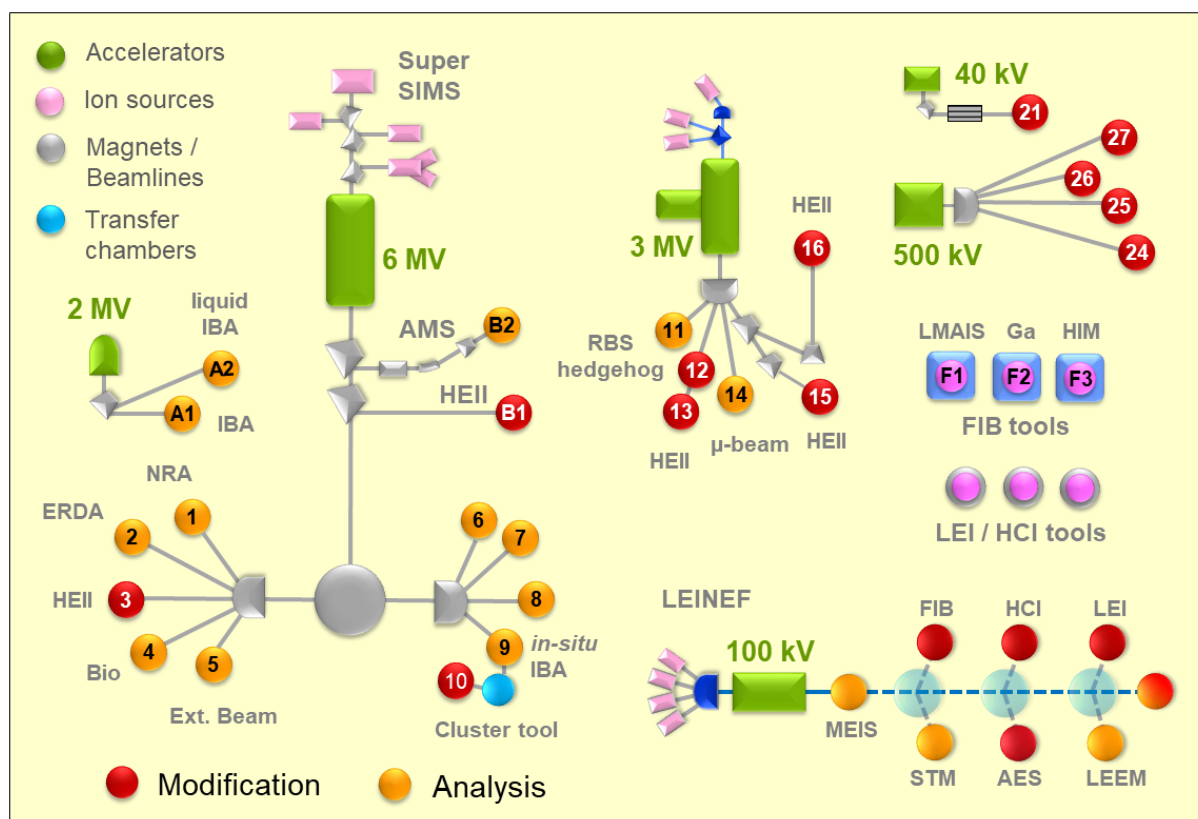
Schematic overview of the HZDR Ion Beam Center

Accelerator Mass Spectrometry (AMS)

AMS	Accelerator Mass Spectrometry	(B2)	*T2*

(focused to long-lived radionuclides: ^{7}Be, ^{10}Be, ^{26}Al, ^{36}Cl, ^{41}Ca, ^{129}I)

Other particle-based analytical techniques

SEM	Scanning Electron Microscope (S4800 II)	1 – 30 keV + EDX	*Hitachi, JP*
TEM	Transmission Electron Microscope (Titan 80-300 with Image Corrector)	80 – 300 keV + EDX, EELS	*FEI, NL*
TEM	Transmission Electron Microscope (Talos F200X)	20 – 200 keV + SuperX EDX	*FEI, NL*
FIB/SEM	Focused Ion/Electron Cross Beam (NVision 40)	1 – 30 keV + EDX, EBSD	*Carl Zeiss Microscopy, DE*
FIB/SEM	Focused Ion/Electron Instrument (Helios 5 CX DualBeam)	0.5 – 30 keV	*Thermo Fisher Sci. - FEI, US*
AES	Auger Electron Spectroscopy	+ SAM, SEM, XPS, EDX, CL	*Scienta Omicron, DE*
LEEM	Low-Energy Electron Microscope (Spec-LEEM-III)	0 eV – 4.5 keV, Resolution < 6 nm + AES	*Elmitec, DE*
SIMS	Secondary Ion Mass Spectrometer (IMS7f-auto)	3 – 15 keV Cs and O beam	*CAMECA, FR*

Photon-based analytical techniques

XRD/XRR	X-Ray Diffractometers	Cu-Kα	
	θ-θ Powder D8 Advance		*Bruker, DE*
	θ-θ 4-Circle Empyrean		*PANalytical, NL*
	θ-θ 4-Circle SmartLab 3kW		*Rigaku, JP*
SE	Angle-Dependent Spectroscopic Ellipsometry	250 – 1700 nm	*Woollam, US*
UV-Vis	Solid Spec 3700 DUV	190 – 3300 nm	*Shimadzu, JP*
FTIR	Fourier-Transform Infrared Spectrometer	50 – 15000 cm^{-1}	*Bruker, DE*
	Ti:Sapphire Femtosecond Laser	78 MHz	*Spectra Physics, US*
	Femtosecond Optical Parametric Osci.		*APE, DE*
	Ti:Sapphire Femtosecond Amplifier	1 kHz, 250 kHz	*Coherent, US*
	Femtosecond Optical Parametric Amplifier		*Light Conversion, LT*
THz-TDS	Terahertz Time-Domain Spectroscopy	0.1 – 4 THz	*Home-built*
Raman	Raman Spectroscopy	> 10 cm^{-1}	*Jobin-Yvon-Horiba, FR*
	In-situ Raman Spectroscopy	> 100 cm^{-1}	*Jobin-Yvon-Horiba, FR*
PL	Photoluminescence (10 – 300 K)	405 – 1550 nm	*Jobin-Yvon-Horiba, FR*
	Micro-Photoluminescence	< 0.5 μm	*Jobin-Yvon-Horiba, FR*
TRPL	Time-Resolved Photoluminescence	τ = 3 ps – 2 ns τ > 5 ns	*Hamamatsu Phot., JP* *Stanford Res., US*
EL	Electroluminescence	300 – 1600 nm	*Jobin-Yvon-Horiba, FR*
	Optical Split-Coil Supercond. Magnet	7 T	*Oxford Instr., UK*
PR	Photomodulated Reflectivity	300 – 1600 nm	*Jobin-Yvon-Horiba, FR*
PLE	Photoluminescence Excitation	300 – 1600 nm	*Jobin-Yvon-Horiba, FR*
OES	Optical Emission Spectroscopy	250 – 800 nm	*Jobin-Yvon-Horiba, FR*
Confocal	Confocal scanning photoluminescence microscope	~1 μm resol. 5 – 300 K	*Attocube, DE*
SSPD	Superconducting single photon detectors	800 – 1500 nm	*Single Quantum, NL*

Magnetic thin film analysis

MFM	Magnetic Force Microscope	~ 50 nm resol.	*VEECO; DI, US*
AFM/MFM	Magnetic Force Microscope	~ 50 nm resol.	*BRUKER ICON tool, US*
SQUID VSM	Vibrating Sample Magnetometer	± 7 T	*Quantum Design, US*
Vector-VSM	Vibrating Sample Magnetometer	± 2 T	*Microsense, US*
MOKE	Magneto-Optic Kerr Effect (in-plane)	± 0.35 T	*Home-built*
MOKE	Magneto-Optic Kerr Effect (perpend.)	± 2 T	*Home-built*
FR-MOKE	Frequency-Resolved Magneto-Optic KE	± 1.1 T	*Home-built*
SKM	Scanning Kerr Microscope		*Home-built*
	Kerr Microscope		*Evico Magnetics, DE*
VNA-FMR	Vector Network Analyzer Ferromagnetic Resonance	50 GHz	*Agilent, DE; Home-built*
Cryo-FMR	Variable-Temperature Ferromagnetic Resonance	3 – 300 K	*Attocube, DE; Home-built*
ME	Magnetoellipsometer		*LOT, DE; AMAC, US*
µBLS	Brillouin Light Scattering Microscope	± 0.8 T, 491 & 532 nm	*Home-built*
SKM	Scanning Kerr Microscope with RF Detection (Spectrum Analyzer)	± 0.5 T, 40 GHz	*Home-built*
MT-50G	High Frequency Magneto-Transport Setup	± 1.5 T, 50 GHz 250 ps	*Home-built*

Other analytical and measuring techniques

STM/AFM	UHV Scanning Probe Microscope (variable T)		*Omicron, DE*
AFM	Atomic Force Microscope (Contact, Tapping, Spreading)		*Bruker, US*
AFM	Atomic Force Microscope (with c-AFM, SCM-Module)		*Bruker, US*
	Dektak Surface Profilometer		*Bruker, US*
	Micro Indenter/Scratch Tester		*Shimatsu, JP*
MPMS	Mechanical Properties Measurement System – Stretcher		*Home-built*
MS	Mass Spectrometers (EQP-300, HPR-30)		*HIDEN, UK*
	Wear Tester (pin-on disc)		*Home-built*
LP	Automated Langmuir Probe		*Impedans, IE*
HMS	Hall Measurement System	2 – 400 K, ≤ 9 T	*LakeShore, US*
	Van-der-Pauw HMS Ecopia	LNT & 300 K, 0.5 T	*Bridge Technol., US*
MTD	Magneto-Transport Device	300 K, ≤ 3 T	*Home-built*
RS	Sheet-Rho-Scanner		*AIT, KR*
Redmag	Redmag Tensormeter System	280 – 350 K, 2.5 T	*Home-built*
Greymag	Greymag Tensormeter System	300 K, 0.7 T (360°)	*Home-built*

Greenmag	Tensormeter System (TMCS)	30 – 320 K, 1.3 T (360°)	*Tensor Instruments (HZDR Inno), DE*
SEM	Scanning Electron Microscope (Phenom XL)	5 – 15 keV + EDS	*Thermo Fisher Sci., US*
IV / CV	I-V and C-V Semi-Automatic Prober	-60 – 300 °C	*Süss, DE; Keithley, US*
IV / CV	I-V and C-V Analyzer		*Keithley, US*
BCS	Battery test system, 8 channels		*Bio-Logic Science, DE*
GC	Gas Chromatography (GC-2010)		*Shimadzu, JP*
ECW	Electrochemical workstation (CHI 760e)		*CH instruments, US*
FDA	Force displacement analysis machine		*Sauter, DE*
IV / VNA	I-V and VNA Prober for VHF, LCR and frequency analysis measurements	20 – 120 MHz	*Süss, DE; Cascade, US; Keysight, US*
OSCI	4-channel real time oscilloscope	1.5 GHz (BW), 5 GSa/s	*Keysight, US*
IR-Cam	TrueIR Thermal Imager	-20 – 350 °C	*Keysight, US*
CM	Confocal Microscope (Smartproof 5)	405 nm LED, z drive res. ~ 1 nm	*Carl Zeiss, DE*
FAS	Fluidic Analytic Setup – microscope, high speed camera, and fluidic pumps	2 GB 120 kfps, 5 modules	*Zeiss, DE; Photron, US; Cetoni, DE*

Deposition and processing techniques

Physical Deposition	2x DC / 2x RF Magnetron Sputter System, up to 4x 6" substrates	*Nordiko, UK*
	Thermal (2 sources) / Electron Beam (12 pockets) Evaporation System	*CREAVAC, DE*
	Thermal Evaporation	*Bal-Tec, LI*
	Thermal (1 source) / Electron Beam (7 pockets) Evaporation System	*BESTEC, DE*
	DC/RF Magnetron Sputter System, 4x 3" + 4x 2" magnetrons, substrate heating: RT – 950 °C, up to 4" wafers	*BESTEC, DE*
	DC/RF Magnetron Sputter System, 6x 2" confocal magnetrons, substrate heating: RT – 650 °C, up to 3" wafers	*AJA International, US*
	Dual Ion Beam Sputtering (IBAD), 6" targets, RT – 500 °C	*Home-built*
	High Power Impulse Magnetron Sputtering	*Melec, DE*
	Magnetron Sputter System (2 targets)	*Home-built*
	Thermal Evaporation System (Cr, Au)	*Leybold GmbH*
	DC/RF Magnetron Sputter System (Au, up to 3" wafers)	*Denton Vacuum, LLC*
PLD	Pulsed Laser Deposition	*SURFACE, DE*
Molecular Beam Epitaxy (MBE)	III-V Semiconductors	*Riber, FR*
	Metals	*CreaTec Fischer, DE*
Chemical Vapor Deposition (CVD)	Plasma Enhanced: a-Si, a-Ge, SiO_2, SiON, Si_3N_4	*Oxford Instr., UK*

Atomic Layer Deposition (ALD)	Al_2O_3, HfO_2, ZnO	*Ultratech, US*
Dry Etching	ICP-RIE, $\varnothing$ 6": CF_4, SF_6, C_4F_8 with interferometric etch-stop monitor	*Sentech, DE*
	RIBE, $\varnothing$ 6": Ar, CF_4 with SIMS etch-stop monitor	*Roth & Rau, DE*
	Barrel reactor, $\varnothing$ 4": O_2, Ar, N_2	*Diener electronic, DE*
Etching/Cleaning	incl. Anisotropic Selective KOH Etching, Metal-Assisted Chemical Etching, Photoelectrochemical Etching	
Photolithography	Mask-Aligner MA6, $\varnothing$ 6", < 2 μm accuracy; with two-side alignment	*Süss, DE*
	Direct Laser Writer DWL 66FS, $\varnothing$ 8"x8", 2 μm accuracy	*Heidelberg Instr., DE*
	Laser Micro Writer ML, 10 μm accuracy	*Durham Magneto Optics, UK*
Electron Beam Lithography	Raith 150-TWO: $\varnothing$ 6", 10 nm resolution	*Raith, DE*
	e-Line Plus: $\varnothing$ 4", 10 nm resolution	*Raith, DE*
Thermal Treatment	Room Temperature – 2000 °C	
Oxidation and annealing furnace		*INNOTHERM, DE*
Rapid Thermal Annealing JETFIRST 100		*JIPELEC, FR*
Rapid Thermal Annealing AW 610		*Allwin21, USA*
Flash-Lamp Units (0.5 – 20 ms)		*Home-built; FHR/DTF, DE*
Combined Flash Lamp Sputter Tool (Magnetron sputtering plus flash lamp annealing 0.3 – 3 ms, up to 10 Hz)		*ROVAK GmbH, DE*
RF Heating (Vacuum)		*JIPELEC, FR*
Laser Annealing (CW, 808 nm, 450 W)		*LIMO, DE*
Laser Annealing (30 ns pulse,10 Hz, 308 nm, 500 mJ)		*COHERENT, USA*
CVD Tube furnace (RT – 1200 °C, three channel gas)		*NBD, CN*
Vacuum oven (RT – 250 °C, Vacuum < 133 Pa)		*LAB-KITS, CN*
Vacuum oven (RT – 800 °C, Vacuum < 10^{-7} mbar)		*Xerion GmbH, DE*
Bonding Techniques	Ultrasonic Wire Bonding	*Kulicke & Soffa, US*
	Semi-automatic Wire-bonder: Gold-ball and wedge-wedge bonding Ultrasonic generator: 60 kHz, 140 kHz Wire deformation control software	*F & S Bondtec, AT*
Cutting, Grinding, Polishing		*Bühler, DE*
TEM Sample Preparation	Plan View and Cross Section incl. Ion Milling Equipment	*Gatan, US*
SEM / HIM Sample Preparation	Mechanical milling, sawing, grinding, polishing	*Leica, AUT*
	Argon cross-section milling, surface polishing	*Hitachi, JP*
Disperse and mixer	Mixer for pastes and emulsions	*IKA, DE*
Centrifuge	Max. 17850 rpm, -10 – 40 °C	*Thermo Scientific, US*

Doctoral training programme

Education programme

This programme for our doctoral researchers fosters not only professional qualification but also personal development by equipping young graduates with competencies for successful careers in a wide variety of positions in academia and industry.

The doctoral training programme aims at attracting and promoting excellence by educating promising doctoral researchers with backgrounds in physics, chemistry, materials science, and electrical engineering. During a period of three to four years, doctoral researchers benefit from well-structured, comprehensive training curricula and multiple mentorship, while performing cutting-edge research projects within one of the institute's departments.

A weekly PhD Seminar gives a training in presenting scientific results and the opportunity of exchange with junior, as well as senior colleagues from all departments. Every doctoral researcher is expected to present the progress of his/her project once a year.

The transferable skills courses offered in 2022 covered the topics "Scientific Presentation" introduced by Millie Baker from London, and "Scientists Need More - effective project and time management tools" by Alexander Schiller from Jena. Both courses were rated very well to excellent by the doctoral researchers.

Workshop NANONET+ FWIO FWIM

The NANONET+ inter-departmental Workshop 2022 was held at the Youth Hostel Görlitz in a very relaxed setting after the Corona restrictions during October 4th – 6th. The topic was "2D Materials and ultra-high doped semiconductors: electronics, photonics and sensing". It was organized by the departments "Nanoelectronics" and "Semiconductor Materials" of our institute, NaMLab gGmbH, and the institute IHM of TU Dresden. The format of a "Hüttenseminar" was generously supported by the Heraeus Foundation Hanau. It was attended by 43 participants of 11 nationalities. The name is derived from the International Helmholtz Research School for Nanoelectronic Networks (IHRS NANONET) which was supported by the Initiative and Networking Fund of the Helmholtz Association between 2012 and 2020, and was coordinated at the Institute of Ion Beam Physics and Materials Research (www.hzdr.de/nanonet).
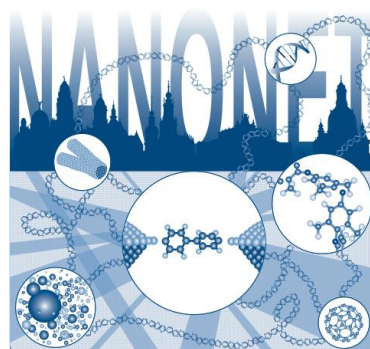
Publications and patents

Books and chapters

1. Makarov, D.; Sheka, D.
Curvilinear Micromagnetism: from fundamentals to applications
Cham, Switzerland: Springer, 2022, 978-3-031-09085-1

2. Canon Bermudez, G.S.; Lopez, M.N.; Evans, B.A.; Yershov, K.; Makarov, D.; Pylypovskyi, O.
Magnetic soft actuators: magnetic soft robots from macro- to nanoscale
in Denys Makarov and Denis D. Sheka: Curvilinear Micromagnetism: from fundamentals to applications, Cham, Switzerland: Springer, 2022, 978-3-031-09085-1

3. Canon Bermudez, G.S.; Makarov, D.
Geometrically Curved Magnetic Field Sensors for Interactive Electronics
in Denys Makarov and Denis D. Sheka: Curvilinear Micromagnetism: from fundamentals to applications, Cham, Switzerland: Springer, 2022, 978-3-031-09085-1

4. Landeros, P.; Otálora, J.A.; Streubel, R.; Kakay, A.
Curvilinear Micromagnetism, From Fundamentals to Applications: Tubular Geometries
in Denys Makarov and Denis D. Sheka: Curvilinear Micromagnetism: from fundamentals to applications, Cham, Switzerland: Springer, 2022, 978-3-031-09085-1

5. Pylypovskyi, O.; Phatak, C.; Volkov, O.
Effects of curvature and torsion on magnetic nanowires
in Denys Makarov and Denis D. Sheka: Curvilinear Micromagnetism: from fundamentals to applications, Cham, Switzerland: Springer, 2022, 978-3-031-09085-1

6. Yershov, K.; Volkov, O.
Geometry-induced magnetic effects in planar curvilinear nanosystems
in Denys Makarov and Denis D. Sheka: Curvilinear Micromagnetism: from fundamentals to applications, Cham, Switzerland: Springer, 2022, 978-3-031-09085-1

7. Ghorbani-Asl, M.; Kretschmer, S.; Krasheninnikov, A.
Two-dimensional materials under ion irradiation: from defect production to structure and property engineering
in Rafik Addou and Luigi Colombo: Defects in Two-Dimensional Materials, Amsterdam, The Netherlands: Elsevier, 2022, 978-0-128-20292-0

8. Ibarlucea, B.; Schütt, J.; Baraban, L.; Makarov, D.; Medina Sánchez, M.; Cuniberti, G.
Real-time tracking of individual droplets in multiphase microfluidics
in Mingzhou Yu: Microfluidics and Nanofluidics - Fundamentals and Applications, London, England: IntechOpen, 2022, 978-1-803-56336-7

9. Komsa, H.-P.; Krasheninnikov, A.
Physics and Theory of Defects in 2D Materials: The Role of Reduced Dimensionality
in Rafik Addou and Luigi Colombo: Defects in Two-Dimensional Materials, Amsterdam, The Netherlands: Elsevier, 2022, 978-0-323-90310-3

10. Zelent, M.; Gruszecki, P.; Moalic, M.; Hellwig, O.; Barman, A.; Krawczyk, M.
Spin dynamics in patterned magnetic multilayers with perpendicular magnetic anisotropy
Solid State Physics - Advances in Research and Applications, volume **73**, Amsterdam, The Netherlands: Elsevier, 2022, DOI: 10.1016/bs.ssp.2022.08.002

Publications in journals

1. Antanovich, A.; Yang, L.; Erwin, S.C.; Martín-García, B.; Hübner, R.; Steinbach, C.; Schwarz, D.; Gaponik, N.; Lesnyak, V.
   CdSe$_x$S$_{1-x}$ Alloyed Nanoplatelets with Continuously Tunable Blue-Green Emission
   Chemistry of Materials **34**, 10361 (2022)

2. Anwar, M.S.; Cansever, H.; Boehm, B.; Gallardo, R.; Hübner, R.; Zhou, S.; Kentsch, U.; Rauls, S.; Eggert, B.; Wende, H.; Potzger, K.; Faßbender, J.; Lenz, K.; Lindner, J.; Hellwig, O.; Bali, R.
   Depth-Adjustable Magnetostructural Phase Transition in Fe$_{60}$V$_{40}$ Thin Films
   ACS Applied Electronic Materials **4**, 3860 (2022)

3. Arora, H.; Fekri, Z.; Vekariya, Y.N.; Chava, P.; Watanabe, K.; Taniguchi, T.; Helm, M.; Erbe, A.
   Fully encapsulated and stable black phosphorus field-effect transistors
   Advanced Materials Technologies **8**, 2200546 (2022)

4. Babin, C.; Stöhr, R.; Morioka, N.; Linkewitz, T.; Steidl, T.; Wörnle, R.; Liu, D.; Hesselmeier, E.; Vorobyov, V.; Denisenko, A.; Hentschel, M.; Gobert, C.; Berwian, P.; Astakhov, G.; Knolle, W.; Majety, S.; Saha, P.; Radulaski, M.; Tien Son, N.; Ul-Hassan, J.; Kaiser, F.; Wrachtrup, J.
   Fabrication and nanophotonic waveguide integration of silicon carbide colour centres with preserved spin-optical coherence
   Nature Materials **21**, 67 (2022)

5. Balan, A.P.; Puthirath, A.B.; Roy, S.; Costin, G.; Oliveira, E.F.; Saadi, M.A.S.R.; Sreepal, V.; Friedrich, R.; Serles, P.; Biswas, A.; Iyengar, S.A.; Chakingal, N.; Bhattacharyya, S.; Saju, S.K.; Pardo, S.C.; Sassi, L.M.; Filleter, T.; Krasheninnikov, A.; Galvao, D.S.; Vajtai, R.; Nair, R.R.; Ajayan, P.M.
   Non-van der Waals quasi-2D materials; recent advances in synthesis, emergent properties and applications
   Materials Today **58**, 164 (2022)

6. Barman, A.; Das, D.; Deshmukh, S.; Sarkar, P.K.; Banerjee, D.; Hübner, R.; Gupta, M.; Saini, C.P.; Kumar, S.; Johari, P.; Dhar, S.; Kanjilal, A.
   Aliovalent Ta-Doping-Engineered Oxygen Vacancy Configurations for Ultralow-Voltage Resistive Memory Devices: A DFT-Supported Experimental Study
   ACS Applied Materials and Interfaces **14**, 34822 (2022)

7. Bhatt, C.S.; Parimi, D.S.; Bollu, T.K.; Madhura, H.U.; Jacob, N.; Korivi, R.; Ponugoti, S.S.; Mannathan, S.; Ojha, S.; Klingner, N.; Motapothula, M.; Suresh, A.K.
   Sustainable Bioengineering of Gold Structured Wide-Area Supported Catalysts for Hand-Recyclable Ultra-Efficient Heterogeneous Catalysis
   ACS Applied Materials and Interfaces **14**, 51579 (2022)

8. Bischoff, A.; Storz, J.; Barrat, J.-A.; Heinlein, D.; Jull, A.J.T.; Merchel, S.; Pack, A.; Rugel, G.
   Blaubeuren, Cloppenburg, and Machtenstein—Three recently recognized H-group chondrite finds in Germany with distinct terrestrial ages and weathering effects
   Meteoritics & Planetary Science **57**, 136 (2022)

9. Bischoff, L.; Klingner, N.; Mazarov, P.; Lenz, K.; Narkovic, R.; Pilz, W.; Meyer, F.
   Dysprosium Liquid Metal Alloy Ion Source For Magnetic Nanostructures
   Journal of Vacuum Science & Technology B **40**, 052802 (2022)

10. Boelens, P.; Bobeth, C.; Hinman, N.; Weiß, S.; Zhou, S.; Vogel, M.; Drobot, B.; Shams Aldin Azzam, S.; Pollmann, K.; Lederer, F.
    Peptide functionalized Dynabeads for the magnetic carrier separation of rare-earth fluorescent lamp phosphors
    Journal of Magnetism and Magnetic Materials **563**, 169956 (2022)

11. Bora, A.; Prudnikau, A.; Fu, N.; Hübner, R.; Borchert, K.B.L.; Schwarz, D.; Gaponik, N.; Lesnyak, V.
   Seed-Mediated Synthesis of Photoluminescent Cu−Zn−In−S Nanoplatelets
   Chemistry of Materials **34**, 9251 (2022)

12. Borysenko, Y.; Sheka, D.; Faßbender, J.; van den Brink, J.; Makarov, D.; Pylypovskyi, O.
   Field-induced spin reorientation transitions in antiferromagnetic ring-shaped spin chains
   Physical Review B **106**, 174426 (2022)

13. Böhm, B.; Hellwig, O.
   Tailoring exchange-dominated synthetic layered antiferromagnets: From collective reversal to exchange bias
   Small **18**, 2204804 (2022)

14. Breev, I.D.; Shang, Z.; Poshakinskiy, A.V.; Singh, H.; Berencen, Y.; Hollenbach, M.; Nagalyuk, S.S.; Mokhov, E.N.; Babunts, R.A.; Baranov, P.G.; Suter, D.; Tarasenko, S.A.; Astakhov, G.; Anisimov, A.N.
   Inverted fine structure of a 6H-SiC qubit enabling robust spin-photon interface
   npj Quantum Information **8**, 23 (2022)

15. Bui, M.N.; Rost, S.; Auge, M.; Tu, J.-S.; Zhou, L.; Aguilera, I.; Blügel, S.; Ghorbani-Asl, M.; Krasheninnikov, A.; Hashemi, A.; Komsa, H.-P.; Jin, L.; Kibkalo, L.; O'Connell, E.N.; Ramasse, Q.M.; Bangert, U.; Hofsäss, H.C.; Grützmacher, D.; Kardynal, B.E.
   Low-energy Se ion implantation in MoS$_2$ monolayers
   npj 2D Materials and Applications **6**, 42 (2022)

16. Cansever, H.; Anwar, M.S.; Stienen, S.; Lenz, K.; Narkovic, R.; Hlawacek, G.; Potzger, K.; Hellwig, O.; Faßbender, J.; Lindner, J.; Bali, R.
   Resonance behavior of embedded and freestanding microscale ferromagnets
   Scientific Reports **12**, 14809 (2022)

17. Chang, S.; He, J.; Prucnal, S.; Zhang, J.; Zhang, J.; Zhou, S.; Helm, M.; Dan, Y.
   Atomically Thin Delta-Doping of Self-Assembled Molecular Monolayers by Flash Lamp Annealing for Si-Based Deep UV Photodiodes
   ACS Applied Materials and Interfaces **14**, 30000 (2022)

18. Chen, Z.; Du, N.; Kiani, M.; Zhao, X.; Skorupa, I.; Schulz, S.; Bürger, D.; Di Ventra, M.; Polian, I.; Schmidt, H.
   Second harmonic generation exploiting ultra-stable resistive switching devices for secure hardware systems
   IEEE Transactions on Nanotechnology **21**, 71 (2022)

19. Chepkasov, I.V.; Smet, J.H.; Krasheninnikov, A.
   Single- and Multilayers of Alkali Metal Atoms Inside Graphene/MoS$_2$ Heterostructures: a Systematic First-Principles Study
   Journal of Physical Chemistry C **126**, 15558 (2022)

20. Choupanian, S.; Nagel, A.; Möller, W.; Pacholski, C.; Ronning, C.
   The disappearance and return of nanoparticles upon low energy ion irradiation
   Nanotechnology **33**, 035703 (2022)

21. Chumak, A.V. et al.
   Roadmap on Spin-Wave Computing
   IEEE Transactions on Magnetics **8**, 0800172 (2022)

22. Das, A.; Altstadt, E.; Kaden, C.; Kapoor, G.; Akhmadaliev, S.; Bergner, F.
     **Nanoindentation response of ion-irradiated Fe, Fe-Cr alloys and ferritic-martensitic steel
     Eurofer 97: The effect of ion energy**
     Frontiers in Materials **8**, 811851 (2022)

23. De, A.; Arekapudi, S.S.P.K.; Koch, L.; Samad, F.; Panda, S.N.; Benny, B.; Hellwig, O.;
     Barman, A.
     **Magnetic Configuration Driven Femtosecond Spin Dynamics in Synthetic
     Antiferromagnets**
     ACS Applied Materials and Interfaces **14**, 13970 (2022)

24. Del Moral, A.; Amat, E.; Engelmann, H.-J.; Pourteau, M.-L.; Rademaker, G.; Quirion, D.; Torres-
     Herrero, N.; Rommel, M.; Heinig, K.-H.; von Borany, J.; Tiron, R.; Bausells, J.; Perez-Murano, F.
     CMOS compatible manufacturing of a hybrid SET-FET circuit
     Semiconductor Science and Technology **37**, 125014 (2022)

25. Deussner, S.; Süss, D.; Abert, C.; Bruckner, F.; Fähler, S.; Heistracher, P.; Reichel, L.; Neu, V.
     **A rigorous single period micromagnetic model of stripe domains - comparison with
     analytics and experiment**
     Physical Review B **106**, 064404 (2022)

26. Diehl, R.; Korn, A.J.; Leibundgut, B.; Lugaro, M.; Wallner, A.
     Cosmic nucleosynthesis: A multi-messenger challenge
     Progress in Particle and Nuclear Physics **127**, 103983 (2022)

27. Diercks, J.S.; Georgi, M.; Herranz, J.; Diklić, N.; Chauhan, P.; Clark, A.H.; Hübner, R.; Faisnel,
     A.; Chen, Q.; Nachtegaal, M.; Eychmüller, A.; Schmidt, T.J.
     **CO_2 Electroreduction on Unsupported PdPt Aerogels: Effects of Alloying and Surface
     Composition on Product Selectivity**
     ACS Applied Energy Materials **5**, 8460 (2022)

28. Dörrer, L.; Heller, R.; Schmidt, H.
     **Tracer diffusion in proton-exchanged congruent $LiNbO_3$ crystals as a function of
     hydrogen content**
     Physical Chemistry Chemical Physics **24**, 16139 (2022)

29. Duan, J.; Chava, P.; Ghorbani-Asl, M.; Lu, Y.; Erb, D.; Hu, L.; Echresh, A.; Rebohle, L.; Erbe, A.;
     Krasheninnikov, A.; Helm, M.; Zeng, Y.-J.; Zhou, S.; Prucnal, S.
     **Self-driven Broadband Photodetector Based on $MoSe_2$/$FePS_3$ Van der Waals n-p Type-II
     Heterostructures**
     ACS Applied Materials and Interfaces **14**, 11927 (2022)

30. Dzekan, D.; Kischnik, T.D.; Diestel, A.; Kornelius, N.; Fähler, S.
     **Origin and avoidance of double peaks in the induced voltage of a thermomagnetic
     generator for harvesting low-grade waste heat**
     Journal of Physics: Energy **4**, 024006 (2022)

31. Echresh, A.; Prucnal, S.; Li, Z.; Hübner, R.; Ganss, F.; Steuer, O.; Bärwolf, F.; Jazavandi
     Ghamsari, S.; Helm, M.; Zhou, S.; Erbe, A.; Rebohle, L.; Georgiev, Y.
     **Fabrication of highly n-type-doped germanium nanowires and Ohmic contacts using ion
     implantation and flash lamp annealing**
     ACS Applied Electronic Materials **4**, 5256 (2022)

32. Erb, D.; Perlich, J.; Roth, S.; Röhlsberger, R.; Schlage, K.
     Real-Time Observation of Temperature-Induced Surface Nanofaceting in M-Plane α-Al_2O_3
     ACS Applied Materials and Interfaces **14**, 31373 (2022)

33. Fernandez Roldan, J.A.; Bran, C.; Asenjo, A.; Vázquez, M.; Sorrentino, A.; Ferrer, S.; Chubykalo-Fesenko, O.; Del Real, R.P.
Spatial magnetic imaging of non-axially symmetric vortex domains in cylindrical nanowire by transmission X-ray microscopy
Nanoscale **14**, 13661 (2022)

34. Fernandez Roldan, J.A.; Chubykalo-Fesenko, O.
Dynamics of chiral domain walls under applied current in cylindrical magnetic nanowires
APL Materials **10**, 111101 (2022)

35. Friedrich, R.; Ghorbani-Asl, M.; Curtarolo, S.; Krasheninnikov, A.V.
Data-Driven Quest for Two-Dimensional Non-van der Waals Materials
Nano Letters **22**, 989 (2022)

36. Gago, R.; Prucnal, S.; Azpeitia, J.; Esteban-Mendoza, D.; Jiménez, I.
Soft X-ray absorption study of sputtered tin oxide films
Journal of Alloys and Compounds **902**, 163768 (2022)

37. Gallardo, R.A.; Alvarado-Seguel, P.; Brevis, F.; Roldán-Molina, A.; Lenz, K.; Lindner, J.; Landeros, P.
Spin-wave channeling in magnetization-graded nanostrips
Nanomaterials **12**, 2785 (2022)

38. Gan, Z.; Paradisanos, I.; Estrada-Real, A.; Picker, J.; Najafidehaghani, E.; Davies, F.; Neumann, C.; Robert, C.; Wiecha, P.; Watanabe, K.; Taniguchi, T.; Marie, X.; Biskupek, J.; Mundszinger, M.; Leiter, R.; Krasheninnikov, A.; Urbaszek, B.; George, A.; Turchanin, A.
Chemical Vapor Deposition of High-Optical-Quality Large-Area Monolayer Janus Transition Metal Dichalcogenides
Advanced Materials **34**, 2205226 (2022)

39. Gao, C.; Lu, Y.; Wang, Y.; Wang, C.; Hübner, R.; Li, Y.; Zhan, J.; Zhao, M.; Cai, B.
Tuning Iron-Oxygen Covalency in Perovskite Oxides for Efficient Electrochemical Sensing
Journal of Physical Chemistry C **126**, 17618 (2022)

40. Gentile, P.; Cuoco, M.; Ying, Z.; Volkov, O.; Vera-Marun, I.J.; Makarov, D.; Ortix, C.
Electronic materials with nanoscale curved geometries
Nature Electronics **5**, 551 (2022)

41. Georgi, M.; Kresse, J.; Hiekel, K.; Hübner, R.; Eychmüller, A.
Expanding the Range: AuCu Metal Aerogels from H_2O and EtOH
Catalysts **12**, 441 (2022)

42. Gottscholl, A.; Wagenhöfer, M.; Klimmer, M.; Scherbel, S.; Kasper, C.; Baianov, V.; Astakhov, G.; Dyakonov, V.; Sperlich, A.
Superradiance of Spin Defects in Silicon Carbide for Maser Applications
Frontiers in Photonics **3**, 886354 (2022)

43. Günther, A.; Wollenberg, A.; Vogel, M.; Drobot, B.; Steudtner, R.; Freitag, L.; Hübner, R.; Stumpf, T.; Raff, J.
Speciation and spatial distribution of Eu(III) in fungal mycelium
Science of the Total Environment **851**, 158160 (2022)

44. Guo, M.X.; Cheng, C.K.; Liu, Y.C.; Wu, C.N.; Chen, W.N.; Chen, Y.-T.; Wu, C.T.; Hsu, C.H.; Zhou, S.; Chang, C.F.; Tjeng, L.H.; Lee, S.F.; Pai, C.F.; Hong, M.; Kwo, J.
Single-crystal epitaxial europium iron garnet films with strain-induced perpendicular magnetic anisotropy: Structural, strain, magnetic, and spin transport properties
Physical Review Materials **6**, 054412 (2022)

45. Hain, K.; Martschini, M.; Gülce, F.; Honda, M.; Lachner, J.; Kern, M.; Pitters, J.; Quinto, F.; Sakaguchi, A.; Steier, P.; Wiederin, A.; Wieser, A.; Yokoyama, A.; Golser, R.
Developing Accelerator Mass Spectrometry Capabilities for Anthropogenic Radionuclide Analysis to Extend the Set of Oceanographic Tracers
Frontiers in Marine Sciences **9**, 837515 (2022)

46. Han, Y.; Xi, F.; Allibert, F.; Radu, I.; Prucnal, S.; Bae, J.-H.; Hoffmann-Eifert, S.; Knoch, J.; Grützmacher, D.; Zhao, Q.-T.
Characterization of fully silicided source/drain SOI UTBB nMOSFETs at cryogenic temperatures
Solid-State Electronics **192**, 108263 (2022)

47. Härtwig, F.; Lorenz, L.; Makowski, S.; Krause, M.; Habenicht, C.; Lasagni, A.F.
Low-Friction of ta-C Coatings Paired with Brass and Other Materials under Vacuum and Atmospheric Conditions
Materials **15**, 2534 (2022)

48. Heller, R.; Klingner, N.; Claessens, N.; Merckling, C.; Meersschaut, J.
Differential evolution optimization of Rutherford back-scattering spectra
Journal of Applied Physics **132**, 165302 (2022)

49. Higley, D.J.; Chen, Z.; Beye, M.; Hantschmann, M.; Reid, A.H.; Mehta, V.; Hellwig, O.; Dakovski, G.L.; Mitra, A.; Engel, R.Y.; Maxwell, T.; Ding, Y.; Bonetti, S.; Bucher, M.; Carron, S.; Chase, T.; Jal, E.; Kukreja, R.; Liu, T.; Föhlisch, A.; Dürr, H.A.; Schlotter, W.F.; Stöhr, J.
Stimulated Resonant Inelastic X-Ray Scattering in a Solid
Communications Physics **5**, 83 (2022)

50. Hoffmann, V.; Gebel, B.; Heller, R.; Gemming, T.
Investigation of matrix independent calibration of oxygen in glow discharge optical emission spectrometry
Journal of Analytical Atomic Spectrometry **32**, 1223 (2022)

51. Holeňák, R.; Lohmann, S.; Primetzhofer, D.
Sensitive multi-element profiling with high depth resolution enabled by time-of-flight recoil detection in transmission using pulsed keV ion beams
Vacuum **204**, 111343 (2022)

52. Hollenbach, M.; Jagtap, N.S.; Fowley, C.; Baratech, J.; Guardia-Arce, V.; Kentsch, U.; Eichler-Volf, A.; Abrosimov, N.V.; Erbe, A.; Shin, C.; Kim, H.; Helm, M.; Lee, W.; Astakhov, G.; Berencen, Y.
Metal-assisted chemically etched silicon nanopillars hosting telecom photon emitters
Journal of Applied Physics **132**, 033101 (2022)

53. Hollenbach, M.; Klingner, N.; Jagtap, N.; Bischoff, L.; Fowley, C.; Kentsch, U.; Hlawacek, G.; Erbe, A.; Abrosimov, N.V.; Helm, M.; Berencen, Y.; Astakhov, G.
Wafer-scale nanofabrication of telecom single-photon emitters in silicon
Nature Communications **13**, 7683 (2022)

54. Huang, D.; Shi, Y.; Younas, M.; Khan, R.T.A.; Nadeem, M.; Shati, K.; Harfouche, M.; Kentsch, U.; Liu, Z.; Li, Y.; Zhou, S.; Kuznestov, A.; Ling, F. C.-C.
High Dielectric Transparent Film Tailored by Acceptor and Donor Codoping
Small **18**, 2107168 (2022)

55. Hula, T.; Schultheiß, K.; Trindade Goncalves, F.J.; Körber, L.; Bejarano, M.; Copus, M.; Flacke, L.; Liensberger, L.; Buzdakov, A.; Kakay, A.; Weiler, M.; Camley, R.; Faßbender, J.; Schultheiß, H.
Spin-wave frequency combs
Applied Physics Letters **121**, 112404 (2022)

56. Ilyakov, I.; Ponomaryov, O.; Klopf, J.M.; Pashkin, O.; Deinert, J.-C.; de Oliveira, T.; Evtushenko, P.; Helm, M.; Winnerl, S.; Kovalev, S.
Field-resolved THz-pump laser-probe measurements with CEP-unstable THz light sources
Optics Express **30**, 42141 (2022)

57. Jager, N.; Meindlhumer, M.; Zitek, M.; Spor, S.; Hruby, H.; Nahif, F.; Julin, J.; Keckes, J.; Mitterer, C.; Daniel, R.
Impact of Si on the high-temperature oxidation of AlCr(Si)N coatings
Journal of Materials Science and Technology **100**, 91 (2022)

58. Jakob, A.M.; Robson, S.G.; Schmitt, V.; Mourik, V.; Posselt, M.; Spemann, D.; Johnson, B.C.; Firgau, H.R.; Mayes, E.; McCallum, J.C.; Morello, A.; Jamieson, D.N.
Deterministic Shallow Dopant Implantation in Silicon with Detection Confidence Upper-Bound to 99.85% by Ion–Solid Interactions
Advanced Materials **34**, 2103235 (2022)

59. Jessat, J.; Moll, H.; John, W.; Bilke, M.-L.; Hübner, R.; Kretzschmar, J.; Steudtner, R.; Drobot, B.; Stumpf, T.; Sachs, S.
A comprehensive study on the interaction of Eu(III) and U(VI) with plant cells (Daucus carota) in suspension
Journal of Hazardous Materials **439**, 129520 (2022)

60. Jiang, G.; Wang, J.; Li, N.; Hübner, R.; Georgi, M.; Cai, B.; Li, Z.; Lesnyak, V.; Gaponik, N.; Eychmüller, A.
Self-Supported Three-Dimensional Quantum Dot Aerogels as a Promising Photocatalyst for CO_2 Reduction
Chemistry of Materials **34**, 2687 (2022)

61. Jiang, H.; Wang, M.; Fu, J.; Li, Z.; Shaikh, M.S.; Li, Y.; Nie, C.; Sun, F.; Tang, L.; Yang, J.; Qin, T.; Zhou, D.; Shen, J.; Sun, J.; Feng, S.; Zhu, M.; Kentsch, U.; Zhou, S.; Shi, H.; Wei, X.
Ultrahigh Photogain Short-Wave Infrared Detectors Enabled by Integrating Graphene and Hyperdoped Silicon
ACS Nano **16**, 12777 (2022)

62. Jiang, K.; Peng, P.; Tranca, D.; Tong, G.; Ke, C.; Lu, C.; Hu, J.; Liang, H.; Li, J.; Zhou, S.; Kymakis, E.; Zhuang, X.
Covalent Triazine Frameworks and Porous Carbons: Perspective from an Azulene-Based Case
Macromolecular Rapid Communications **43**, 2200392 (2022)

63. John, W.; Lückel, B.; Matschiavelli, N.; Hübner, R.; Matschi, S.; Hoehenwarter, W.; Sachs, S.
Endocytosis is a significant contributor to uranium(VI) uptake in tobacco (Nicotiana tabacum) BY-2 cells in phosphate-deficient culture
Science of the Total Environment **823**, 153700 (2022)

64. Jóźwik, I.; Jagielski, J.; Caban, P.; Kamiński, M.; Kentsch, U.
Direct visualization of highly resistive areas in GaN by means of low-voltage scanning electron microscopy
Materials Science in Semiconductor Processing **138**, 106293 (2022)

65. Kalanda, N.; Yarmolich, M.; Burko, A.; Temirov, A.; Kislyuk, A.; Demyanov, S.; Lenz, K.; Lindner, J.; Kim, D.-H.
Superparamagnetism and ferrimagnetism in the $Sr_2FeMoO_{6-\delta}$ nanoscale powder
Ceramics International **48**, 23931 (2022)

66. Klingner, N.; Heinig, K.-H.; Tucholski, D.; Möller, W.; Hübner, R.; Bischoff, L.; Hlawacek, G.; Facsko, S.
Epitaxial lateral overgrowth of tin spheres driven and directly observed by helium ion microscopy
Journal of Physical Chemistry Letters **126**, 16332 (2022)

67. Koll, D.; Wallner, A.; Battisson, S.; Fichter, S.; Fifield, L.K.; Froehlich, M.B.; Lachner, J.; Merchel, S.; Pavetich, S.; Rugel, G.; Slavkovská, Z.; Tims, S.G.; Ziegenrücker, R.
Element separation chemistry and cosmogenic ^{10}Be dating of a ferromanganese crust
Nuclear Instruments and Methods in Physics Research B **530**, 53 (2022)

68. Körber, L.; Hempel, A.; Otto, A.; Gallardo, R.A.; Henry, Y.; Lindner, J.; Kakay, A.
Finite-element dynamic-matrix approach for propagating spin waves: Extension to mono- and multilayers of arbitrary spacing and thickness
AIP Advances **12**, 115206 (2022)

69. Körber, L.; Kézsmárki, I.; Kakay, A.
Mode splitting of spin waves in magnetic nanotubes with discrete symmetries
Physical Review B **105**, 184435 (2022)

70. Körber, L.; Verba, R.; Otálora, J.A.; Kravchuk, V.; Lindner, J.; Faßbender, J.; Kakay, A.
Curvilinear spin-wave dynamics beyond the thin-shell approximation: Magnetic nanotubes as a case study
Physical Review B **106**, 014405 (2022)

71. Köster, J.; Storm, A.; Ghorbani-Asl, M.; Kretschmer, S.; Gorelik, T.E.; Krasheninnikov, A.; Kaiser, U.
Structural and Chemical Modifications of Few-layer Transition Metal Phosphorous Trisulfides by Electron Irradiation
Journal of Physical Chemistry C **126**, 15446 (2022)

72. Krawczyk-Bärsch, E.; Ramtke, J.; Drobot, B.; Müller, K.; Steudtner, R.; Kluge, S.; Hübner, R.; Raff, J.
Peptidoglycan as major binding motif for Uranium bioassociation on *Magnetospirillum magneticum* AMB-1 in contaminated waters
Journal of Hazardous Materials **437**, 129376 (2022)

73. Lasek, K.; Ghorbani-Asl, M.; Pathirage, V.; Krasheninnikov, A.; Batzill, M.
Controlling stoichiometry in ultrathin van der Waals films: $PtTe_2$, Pt_2Te_3, Pt_3Te_4, and Pt_2Te_2
ACS Nano **16**, 9908 (2022)

74. Lasek, K.; Li, J.; Ghorbani-Asl, M.; Khatun, S.; Alanwoko, O.; Pathirage, V.; Krasheninnikov, A.; Batzill, M.
Formation of In-Plane Semiconductor-Metal Contacts in 2D Platinum Telluride by Converting $PtTe_2$ to Pt_2Te_2
Nano Letters **22**, 9571 (2022)

75. Le Guyader, L.; Higley, D.J.; Pancaldi, M.; Liu, T.; Chen, Z.; Chase, T.; Granitzka, P.W.; Coslovich, G.; Lutman, A.A.; Dakovski, G.L.; Schlotter, W.F.; Shafer, P.; Arenholz, E.; Hellwig, O.; Lalieu, M.L.M.; Koopmans, B.; Reid, A.H.; Bonetti, S.; Stöhr, J.; Dürr, H.A.
State-resolved ultrafast charge and spin dynamics in [Co/Pd] multilayers
Applied Physics Letters **120**, 032401 (2022)

76. Lehninger, D.; Honeit, F.; Rafaja, D.; Klemm, V.; Röder, C.; Khomenkova, L.; Schneider, F.; von Borany, J.; Heitmann, J.
Size- and position-controlled Ge nanocrystals separated by high-*k* dielectrics
MRS Bulletin **47**, 773 (2022)

77. Lei, Z.; Fritzsche, B.; Salikhov, R.; Schwarzenberger, K.; Hellwig, O.; Eckert, K.
Magnetic separation of rare-earth ions: property database and Kelvin force distribution
Journal of Physical Chemistry C **126**, 2226 (2022)

78. Lewandowska-Andralojc, A.; Gacka, E.; Pedzinski, T.; Burdzinski, G.; Lindner, A.A.; O'Brien,
J.M.; Senge, M.O.; Siklitskaya, A.; Kubas, A.G.; Marciniak, B.; Walkowiak-Kulikowska, J.
**Understanding structure–properties relationships of porphyrin linked to graphene oxide
through π–π-stacking or covalent amide bonds**
Scientific Reports **12**, 13420 (2022)

79. Li, J.; Joseph, T.; Ghorbani-Asl, M.; Kolekar, S.; Krasheninnikov, A.; Batzill, M.
Edge and Point-Defect Induced Electronic and Magnetic Properties in Monolayer PtSe$_2$
Advanced Functional Materials **32**, 2110428 (2022)

80. Li, J.; Zhang, K.; Pang, C.; Zhao, Y.; Zhou, H.; Chen, H.; Lu, G.; Liu, F.; Wu, A.; Du, G.;
Akhmadaliev, S.; Zhou, S.; Chen, F.
Tunable structural colors in all-dielectric photonic crystals using energetic ion beams
Optics Express **30**, 23463 (2022)

81. Li, S.; Cao, P.; Li, F.; Asghar, W.; Wu, Y.; Xiao, H.; Liu, Y.; Zhou, Y.; Yang, H.; Zhang, Y.; Shang,
J.; Makarov, D.; Li, R.-W.
Self-powered Stretchable Strain Sensors for Motion Monitoring and Wireless Control
Nano Energy **92**, 106754 (2022)

82. Li, Z.; Yuan, Y.; Begeza, V.; Rebohle, L.; Helm, M.; Nielsch, K.; Prucnal, S.; Zhou, S.
On Curie temperature of B20-MnSi films
Scientific Reports **12**, 16388 (2022)

83. Lorenz, L.; Makowski, S.; Weihnacht, V.; Krause, M.; Lasagni, A.F.
**Advantages of Using Triboscopic Imaging: Case Studies on Carbon Coatings in Non-
Lubricated Friction Conditions**
Materials **15**, 4317 (2022)

84. Lu, Y.; Zhang, Y.; Yang, C.-Y.; Revuelta, S.; Qi, H.; Huang, C.; Jin, W.; Li, Z.; Vega-Mayoral, V.;
Liu, Y.; Huang, X.; Pohl, D.; Položij, M.; Zhou, S.; Cánovas, E.; Heine, T.; Fabiano, S.; Feng, X.;
Dong, R.
**Precise tuning of interlayer electronic coupling in layered conductive metal-organic
frameworks**
Nature Communications **13**, 7240 (2022)

85. Lumetzberger, J.; Ney, V.; Zhakarova, A.; Primetzhofer, D.; Lenz, K.; Ney, A.
**Control of site occupancy by variation of the Zn and Al content in NiZnAl ferrite epitaxial
films with low magnetic damping**
Physical Review B **105**, 134412 (2022)

86. Macková, A.; Malinský, P.; Jagerová, A.; Mikšová, R.; Lalik, O.; Nekvindová, P.; Mistrík, J.;
Marvan, P.; Sofer, Z.; Holý, V.; Schutter, J.D.; Kentsch, U.; Azarov, A.; Galeckas, A.
Energetic Au ion beam implantation of ZnO nanopillars for optical response modulation
Journal of Physics D: Applied Physics **55**, 215101 (2022)

87. Makarov, D.; Volkov, O.; Kakay, A.; Pylypovskyi, O.; Budinska, B.; Dobrovolskiy, O.
**New dimension in magnetism and superconductivity: 3D and curvilinear nano-
architectures**
Advanced Materials **34**, 2101758 (2022)

88. Makushko, P.; Kosub, T.; Pylypovskyi, O.; Hedrich, N.; Li, J.; Pashkin, O.; Avdoshenko, S.; Hübner, R.; Ganss, F.; Liedke, M.O.; Butterling, M.; Wagner, A.; Wagner, K.; Shields, B.J.; Lehmann, P.; Veremchuk, I.; Faßbender, J.; Maletinsky, P.; Makarov, D.
Flexomagnetism and vertically graded Néel temperature of antiferromagnetic Cr_2O_3 thin films
Nature Communications **13**, 6745 (2022)

89. Marqués Marchán, J.; Fernandez Roldan, J.A.; Bran, C.; Puttock, R.; Barton, C.; Moreno, J.A.; Kösel, J.; Vazquez, M.; Kazakova, O.; Chubykalo-Fesenko, O.; Asenjo, A.
Distinguishing local demagnetization contribution to the magnetization process in multisegmented nanowires
Nanomaterials **12**, 1968 (2022)

90. Mavridou, K.; Katsikini, M.; Othonos, A.; Florini, N.; Komninou, P.; Zervos, M.
Cu_3N/Cu_2O core-shell nanowires: growth and properties
Materials Advances **3**, 5163 (2022)

91. Meng, F.; Han, F.; Kentsch, U.; Pashkin, O.; Fowley, C.; Rebohle, L.; Thomson, M.D.; Suzuki, S.; Asada, M.; Roskos, H.G.
Coherent coupling of metamaterial resonators with dipole transitions of boron acceptors in Si
Optics Letters **47**, 4969 (2022)

92. Meng, F.; Walla, F.; Ul-Islam, Q.; Pashkin, O.; Schneider, H.; Jungemann, C.; Thomson, M.D.; Roskos, H.G.
Importance of valence-band anharmonicity and carrier distribution for third- and fifth-harmonic generation in Si:B pumped with intense terahertz pulses
Physical Review B **106**, 075203 (2022)

93. Murton, J.B.; Opel, T.; Toms, P.; Blinov, A.; Fuchs, M.; Wood, J.; Gärtner, A.; Merchel, S.; Rugel, G.; Savvinov, G.; Wetterich, S.
A multimethod dating study of ancient permafrost, Batagay megaslump, east Siberia
Quaternary Research **105**, 1 (2022)

94. Neeraj, K.; Sharma, A.; Almeida, M.; Matthes, P.; Samad, F.; Salvan, G.; Hellwig, O.; Bonetti, S.
Terahertz charge and spin transport in metallic ferromagnets: The role of crystalline and magnetic order
Applied Physics Letters **120**, 102406 (2022)

95. Nembach, H.T.; Jué, E.; Potzger, K.; Faßbender, J.; Silva, T.J.; Shaw, J.M.
Tuning of the Dzyaloshinskii-Moriya interaction by He^+ ion irradiation
Journal of Applied Physics **131**, 143901 (2022)

96. Nguyen, T.N.H.; Rasabathina, L.; Hellwig, O.; Sharma, A.; Salvan, G.; Yochelis, S.; Paltiel, Y.; Baczewski, L.T.; Tegenkamp, C.
Cooperative Effect of Electron Spin Polarization in Chiral Molecules Studied with Non-Spin-Polarized Scanning Tunneling Microscopy
ACS Applied Materials and Interfaces **14**, 38013 (2022)

97. Nichterwitz, M.; Duschek, K.; Zehner, J.; Oswald, S.; Heller, R.; Leistner, K.
Stabilization of nanoscale iron films by self-terminated electrodeposition in sulfate electrolyte
Electrochimica Acta **415**, 140170 (2022)

98. Niggas, A.; Schwestka, J.; Balzer, K.; Weichselbaum, D.; Schlünzen, N.; Heller, R.; Sascha, C.; Inani, H.; Tripathi, M.; Speckmann, C.; McEvoy, N.; Susi, T.; Kotakoski, J.; Gan, Z.; George, A.; Turchanin, A.; Bonitz, M.; Aumayr, F.; Wilhelm, R.A.
Ion-Induced Surface Charge Dynamics in Freestanding Monolayers of Graphene and MoS$_2$ Probed by the Emission of Electrons
Physical Review Letters **129**, 086802 (2022)

99. Nuzhnyy, D.; Bovtun, V.; Buixaderas, E.; Petzelt, J.; Savinov, M.; Kempa, M.; Paściak, M.; Rafalovskyi, I.; Chelod Paingad, V.; Kužel, P.; Kamba, S.; Repček, D.; Pashkin, O.; Trepakov, V.A.; Trybuła, Z.
Unusual dynamics of the ferroelectric phase transition in K$_{1-x}$Li$_x$TaO$_3$ crystals
Physical Review B **105**, 184103 (2022)

100. Oleg, H.; Hanuš, S.; Fähler, S.
Coupling between ferromagnetic and ferroelastic transitions and ordering in Heusler alloys produces new multifunctionality
MRS Bulletin **47**, 618 (2022)

101. Oliveros Mata, E.S.; Voigt, C.; Canon Bermudez, G.S.; Zabila, Y.; Valdez-Garduño, N.M.; Fritsch, M.; Mosch, S.; Kusnezoff, M.; Faßbender, J.; Vinnichenko, M.; Makarov, D.
Dispenser printed bismuth-based magnetic field sensors with non-saturating large magnetoresistance for touchless interactive surfaces
Advanced Materials Technologies **7**, 2200227 (2022)

102. Oommen, S.M.; Fallarino, L.; Heinze, J.; Hellwig, O.; Pisana, S.
Role of vibrational properties and electron-phonon coupling on thermal transport across metal-dielectric interfaces with ultrathin metallic interlayers
Journal of Physics: Condensed Matter **34**, 465701 (2022)

103. Pan, S.; Ganss, F.; Panda, S.; Sellge, G.; Banerjee, C.; Sinha, J.; Hellwig, O.; Barman, A.
Mechanism of femtosecond laser induced ultrafast demagnetization in ultrathin film magnetic multilayers
Journal of Materials Science **57**, 6212 (2022)

104. Pang, C.; Li, R.; Dong, H.; Saggau, C.N.; Kern, F.L.; Potapov, P.; Schultz, J.; Lubk, A.; Hübner, R.; Kentsch, U.; Zhou, S.; Helm, M.; Chen, F.; Ma, L.; Schmidt, O.G.
Plasmonic Nanoparticles Embedded in Nanomembrane Microcavity for Flexible Optical Tuning
Advanced Optical Materials **10**, 2200765 (2022)

105. Pantousa, S.; Mergia, K.; Ionescu, A.; Manios, E.; Dellis, S.; Kinane, C.; Langridge, S.; Caruana, A.; Kentsch, U.; Messoloras, S.
Fe+ ion irradiation effects in Fe-10at%Cr films irradiated at 300 °C
Nuclear Materials and Energy **30**, 101147 (2022)

106. Park, S.; Zhang, Z.; Qi, H.; Liang, B.; Mahmood, J.; Noh, H.-J.; Hambsch, M.; Wang, M.; Wang, M.; Hoang Ly, K.; Wang, Z.; Weidinger, I.M.; Zhou, S.; Baek, J.-B.; Kaiser, U.; Mannsfeld, S.C.B.; Feng, X.; Dong, R.
In-Plane Oriented Two-Dimensional Conjugated Metal–Organic Framework Films for High-Performance Humidity Sensing
ACS Materials Letters **4**, 1146 (2022)

107. Patra, S.; Das, P.; Rajbhar, M.K.; Facsko, S.; Möller, W.; Chatterjee, S.
Formation of core-shell nanostructure through wrapping of cuprous oxide nanowires by hydrogen titanate nanotubes
Radiation Physics and Chemistry **196**, 110103 (2022)

108. Pavetich, S.; Wallner, A.; Bottero, H.; Fifield, L.K.; Froehlich, M.B.; Huang, Y.; Koll, D.; Révay, Z.; Slavkovská, Z.; Sterba, J.H.; Tims, S.G.
Accelerator mass spectrometry measurements of ^{93}Zr for astrophysical and nuclear technology applications
Nuclear Instruments and Methods in Physics Research B **527**, 45 (2022)

109. Pedan, R.; Makushko, P.; Dubikovskyi, O.; Bodnaruk, A.; Burmak, A.; Sidorenko, S.; Voloshko, S.; Kalita, V.; Hübner, R.; Makarov, D.; Vladymyrskyi, I.
Homogenization and short-range chemical ordering of Co-Pt alloys driven by the grain boundary migration mechanism
Journal of Physics D: Applied Physics **55**, 405004 (2022)

110. Pile, S.; Stienen, S.; Lenz, K.; Narkovic, R.; Wintz, S.; Förster, J.; Mayr, S.; Buchner, M.; Weigand, M.; Ney, V.; Lindner, J.; Ney, A.
Nonstationary spin waves in a single rectangular permalloy microstrip under uniform magnetic excitation
Physical Review B **105**, 094415 (2022)

111. Pinteric, M.; Roh, S.; Hammer, S.; Pflaum, J.; Dressel, M.; Uykur, E.
Distinction of charge transfer and Frenkel excitons in pentacene traced via infrared spectroscopy
Journal of Materials Chemistry C **10**, 5582 (2022)

112. Porz, L.; Scherer, M.; Huhn, D.; Heine, L.-M.; Britten, S.; Rebohle, L.; Neubert, M.; Brown, M.; Lascelles, P.; Kitson, R.; Rettenwander, D.; Fulanovic, L.; Bruder, E.; Breckner, P.; Isaia, D.; Frömling, T.; Rödel, J.; Rheinheimer, W.
Blacklight sintering of ceramics
Materials Horizons **9**, 1717 (2022)

113. Posselt, M.; Bracht, H.; Ghorbani-Asl, M.; Radić, D.
Atomic mechanisms of self-diffusion in amorphous silicon
AIP Advances **12**, 115325 (2022)

114. Posselt, M.; Bracht, H.; Radic, D.
Atomistic simulations on the relationship between solid-phase epitaxial recrystallization and self-diffusion in amorphous silicon
Journal of Applied Physics **131**, 035102 (2022)

115. Qian, C.; Villafañe, V.; Schalk, M.; Astakhov, G.; Kentsch, U.; Helm, M.; Soubelet, P.; Wilson, N.P.; Rizzato, R.; Mohr, S.; Holleitner, A.W.; Bucher, D.B.; Stier, A.V.; Finley, J.J.
Unveiling the Zero-Phonon Line of the Boron Vacancy Center by Cavity-Enhanced Emission
Nano Letters **22**, 5137 (2022)

116. Racz, A.S.; Fogarassy, Z.; Kentsch, U.; Panjan, P.; Menyhard, M.
Design and production of tungsten-carbide rich coating layers
Applied Surface Science **586**, 152818 (2022)

117. Radic, D.; Peterlechner, M.; Posselt, M.; Bracht, H.
Treating Knock-On Displacements in Fluctuation Electron Microscopy Experiments
Microscopy and Microanalysis **28**, 2036 (2022)

118. Ramasubramanian, L.; Iurchuk, V.; Sorokin, S.; Hellwig, O.; Deac, A.M.
Effects of the rf current and bias field direction on the transition from linear to non-linear gyrotropic dynamics in magnetic vortex structures
Physical Review B **106**, 214413 (2022)

119. Rebohle, L.; Prucnal, S.; Berencen, Y.; Begeza, V.; Zhou, S.
A snapshot review on flash lamp annealing of semiconductor materials
MRS Advances **7**, 1301 (2022)

120. Rebohle, L.; Quade, A.; Schumann, T.; Blaschke, D.; Hübner, R.; Heller, R.; Foest, R.; Schäfer, J.; Skorupa, W.
Deposition of silicon oxide films on silicon using HelixJet – an atmospheric-pressure plasma jet process below 100 °C
Thin Solid Films **753**, 139257 (2022)

121. Redondo-Cubero, A.; Palomares, F.J.; Lorenz, K.; Rubio-Zuazo, J.; Hübner, R.; Mompéan, F.J.; García-Hernández, M.; Castro, G.R.; Vázquez, L.
Role of the metal supply pathway on silicon patterning by oblique ion beam sputtering
Applied Surface Science **580**, 152267 (2022)

122. Ren, Y.; Wang, C.; Cui, Z.; Liu, H.; Han, X.; Liu, P.; Akhmadaliev, S.; Zhou, S.; Cai, Y.
Tailored engineering of crystalline surface enabled by ion-irradiation-assisted femtosecond laser ablation
Vacuum **204**, 111334 (2022)

123. Rodriguez, R.; Regmi, S.; Zhang, H.; Yuan, W.; Makushko, P.; Montoya, E.A.; Veremchuk, I.; Hübner, R.; Makarov, D.; Shi, J.; Cheng, R.; Barsukov, I.
Robust spin injection via thermal magnon pumping in antiferromagnet/ferromagnet hybrid systems
Physical Review Research **4**, 033139 (2022)

124. Rugel, G.; Ziegenrücker, R.; Koll, D.; Lachner, J.; Noga, P.; Vivo-Vilches, C.; Renno, A.; Wallner, A.; Wiedenbeck, M.
Super-SIMS at DREAMS: Status of a unique and complex endeavour
Nuclear Instruments and Methods in Physics Research B **532**, 52 (2022)

125. Ruszkiczay-Rüdiger, Z.; Kern, Z.; Temovski, M.; Madarász, B.; Milevski, I.; Lachner, J.; Steier, P.
Late Pleistocene glacial advances, equilibrium-line altitude changes and paleoclimate in the Jakupica Mt. (North Macedonia)
Catena **216**, 106383 (2022)

126. Salikhov, R.; Samad, F.; Arekapudi, S.S.P.K.; Ehrler, R.; Lindner, J.; Kiselev, N.S.; Hellwig, O.
Control and tunability of magnetic bubble states in multilayers with strong perpendicular magnetic anisotropy at ambient conditions
Physical Review B **106**, 054404 (2022)

127. Schaber, J.; Xiang, R.; Teichert, J.; Arnold, A.; Murcek, P.; Zwartek, P.; Ryzhov, A.; Ma, S.; Gatzmaga, S.; Michel, P.; Gaponik, N.
Influence of surface cleaning on quantum efficiency, lifetime and surface morphology of p-GaN:Cs photocathodes
Micromachines **13**, 849 (2022)

128. Schefer, T.A.; Narkovic, R.; Lenz, K.; Ganss, F.; Roberts, M.P.; Hellwig, O.; Martyniuk, M.; Lindner, J.; Kostylev, M.
Application of a Microfabricated Microwave Resonator in a Co-Pd–Based Magnetic Hydrogen-Gas Sensor
Physical Review Applied **18**, 024015 (2022)

129. Schuster, A.K.; Voigt, K.; Klemmed, B.; Hartley, N.J.; Lütgert, B.J.; Bähtz, C.; Benad, A.; Brabetz, C.; Cowan, T.; Doeppner, T.; Erb, D.; Eychmueller, A.; Facsko, S.; Falcone, R.W.; Fletcher, L.B.; Frydrych, S.; Ganzenmüller, G.C.; Gericke, D.O.; Glenzer, S.H.; Grenzer, J.; Helbig, U.; Hiermaier, S.; Hübner, R.; Laso García, A.; Lee, H.J.; Macdonald, M.J.; McBride, E.E.; Neumayer, P.; Pak, A.; Pelka, A.; Prencipe, I.; Prosvetov, A.; Rack, A.; Ravasio, A.; Redmer, R.; Reemts, D.; Rödel, M.; Schoelmerich, M.; Schumacher, D.; Tomut, M.; Turner, S.J.; Saunders, A.M.; Sun, P.; Vorberger, J.; Zettl, A.; Kraus, D.
Recovery of Release Cloud from Laser Shock-Loaded Graphite and Hydrocarbon Targets: In Search of Diamonds
Journal of Physics D: Applied Physics **56**, 025301 (2022)

130. Schwabe, S.; Lünser, K.; Schmidt, D.; Nielsch, K.; Gaal, P.; Fähler, S.
What is the speed limit of martensitic transformations?
Science and Technology of Advanced Materials **23**, 633 (2022)

131. Sedmak, I.; Podlipec, R.; Urbancic, I.; Strancar, J.; Mortier, M.; Golobic, I.
Spatially resolved temperature distribution in a rare-earth-doped transparent glass-ceramic
Sensors **22**, 1970 (2022)

132. Seidl, A.; Anvari, R.; Dignam, M.M.; Richter, P.; Seyller, T.; Schneider, H.; Helm, M.; Winnerl, S.
Pump-induced terahertz anisotropy in bilayer graphene
Physical Review B **105**, 085404 (2022)

133. Sequeira, M.; Djurabekova, F.; Nordlund, K.; Mattei, J.-G.; Monnet, I.; Grygiel, C.; Alves, E.; Lorenz, K.
Examining different regimes of ionization-induced damage in GaN through atomistic simulations
Small **18**, 2102235 (2022)

134. Sheka, D.; Pylypovskyi, O.; Volkov, O.; Yershov, K.; Kravchuk, V.P.; Makarov, D.
Fundamentals of curvilinear ferromagnetism: statics and dynamics of geometrically curved wires and narrow ribbons
Small **18**, 2105219 (2022)

135. Shi, Y.-L.; Huang, D.; Kentsch, U.; Zhou, S.; Ling, F. C.-C.
A high-k Cu-doped ZnO film formed via Ga-ion implantation: The acceptor-donor co-doping approach
Journal of Alloys and Compounds **911**, 165057 (2022)

136. Shimamoto, Y.; Matsushima, Y.; Hasegawa, T.; Kousaka, Y.; Proskurin, I.; Kishine, J.; Ovchinnikov, A.S.; Trindade Goncalves, F.J.; Togawa, Y.
Observation of Collective Resonance Modes in a Chiral Spin Soliton Lattice with Tunable Magnon Dispersion
Physical Review Letters **128**, 247203 (2022)

137. Sloika, M.; Gaididei, Y.; Kravchuk, V.; Pylypovskyi, O.; Makarov, D.; Sheka, D.
Impact of curvature-induced Dzyaloshinskii-Moriya interaction on magnetic vortex texture in spherical caps
Low Temperature Physics **48**, 956 (2022)

138. Solano, J.; Gladii, O.; Kuntz, P.; Henry, Y.; Halley, D.; Bailleul, M.
Spin-wave study of magnetic perpendicular surface anisotropy in single crystalline MgO/Fe/MgO films
Physical Review Materials **6**, 124409 (2022)

139. Sruthil Lal, S.B.; Devaraj, M.; Posselt, M.; Aravindh Sd, A.; Sharan, A.
Modified HSE06 functional applied to anatase TiO$_2$: influence of exchange fraction on the quasiparticle electronic structure and optical response
Electronic Structure **4**, 045001 (2022)

140. Strusch, T.; Lenz, K.; Meckenstock, R.; Bali, R.; Ehrler, J.; Lindner, J.; Faßbender, J.; Farle, M.; Potzger, K.; Semisalova, A.
Spin pumping at interfaces with ferro- and paramagnetic Fe$_{60}$Al$_{40}$ films acting as spin source and spin sink
Journal of Applied Physics **132**, 213906 (2022)

141. Sun, B.; Lu, Q.; Chen, K.; Zheng, W.; Liao, Z.; Lopatik, N.; Li, D.; Hantusch, M.; Zhou, S.; Wang, H.I.; Sofer, Z.; Brunner, E.; Zschech, E.; Bonn, M.; Dronskowski, R.; Mikhailova, D.; Liu, Q.; Zhang, D.; Yu, M.; Feng, X.
Redox-Active Metaphosphate-Like Terminals Enable High-Capacity MXene Anodes for Ultrafast Na-Ion Storage
Advanced Materials **34**, 2108682 (2022)

142. Sun, X.; Zhang, Y.; Ge, W.
Photo-induced macro/mesoscopic scale ion displacement in mixed-halide perovskites: ring structures and ionic plasma oscillations
Light: Science and Applications **11**, 262 (2022)

143. Sun, Z.; Hübner, R.; Li, J.; Wu, C.
Artificially sporulated Escherichia coli cells as a robust cell factory for interfacial biocatalysis
Nature Communications **13**, 3142 (2022)

144. Sun, Z.; Jurica, J.; Hübner, R.; Wu, C.
Pickering interfacial catalysts for asymmetric organocatalysis
Catalysis Science & Technology **12**, 4811 (2022)

145. Tabean, S.; Mousley, M.; Pauly, C.; de Castro, O.; Serralta Hurtado De Menezes, E.; Klingner, N.; Hlawacek, G.; Wirtz, T.; Eswara, S.
Quantitative nanoscale imaging using transmission He ion channelling contrast: Proof-of-concept and application to study isolated crystalline defects
Ultramicroscopy **233**, 113439 (2022)

146. Tielrooij, K.J.; Principi, A.; Saleta Reig, D.; Block, A.; Varghese, S.; Schreyeck, S.; Brunner, K.; Karczewski, G.; Ilyakov, I.; Ponomaryov, O.; de Oliveira, T.; Chen, M.; Deinert, J.-C.; Gomez Carbonell, C.; Valenzuela, S.O.; Molenkamp, L.W.; Kiessling, T.; Astakhov, G.; Kovalev, S.
Milliwatt terahertz harmonic generation from topological insulator metamaterials
Light: Science and Applications **11**, 315 (2022)

147. Vagadia, M.; Sardar, S.; Tank, T.; Das, S.; Gunn, B.; Pandey, P.; Hübner, R.; Rodolakis, F.; Fabbris, G.; Choi, Y.; Haskel, D.; Frano, A.; Rana, D.S.
Extraordinary anisotropic magnetoresistance in CaMnO$_3$/CaIrO$_3$ heterostructures
Physical Review B **105**, L020402 (2022)

148. Vegesna, S.V.; Lanka, S.V.; Bürger, D.; Li, Z.; Linzen, S.; Schmidt, H.
Analysis of Low-Temperature Magnetotransport Properties of NbN Thin Films Grown by Atomic Layer Deposition
Magnetochemistry **8**, 33 (2022)

149. Venanzi, T.; Selig, M.; Pashkin, A.; Winnerl, S.; Katzer, M.; Arora, H.; Erbe, A.; Patanè, A.; Kudrynskyi, Z.R.; Kovalyuk, Z.D.; Baldassarre, L.; Knorr, A.; Helm, M.; Schneider, H.
Terahertz control of photoluminescence emission in few-layer InSe
Applied Physics Letters **120**, 092104 (2022)

150. Veremchuk, I.; Liedke, M.O.; Makushko, P.; Kosub, T.; Hedrich, N.; Pylypovskyi, O.; Ganss, F.; Butterling, M.; Hübner, R.; Attallah, A.G.; Wagner, A.; Wagner, K.; Shields, B.; Maletinsky, P.; Faßbender, J.; Makarov, D.
Defect nanostructure and its impact on magnetism of α-Cr$_2$O$_3$ thin films
Small **18**, 2201228 (2022)

151. Veremchuk, I.; Makushko, P.; Hedrich, N.; Zabila, Y.; Kosub, T.; Liedke, M.O.; Butterling, M.; Attallah, A.G.; Wagner, A.; Burkhardt, U.; Pylypovskyi, O.; Hübner, R.; Faßbender, J.; Maletinsky, P.; Makarov, D.
Magnetism and magnetoelectricity of textured polycrystalline bulk Cr$_2$O$_3$ sintered in conditions far out of equilibrium
ACS Applied Electronic Materials **4**, 2943 (2022)

152. Vitanov, P.; Ivanova, T.; Dikov, H.; Terziyska, P.; Ganchev, M.; Petkov, N.; Georgiev, Y.; Asenov, A.
Effect of a Discontinuous Ag Layer on Optical and Electrical Properties of ZnO/Ag/ZnO Structures
Coatings **12**, 1324 (2022)

153. Wang, M.; Yu, Y.; Prucnal, S.; Berencén, Y.; Shaikh, M.S.; Rebohle, L.; Khan, M.B.; Zviagin, V.; Hübner, R.; Pashkin, A.; Erbe, A.; Georgiev, Y.M.; Grundmann, M.; Helm, M.; Kirchner, R.; Zhou, S.
Mid- and far-infrared localized surface plasmon resonances in chalcogen-hyperdoped silicon
Nanoscale **14**, 2826 (2022)

154. Wei, W.; Hübner, R.; Georgi, M.; Wang, C.; Wu, X.; Eychmüller, A.
Controllable electrostatic manipulation of structure building blocks in noble metal aerogels
Materials Advances **3**, 5760 (2022)

155. Wenzel, M.; Ortiz, B.R.; Wilson, S.D.; Dressel, M.; Tsirlin, A.A.; Uykur, E.
Optical study of RbV$_3$Sb$_5$: Multiple density-wave gaps and phonon anomalies
Physical Review B **105**, 245123 (2022)

156. Wenzel, M.; Tsirlin, A.; Iakutkina, O.; Yin, Q.; Lei, H.C.; Dressel, M.; Uykur, E.
Effect of magnetism and phonons on localized carriers in ferrimagnetic kagome metals GdMn$_6$Sn$_6$ and TbMn$_6$Sn$_6$
Physical Review B **106**, L241108 (2022)

157. Werbrouck, A.; Mattelaer, F.; Nisula, M.; Minjauw, M.; Munnik, F.; Dendooven, J.; Detavernier, C.
Surface Reactions Between LiHMDS, TMA and TMP Leading to Deposition of Amorphous Lithium Phosphate
Journal of Materials Chemistry A **10**, 3543 (2022)

158. Werner, Z.; Barlak, M.; Ratajczak, R.; Kentsch, U.; Heller, R.; Munnik, F.; Konarski, P.; Dłużewski, P.; Pisarek, M.; Kozłowski, M.; Ażgin, J.; Zagórski, J.; Staszkiewicz, B.
The recovery effects of electron-beam pulse treatment in Sn implanted Ge
Radiation Effects and Defects in Solids **177**, 1088 (2022)

159. Winter, M.; Trindade Goncalves, F.J.; Soldatov, I.; He, Y.; Zuniga Cespedes, B.E.; Milde, P.; Lenz, K.; Hamann, S.; Uhlarz, M.; Vir, P.; König, M.; Moll, P.J.W.; Schlitz, R.; Goennenwein, S.T.B.; Eng, L.M.; Schäfer, R.; Wosnitza, J.; Felser, C.; Gayles, J.; Helm, T.
Antiskyrmions and their electrical footprint in crystalline mesoscale structures of Mn$_{1.4}$PtSn
Communications Materials **3**, 102 (2022)

160. Xie, Y.; Birowska, M.; Funk, H.S.; Fischer, I.A.; Schwarz, D.; Schulze, J.; Zeng, Y.-J.; Helm, M.; Zhou, S.; Prucnal, S.
Tuning of Curie temperature in Mn$_5$Ge$_3$ films
Journal of Applied Physics **131**, 105102 (2022)

161. Xie, Y.; Li, Z.; Begeza, V.; Funk, H.S.; Fischer, I.A.; Zeng, Y.-J.; Helm, M.; Zhou, S.; Prucnal, S.
Influence of fabrication parameters on the magnetic and structural properties of Mn$_5$Ge$_3$
Semiconductor Science and Technology **37**, 065009 (2022)

162. Xu, H.; Li, Z.; Pang, C.; Li, R.; Li, G.; Akhmadaliev, S.; Zhou, S.; Lu, Q.; Jia, Y.; Chen, F.
Second harmonic generation from precise diamond blade diced ridge waveguides
Chinese Physics B **31**, 094209 (2022)

163. Xu, R.; Canon Bermudez, G.S.; Pylypovskyi, O.; Volkov, O.; Oliveros Mata, E.S.; Zabila, Y.; Illing, R.; Makushko, P.; Milkin, P.; Ionov, L.; Faßbender, J.; Makarov, D.
Self-healable printed magnetic field sensors using alternating magnetic fields
Nature Communications **13**, 6587 (2022)

164. Yagodkin, D.; Greben, K.; Eljarrat Ascunce, A.; Kovalchuk, S.; Ghorbani-Asl, M.; Jain, M.; Kretschmer, S.; Severin, N.; Rabe, J.P.; Krasheninnikov, A.; Koch, C.T.; Bolotin, K.I.
Extrinsic localized excitons in patterned 2D semiconductors
Advanced Functional Materials **32**, 2203060 (2022)

165. Yastremsky, I.A.; Faßbender, J.; Ivanov, B.A.; Makarov, D.
Enhanced Longitudinal Relaxation of Magnetic Solitons in Ultrathin Films
Physical Review Applied **17**, L061002 (2022)

166. Yershov, K.; Kakay, A.; Kravchuk, V.P.
Curvature-induced drift and deformation of magnetic skyrmions: Comparison of the ferromagnetic and antiferromagnetic cases
Physical Review B **105**, 054425 (2022)

167. Yu, Z.; Guo, H.; Sun, Z.; Li, Y.; Liu, Y.; Yang, W.; Zhu, M.; Jin, H.; Li, Y.; Feng, L.; Li, S.; Prucnal, S.; Li, W.
U7Co 3d impurity energy level mediated photogenerated carriers transfer in Bi$_2$S$_3$/ZnS:Co/TiO$_2$ photoanode
Chemical Engineering Journal **433**, 134458 (2022)

168. Yuan, S.; Peng, J.; Cai, B.; Huang, Z.; Garcia-Esparza, A.T.; Sokaras, D.; Zhang, Y.; Giordano, L.; Akkiraju, K.; Guang Zhu, Y.; Hübner, R.; Zou, X.; Román-Leshkov, Y.; Shao-Horn, Y.
Tunable metal hydroxide–organic frameworks for catalysing oxygen evolution
Nature Materials **21**, 673 (2022)

169. Yuan, Y.; Zhou, S.; Wang, X.
Modulating properties by light ion irradiation: From novel functional materials to semiconductor power devices
Journal of Semiconductors **43**, 063101 (2022)

170. Yuk, T.C.; Elliger, N.; Klis, B.; Kollar, M.; Horvath, E.; Forro, L.; Dressel, M.; Uykur, E.
High-pressure investigations in CH$_3$NH$_3$PbX$_3$ (X = I, Br and Cl): suppression of ion migration and stabilization of low-temperature structure
Physical Review B **106**, 214106 (2022)

171. Zaiets, O.; Kravchuk, V.; Pylypovskyi, O.; Makarov, D.; Sheka, D.
Circular stripe domains and cone state vortices in disk-shaped exchange coupled magnetic heterostructures
Journal of Physics D: Applied Physics **55**, 445003 (2022)

172. Zhang, Q.; Liang, J.; Bi, K.; Zhao, L.; Bai, H.; Cui, Q.; Zhou, H.-A.; Bai, H.; Feng, H.; Song, W.; Chai, G.; Gladii, O.; Schultheiß, H.; Zhu, T.; Zhang, J.; Peng, Y.; Yang, H.; Jiang, W.
Quantifying the Dzyaloshinkii-Moriya Interaction Induced by the Bulk Magnetic Asymmetry
Physical Review Letters **128**, 167202 (2022)

173. Zheng, W.; Sun, B.; Li, D.; Gali, S.M.; Zhang, H.; Fu, S.; Di Virgilio, L.; Li, Z.; Yang, S.; Zhou, S.; Beljonne, D.; Yu, M.; Feng, X.; Wang, H.I.; Bonn, M.
Band transport by large Fröhlich polarons in MXenes
Nature Physics **18**, 544 (2022)

174. Zhu, L.-G.; Sheng, Z.; Schneider, H.; Chen, H.-T.; Tani, M.
Ultrafast phenomena and terahertz waves: introduction
Journal of the Optical Society of America B **39**, UPT1 (2022)

Active Patents and Patent Applications

(Effective April 1st, 2023)

1. **Quantum Cascade Laser Structure**
   P0404   *102004009531.0*   *DE, US*

2. **Coherent terahertz radiation source**
   P0410   *05787095.8*   *DE, GB*

3. **Flüssigmetall-Ionenquelle zur Erzeugung von Lithium-Ionenstrahlen**
   P0709   *102007027097.8*   *DE*

4. **Strahlungsdetektor, Verwendung eines Strahlungsdetektors und Verfahren zur Herstellung eines Strahlungsdetektors**
   P0907   *102009017505.9*   *DE*

5. **Integrated non-volatile memory elements, design and use**
   P1108   *102011051767.7*   *DE, US*

6. **Magnetisierbare Einzel- und Mehrschichtstrukturen, deren Herstellung und Verwendung**
   P1109   *102011052217.4*   *DE*

7. **Carrier material for electrically polarizable biomaterials, polyelectrolyte materials, atoms, ions and molecules; its manufacture and use**
   P1112   *12772707.1*   *AT, CH, DE, US*

8. **Integrierter nichtflüchtiger Analogspeicher**
   P1204   *102012102326.3*   *DE*

9. **Integrierte Elektrode mit nichtflüchtig positionierbarer, statisch geladener Grenzschicht, Aufbau und Verwendung**
   P1205   *102012104425.2*   *DE*

10. **Magnetooptik mit optischen Polarisationsgittern aus strukturierten unmagnetischen Metallen**
    P1309   112014001145.2   DE

11. **Magnetisierbare Halbleiter und Oxide mit permanenter Magnetisierung, deren Herstellung und Verwendung**
    P1313   *102013209278.4*   *DE*

12. **Variable capacitance diode, method for producing a variable capacitance diode, and storage device and detector comprising such a variable capacitance diode**
    P1403   *102014105639.6*   *CN, DE, US*

13. **Strukturierungsverfahren**
    P1404   *102014107458.0*   *CN, DE*

14. **Complementary resistance switch**
    P1505   *15166520.5*   *BE, DE, FR, GB*

15. **Complementary resistance switch, contact-connected polycrystalline piezo- or ferroelectric thin-film layer, method for encrypting a bit sequence**
    P1506   *14/761,319*   *US*

16. **Method and circuit arrangement for encrypting and decrypting a bit sequence**
    P1507   *14703281.7*   *DE, FR, GB*

17. **Complementary resistance switch, contact-connected polycrystalline piezo- or ferroelectric thin-film layer, method for encrypting a bit sequence**
    P1508   *14/800,785*   *US*

18. **Self-cleaning high temperature resistant solar selective coating**
    P1510   *P201431972*   *ES*

19. **Method for producing silicon-based anodes for secondary batteries**
    P1603   *201780011186.2*   *AT, CH, CN, DE, ES, FR, GB, IT, PL, US*

20. **Method and means for operating a complementary analogue reconfigurable memristive resistive switch and use thereof as an artificial synapse**
    P1604   *102016205860.6*   *CN, DE, US*

21. **Ionenmikroskopievorrichtung**
    P1608   *102016112328.5*   *DE*

22. **THz-Antenne und Vorrichtung zum Senden und/oder Empfangen von THz-Strahlung**
    P1609   *102016116900.5*   *DE*

23. **Vorrichtung und Verfahren zur Umwandlung thermischer Energie in elektrische Energie**
    P1614   *102017126803.0*   *DE*

24. **Apparatus for characterizing the electrical resistance of a measurement object**
    P1702   *102017105317.4*   *CN, DE, EP, US*

25. **Schichtanordnung, elektronisches Bauteil mit einer Schichtanordnung und Verwendung einer Schichtanordnung**
    P1703   *102017109082.7*   *DE*

26. **Vorrichtung und Verfahren zum Erzeugen von Ionenpulsen**
    P1709   *102017218456.6*   *DE*

27. **Teilchenspektrometer und Teilchenspektrometrieverfahren**
    P1803   *102018106412.8*   *DE*

28. **Method for continuously determining all of the components of the resistance tensor of thin films**
    P1804   *102018106466.7*   *CN, DE, EP, US*

29. **Transparent specimen slide**
    P1805   *102018107810.2*   *DE, US*

30. **Method for the reconfiguration of a vortex density in a rare earth manganate, a non-volatile impedance switch and use thereof**
    P1809   *102018112605.0*   *CN, DE, EP, US*

31. **Schichtabfolge zur Erzeugung von Elektrolumineszenz und deren Verwendung**
    P1813   *102018117210.9*   *DE*

32. **Verfahren zur Herstellung eines keramischen Materials mit lokal einstellbarem Permeabilitätsgradienten, dessen Anwendung in einem Beschichtungsverfahren sowie dessen Verwendung**
    P1819   *102018125270.6*   *DE*

33. **Verfahren zum Herstellen eines gedruckten magnetischen Funktionselements und gedrucktes magnetisches Funktionselement**
    P1908   *102019211970.0*   *DE, EP*

34. **Magnetische Streufeld-Struktur, magnonisches Bauelement und Verfahren zur Herstellung einer magnetischen Streufeldstruktur**
   P1915   102019129203.4   DE

35. **Vorrichtung zur gezielten Anordnung von in einem Analyten gelösten, elektrisch polarisierbaren Materialien, Verfahren zur Bestimmung eines isoelektrischen Punktes eines elektrisch isolierenden Materials, Verfahren zum gezielten Anordnen eines in einem Analyten gelösten elektrisch polarisierbaren Materials**
   P2001   102020200470.6   DE, EP

Concluded scientific degrees

PhD theses

1. Anwar, Md. Shadab
   Magnetostructural phase transition in $Fe_{60}V_{40}$ thin films
   TU Dresden, 21.12.2022

2. Creutzburg, Sascha
   Neutralisation langsamer hochgeladener Ionen in zwei-dimensionalen Materialien
   TU Dresden, 15.03.2022

3. Duan, Juanmei
   Optoelectronic applications of heavily doped GaAs and $MoSe_2$/$FePS_3$ heterostructures
   TU Dresden, 14.01.2022

4. Fotev, Ivan
   Evolution of electronic order in $BaFe_2As_2$ under high pressures investigated by pump-probe spectroscopy
   TU Dresden, 28.04.2022

5. Ghaderzadeh, Sadegh
   Atomistic simulations of irradiation-induced phenomena in low-dimensional materials
   TU Dresden, 17.03.2022

6. Hollenbach, Michael
   Ion-induced telecom single-photon emitters in silicon for scalable quantum photonics
   TU Dresden, 19.12.2022

7. Khan, M. Bilal
   Towards scalable reconfigurable field effect transistors: fabrication and characterization
   TU Dresden, 17.01.2022

8. Lünser, Klara
   Martensitische Phasenumwandlungen und Zwillingsbildung in epitaktisch gewachsenen Nickel-Titan-Schichten
   TU Dresden, 02.12.2022

9. Ramasubramanian, Lakshmi
   Tunable magnetic vortex dynamics
   TU Chemnitz, 23.03.2022

10. Schumann, Erik
    Percolated Si:SiO_2 nanocomposite: Oven- vs. laser-liduced crystallization of SiO_x thin films
    TU Chemnitz, 05.05.2022

11. Seidl, Angelika
    Nichtgleichgewichtsdynamik in Graphen bei geringen Photonenergien
    TU Dresden, 22.11.2022

Bachelor/Master/Diploma theses

1. Hergenhan, Felix
   Superconducting germanium for quantum technology
   TU Dresden (B.Sc.), 13.10.2022

Awards and honors

1.   **Erbe, Artur**

Head of the department "Nanoelectronics" was appointed as **Honorary Professor** for 'Nanostructures for electronics and sensorics' at the Faculty of Electrical and Computer Engineering of TU Dresden.

2.   **Salikhov, Ruslan**

PostDoc in the department "Magnetism" was awarded the **HZDR Research Award 2022** for "outstanding research in the fields of magnetization dynamics and THz spectroscopy", together with Dr. Sergey Kovalev from Institute of Radiation Physics.

3.   **Lünser, Klara**

Former doctoral researcher in the department "Magnetism" received the **HZDR PhD Award 2022** for her dissertation "Martensitische Phasenumwandlungen und Zwillingsbildung in epitaktisch gewachsenen Nickel-Titan-Schichten".

4.   **Fekri, Zahra**

Doctoral researcher in the department "Nanoelectronics" received a **Student Travel Grant** of the Graphene-2022 conference, Aachen, Germany, July 5 - 8, 2022 for her poster presentation "Modification of charge transport in single layer MoS_2".

5.   **Ghosh, Sayantan**

Doctoral researcher in the department "Nanoelectronics" received the **Student Award** of the NanoNet+ Workshop *2D Materials and ultra-high doped semiconductors: electronics, photonics and sensing*, Görlitz, Germany, October 4 – 6, 2022 for his oral contribution 'Novel Mixed Dimensional Reconfigurable Field Effect Transistors: Fabrication and Characterization'.

6.   **Jagtap, Nagesh**

Doctoral researcher in the department "Nanoelectronics" was elected as Helmholtz Juniors, the council of the doctoral researchers at the Helmholtz Association of German Research Centers. He is speaker of the committee on *Working Conditions*.

7.   **Koll, Dominik**

Doctoral researcher in the department "Accelerator Mass Spectrometry and Isotope Research" received an **Award** of the science communication contest "I'm a scientist" of the Wissenschaft im Dialog GmbH.

8.   **Krasheninnikov, Arkady**

Head of the group "Atomistic Simulations of Irradiation-induced Phenomena" was once again announced as **Highly Cited Researcher 2022** by Clarivate Analytics (Web of Science), Jersey, UK.

9.   **Li, Rang**

PostDoc in the department "Semiconductor Materials" won the **Best Poster Prize** of the E-MRS Spring Meeting, May 30 – June 03, 2022, (virtual event) for his poster contribution "Plasmonic Hyper-doped Semiconductors for Infrared Q-switched lasing".

10. **Schultheiß, Katrin**

PostDoc in the department "Magnetism" received funding for her EU project *NIMFEIA - Nonlinear magnons for reservoir computing in reciprocal space* of about 3 Mio. Euro for 4 years.

11. **Steuer, Oliver**

Doctoral researcher in the department "Semiconductor Materials" received the Second Prize of the **Student Award** of the NanoNet+ Workshop *2D Materials and ultra-high doped semiconductors: electronics, photonics and sensing*, Görlitz, Germany, October 4 – 6, 2022 for his oral contribution "Band-gap and strain engineering in $Ge_{1-x}Sn_x$ alloys using post-growth pulsed laser melting".

Invited conference contributions

1. Astakhov, G.
   Scalable fabrication of single quantum emitters in silicon
   Flagship Workshop: Defects in solids for quantum technologies, 12. - 17.06.2022, Stockholm, Sweden

2. Berencen, Y.; Hollenbach, M.; Klingner, N.; Jagtap, N.S.; Bischoff, L.; Fowley, C.; Kentsch, U.; Hlawacek, G.; Erbe, A.; Abrosimov, N.V.; Helm, M.; Astakhov, G.V.
   Telecom-wavelength single-photon sources in silicon for scalable photonic quantum technology
   2022 E-MRS Fall Meeting / Symposium I: Group-IV semiconductor materials for nanoelectronics and cryogenic electronics, 19. - 22.09.2022, Warsaw, Poland

3. Escobar-Galindo, R.; Heras, I.; Guillén, E.; Munnik, F.; Azkona, I.; Caro, A.; Rojas, T.C.; Sánchez-López, J.C.; Krause, M.
   Optical design, microstructural characterization and high-temperature in-air stability study of solar selective coatings based on aluminium- (titanium, chromium) oxynitride multilayers
   SICT 2022 / PlasmaTech 2022 / Tribology 2022 Joint Hybrid Conferences, 27. - 29.04.2022, Barcelona, Spain

4. Fähler, S.; Schwabe, S.; Lünser, K.; Schmidt, D.; Nielsch, K.; Gaal, P.
   What is the speed limit of martensitic transformations?
   MSE2022, 27. - 30.09.2022, Darmstadt, Germany

5. Fernandez Roldan, J.A.
   Current- and field- induced magnetization dynamics and magnetic configurations in cylindrical nanowires
   Magnetic Resonance Laboratory Seminars, 17.05.2022, San Carlos de Bariloche, Argentina

6. Fichter, S.
   Synthesis and characterization of tri- and tetravalent actinide amidinates
   Jahrestagung der Fachgruppe Nuklearchemie 2022, 06.10.2022, Bergisch Gladbach, Germany

7. Friedrich, R.
   Data-driven design of two-dimensional non-van der Waals systems and ionic materials
   Seminar Theoretische Chemie TU Dresden, 19.04.2022, Dresden, Germany

8. Friedrich, R.
   Data-driven design of two-dimensional non-van der Waals materials
   CASUSCON, 13.07.2022, Wrocław, Poland

9. Friedrich, R.
   Data-driven design of two-dimensional non-van der Waals materials
   CECAM Workshop Virtual Materials Design, 18.07.2022, Karlsruhe, Germany

10. Friedrich, R.
    Data-driven research for the discovery of novel two-dimensional materials
    DFG CRC 1415 Young Investigator Symposium, 21.11.2022, Dresden, Germany

11. Ghorbani Asl, M.
    Defect engineering in two-dimensional materials
    Webinar talks from leading international experts from various fields of STEM, 12.09.2022, Bengaluru, India

12. Hellwig, O.
    Exploring magnetic reversal behavior and domain structure in perpendicular anisotropy layered synthetic antiferromagnets
    Webinar series on Spintronics (W2S, online), National Institute of Science Education and Research, 07.07.2022, Bhubaneswar, India

13. Hellwig, O.
Exploring magnetic reversal behavior and domain structure in perpendicular anisotropy layered synthetic antiferromagnets
AVS Conference, 06.11.-11.11.2022, Pittsburgh, USA

14. Hellwig, O.
Exploring magnetic reversal behavior and domain structure in perpendicular anisotropy layered synthetic antiferromagnets
Condensed Matter Seminar, UC Santa Cruz, 14.11.2022, Santa Cruz, USA

15. Hellwig, O.
Exploring magnetic reversal behavior and domain structure in perpendicular anisotropy layered synthetic antiferromagnets
Condensed Matter Seminar, Western Digital, 16.11.2022, San Jose, USA

16. Hellwig, O.
Exploring magnetic reversal behavior and domain structure in perpendicular anisotropy layered synthetic antiferromagnets
Condensed Matter Seminar, Lawrence Berkeley National Laboratory, 18.11.2022, Berkeley, USA

17. Helm, M.
Nonlinear THz spectroscopy of two-dimensional systems
Workshop on "Semiconductors, nanostructures, 2D systems, and Dirac matter",
20. - 22.06.2022, Grenoble, France

18. Helm, M.
Free-electron lasers: past, present, and future challenges
International Conference on Free Electron Laser Applications and THz Studies of New States of Matter (TERFEL), 05. - 08.07.2022, Warsaw, Poland

19. Helm, M.
THz sources: from semiconductor antennas to relativistic electrons
47th International Conference on Infrared, Millimeter and Terahertz Waves (IRMMW-THz) 2022,
28.08. - 02.09.2022, Delft, The Netherlands

20. Helm, M.; Singh, A.; Pashkin, O.; Winnerl, S.; Beckh, C.; Sulzer, P.; Leitenstorfer, A.; Schneider, H.
Germanium ultrabroadband THz photoconductive antennas
International School on Terahertz Photonics and Electronics, 08. - 14.05.2022, Pisa, Italy

21. Hlawacek, G.
Spatially resolved materials property tuning using GFIS and LMAIS based FIBs
4th International Conference on Radiation and Emission in Materials, 06. - 08.04.2022, Pattaya, Thailand

22. Hlawacek, G.
Beyond gallium: FIB based local materials property tuning with advanced ion sources
2022 E-MRS Spring Meeting, 30.05. - 03.06.2022, Online

23. Hlawacek, G.
Adding "color" to helium ion microscopy images
Conference on the Application of Accelerators in Research & Industry, 31.10. - 03.11.2022, Denton, USA

24. Hlawacek, G.
Focused ion beam applications using gas field and liquid metal alloy ion sources
Conference on the Application of Accelerators in Research & Industry, 31.10. - 03.11.2022, Denton, USA

25. Hübner, R.
Transmission electron microscopy for the characterization of nanoscale materials
Spezialseminar des Instituts für Werkstoffwissenschaft der TU Bergakademie Freiberg,
20.06.2022, Freiberg, Germany

26. Khan, M.B.; Echresh, A.; Ghosh, S.; Arora, H.; Chava, P.; Jazavandi Ghamsari, S.; Khan, M.M.; Steuer, O.; Prucnal, S.; Hübner, R.; Rebohle, L.; Zhou, S.; Helm, M.; Erbe, A.; Georgiev, Y.
Group IV nanowires: fabrication, characterisation and applications
14th International Conference on Electron Beam Technologies EBT 2022, 26.06. - 01.07.2022, Varna, Bulgaria

27. Khan, M.B.; Echresh, A.; Ghosh, S.; Arora, H.; Chava, P.; Jazavandi Ghamsari, S.; Khan, M.M.; Steuer, O.; Prucnal, S.; Hübner, R.; Rebohle, L.; Zhou, S.; Helm, M.; Erbe, A.; Georgiev, Y.
Group IV nanowires: a versatile toolbox for nano-and optoelectronic device
2022 E-MRS Fall Meeting, 19. - 22.09.2022, Warsaw, Poland

28. Klopf, J.M.; Evtushenko, P.; Helm, M.; Kehr, S.C.; Lehnert, U.; Michel, P.; Pashkin, O.; Winnerl, S.; Zvyagin, S.
The FELBE THz/IR FEL: Overview of the facility and user activities
International Conference on Free Electron Laser Applications and THz Studies of New States of Matter (TERFEL), 05. - 08.07.2022, Warsaw, Poland

29. Lachner, J.; Findeisen, S.; Golser, R.; Kern, M.; Marchhart, O.; Martschini, M.; Wallner, A.; Wieser, A.
Isobar separation with cooled ions and laser light for compact AMS facilities
DPG Frühjahrstagung der Sektion Atome, Moleküle, Quantenoptik und Photonik, 14. - 18.03.2022, Erlangen, Germany

30. Lenz, K.; Pablo-Navarro, J.; Klingner, N.; Hlawacek, G.; Samad, F.; Narkovic, R.; Hübner, R.; Kakay, A.; Canzever, H.; Pilz, W.; Meyer, F.; Mazarov, P.; Bischoff, L.; Bali, R.; Lindner, J.
Magnetic patterning using Ne, Co, and Dy FIB
5. European FIB Network Workshop 2022, 31.08. - 02.09.2022, Hamburg, Germany

31. Lünser, K.
How martensitic transitions make materials smart
Leibniz IKZ Summer School, 31.08. - 02.09.2022, Berlin, Germany

32. Makarov, D.
From curvilinear magnetism to shapeable magnetoelectronics
Yuri Gaididei memorial workshop, 02. - 03.02.2022, Kyiv, Ukraine

33. Makarov, D.
FlexiSens: smart magnetic field sensor technologies
Annual workshop for partners of scia Systems GmbH, 16.03.2022, Chemnitz, Germany

34. Makarov, D.
Druckbare Hochleistungs-Magnetoelektronik
8. Dresdner Werkstoffsymposium – Innovative Werkstoffe für neue Produkte, 02. - 03.06.2022, Dresden, Germany

35. Makarov, D.
Nanomagnetism of magnetoelectric granular thin-film antiferromagnets
15th International Conference on Modern Materials and Technologies: 9th Forum on New Materials, 24. - 29.06.2022, Perugia, Italy

36. Makarov, D.
Skin conformal and printable magnetoelectronics for human-machine interfaces and soft robotics
International Intelligent Materials (IIM) 2022, 29.06. - 01.07.2022, Kiel, Germany

37. Makarov, D.
Geometrically curved and skin-conformal magnetoelectronics
2022 IEEE 22nd International Conference on Nanotechnology (NANO), 04. - 08.07.2022, Palma de Mallorca, Spain

38. Makarov, D.
Flexible und druckbare low-power-Magnetfeldsensoren
11. GMM-Fachtagung Energieautonome Sensorsysteme (EASS), 05. - 06.07.2022, Erfurt, Germany

39. Makarov, D.
Flexible and printed electronics: from interactive on-skin devices to bio/medical applications
Joint European Magnetic Symposia (JEMS), 24. - 29.07.2022, Warsaw, Poland

40. Makarov, D.
Curvilinear magnetism: fundamentals and applications
2022 IEEE 12th International Conference Nanomaterials: Applications & Properties,
11. - 16.09.2022, Krakow, Poland

41. Makarov, D.
Magnetosensitive e-skins and stretchable giant magnetoresistive sensors
"Magnetism and the effect of Electric Field" (MagnEFi) conference, 10. - 14.10.2022, Crete, Greece

42. Makarov, D.
Curvature effects in curvilinear and 3D low dimensional magnetic architectures
8th Spanish Workshop in Nanolithography, Nanolito 2022, 26. - 28.10.2022, Valencia, Spain

43. Makarov, D.
Magnetic composites: from printed magnetoelectronics to smart magnetic soft robots
MRS Fall Meeting, 27.11. - 02.12.2022, Boston, USA

44. Pile, S.; Stienen, S.; Lenz, K.; Narkovic, R.; Wintz, S.; Förster, J.; Mayr, S.; Buchner, M.; Weigand, M.; Ney, V.; Lindner, J.; Ney, A.
Nonstationary spin waves under a uniform excitation in a confined permalloy microstrip directly imaged with STXM-FMR
NESY User Symposium 2022, 29. - 30.09.2022, Leoben, Austria

45. Prucnal, S.
Defect engineering in degenerate semiconductors using intense pulsed light
Ion Implantation and Other Applications of Ions and Electrons, 27. - 30.06.2022, Kazimierz Dolny, Poland

46. Prucnal, S.
Dissolution of dopant-vacancy clusters in semiconductors
2022 E-MRS Spring Meeting, 30.05. - 03.06.2022, Online

47. Pylypovskyi, O.
Computer simulations of magnetic nanoarchitectures
Winter school on theoretical physics, 20.01.2022, Kyiv, Ukraine

48. Pylypovskyi, O.
Exchange and anisotropy-driven effects in antiferromagnetic spin chains
Yuri Gaididei memorial workshop, 02. - 03.02.2022, Kyiv, Ukraine

49. Pylypovskyi, O.
Domain walls in Cr_2O_3
Ukrapro workshop, 01.06.2022, Dresden, Germany

50. Pylypovskyi, O.
Curvilinear antiferromagnets for spintronics applications
2022 IEEE 22nd International Conference on Nanotechnology (NANO), 04. - 08.07.2022, Palma de Mallorca, Spain

51. Pylypovskyi, O.
Three-dimensional antiferromagnetic architectures
12th International Conference on Metamaterials, Photonic Crystals and Plasmonics (META),
19. - 22.07.2022, Torremolinos, Spain

52. Rebohle, L.
Tutorial: Thermal processes in short time annealing: Application examples and current trends
18th International Conference on Plasma Surface Engineering, 12. - 15.09.2022, Erfurt, Germany

53. Rebohle, L.; Prucnal, S.; Berencen, Y.; Begeza, V.; Zhou, S.
A snapshot review on flash lamp annealing of semiconductor materials
International Conference on Ion Implantation Technology, 25. - 29.09.2022, San Diego, USA

54. Rugel, G.
Nuclear astrophysics with accelerator mass spectrometry
17th Rußbach School on Nuclear Astrophysics, 13. - 19.03.2022, Rußbach, Austria

55. Rugel, G.
Combining a SIMS with AMS: Super-SIMS at DREAMS - Status of this challenging initiative
National Workshop on "Chronological systematics and their applications in Earth Sciences", 19. - 21.04.2022, New Delhi, India

56. Schultheiß, K.
Neuromorphic computing with magnons
7th Workshop on Magnonics, 01.08.2022, Oxnard, USA

57. Schultheiß, K.
Neuromorphic computing with magnons
CMD29 Conference, 22.08.2022, Manchester, UK

58. Singh, A.; Pashkin, O.; Winnerl, S.; Welsch, M.; Beckh, C.; Sulzer, P.; Leitenstorfer, A.; Helm, M.; Schneider, H.
Ultrabroadband terahertz pulses from a Ge:Au photoconductive emitter
8th International Conference on Antennas and Electromagnetic Systems (AES2022), 24. - 27.05.2022, Marrakesh, Morocco

59. Uykur, E.
Optical fingerprints of unconventional carriers in Kagome metals
APS March Meeting, 14. - 18.03.2022, Chicago, USA

60. Volkov, O.
Local and non-local curvature-induced chiral effects in nanomagnetism
2022 Joint MMM-INTERMAG, 10. - 14.01.2022, New Orleans, USA / Online

61. Volkov, O.
Curvilinear nanomagnetism
International Conference on Materials Science, 26. - 28.10.2022, Verona, Italy

62. Winnerl, S.
Nonequelibrium carrier dynamics in Landau quantized graphene and mercury cadmium telluride
Advanced Properties and Processes in Optoelectronic Materials and Systems (APROPOS 18), 05. - 07.10.2022, Vilnius, Litauen

63. Winnerl, S.
Auger scattering in massless Dirac and Kane materials
International Conference on Free Electron Laser Applications and THz Studies of New States of Matter (TERFEL), 05. - 08.07.2022, Warsaw, Poland

64. Ziegenrücker, R.
Super-SIMS; Combining a SIMS with AMS – Status of this challenging initiative
GEOANALYSIS 2022 - Workshop SIMS ANALYSIS, 06. - 15.08.2022, Freiberg/Dresden, Germany

Conferences, workshops, colloquia and seminars

Organization of conferences and workshops

1. Rebohle, L.
   Ultrakurzzeitprozessierung: Transfer in die Industrie
   05.04.2022, Dresden, Germany

2. Helm, M.; Evtushenko, P.; Michel, P.; Klopf, M.
   FELs of Europe: topical workshop on selected problems in FEL physics: from soft X-rays to THz
   25. – 27.04.2022, Dresden, Germany

3. Yang, D.; Hemme, E.G.; Sher, M.-J.; Zhou, S.
   E-MRS Spring Meeting, Symposium B "Ultra-doped semiconductors by non-equilibrium processing for electronic, photonic and spintronic applications"
   30.05. – 03.06.2022, virtual event

4. Grin, Y.; Makarov, D.; Büchner, B.; van den Brink, J.
   UKRAPRO workshop: Condensed matter physics and material science assisted by machine learning: Potential, results and challenges
   01.06.2022, Leibniz IFW Dresden, Dresden, Germany

5. Makarov, D.
   Workshop "Transfer to Industry" of COST action MAGNETOFON: Ultrafast opto-magneto-electronics for non-dissipative information technology
   07.06. – 08.06.2022; HZDR, Dresden, Germany

6. Mika, F.; Sobola,D.; Hlawacek, G.
   FIT4NANO Summerschool
   20. – 24.06.2022, Brno, Czech Republic

7. Marszałek, M.; Mitura-Nowak, M.; Hlawacek, G.
   FIT4NANO Workshop
   11. – 13.07.2022, Krakow, Poland

8. Erbe, A.
   DNA Mitteldeutschland Workshop
   26.08.2022, Dresden, Germany

9. Audoit, G; Moll, P.; Córdoba, R.; Bábor, P.; Hlawacek, G.; Hobler, G.; Mosberg, A.; Reuteler, J.;Winkler, R.
   5th Eu-F-N workshop
   31.08. – 02.09.2022, Hamburg, Germany

10. Erbe, A.; Zahn, P.
    NANONET+ FWIO FWIM NaMLab Workshop 2022 - 2D Materials and ultra-high doped semiconductors: electronics, photonics and sensing
    04. – 06.10.2022, Görlitz, Germany

Colloquia

1. Chen, J.
   National University of Singapore
   Symmetry breaking by materials engineering for spin-orbit-torque technology
   30.08.2022

2. Manchon, A.
   Aix-Marseille Université, Centre Interdisciplinaire de Nanoscience de Marseille (CINaM), France
   Exploring the potential of spin-orbitronics
   30.05.2022

3. Napolitani, E.
University of Padova, Italy
Hyperdoping of group-IV semiconductors by pulsed laser melting
03.11.2022

Seminars

1. Bradely, M.
University of Colorado, USA
Recent progress in the theory of nanoscale surface patterns produced by ion bombardment
13.09.2022

2. Costina, I.
Leibniz IHP, Frankfurt/Oder, Germany
Analytical techniques for semiconductor characterization and failure analysis
23.02.2022

3. Devolder, T.
CNRS, Université Paris-Saclay, France
Inductive experiments with spin waves as energy and information carriers
11.11.2022

4. Donnelly, C.
MPI-CPfS Dresden, Germany
Three-dimensional spin textures: from the bulk to patterned nanostructures
03.05.2022

5. Duffy, R.
Tyndall National Institute, Cork, Ireland
Fabrication and electronic functionality in nano-structures and nano-films – a case study in doping strategies
23.11.2022

6. Khurgin, J. B.
Johns Hopkins University, Baltimore/MD, USA
Epsilon (and mu) near zero materials – photonics on steroids?
09.09.2022

7. Li, F.
MPI Halle,Germany
Defects in semiconductors for quantum applications
16.02.2022

8. Lüdge, K.
TU Ilmenau, Germany
Photonic reservoir computing: analytic insights and possibilities for optimization
25.04.2022

9. Meyer, J.
Universität Tübingen, Germany
Analyzing and assembling layered materials, atom by atom and layer by layer, in 2D and 3D
26.07.2022

10. Pané i Vidal, S.
ETH Zurich, Institute of Robotics and Intelligent Systems, Switzerland
Materials for small-scale robotics
22.08.2022

11. Slavkovska, Z.
ANU, Canberra, Australia
Radio-impurity measurements for dark matter detection
25.05.2022

12. Solina, D.
University of Technology Sydney, Australia
Gold-manganese: Phase transformations and diffusion studies
22.07.2022

13. Sun, N.
W.M. Keck Laboratory for Integrated Ferroics, ECE Department, Northeastern University, Boston/MA, USA
Magnetoelectric materials and M/NEMS: A path toward novel electronics with ultra-low size, weight, and power consumption
23.05.2022

14. Suess, D.
University of Vienna, Austria
From inverse design to optimized sensor and permanent magnets
14.11.2022

15. Wittmann, A.
JGU Mainz, Germany
Spintronic phenomena at unconventional hybrid interfaces
17.06.2022

Projects

The projects are listed by funding institution and project starting date. In addition, the institute has several bilateral service collaborations with industrial partners and research institutions. These activities are not included in the following overview.

European Projects

1. 01/2019 – 06/2023   European Union   EU
RADIATE – Research and development with ion beams - Advancing technology in Europe
Prof. J. Faßbender   Phone: 0351 260 3096   j.fassbender@hzdr.de

2. 10/2020 – 04/2024   European Union   EU
BIONANOSENS – Deeping collaboration on novel biomolecular electronics based on "smart" nanomaterials
Dr. D. Makarov   Phone: 0351 260 3273   d.makarov@hzdr.de

3. 10/2020 – 09/2023   NATO   NATO
natoMYP – Spintronic devices for microwave detection and energy harvesting applications
Dr. D. Makarov   Phone: 0351 260 3273   d.makarov@hzdr.de

4. 11/2020 – 10/2023   European Cooperation in Science and Technology   COST
FIT4NANO – Focused ion technology for nanomaterials
Dr. G. Hlawacek   Phone: 0351 260 3409   g.hlawacek@hzdr.de

5. 11/2020 – 10/2024   European Union   EU
RADICAL – Fundamental breakthrough in detection of atmospheric free radicals
Dr. Y. Georgiev   Phone: 0351 260 2321   y.georgiev@hzdr.de

6. 05/2021 – 04/2025   European Union   EU
Chemical elements as tracers of the evolution of the cosmos - infrastructures for nuclear astrophysics
Prof. A. Wallner   Phone: 0351 260 3274   a.wallner@hzdr.de

7. 10/2022 – 09/2025   European Union   EU
Metrology for the harmonisation of measurements of environmental pollutants in Europe
Dr. S. Winkler   Phone: 0351 260 3802   stephan.winkler@hzdr.de

8. 10/2022 – 09/2026   European Union   EU
Nonlinear magnons for reservoir computing in reciprocal space
Dr. K. Schultheiß   Phone: 0351 260 2919   k.schultheiss@hzdr.de

9. 10/2022 – 09/2026   European Union   EU
Cognitive robotic tools for human-centered small-scale multi-robot operations
Dr. D. Makarov   Phone: 0351 260 3273   d.makarov@hzdr.de

10. 09/2022 – 08/2026   European Union   EU
Recyclable materials development at analytical research infrastructures
Dr. S. Facsko   Phone: 0351 260 2987   s.facsko@hzdr.de

Helmholtz Association Projects

1   01/2019 – 12/2023   Helmholtz-Gemeinschaft   HGF
CROSSING – Crossing borders and scales - an interdisciplinary approach
Dr. J. v. Borany   *Phone: 0351 260 3378*   *j.v.borany@hzdr.de*

2   12/2019 – 11/2024   Helmholtz-Gemeinschaft   HGF
Helmholtz Innovation Lab – FlexiSens
Dr. D. Makarov   *Phone: 0351 260 3273*   *d.makarov@hzdr.de*

3   02/2020 – 01/2025   Helmholtz-Gemeinschaft   HGF
Helmholtz Innovation Lab – UltraTherm
Dr. L. Rebohle   *Phone: 0351 260 3368*   *l.rebohle@hzdr.de*

4   02/2022 – 09/2023   Helmholtz-Gemeinschaft   HGF
Helmholtz Enterprise – Memristor applications, artificial intelligence and fabrication
S. Krüger   *Phone: 0351 260 2180*   *s.krueger@hzdr.de*

5   09/2022 – 12/2022   Helmholtz-Gemeinschaft   HGF
Helmholtz Enterprise – Field study fellowship "MagFeel"
Dr. D. Makarov   *Phone: 0351 260 3273*   *d.makarov@hzdr.de*

German Science Foundation Projects

1   04/2018 – 02/2022   Deutsche Forschungsgemeinschaft   DFG
IMASTE – Graphene encapsulated quasi-2D materials
Dr. A. Krasheninnikov *Phone: 0351 260 3148*   *a.krasheninnikov@hzdr.de*

2   01/2019 – 03/2022   Deutsche Forschungsgemeinschaft   DFG
Printable giant magnetoresistive sensors with high sensitivity at small magnetic fields
Dr. D. Makarov   *Phone: 0351 260 3273*   *d.makarov@hzdr.de*

3   06/2019 – 09/2022   Deutsche Forschungsgemeinschaft   DFG
Interacting magnonic currents and chiral spin textures for energy efficient spintronics
Dr. H. Schultheiß   *Phone: 0351 260 3243*   *h.schultheiss@hzdr.de*

4   07/2019 – 12/2022   Deutsche Forschungsgemeinschaft   DFG
3D tailoring of all-oxide heterostructures by ion beams
Dr. S. *Zhou*   *Phone: 0351 260 2484*   *s.zhou@hzdr.de*

5   07/2019 – 06/2022   Deutsche Forschungsgemeinschaft   DFG
Lab-on-chip systems carrying artificial motors for multiplexed and multiparametric biochemical assays
Dr. D. Makarov   *Phone: 0351 260 3273*   *d.makarov@hzdr.de*

6   10/2019 – 03/2023   Deutsche Forschungsgemeinschaft   DFG
3D transport of spin waves in curved nano-membranes
Dr. A. Kakay   *Phone: 0351 260 2689*   *a.kakay@hzdr.de*

7   11/2019 – 04/2023   Deutsche Forschungsgemeinschaft   DFG
Functionalization of ultrathin MoS_2 by defect engineering
Dr. A. Krasheninnikov *Phone: 0351 260 3148*   *a.krasheninnikov@hzdr.de*

8   02/2020 – 05/2023   Deutsche Forschungsgemeinschaft   DFG
TRIGUS - Friction-induced interface and structure-changing processes in dry lubrication systems under defined atmospheres
Dr. M. Krause   *Phone: 0351 260 3578*   *matthias.krause@hzdr.de*

9   04/2020 – 08/2024   Deutsche Forschungsgemeinschaft   DFG
CurvMag – Non-local chiral interactions in corrugated magnetic nanoshells
Dr. D. Makarov   *Phone: 0351 260 3273*   *d.makarov@hzdr.de*

| 10 | 07/2020 – 06/2024 | Deutsche Forschungsgemeinschaft | DFG |

SFB 1415 – Chemistry of synthetic two-dimensional materials
Dr. A. Krasheninnikov Phone: 0351 260 3148   a.krasheninnikov@hzdr.de

| 11 | 08/2020 – 07/2023 | Deutsche Forschungsgemeinschaft | DFG |

AMSIGE – Topological order and its correlation to self-atom transport in amorphous materials:silicon and germanium as model systems
Dr. M. Posselt   Phone: 0351 260 3279   m.posselt@hzdr.de

| 12 | 09/2020 – 08/2023 | Deutsche Forschungsgemeinschaft | DFG |

3Dmag – Krümmungsinduzierte Effekte in magnetischen Nanostrukturen
Dr. D. Makarov   Phone: 0351 260 3273   d.makarov@hzdr.de

| 13 | 11/2020 – 10/2023 | Deutsche Forschungsgemeinschaft | DFG |

miracuSi – Room-temperature broadband MIR photodetector based on Si:Te for wafer-scale integration
Dr. S. *Zhou*   *Phone: 0351 260 2484   s.zhou@hzdr.de*

| 14 | 12/2020 – 11/2023 | Deutsche Forschungsgemeinschaft | DFG |

MUMAGI II – Microscopic understanding of disorder induced ferromagnetism in B2-alloy thin films II
Dr. R. Bali   Phone: 0351 260 2919   r.bali@hzdr.de

| 15 | 01/2021 – 12/2023 | Deutsche Forschungsgemeinschaft | DFG |

eSensus – Compliant and breathable magnetoelectronics: towards electronic proprioception
Dr. D. Makarov   Phone: 0351 260 3273   d.makarov@hzdr.de

| 16 | 04/2021 – 03/2024 | Deutsche Forschungsgemeinschaft | DFG |

Hybrid nanomechanical systems including atom-scale defects based on silicon carbide
Dr. A. Erbe   Phone: 0351 260 2366   a.erbe@hzdr.de

| 17 | 06/2021 – 05/2024 | Deutsche Forschungsgemeinschaft | DFG |

Hybrid nanomechanical systems including atom-scale defects based on silicon carbide
Dr. G. Astakhov   Phone: 0351 260 3894   g.astakhov@hzdr.de

| 18 | 06/2021 – 05/2024 | Deutsche Forschungsgemeinschaft | DFG |

TRANSMAX – Transport and magnetic properties of disordered Cr_2AlC MAX phases
Dr. R. Bali   Phone: 0351 260 2919   r.bali@hzdr.de

| 19 | 08/2021 – 07/2024 | Deutsche Forschungsgemeinschaft | DFG |

TOPCURVE – Curvature-induced effects in magnetic nanostructures
Dr. A. Kakay   Phone: +49 351 260 2689   a.kakay@hzdr.de

| 20 | 10/2021 – 10/2023 | Deutsche Forschungsgemeinschaft | DFG |

Coupling effects in re-programmable micro-matter
Dr. S. Fähler   Phone: 0351 260 2775   s.faehler@hzdr.de

| 21 | 01/2022 – 12/2024 | Deutsche Forschungsgemeinschaft | DFG |

Search for magnetochiral responses in curvilinear geometries
Dr. O. Volkov   Phone: 0351 260 2186   o.volkov@hzdr.de

| 22 | 01/2022 – 12/2024 | Deutsche Forschungsgemeinschaft | DFG |

Spin-momentum relaxation dynamics of Dirac fermions in HgTe-based topological insulators
Dr. G. Astakhov   Phone: 0351 260 3894   g.astakhov@hzdr.de

| 23 | 01/2022 – 06/2023 | Deutsche Forschungsgemeinschaft | DFG |

Martensitic phase transformations and twinning in epitaxially grown nickel titanium films
Dr. S. Fähler   Phone: 0351 260 2775   s.faehler@hzdr.de

| 24 | 02/2022 – 01/2025 | Deutsche Forschungsgemeinschaft | DFG |

Design of nanostructured noble-metal chalcogenide electrocatalysts for hydrogen evolution reaction
Dr. A. Krasheninnikov Phone: 0351 260 3148   a.krasheninnikov@hzdr.de

| 25 | 02/2022 – 02/2025 | Deutsche Forschungsgemeinschaft | DFG |

Spin wave quantisation and non-linear scattering in non-reciprocal materials
Dr. O. Gladii *Phone: 0351 260 3151* *o.gladii@hzdr.de*

| 26 | 03/2022 – 09/2025 | Deutsche Forschungsgemeinschaft | DFG |

Interplay between frustrated, correlated and topological quantum electronic states in magnetic Kagome metals
Dr. E. Uykur *Phone: 0351 260 2494* *e.uykur@hzdr.de*

| 27 | 04/2022 – 03/2025 | Deutsche Forschungsgemeinschaft | DFG |

Influences and resistance development of microorganisms on low concentrations of nanomaterials in geometrically defined environments
Dr. D. Makarov *Phone: 0351 260 3273* *d.makarov@hzdr.de*

| 28 | 04/2022 – 03/2025 | Deutsche Forschungsgemeinschaft | DFG |

A DNA origami-brick system for the fabrication of nanoelectronic elements
Dr. A. Erbe *Phone: 0351 260 2366* *a.erbe@hzdr.de*

| 29 | 04/2022 – 09/2026 | Deutsche Forschungsgemeinschaft | DFG |

Graduiertenkolleg 2767 – Supracolloidal structures: From materials to optical and electronic devices
Dr. A. Erbe *Phone: 0351 260 2366* *a.erbe@hzdr.de*

| 30 | 07/2022 – 06/2024 | Deutsche Forschungsgemeinschaft | DFG |

Strain-tunable magnetic vortex oscillators
Dr. V. Iurchuk *Phone: 0351 260 2049* *v.iurchuk@hzdr.de*

| 31 | 07/2022 – 06/2025 | Deutsche Forschungsgemeinschaft | DFG |

New avenues to nanofabrication: assembly of vertical heterostructures from nanopatterned two-dimensional materials
Dr. A. Krasheninnikov *Phone: 0351 260 3148* *a.krasheninnikov@hzdr.de*

| 32 | 08/2022 – 07/2025 | Deutsche Forschungsgemeinschaft | DFG |

Organic chromophores on ferromagnets illuminated: photochemical and magnetic study
Dr. A. Lindner *Phone: 0351 260 2435* *a.lindner@hzdr.de*

| 33 | 08/2022 – 06/2023 | Deutsche Forschungsgemeinschaft | DFG |

Thermal micro energy harvesting by thermomagnetic film actuation
Dr. S. Fähler *Phone: 0351 260 2775* *s.faehler@hzdr.de*

| 34 | 11/2022 – 10/2024 | Deutsche Forschungsgemeinschaft | DFG |

Effects of atomic defects at lateral and vertical metal-semiconductor interfaces on the properties of two-dimensional transition-metal dichalcogenide heterostructures
Dr. A. Krasheninnikov *Phone: 0351 260 3148* *a.krasheninnikov@hzdr.de*

Federally and Saxony State Funded Projects

1   11/2018 – 03/2022   Bundesministerium für Bildung und Forschung   BMBF
Metal-germanium interface: Schottky barrier and ohmic contacts
Dr. S. Prucnal   Phone: 0351 260 2065   s.prucnal@hzdr.de

2   07/2019 – 01/2022   Sächsische Aufbaubank   SAB
GNSS – Innovative product platform for space-based global navigation satellite systems
Dr. J. v. Borany   Phone: 0351 260 3378   j.v.borany@hzdr.de

3   10/2019 – 09/2023   Bundesministerium für Bildung und Forschung   BMBF
SiGeSn – Group IV-heterostructures for most advanced nanoelectronics devices
Dr. Y. Georgiev   Phone: 0351 260 2321   y.georgiev@hzdr.de
Dr. S. Prucnal   Phone: 0351 260 2065   s.prucnal@hzdr.de

4   10/2019 – 09/2023   Bundesministerium für Bildung und Forschung   BMBF
SPES3 – Black phosphorus in sensitive, selective, and stable sensors
Dr. A. Erbe   Phone: 0351 260 2366   a.erbe@hzdr.de

5   03/2020 – 08/2022   Arbeitsgemeinschaft industrielle Forschung   AiF
Magnetic nanostructures
Dr. L. Bischoff   Phone: 0351 260 2866   l.bischoff@hzdr.de

6   06/2020 – 05/2022   EFDS e. V.   EFDS
Novel Eddy current sensors based on flexible GMR sensor arrays for the analysis of components of complex shape
Dr. D. Makarov   Phone: 0351 260 3273   d.makarov@hzdr.de

7   10/2020 – 09/2023   Bundesministerium für Wirtschaft und Klimaschutz   BMWK
RoSiLIB – Nanoporous Si anodes of lithium ion batteries by microdroplet quenching
Dr. K.-H. Heinig   Phone: 0351 260 3288   k.h.heinig@hzdr.de

8   12/2020 – 01/2022   Sächsische Aufbaubank   SAB
NanoNeuroNet – Nanostructures for neural networks
Dr. A. Erbe   Phone: 0351 260 2366   a.erbe@hzdr.de

9   04/2021 – 03/2024   Bundesministerium für Bildung und Forschung   BMBF
MAG4INK – Design and manufacture of printed magnetic field sensors for flexible electronics
Dr. D. Makarov   Phone: 0351 260 3273   d.makarov@hzdr.de

10 05/2021 – 05/2022   Sächsische Aufbaubank   SAB
Contactless human-machine interface based on flexible magnetic field sensors
Dr. D. Makarov   Phone: 0351 260 3273   d.makarov@hzdr.de

11 07/2021 – 06/2024   LeibnizX   LX
Defect-engineering in graphene via focused ion beam for tailored van der Waals epitaxy of h-BN
Dr. A. Krasheninnikov Phone: 0351 260 3148   a.krasheninnikov@hzdr.de

12 05/2021 – 04/2025   Sächsische Aufbaubank   SAB
Gallium oxide fabrication with ion beams (GoFIB)
Dr. G. Hlawacek   Phone: 0351 260 3409   g.hlawacek@hzdr.de

13 10/2022 – 09/2027   Bundesministerium für Bildung und Forschung   BMBF
Diamond based quantum sensing for NeurOSurgery (DiaQNOS) – Multiplex sensorics and imaging
Dr. G. Balasubramanian Phone: 0351 260 3799   g.balasubramanian@hzdr.de

Personnel Exchange Projects and Society Chairs

1   05/2017 – 12/2023   Institute of Electrical and Electronics Engineers   IEEE
     IEEE Magnetics Society – German chapter chair
     Prof. J. Faßbender   Phone: 0351 260 3096   j.fassbender@hzdr.de

2   03/2021 – 06/2024   Sino-German-Center   SGC
     Magnetosensitive e-skins for magnetic perception ability of human and soft robots
     Dr. D. Makarov   Phone: 0351 260 3273   d.makarov@hzdr.de

3   04/2021 – 03/2023   Alexander-von-Humboldt-Stiftung   AvH
     Alexander von Humboldt fellowship Dr. Li
     Prof. M. Helm   Phone: 0351 260 2260   m.helm@hzdr.de

4   04/2022 – 03/2024   Alexander-von-Humboldt-Stiftung   AvH
     Alexander von Humboldt fellowship Dr. Roldan
     Dr. D. Makarov   Phone: 0351 260 3273   d.makarov@hzdr.de

Organization chart

Institute of Ion Beam Physics and Materials Research
Prof. Dr. Jürgen Faßbender   *Prof. Dr. Manfred Helm*

Ion Beam Center
Dr. Stefan Facsko,
Dr. René Heller

Nanoelectronics
Prof. Dr. Artur Erbe

Accelerator Mass Spectrometry
Prof. Dr. Anton Wallner

Ion Accelerators
Dr. Shavkat Akhmadaliev

Nanomaterials and Transport
Prof. Dr. Artur Erbe,
Dr. Matthias Krause

Intelligent Materials and Systems
Dr. Denys Makarov

Ion Implantation and Modification of Materials
Ulrich Kentsch

Nanofabrication and Analysis
Dr. Ciaran Fowley,
Dr. Yordan Georgiev

Ion Beam Analysis
Dr. René Heller

Semiconductor Materials
Dr. Shengqiang Zhou

Ion Induced Nanostructures
Dr. Gregor Hlawacek

Magnetism
Dr. Jürgen Lindner

Spectroscopy
Dr. Stephan Winnerl

Structural Analysis
Dr. René Hübner

Micromagnetic Modeling
Dr. Attila Kákay

Atomistic Simulations
Dr. Arkady Krasheninnikov

Magnonics
Dr. Helmut Schultheiß

Quantum Materials and Technology
Dr. Georgy Astakhov

FWI Doctoral Training Programme
Coordinator: Dr. Peter Zahn

List of personnel 2022

DIRECTORS	OFFICE
Prof. Dr. M. Helm, Prof. Dr. J. Faßbender	**S. Gebel, S. Kirch**

SCIENTIFIC STAFF

Permanent staff

Dr. C. Akhmadaliev
Dr. G. Astakhov
Dr. R. Bali
Dr. E. Dimakis
Dr. D. Erb
Prof. Dr. A. Erbe
Dr. S. Facsko
Dr. S. Fähler
Dr. C. Fowley
Dr. Y. Georgiev
Dr. M. Ghorbani-Asl
Dr. R. Heller
Dr. G. Hlawacek
Dr. R. Hübner
Dr. A. Kákay
Dr. A. Krasheninnikov
Dr. M. Krause
Dr. J. Lachner
Dr. K. Lenz
Dr. J. Lindner
Dr. D. Makarov
Dr. F. Munnik
Dr. A. Pashkin
Dr. K. Potzger
Dr. S. Prucnal
Dr. L. Rebohle
Dr. G. Rugel
Dr. H. Schultheiß
Prof. Dr. A. Wallner
Dr. S. Winnerl
Dr. P. Zahn
Dr. S. Zhou

Non-permanent

Dr. H. Arora
Dr. G. Balasubramanian
Dr. Y. Berencén
Dr. L. Bischoff
Dr. G. S. Canon Bermudez (P)
Dr. C. Cherkouk (P)
Dr. F. Davies (P)
Dr. J. Duan
Dr. H.-J. Engelmann (P)
Dr. J.A. Fernandez-Roldan (P)
Dr. S. Fichter
Dr. C. Folgner (P)
Dr. R. Friedrich (P)
Dr. F. Ganss
Dr. A. Garcia Valenzuela (P)
Dr. O. Gladii (P)
Dr. F. Goncalves (P)
Dr. K.-H. Heinig (P)
Prof. Dr. O. Hellwig
Dr. M. Hollenbach
Dr. V. Iurchuk
Dr. M.B. Khan (P)
Dr. C. Kielar (P)
Dr. N. Klingner (P)
Dr. S. Kretschmer (P)
Dr. N. Lambeva
Dr. R. Li (P)

Dr. A. Lindner
Dr. S. Lohmann (P)
Dr. K. Lünser (P)
Prof. Dr. W. Möller (P)
Dr. I. Mönch (P)
Dr. R. Podlipec (P)
Dr. M. Posselt (P)
Dr. O. Pylypovskyi
Dr. R. Rana
Dr. R. Salikhov (P)
Dr. K. Schultheiß
Dr. J. Schütt (P)
Dr. M. Sequeira (P)
Dr. A. Singh
Dr. S. Sorokin (P)
Dr. K. Stübner
Dr. X. Sun
Dr. E. Uykur
Dr. I. Veremchuk
Dr. C. Vivo Vilches (P)
Dr. O. Volkov
Dr. S. Winkler
Dr. R. Xu (P)
Dr. Y. Zabila (P)

TECHNICAL STAFF

Permanent staff   ### Non-permanent

Rb. Aniol	D. Medger	M. Steinert	M. Baum
Rm. Aniol	R. Mester	T. Tarnow	A. Berens (P)
C. Bischoff	Dr. R. Narkovic	Dr. T. Voitsekhivska	K. Jarschel
T. Döring	T. Naumann	J. Wagner	S. Krüger (P)
S. Eisenwinder	C. Neisser	A. Weise	R. Lehmann (P)
M. Görlich	F. Nierobisch	A. Weißig	Dr. L. Ramasubramanian (P)
H. Gude	T. Putzke	J. Winkelmann	
J. Heinze	A. Reichel	R. Ziegenrücker	L. Scharf
A. Henschke	B. Scheumann	L. Zimmermann	C. Schmoldt (P)
H. Hilliges	G. Schnabel	J. Zscharschuch	A. Vollmer
Dr. R. Illing	A. Schneider		A. Worbs
U. Kentsch	A. Scholz		S. Worm
S. Klare	T. Schönherr		
R. Krause	C. Schubert		
A. Kunz	J. Schulz		
K. Lang	T. Schumann		
H. Lange			
U. Lucchesi			
F. Ludewig			

(P) Projects

PhD STUDENTS

Y. Alsaadawi	P. Heinig	A. Luferau	S. Shakeel
V. Begeza	C. Heins	P. Makushko	O. Steuer
M. Bejarano	D. Hilliard	E.S. Oliveros Mata	Y. Sun
U. Bektas	T. Hula	K. Mavridou	T. Svetikova Uaman
O. Bezsmertna	N. Jagtap	B. Neumann	D. Tucholski
J. Cabaco Salgado	M. Jain	G. Patel	T. Weinert
P. Chava	M.M. Khan	B. Rodriguez Barea	S. Wen
A. Echresh	D. Koll	F. Samad	J. Wolf
M. Faria	L. Körber	P. Santra	N. Yuan
Z. Fekri	Yi Li	S. Schuba	G. Zhang
I. Fotev	K. Lin	A. Seidl	Y. Zhou
Y. Ge	F. Long	M.S. Shaikh	S. Zwickel
S. Ghosh			

STUDENTS (Diploma / MSc / BSc)

D. Bhattacharya	M. Chennur	A. Pandey	P. Singh
M. Bhavsar	F. Hergenhan	G. Schmidt	A. Wendler